

---

# Breaking symmetry: reconstitution of unmixing and polarization events in model membranes

Ilaria Visco

---



München 2015





---

# **Breaking symmetry: reconstitution of unmixing and polarization events in model membranes**

**Ilaria Visco**

---

Dissertation  
an der Fakultät für Biologie  
der Ludwig-Maximilians-Universität  
München

vorgelegt von  
Ilaria Visco  
aus Latina (Italien)

München, den 05. März 2015

Erstgutachter: Prof. Dr. Kirsten Jung  
Zweitgutachter: Prof. Dr. Marc Bramkamp  
Tag der mündlichen Prüfung: 30. Juli 2015

# Eidesstattliche Erklärung

Hiermit versichere ich an Eides statt, dass die vorliegende Dissertation von mir selbstständig und ohne unerlaubte Hilfe angefertigt wurde. Des Weiteren erkläre ich, dass ich nicht anderweitig ohne Erfolg versucht habe, eine Dissertation einzureichen oder mich der Doktorprüfung zu unterziehen. Die vorliegende Dissertation liegt weder ganz, noch in wesentlichen Teilen einer anderen Prüfungskommission vor.

München, 05. März 2015

(Ilaria Visco)



# Contents

<b>Eidesstattliche Erklärung</b>	<b>v</b>
<b>List of Figures</b>	<b>xiii</b>
<b>List of Tables</b>	<b>xv</b>
<b>List of Publications</b>	<b>xvii</b>
<b>Abstract</b>	<b>xix</b>
<b>Zusammenfassung</b>	<b>xxi</b>
<b>I INTRODUCTION</b>	<b>1</b>
<b>1 Introduction</b>	<b>3</b>
1.1 Relevance of polarity for living systems . . . . .	3
1.2 Bottom-up synthetic biology: a viable approach to understand polarity . . . .	6
1.3 GUVs and SLBs as model membranes to reconstitute polarization events . .	9
1.4 Biophysical characterization of model membranes dynamics and lipid-protein interactions . . . . .	13
1.5 Experimental approaches to reconstitute unmixing and polarization events in model membranes . . . . .	16
<b>II MATERIALS AND METHODS</b>	<b>19</b>
<b>2 Materials and sample preparation</b>	<b>21</b>
2.1 Materials . . . . .	21
2.1.1 Lipids . . . . .	21
2.1.2 Protonation of phosphoinositides using acid . . . . .	21
2.1.3 Fluorescent lipids . . . . .	22
2.1.4 Fluorescent dyes . . . . .	22
2.1.5 eGFP-His6 expression and purification . . . . .	22
2.1.6 PLAP purification and labeling . . . . .	22
2.1.7 HA TM peptides synthesis and labeling . . . . .	22
2.1.8 LGL-1 expression and purification . . . . .	23
2.1.9 LGL-1 MTS peptides synthesis and labeling . . . . .	23

2.1.10	Additional materials . . . . .	23
2.2	<i>In vitro</i> LGL-1 phosphorylation by human PKC- $\zeta$ . . . . .	24
2.3	Model membranes . . . . .	24
2.3.1	Preparation of SUVs for circular dichroism measurements . . . . .	24
2.3.2	Preparation of LUVs . . . . .	24
2.3.3	Preparation of GUVs . . . . .	25
2.3.4	Preparation of SLBs . . . . .	26
2.4	Budding of intramembrane domains in GUVs . . . . .	27
2.5	Protein reconstitution in model membranes . . . . .	27
2.5.1	PLAP reconstitution in SLBs . . . . .	27
2.5.2	HA TM peptide reconstitution in SLBs . . . . .	29
2.5.3	HA TM peptide reconstitution in GUVs . . . . .	29
2.6	Cyclodextrin-mediated lipid exchange . . . . .	29
2.6.1	Cyclodextrin-lipid complexes preparation . . . . .	29
2.6.2	Formation of asymmetric SLBs . . . . .	30
2.6.3	Formation of asymmetric GUVs . . . . .	30
2.6.4	Cyclodextrin-mediated GUV shape transformation . . . . .	30
2.7	Leaflet specific labeling . . . . .	30
2.7.1	Leaflet specific labeling in SLBs . . . . .	30
2.7.2	Leaflet specific labeling in GUVs . . . . .	31
<b>3</b>	<b>Methods</b>	<b>33</b>
3.1	Confocal fluorescence microscopy and correlation spectroscopy . . . . .	33
3.1.1	Optical Setup . . . . .	33
3.1.2	FRAP on GUVs . . . . .	33
3.1.3	Point-FCS on SLBs . . . . .	34
3.1.4	Point-FCS on GUVs and in presence of LUVs . . . . .	35
3.1.5	Line-scan FCS on SLBs and GUVs . . . . .	36
3.2	GUV image analysis for determining partitioning coefficients . . . . .	37
3.3	Image processing and analysis . . . . .	38
3.3.1	Measurements in thresholded images . . . . .	38
3.3.2	Determination of $L_o$ partitioning coefficients in GUVs . . . . .	39
3.3.3	Determination of protein binding to GUVs . . . . .	39
3.3.4	Determination of protein binding to SLBs . . . . .	39
3.4	Circular dichroism spectroscopy . . . . .	40
3.5	Dynamic light scattering and $\zeta$ -potential . . . . .	40
3.6	Statistical analysis . . . . .	40
<b>III</b>	<b>RESULTS AND DISCUSSION</b>	<b>41</b>
<b>4</b>	<b>Asymmetric supported lipid bilayer formation via methyl-<math>\beta</math>-cyclodextrin mediated lipid exchange</b>	<b>43</b>
4.1	The upper leaflet of DOPC SLBs can be enriched with SM to form asymmetric bilayers. . . . .	45
4.2	Leaflet asymmetry is stable for several hours . . . . .	47

4.3	The asymmetry in a SLB can also be generated in the presence of a reconstituted membrane protein . . . . .	49
4.4	SM in the lower leaflet of an aSLB is required for phase separation in both leaflets . . . . .	52
<b>5</b>	<b>Shape transformations of asymmetric giant unilamellar vesicles</b>	<b>61</b>
5.1	Bulging of intramembrane asymmetric domains in GUVs . . . . .	62
5.2	Shape transformations in GUVs asymmetrically enriched with PG . . . . .	64
5.3	FRAP assay for vesicle fission . . . . .	67
<b>6</b>	<b>Lateral organization of the influenza virus hemagglutinin transmembrane helix into asymmetric model membranes</b>	<b>73</b>
6.1	Line-scan FCS can probe lipid dynamics independently in each SLB leaflet . . . . .	75
6.2	Partitioning of influenza HA into symmetric and asymmetric domains in SLBs . . . . .	75
6.3	Partitioning of influenza HA into symmetric and asymmetric domains in GUVs . . . . .	77
6.3.1	Both WT and GS520AA mutant HA TM peptides partition into the Ld domains of symmetric GUVs . . . . .	77
6.3.2	Both WT and GS520AA mutant HA TM peptides partition into the Ld domains of asymmetric GUVs . . . . .	78
6.3.3	The WT HA TM peptide induce phase separation in symmetric and asymmetric GUVs . . . . .	79
6.4	Discussion . . . . .	79
<b>7</b>	<b>Quantification of protein partitioning into giant unilamellar vesicles by fluorescence correlation spectroscopy and confocal imaging</b>	<b>83</b>
7.1	Theory . . . . .	84
7.1.1	Measurement of $K_P$ by fluorescence correlation spectroscopy in GUVs . . . . .	86
7.1.2	Measurement of $K_P$ by fluorescence confocal imaging in GUVs . . . . .	88
7.1.3	Measurement of $K_P$ by fluorescence correlation spectroscopy in LUVs . . . . .	88
7.2	GUV-FCS assay . . . . .	89
7.3	GUV-imaging assay . . . . .	92
7.4	LUV-FCS assay . . . . .	93
7.5	Comparison of methods . . . . .	95
<b>8</b>	<b>Reconstitution of a functional LGL/aPKC membrane binding switch</b>	<b>99</b>
8.1	LGL-1 directly binds membranes containing negatively charged lipids via a stretch of basic amino acids . . . . .	101
8.1.1	The position of the basic amino acids modulate LGL-1 membrane binding specificity . . . . .	102
8.1.2	LGL-1 binds preferentially PIP2-containing membranes . . . . .	102
8.1.3	LGL-1 MTS fold into an $\alpha$ -helix upon binding to negatively charged membranes . . . . .	106
8.2	Phosphorylation by aPKC abolishes the binding of LGL-1 to negatively charged membranes . . . . .	106
8.2.1	Phosphomimetic LGL-1 does not bind GUVs containing negative-charged lipids . . . . .	107
8.2.2	LGL-1 can be phosphorylated <i>in vitro</i> by the human PKC- $\zeta$ . . . . .	107

8.2.3	Phosphorylation of LGL-1 inside GUVs induce its detachment from the vesicle membrane . . . . .	108
8.3	Determination of the LGL-1 partitioning coefficient to negatively charged membranes . . . . .	110
8.3.1	$K_P$ can be determined from images of GUVs encapsulating LGL-1 . .	110
8.3.2	LGL-1 $K_P$ determined with a LUV-FCS based method . . . . .	115
<b>IV</b>	<b>CONCLUSION AND OUTLOOK</b>	<b>117</b>
<b>9</b>	<b>Conclusion and Outlook</b>	<b>119</b>
9.1	Pure lipid systems . . . . .	119
9.1.1	Reconstitution of lipid transbilayer asymmetry in model membranes .	119
9.1.2	Reconstitution of lipid lateral segregation in model membranes . . . .	120
9.1.3	Using lipid transbilayer asymmetry to induce shape transformations of GUVs . . . . .	120
9.2	Lipid-protein systems . . . . .	121
9.2.1	Lipid transbilayer asymmetry is not sufficient to restore the correct lateral organization of the influenza virus HA TM helix in model membranes	121
9.2.2	Direct quantification of protein-lipid interactions in GUVs . . . . .	121
9.2.3	Reconstitution of a functional LGL/aPKC membrane binding switch .	122
	<b>Acronyms</b>	<b>125</b>
	<b>References</b>	<b>143</b>
	<b>Acknowledgement</b>	<b>145</b>
	<b>Curriculum Vitae</b>	<b>147</b>



# List of Figures

1.1	Membrane transbilayer and lateral asymmetry . . . . .	4
1.2	Examples of cell polarity in model cells and organisms . . . . .	5
1.3	Sorting of polarity determinants within a cell . . . . .	7
1.4	Categorization of the synthetic biology approaches . . . . .	8
1.5	Reconstitution of minimal actin comet tails . . . . .	9
1.6	Liposomes . . . . .	10
1.7	Supported lipid bilayers . . . . .	11
1.8	Lipid lateral organization in model membranes . . . . .	12
1.9	Principle of fluorescence correlation spectroscopy . . . . .	13
1.10	Characterization of lipid bilayers and lipid-protein interactions with FCS . . .	15
1.11	Experimental approaches to reconstitute unmixing and polarization events in model membranes . . . . .	16
1.12	PAR-6/PKC-3/LGL-1 mutual elimination model . . . . .	17
2.1	PLAP reconstitution via direct incorporation. . . . .	28
3.1	FRAP ROI . . . . .	34
3.2	Point-FCS on lower and upper leaflets. . . . .	35
3.3	GUV image analysis . . . . .	38
3.4	Determination of $L_o$ partitioning coefficients in GUVs . . . . .	39
4.1	aSLB leaflet-specific labeling . . . . .	44
4.2	SLB integrity upon M $\beta$ CD-SM treatment. . . . .	46
4.3	aSLB formation via M $\beta$ CD-mediated lipid exchange method . . . . .	47
4.4	SLB fluidity in presence of bSM . . . . .	48
4.5	SLBs treated with M $\beta$ CD-DOPC . . . . .	49
4.6	aSLB stability over time . . . . .	50
4.7	aSLB formation in the presence of reconstituted PLAP . . . . .	51
4.8	Phase separation in symmetric SLB after cholesterol addition. . . . .	53
4.9	Cholesterol incorporation in aSLBs . . . . .	54
4.10	Phase separation in scrambled, fully and partially asymmetric SLBs after cholesterol addition . . . . .	55
4.11	Phase separation dynamics in aSLBs . . . . .	56
4.12	Phase separation and coupling in symmetric, scrambled, fully and partially asymmetric GUVs . . . . .	58
5.1	HP $\alpha$ CD-mediated asymmetric domain induction in GUVs . . . . .	63

5.2	Bulging of intramembrane asymmetric Lo domains in GUVs . . . . .	64
5.3	GUV transformation: prolate ellipsoid to spherical vesicle . . . . .	65
5.4	GUV transformation: discocyte to stomatocyte . . . . .	65
5.5	GUV transformation: vesicle budding . . . . .	66
5.6	GUV transformation: endocytosis . . . . .	66
5.7	Imaging of adjacent GUVs . . . . .	68
5.8	FRAP assay for vesicle fission . . . . .	69
5.9	Budding of intramembrane domains after hyperosmotic shock . . . . .	69
5.10	FRAP measurements of budded intramembrane domains after hyperosmotic shock . . . . .	70
6.1	Partitioning of the HA TM peptide in SLBs containing symmetric and asymmetric domains . . . . .	74
6.2	Line-scan FCS on SLBs containing asymmetric domains . . . . .	76
6.3	Line-scan FCS on SLBs and GUVs containing the HA WT peptide . . . . .	77
6.4	Partitioning of the HA TM WT and GS520AA peptides into the symmetric domains of GUVs . . . . .	78
6.5	Partitioning of the HA TM WT and GS520AA peptides into the asymmetric domains of GUVs . . . . .	79
6.6	The WT HA TM peptide induces phase separation in symmetric GUVs . . .	80
6.7	The WT HA TM peptide induces phase separation in asymmetric GUVs . . .	81
7.1	GUV- and LUV-based methods to measure protein-lipid affinity . . . . .	85
7.2	Membrane volume and surface concentrations of proteins with different membrane affinities . . . . .	86
7.3	Protein concentrations determined by GUV-FCS assay . . . . .	90
7.4	$K_P$ and $K_d$ determined by GUV assay . . . . .	92
7.5	Diffusion coefficients determined by GUV-FCS assay . . . . .	93
7.6	Calibration curve for GUV-image analysis . . . . .	94
7.7	LUV-FCS assay . . . . .	95
8.1	BH-search identified a putative membrane binding region in LGL-1 . . . . .	101
8.2	LGL-1 binds GUVs containing negative-charged lipids . . . . .	103
8.3	LGL-1-AAAA binds bPI(4,5)P2-containing membranes less than LGL-1-WT . . .	104
8.4	LGL-1 MTS binds preferentially PIP2-containing membranes . . . . .	105
8.5	LGL-1 MTS fold into an $\alpha$ -helix upon binding to negatively charged membranes . . .	107
8.6	LGL-1 MTS $\alpha$ -helix content . . . . .	108
8.7	The phosphomimetic LGL-1 EEE mutant does not bind GUVs containing negative-charged lipids . . . . .	109
8.8	LGL-1 can be phosphorylated <i>in vitro</i> by the human PKC- $\zeta$ . . . . .	110
8.9	Phosphorylated LGL-1 MTS does not bind GUVs containing negative-charged lipids . . . . .	111
8.10	<i>In situ</i> LGL-1 phosphorylation inside a GUV . . . . .	112
8.11	LGL-1 bound to the membrane is protected from the action of PKC- $\zeta$ . . . .	112
8.12	LGL-1 MTS encapsulated in GUVs via droplet transfer method . . . . .	113
8.13	LGL-1 MTS encapsulation variability . . . . .	113
8.14	Determination of the LGL-1 MTS partitioning coefficient in GUVs . . . . .	114

---

8.15	Determination of the LGL-1 MTS partitioning coefficient with the LUV-FCS method . . . . .	116
9.1	Secondary structure of the LGL-1 MTS WT and AAAA peptide at the membrane	123



# List of Tables

3.1	Line-scan FCS parameters . . . . .	37
6.1	Diffusion and Lo partitioning coefficients of fluorescent lipids in each leaflet of asymmetric SLBs . . . . .	75
6.2	Lo partitioning coefficients of HA TM peptides in symmetric and asymmetric SLBs . . . . .	76
6.3	Comparison of Lo partitioning coefficients . . . . .	78
7.1	Comparison of $K_{Ps}$ . . . . .	91
7.2	$K_d$ determined by GUV-FCS assay . . . . .	91
7.3	Comparison of methods . . . . .	96
8.1	Particle Size and polydispersity index values . . . . .	104
8.2	LGL-1 MTS $K_P$ and $K_B$ values . . . . .	114



# List of Publications

The results presented in this work have, in part, been communicated before in the following articles:

**Visco, I.**; Chiantia, S.; Schwille, P. Asymmetric Supported Lipid Bilayer Formation via Methyl- $\beta$ -Cyclodextrin Mediated Lipid Exchange: Influence of Asymmetry on Lipid Dynamics and Phase Behavior. *Langmuir* **2014**, *30*, 7475-7484.

Thomas, F.; **Visco, I.**; Petrasek Z.; Heinemann, F.; Schwille, P. Introducing a Fluorescence-based Standard to Quantify Protein Partitioning into Membranes. *Biochim. Biophys. Acta, Biomembr.*, submitted.





# Abstract

Polarity is a fundamental feature of almost all cells. It generally refers to the asymmetric organization of several cellular components. The plasma membrane, for example, exhibits both a transbilayer and a lateral asymmetry in most eukaryotic cells. Lipids are asymmetrically distributed between the cytoplasmic and the extracellular leaflet of the membrane and segregate laterally together with specific proteins to form dynamic nanoscale assemblies, known as rafts. Polarity can also specifically describe the asymmetric distribution of key molecules within a cell. These molecules, known as polarity determinants, can orient a multitude of specialized cellular functions, such as cell shape, cell division and fate determination.

In the framework of this thesis, we aimed to reconstitute essential features of membrane unmixing and cell polarity with a “bottom-up” synthetic biology approach. We worked with both: pure lipid systems, whose unmixing is driven by the asymmetric distribution of lipids in the two leaflets, and a lipid-protein system, whose polarization is instead due to reaction-diffusion mechanisms. In both cases, we used Giant Unilamellar Vesicles (GUVs) and Supported Lipid Bilayers (SLBs) to model biological membranes and employed modern biophysical techniques, such as fluorescence correlation spectroscopy, to quantitatively characterize lipid bilayers and protein-lipid interactions.

In the pure lipid systems, we first reconstituted membrane transbilayer asymmetry, applying a cyclodextrin-mediated lipid exchange method, which enables us to enrich membranes with lipids of choice. The enrichment of the membrane with sphingomyelin and/or cholesterol triggers the segregation of lipids into two coexisting asymmetric phases both in SLBs and GUVs, whereas exchanging different amounts of phosphatidylglycerol with the outer leaflet of the GUV membranes controls vesicle shape. Tuning the lipid content of model membranes revealed that small changes in the composition of one leaflet affect the overall lipid miscibility of the bilayer and that membrane shape transformations are possible also in absence of a protein machinery and as a consequence of the lipid redistribution in the membrane.

In the protein-lipid system, we aimed to reconstitute a minimal polarization system inspired by the *C. elegans* embryo at one-cell stage, which polarize along the anterior-posterior axis by sorting the PARtitioning defective (PAR) proteins into two distinct cortical domains. In this system polarity is maintained by the mutual inhibition between anterior (aPARs: PAR-3, PAR-6 and PKC-3) and posterior (pPARs: PAR-1, PAR-2 and LGL-1) PARs, which reciprocally antagonize their binding to the cortex, mutually excluding each other. We focused on LGL-1, which acts directly on PAR-6. Submitting LGL-1 to model membranes allowed us to identify a conserved region of the protein that binds negatively-charged membranes and to determine its lipid binding affinity and specificity. Selected LGL-1 mutants were then generated to better understand the electrostatic mechanism involved in the membrane binding. LGL-1 was finally combined with PKC-3 to generate a functional membrane binding switch.



# Zusammenfassung

Polarität ist eine Grundeigenschaft fast aller Zellen und bezeichnet die asymmetrische Organisation verschiedener zellulärer Bestandteile. Zum Beispiel besitzt die Zellmembran bei den meisten eukaryotischen Zellen sowohl eine Asymmetrie zwischen als auch innerhalb der Lipidschichten. Das heißt, Lipide sind asymmetrisch in der zytoplasmatischen und der extrazellulären Lipidschicht der Membran verteilt und bilden zusammen mit spezifischen Proteinen auf lateraler Ebene dynamisch-geordnete Nanostrukturen, sogenannte Lipid Rafts.

Polarität kann zudem die asymmetrische Verteilung bestimmter Schlüssel-moleküle innerhalb einer Zelle beschreiben. Diese als Polaritätsdeterminanten bekannten Moleküle bedingen eine Vielfalt spezieller Zellfunktionen so wie z.B. Zellform, Zellteilung und Zellschicksal. Diese Arbeit versucht wesentliche Eigenschaften von Zell- und Membranpolarität mit Hilfe des sogenannten “Bottom-up”-Ansatzes (“von unten nach oben”) der synthetischen Biologie nachzubilden. Es wurden zwei Systeme etabliert, um Polarisation mit Minimalsystemen zu reproduzieren. Zum einen reine Lipidsysteme, deren Polarisation durch die asymmetrische Verteilung von Lipiden in den zwei Lipidschichten entsteht, zum anderen Lipid-Proteinsysteme, deren Polarisation sich stattdessen aus Reaktions-Diffusions Mechanismen herleitet. In beiden Fällen wurden Riesenvesikel (GUVs) sowie gestützte Lipiddoppelschichten (SLBs) für die Modellierung biologischer Membranen verwendet und moderne biophysikalische Techniken, wie die Fluoreszenz-Korrelations-Spektroskopie, für eine quantitative Charakterisierung von Lipiddoppelschichten und Protein-Lipid Interaktionen angewendet.

Um die Asymmetrie der Membrandoppelschicht in reinen Lipidsystemen zu rekonstruieren, wurde eine Anreicherung einer der Lipidschichten der Membran mit den gewünschten Lipiden durch Anwendung eines mit Cyclodextrin kontrollierten Lipidaustauschprotokolls vorgenommen. Die Anreicherung der Membran mit Sphingomyelin und/oder Cholesterol induzierte die Aufteilung der Lipide in zwei koexistierende, asymmetrische Phasen sowohl in SLBs als auch GUVs. Die Vesikelform hingegen wurde durch den Austausch verschiedener Mengen Phosphatidylglycerol in der äusseren Lipidschicht der GUV-Membranen verändert. Eine Anpassung des Lipidgehaltes von Membranen im Modellsystem zeigte, dass kleine Änderungen in der Zusammensetzung einer Lipidschicht die Mischbarkeit der Lipide der Doppelschicht beeinflusst und dass Formveränderungen der Membran, selbst in Abwesenheit eines Proteingerüsts, als Konsequenz einer Lipidumverteilung in der Membran möglich sind.

Im Protein-Lipid System wurde die Nachbildung eines Minimalpolarisationssystems angestrebt, wie man es beim *C. elegans* Embryo im Einzellstadium beobachten kann. Dieser wird durch Anordnung der PARtitioning defective (PAR) Proteine in zwei unterschiedliche kortikale Bereiche entlang der Vorder-Hinterachse polarisiert. In dem PAR-System wird die Polarität durch gegenseitige Inhibition der vorderen (aPARs: PAR-3, PAR-6 und PKC-3) und hinteren (pPARs: PAR-1, PAR-2 und LGL-1) PAR-Proteine aufrechterhalten. Diese hemmen die gegenseitige Bindung an den Kortex. Da LGL-1 direkt auf PAR-6 einwirkt, wurde es

als potentielltes Schlüssel-molekül der Zellpolarization in künstlichen Membranen rekonstruiert. Durch Rekonstruktion von LGL-1 in Membranmodellen konnte die konservierte Region des Proteins, die mit negativ geladenen Membranen interagiert, sowie dessen Bindungsaffinität und -Spezifität gegenüber Lipiden quantitativ gemessen werden. Darauf folgend wurden LGL-1 Mutationen hergestellt, um die bei der Membranbindung auftretenden elektrostatischen Mechanismen besser zu verstehen. Zuletzt wurden LGL-1 und PKC-3 kombiniert, um die Membranbindung von LGL-1 reproduzierbar zu inhibieren.

## Part I

# INTRODUCTION



# Chapter 1

## Introduction

### 1.1 Relevance of polarity for living systems

Polarity is a fundamental feature of almost all cells [1], it generally refers to the asymmetric spatial organization of several cellular components, including cytoskeleton, cellular organelles, and plasma membrane [2]. The plasma membrane, for example, exhibits both a transbilayer and a lateral asymmetry in most eukaryotic cells. Lipids are asymmetrically distributed between the cytoplasmic and the extracellular leaflet of the membrane (Figure 1.1, A), with SphingoMyelin (SM) being enriched in the extracellular leaflet and PhosphatidylEthanolamine (PE) and PhosphatidylSerine (PS) in the cytoplasmic one. In cells transbilayer asymmetry results from the movement of selected lipids across the bilayer. At least three mechanisms to exchange lipids between leaflets are known: (1) spontaneous lipid transbilayer movement, whose rate is determined by the biophysical properties of both the lipid and the membrane; (2) ATP-independent protein-mediated transbilayer movement, which can be lipid selective, but cannot move lipids against gradient. (3) ATP-dependent protein-mediated lipid translocation, which is lipid-selective and can move lipids against gradient upon ATP hydrolysis [3]. At the same time, lipids segregate laterally in the membrane and form dynamic nanoscale assemblies together with specific proteins (Figure 1.1, B). Those assemblies, also known as rafts, are rich in sterols and sphingolipids and are responsible for membrane subcompartmentalization and functions such as trafficking, endocytosis and signaling [4].

Polarity can also specifically describes the asymmetric distribution of key molecules within the cell [5]. These molecules, known as polarity determinants or regulators, are essential for polarity and can orient a multitude of specialized cellular functions, such as cell shape, cell adhesion and migration, the uptake and release of molecules, and cell division and fate determination [1]. Examples of model cells and organisms to study polarity are:

**Epithelial cells** show an apical-basal polarization pattern with four distinct cortical domains: the apical domain, the Tight Junction (TJ), the Adherens Junction (AJ), and the basolateral domain (Figure 1.2, A). This polarized organization allows epithelial cells to arrange in sheets, which function as barriers between compartments and to regulate the transport of molecules between them [6].

**Motile cells** assume an elongated morphology (Figure 1.2, B) and relocate selected proteins or restrict their activities either to the leading or lagging edge [7]. This polarized

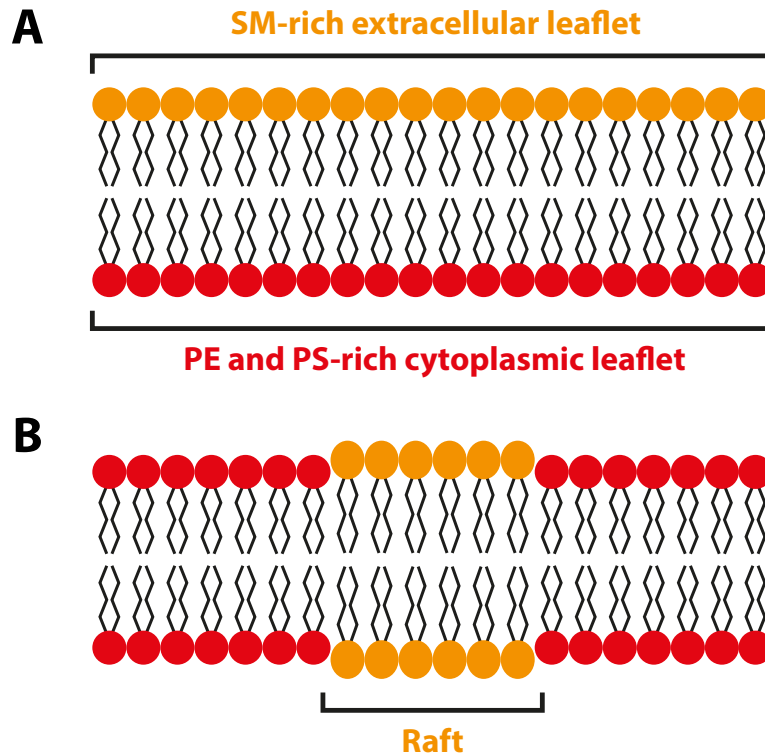


**Figure 1.1** – Membrane transbilayer and lateral asymmetry. [A] SM is enriched in the extracellular leaflet, whereas PE and PS in the cytoplasmic leaflet. [B] Lipids segregate laterally in the membrane and form dynamic nanoscale assemblies rich in sterols and sphingolipids known as rafts.

distribution allows motile cells to generate a distinct front and back and thus to move in one direction [5].

**Neurons** polarize by forming a single axon and multiple dendrites [8], which are radically different in morphology, signaling properties, cytoskeletal organization, and physiological function [9] (Figure 1.2, C). This polarization provides neurons with specialized domains for either receiving (dendrites) or transmitting (axons) cellular signals, thus allowing neural activities [9].

**The budding yeast *Saccharomyces cerevisiae*** breaks symmetry to switch from isotropic growth to growth along a polarized axis in order to enter the mitotic cell cycle and grow a bud or to form a mating projection (shmoo) toward a cell of the opposite mating type [10] (Figure 1.2, D).

**The soil nematode *Caenorhabditis elegans*** at one-cell stage polarizes along the anterior-posterior axis by sorting polarity determinants, the PARtitioning defective (PAR) proteins, into distinct cortical domains [11] (Figure 1.2, E). The posterior PARs (pPARs: PAR-1, PAR-2 and LGL-1) localize to the posterior pole where the fertilizing spermatozoan entered the oocyte [12, 13, 14, 15], whereas the anterior PARs (aPARs: PAR-3, PAR-6 and PKC-3) localize to the opposite anterior pole [16, 17, 18]. This polarized distribution allows the *C. elegans* embryo to undergo asymmetric cell



division, thus generating two daughter cells that inherit distinct molecular components and, ultimately, distinct fates [5].

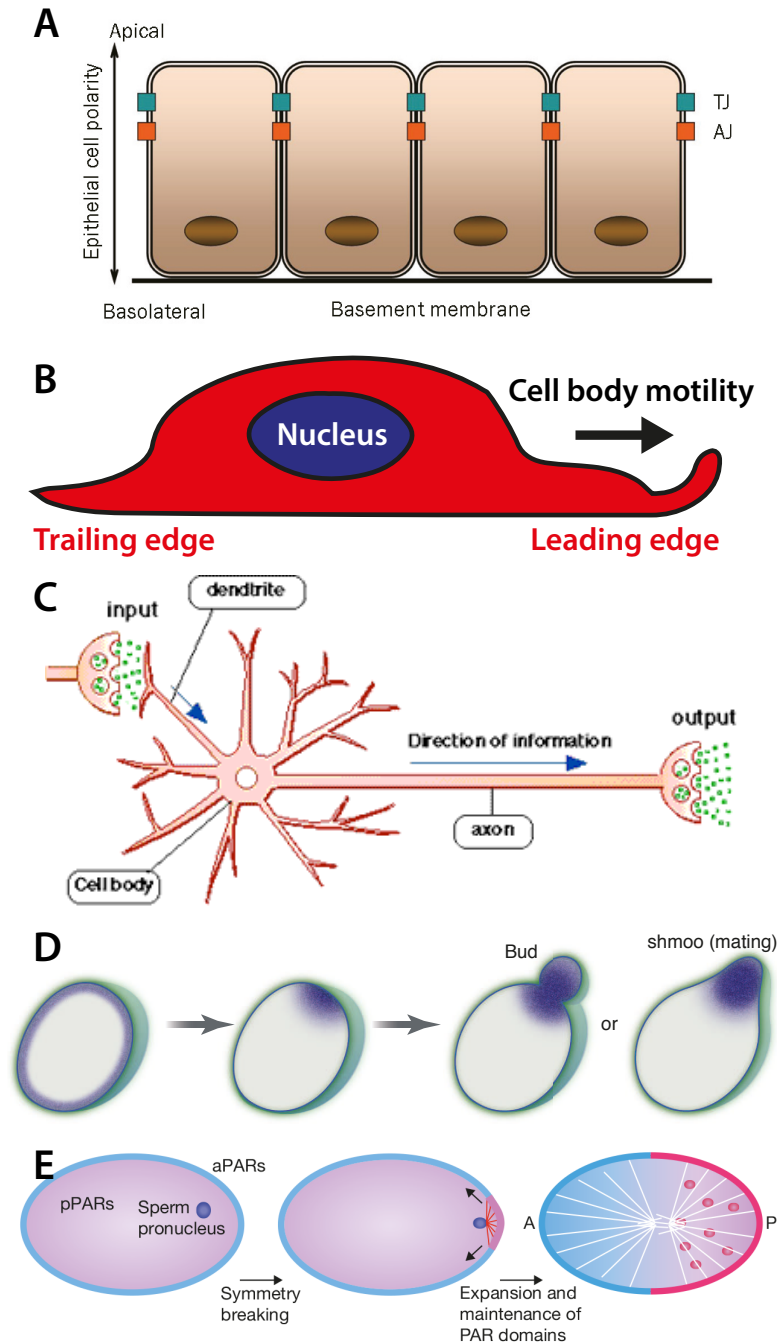


**Figure 1.2** – Examples of cell polarity in model cells and organisms: [A] epithelial cells (adapted from Coradini and colleagues [19]), [B] a motile cell (adapted from Cramer [20]), [C] a neuron (adapted from [http://www.med.nagoya-u.ac.jp/Yakuri/projects\\_e/projects\\_e03.htm](http://www.med.nagoya-u.ac.jp/Yakuri/projects_e/projects_e03.htm)), [D] the budding yeast *S. cerevisiae* (adapted from Mogilner and colleagues [21]), and [E] the *C. elegans* embryo at one-cell stage (adapted from Seydoux [22]).

The importance of polarity for living systems is emphasized by the close connection be-

tween its loss and tumor formation and development [23, 24, 25]. The first tumor suppressor gene discovered and described in the modern scientific literature was in fact a polarity regulator, the *Drosophila* Lethal (2) Giant Larvae (LGL). Loss of LGL causes massive tissue disorganization, tumor-like growth and lethal phenotypes in several organisms. At the cellular level it leads to disruption of cell polarity, failure of asymmetric cell division, and thus loss of proper cell fate determination [26].

Tracing back the discoveries that led to the current understanding of polarity, one realizes that multiple research approaches were necessary and contributed synergically to unravel the cell biological roles and working mechanisms of polarity determinants. The polarity determinants of the *C. elegans* embryo, for example, were discovered by genetic analysis, which also provided first indications about their corresponding protein functions. Following gene cloning and sequence analyses provided details about protein domains whereas cell biology approaches and biochemical investigations shedded light on both protein cell localization and interactions [27]. At the same time, models characterized by different levels of biological detail and mathematical complexity were developed and started to play an increasingly important role in the discovery of polarity mechanisms [21]. In particular the combination of computer modeling and experimental testing, the so called experiment-theory feedback loop appears to be an extremely powerful tool.

Besides individual differences of each system, the distribution of polarity determinants could be mathematically described with reaction-diffusion models. In a reaction-diffusion system, pattern formation arises by the interaction of two components with different diffusion rates [28]: a slowly diffusing “activator” and a rapidly diffusing “inhibitor”. Gierer and Meinhardt specified that pattern formation is possible only if a locally restricted self-enhancing reaction is coupled with a long-ranging antagonistic reaction [29]. In these conditions a homogeneous distribution of the two components is unstable and any random fluctuation can initiate pattern formation. There are different conceivable ways to satisfy these general requirements for pattern formation within a cell [30]: the self-enhancing reaction can take place at the membrane in the form of a cooperative binding of one component *to* the membrane or of a mutual exclusion of the two components *from* the membrane; the antagonistic reaction on the other hand must spread more rapidly within the cytoplasm in the form of a depletion *of* or an equilibrium *with* the unbound molecules (Figure 1.3, A-B).

Recently, a synthetic biology approach was presented as an alternative and complementary strategy to investigate polarity. Chau and colleagues engineered an artificial polarization circuit that produces phosphatidylinositol (3,4,5)-trisphosphate poles when expressed in yeast, demonstrating that it is possible to design a polarizing system from scratch and that synthetic biology could potentially reveal the design principles of polarity [5].

## 1.2 Bottom-up synthetic biology: a viable approach to understand polarity

Reconstituting essential features of polarity with a minimal set of physically controllable molecules represents a parallel and viable approach to understand polarity. This strategy, also known as “bottom-up”, belongs to the large and heterogeneous field of synthetic biology, whose different streams were attemptively categorized in five interconnected branches [31, 32]: bio-engineering, synthetic genomics, unnatural molecular biology, protocell, and *in silico* (Figure 1.5).

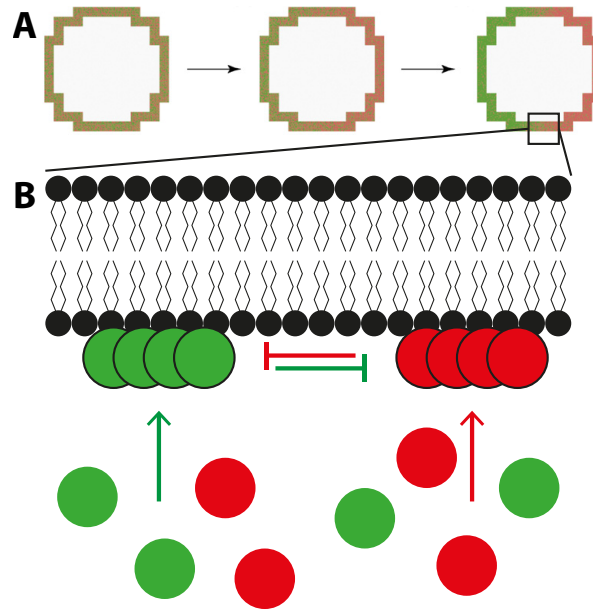


**Figure 1.3** – Sorting of polarity determinants within a cell. [A] Simulations showed that two polarity determinants (red and green) can sort into distinct cortical domains within a cell. [B] In this model, both molecules are assumed to aggregate at the membrane, but their aggregation is mutually exclusive (locally restricted self-enhancing reaction). At the same time, any aggregation at the membrane reduces the number of monomers dispersed in the cytoplasm (long-ranging antagonistic reaction) (adapted from Meinhardt [30]).

Bio-engineering, synthetic genomics and unnatural molecular biology work all at the genetic level, either to integrate designed genetic circuits in a cell [33], to replace the natural genome with a minimal chemically-synthesized one [34], or to develop new types of nucleic acid and genetic codes [35]. On the other hand, the protocell branch of synthetic biology aims to construct a synthetic cell that shows the minimal and sufficient structural conditions for life [36], either incorporating a minimal and sufficient amount of existing macromolecules into liposomes (protocell “top down” approach), or building more and more complex biological structures from very simple molecules with prebiotic reactions. The interest of *in silico* synthetic biology, instead, crosses all other branches, providing them with computational models, e.g. for the design of standard biological components or synthetic circuits [31].

Although the “bottom-up” approach could be assimilated to the protocell “top down” approach and shares with it the common ultimate goal of designing a minimal cell [37, 38], the originating scientific disciplines as well as the techniques and strategies used to achieve this goal differ significantly. “Bottom-up” synthetic biology originates from biophysics and quantitative biology, from which it inherited the reductionist and quantitative nature, and aims to understand a biological system identifying the smallest functional unit that reproduce the essential features of the system, and at the same time can also be quantitatively understood and technically mastered [37]. Several biological functions, such as cytoskeletal rearrangements, protein-driven membrane transformations, and circadian oscillations were already successfully reconstituted in *in vitro* systems of reduced complexity [37]. Among those systems, the reconstitution of actin comet tails (Figure 1.5) perfectly exemplifies the “bottom-up” synthetic biology approach and demonstrates that it is indeed possible to re-

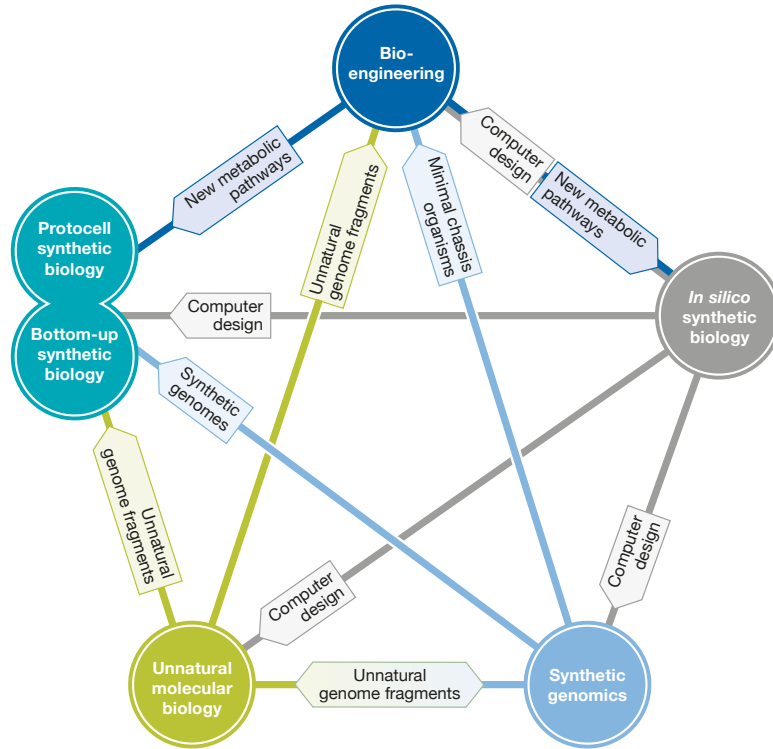


**Figure 1.4** – Categorization of the synthetic biology approaches. Synthetic biology comprises five interconnected branches: bio-engineering, synthetic genomics, unnatural molecular biology, bottom-up/protocell, and *in silico* (adapted from Deplazes [31]).

constitute polarization events with a small and well-characterized sets of molecules, and by doing this to learn more about the fundamental requirements of the system.

Actin comet tails are cylindrical structures made of a large number of short actin filaments cross-linked together in a dendritic meshwork [43]; they are formed by several intracytoplasmic pathogens (e.g. *Listeria monocytogenes*, *Shigella flexneri*, and *Rickettsia* spp.) to move rapidly through the host cell. This network of cross-linked actin filaments can be stripped down to five key components: (1) actin, (2) Actin-Related-Protein 2 and 3 complex (Arp2/3), which nucleates branched actin networks, (2) a Nucleation Promoting Factor (NPF), such as the Wiskott-Aldrich Syndrome protein (WASp) or the Actin assembly-inducing protein (ActA), which recruits and activates Arp2/3, (4) an Actin Depolymerizing Factor (ADF)/Cofilin, which disassembles actin filaments, and (5) a capping protein, which prevents the further growth of actin filaments by capping their barbed ends [44, 42]. When NPFs are bound to the surface of bacteria (Figure 1.5, A) [39], immobilized on plastic beads (Figure 1.5, B) [40] or anchored on phospholipids vesicles (Figure 1.5, C) [41, 45], in presence of the other four components, the actin filaments polymerize all over their surface forming a homogeneous cloud. The actin-coated particles do not move at first, the actin cloud gets eventually polarized resulting in a directed movement of the particle (Figure 1.6, D). This symmetry breaking in the polymerization of the actin filaments is thought to be a consequence of the stochastic variation in actin filament polymerization and crosslinking dynamics in the cloud surrounding the particle. Random local fluctuations in filament density and crosslinking are in fact self-reinforced and can lead to the symmetrically coated particle being forced

out of the cloud and initiating a comet tail formation [43]. The reconstitution of minimal actin comet tails allowed to individually probe each system component, such as actin regulators [46], protein surface density [40], particle size [43] and shape [47], revealing their specific role and interplay with other components. Additionally, this approach helped to clarify the general mechanism of actin-based motility [44] and to quantitatively describe its fundamental parameters, i.e., the forces arising from actin polymerization [41, 45].

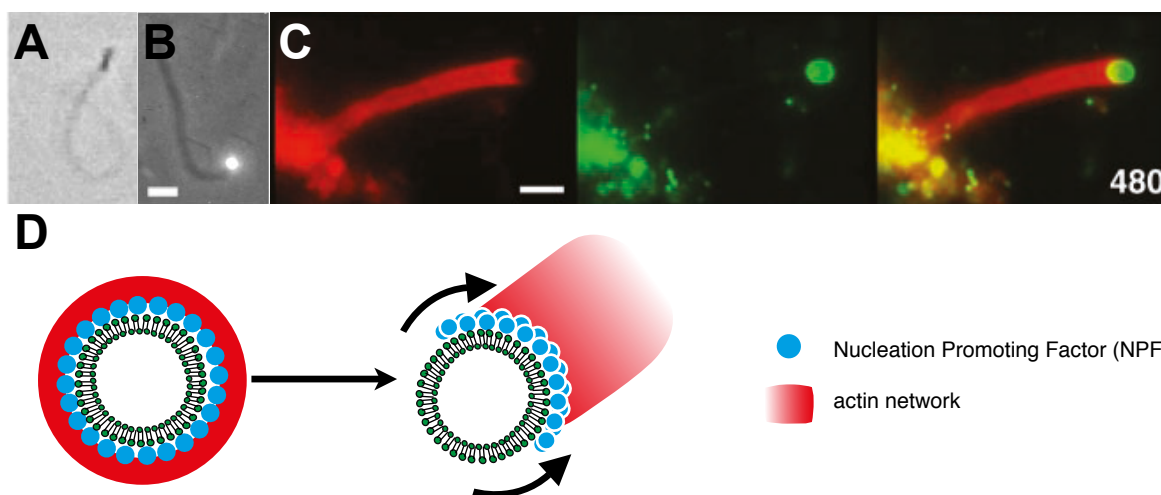


**Figure 1.5** – Reconstitution of minimal actin comet tails. Actin comet tails can be reconstituted anchoring NPFs: [A] on the surface of bacteria (adapted from Loisel and colleagues [39]), [B] on plastic beads (adapted from Bernheim-Groswasser and colleagues [40]) or [C] on phospholipids vesicles (adapted from Upadhyaya and colleagues [41]). [D] Actin-coated particles do not move at first, the actin network gets eventually polarized resulting in a directed movement of the particle (adapted from Loose and Schwille [42]).

### 1.3 GUVs and SLBs as model membranes to reconstitute polarization events

In order to reconstitute minimal actin comet tails, NPFs needed to be localized on a spherical object that mimic the bacterial surface. ActA, which acts as a NPF in *L. monocytogenes*, is in fact localized on the bacterial surface. Moreover, ActA is not homogeneously distributed, but it is rather polarized and its density is higher at the site of the comet tail [43]. Similar to ActA, most other polarity determinants localize to specific domains of the plasma membrane where they polarize the action of other cellular systems [1]. Therefore any attempt to reconstitute polarization events with a “bottom-up” synthetic biology approach cannot prescind from using model systems for phospholipid membranes that resemble their biological counterparts.

Phospholipid model membranes can be either free-standing or supported on a solid surface. Liposomes are an example of free-standing membranes. They are vesicles whose lumina are enclosed by a lipid bilayer made of phospholipids, and they are usually categorized according to their size, lamellarity and production strategy in four main groups (Figure 1.7):

**MLVs** are large (hundreds of nanometers to several microns), their walls are made of multiple concentric layers of lipid bilayer which confer them the characteristic “onion-like”

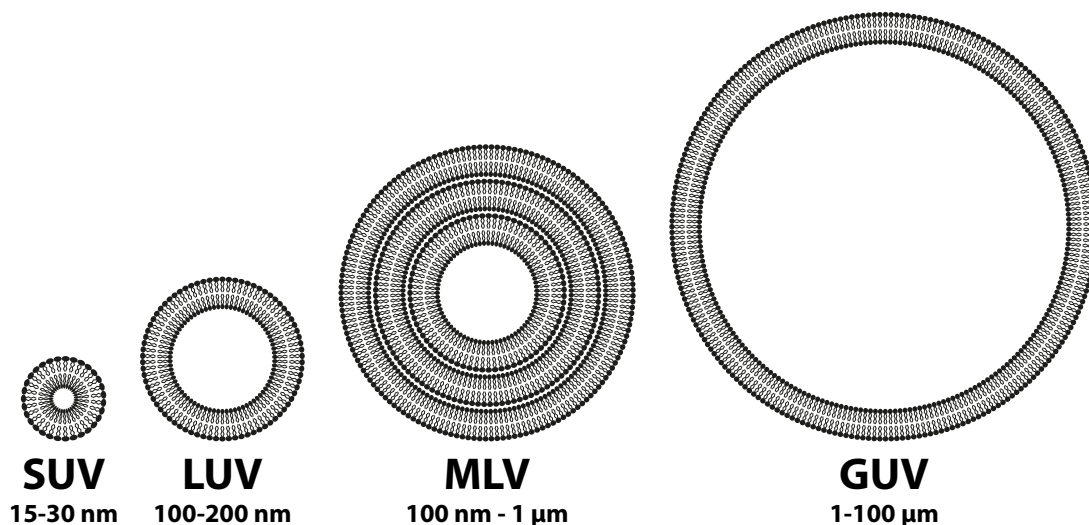


**Figure 1.6** – Liposomes. Liposomes with different sizes and lamellarity can be generated with distinct methods: Small Unilamellar Vesicles (SUVs), Large Unilamellar Vesicles (LUVs), Multi-Lamellar Vesicles (MLVs) and Giant Unilamellar Vesicles (GUVs). Liposomes are not drawn to scale.

structure, and they form when phospholipids dried in sheets are hydrated. MLVs are the starting point for the production of small and large unilamellar vesicles.

**SUVs** are small (few nanometers), their walls are made of a single lipid bilayer and are usually prepared from MLVs by sonication using a cuphorn, bath, or probe tip sonicator. SUVs are unstable and fuse spontaneously at temperatures below the phase transition of the lipid forming the vesicle [48], which makes them ideal to prepare supported membranes. Their small size helps minimizing unwanted light scattering in circular dichroism measurements.

**LUVs** are large (hundreds of nanometers), their walls are made of a single lipid bilayer and can be prepared by a variety of methods including extrusion of MLVs, detergent dialysis, fusion of SUVs, reverse evaporation, and ethanol injection. Alike SUVs, LUVs are stable few days on storage [48] and can be produced within a very narrow diameter range.

**GUVs** are giant (few to hundreds of microns), their walls are made of a single lipid bilayer and can be formed in several ways [49] including electroformation [50] and inverted emulsion [51, 52, 53]. Their giant size made those vesicles extremely appealing for scientists: they are, in fact, in the range of most biological cells, they can easily be investigated by optical microscopy, and their membranes are almost flat with vanishing curvature.

Supported Lipid Bilayers (SLBs) are, on the other hand, a supported membrane model system. They consist of a lipid bilayer made of phospholipids adsorbed on the surface of a solid substrate, such as glass or mica, and they can also be produced using different strategies (Figure 1.8), which confer them specific characteristics and experimental advantages [54]:



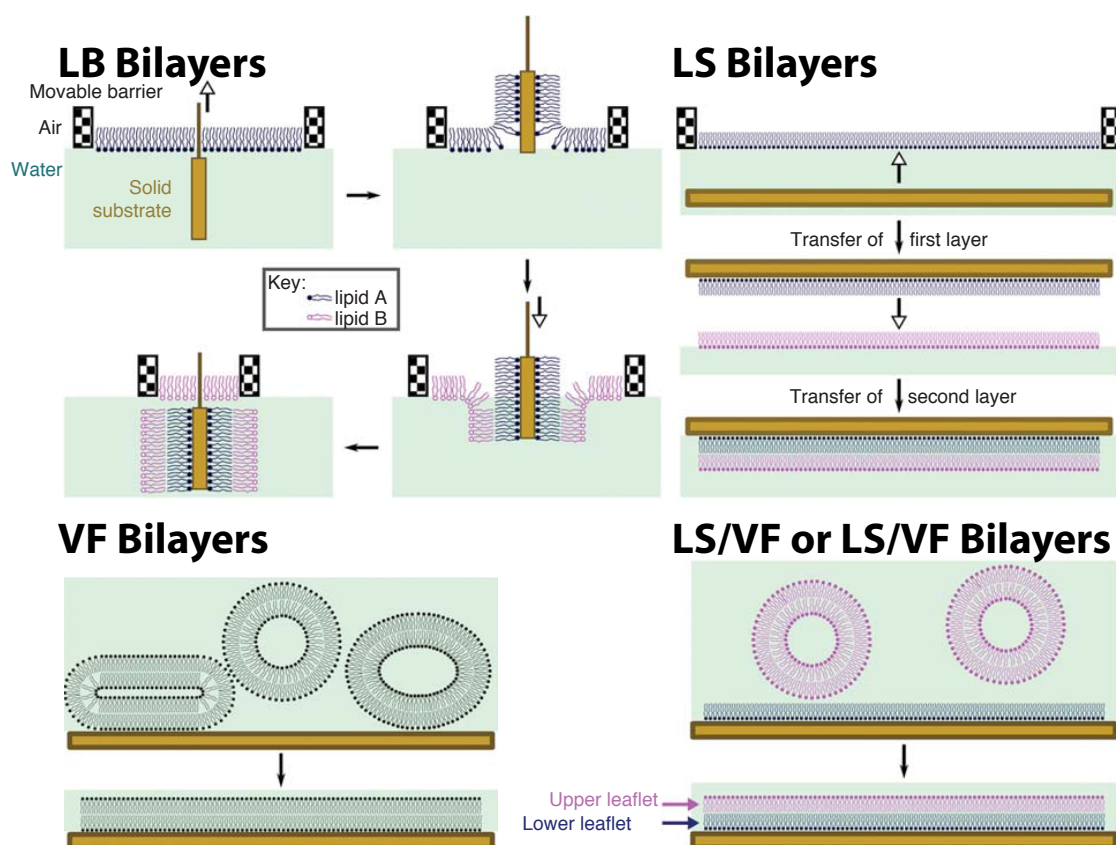


**Figure 1.7** – Supported lipid bilayers. SLB can be prepared by a variety of methods which confer them specific characteristics and experimental advantages: Langmuir-Blodgett (LB), Langmuir-Schaeffer (LS), Vesicle Fusion (VF) and hybrid LB/VF or LS/VF bilayers. Adapted from Sanderson [54].

**LB and LS bilayers** are assembled, transferring each preformed monolayer from an air/water interface to the support in two subsequent steps [55]. These methods allow to control the lateral pressure and the lipid composition of each leaflet [56].

**VF bilayers** are formed, exposing an hydrophilic support to SUVs, which adsorb to it, eventually rupturing and spreading into a planar membrane [57]. This method is usually preferred to any other because of its simplicity and protein compatibility. However, it did not traditionally allow to control the lipid composition of each leaflet [58] - a feature that we implemented as described in details in Chapter 4.

**Hybrid LB/VF and LS/VF bilayers** are produced fusing vesicles onto an existing monolayer. This method combined some of the advantages of the original methods.

Independently from the used method, the bilayer is not in direct contact with the support: a thin layer of water (10-20 Å) separates the absorbed bilayer from the solid support [59]. This water layer makes possible that the lipids in the leaflet close to the support (lower leaflet) are kept mobile; their lateral mobility, in fact, does not differ significantly from the upper leaflets' one [60]. Nevertheless, the support influences the bilayer, e.g. slowing its overall lipid mobility in comparison to free-standing membranes [61]. In order to minimize the effect of

the support on the bilayer, a polymer cushion can be introduced between the solid support and the bilayer, providing a deeper water layer, which not only reduces the frictional drag between bilayer and solid surface [62], but is also convenient when transmembrane proteins with bulky cytosolic or extracellular domains need to be reconstituted in SLBs [63].

GUVs and SLBs have been a particularly successful tool to model biological membranes. They can in fact be produced with almost any biologically relevant lipid composition and therefore exhibit features similar to their biological counterparts. Lipid lateral organization, for example, could be investigated in both membrane model systems using raft-mimicking mixtures of saturated and unsaturated lipids mixed with Cholesterol (Chol). The lipids of a raft-mimicking mixture segregate into two different liquid phases coexistent in the same membrane: a Liquid disordered (Ld) phase rich in unsaturated lipids and a Liquid Ordered (Lo) phase rich in saturated lipids and Chol (Figure 1.9, A-B). GUVs and SLBs allow to thoroughly and quantitatively characterize the lipid dynamics and structure of each phase, being fully compatible with modern biophysical techniques including Fluorescence Correlation Spectroscopy (FCS) [64, 65].

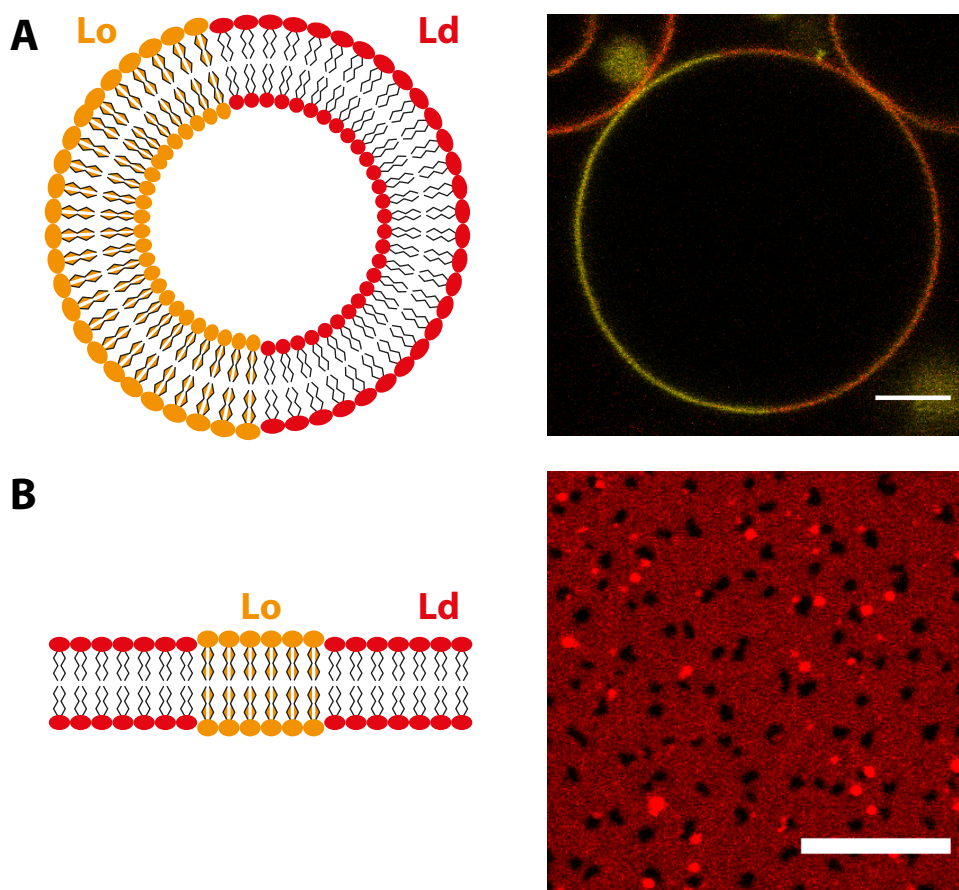


**Figure 1.8** – Lipid lateral organization in model membranes. Lipids of a raft-mimicking mixture segregate in GUVs [A] and SLBs [B] into two different liquid phases: a Ld phase rich in unsaturated lipids and a Lo phase rich in saturated lipids and Chol. Scale bars are 5 and 10  $\mu\text{m}$ , respectively



## 1.4 Biophysical characterization of model membranes dynamics and lipid-protein interactions

Introduced in 1972 by Magde and colleagues [66], FCS became a popular technique for the investigation of dynamic processes, which take place in solution or at the membrane, and is now commonly used to measure local fluorophore concentrations and translational and rotational diffusion coefficients [67, 68].

FCS is a single molecule technique based on the temporal autocorrelation analysis of the signal fluctuations detected from fluorophores within a very small volume ( $\sim$  fL). Such a small detection volume can be provided by any Confocal Laser Scanning Microscope (CLSM) setup, where the laser is focused to a diffraction limited spot by the objective and where a pinhole in the emission channel provides tight axial confinement (Figure 1.9, A). The fluorescence signal in the detection volume can vary both because the fluorophores move into and out of the detection volume, as a consequence of diffusion or transport, and because of photophysical or photochemical reactions, which cause fluctuations in the detected emission. This fluctuating fluorescence signal is recorded as a fluorescence intensity trace (Figure 1.9, B) and analyzed by calculating the autocorrelation curve (Figure 1.9, C), which measures the self-similarity of the signal in time, relating the fluorescence signal with itself at different lag times.

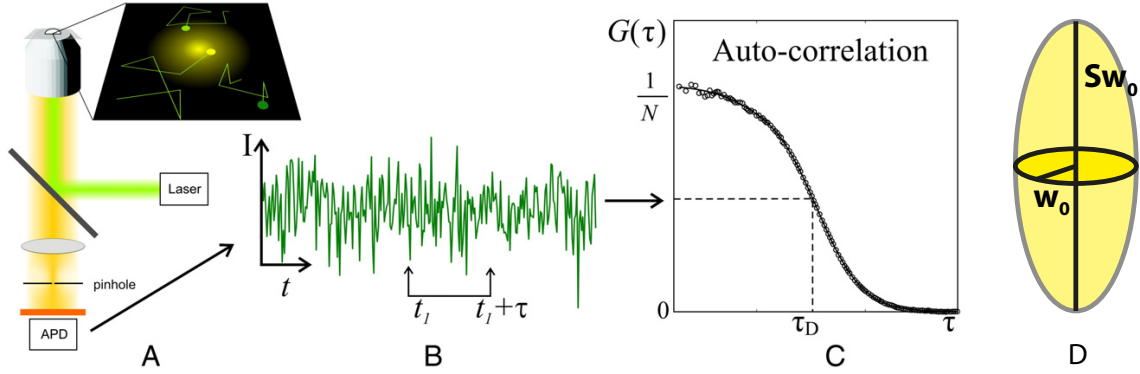


**Figure 1.9** – Principle of fluorescence correlation spectroscopy. [A] Typical FCS setup: fluorophores in the detection volume are excited with an appropriate laser beam, emitted photons are collected by the objective, spectrally filtered and detected with an Avalanche PhotoDiode (APD). Fluorescence fluctuations are recorded as a fluorescence intensity trace [B] and correlated to yield an autocorrelation curve.[C]. The autocorrelation curve (black circles) is fitted to an appropriate model function (solid line), thus determining the Diffusion time ( $\tau_D$ ) and the number of particles  $N$  of the fluorophore. [D] Three-dimensional Gaussian detection volume with radius  $w_0$  and aspect ratio  $S$ . In order to transform  $N$  into concentration  $C$  and  $\tau_D$  into Diffusion coefficient ( $D$ ),  $w_0$  and  $S$  have to be known. Adapted from Chiantia and colleagues [68].

The autocorrelation curve is calculated from the fluorescence intensity trace as follows:

$$G(\tau) = \frac{\langle \delta F(t) \cdot \delta F(t+\tau) \rangle}{\langle F(t) \rangle^2} \quad (1.1)$$

Here  $G(\tau)$  is the autocorrelation function as a function of the lag time  $\tau$ ,  $F$  is the fluorescence intensity as a function of the time  $t$  or  $t + \tau$ , and the angular brackets  $\langle \rangle$  refer to the time average, so that  $\delta F(t) = F(t) - \langle F(t) \rangle$ .

The autocorrelation curve is then fitted to a mathematical function (Figure 1.9, C), which best models the fluorescence fluctuations inside the detection volume, according to the char-

acteristics of the system under investigation, e.g. single or multiple diffusing fluorophores species. The model function should also account for fluorescence fluctuations which do not originate from the diffusion of the fluorophores in the detection volumes, e.g. from photo-physical phenomena such as triplet transitions and fluorophore blinking. Most importantly, the model function takes into account the size and shape of the detection volume, which is approximated by a three- or a two-dimensional Gaussian profile for measurements in solution and at the membrane, respectively (Figure 1.9, D). As an example the autocorrelation model functions describing three- and two-dimensional Brownian diffusion through these profile are:

$$G(\tau) = \frac{1}{N} \left(1 + \frac{\tau}{\tau_D}\right)^{-1} \left(1 + \frac{\tau}{S^2 \tau_D}\right)^{1/2} \quad (1.2)$$

$$G(\tau) = \frac{1}{N} \left(1 + \frac{\tau}{\tau_D}\right)^{-1} \quad (1.3)$$

Fitting the autocorrelation curve to the appropriate mathematical model function allows to extract parameters of interest, such as the average number of particles  $N$  and the diffusion time of the fluorophore  $\tau_D$ .  $N$  is the average number of fluorophores in the detection volume  $V_{FCS} = \pi^{2/3} S w_0^3$  (measurements in solution) or area  $A_{FCS} = \pi w_0^2$  (measurements at the membrane) and can be used to calculate the fluorophore concentrations  $C = N/V_{FCS}$  or  $C = N/A_{FCS}$ .  $\tau_D$  is the decay time of the correlation curve and can be used to calculate the fluorophore diffusion coefficient  $D = \frac{w_0^2}{4\tau_D}$ . In order to transform  $N$  and  $\tau_D$  into  $C$  and  $D$ , the radial dimension  $w_0$  and eventually the aspect ratio  $S$  of the Gaussian detection volume have to be known (Figure 1.10, D). Those parameters are usually determined calibrating the system with a dye of known  $D$ .

Standard FCS as well as several improved FCS variations have been used to investigate the properties of lipid bilayers [69, 67, 68, 70] and different aspects of protein-lipid interactions [71] both in GUVs and SLBs. In particular:

**The lateral organization of lipids** can be investigated measuring the  $D$  of lipids in model membranes [64]. Lipids in different domains show distinct dynamics, i.e. lipids in Lo domains diffuse slower than lipids in Ld domains due to the higher lipid order and packing (Figure 1.10, A).

**Protein partitioning into lipid domains** can be assessed measuring local concentrations of fluorescently labeled proteins in different domains of the membrane (Figure 1.10, B). These studies provided new insights into how lipid environment regulates protein localization [72, 73, 65].

**Membrane binding affinity and specificity of peripheral proteins** can be probed measuring changes in the  $\tau_D$  of fast-diffusing proteins upon their binding to slowly diffusing liposomes [74, 75, 76, 77, 78] (Figure 1.10, C). Measurement of membrane binding affinities with FCS was only reported for LUVs. In order to determine membrane-protein affinities in GUVs, we developed two complementary strategies to measure Partitioning Coefficients ( $K_{Ps}$ ), in which the ligand is either added to the external solution (Chapter 7) or encapsulated in GUVs (Chapter 8). These strategies combine the advantages of both established separation and titration methods, that is they allow to directly measure the free and membrane bound ligand concentrations without the need of physically separating them.

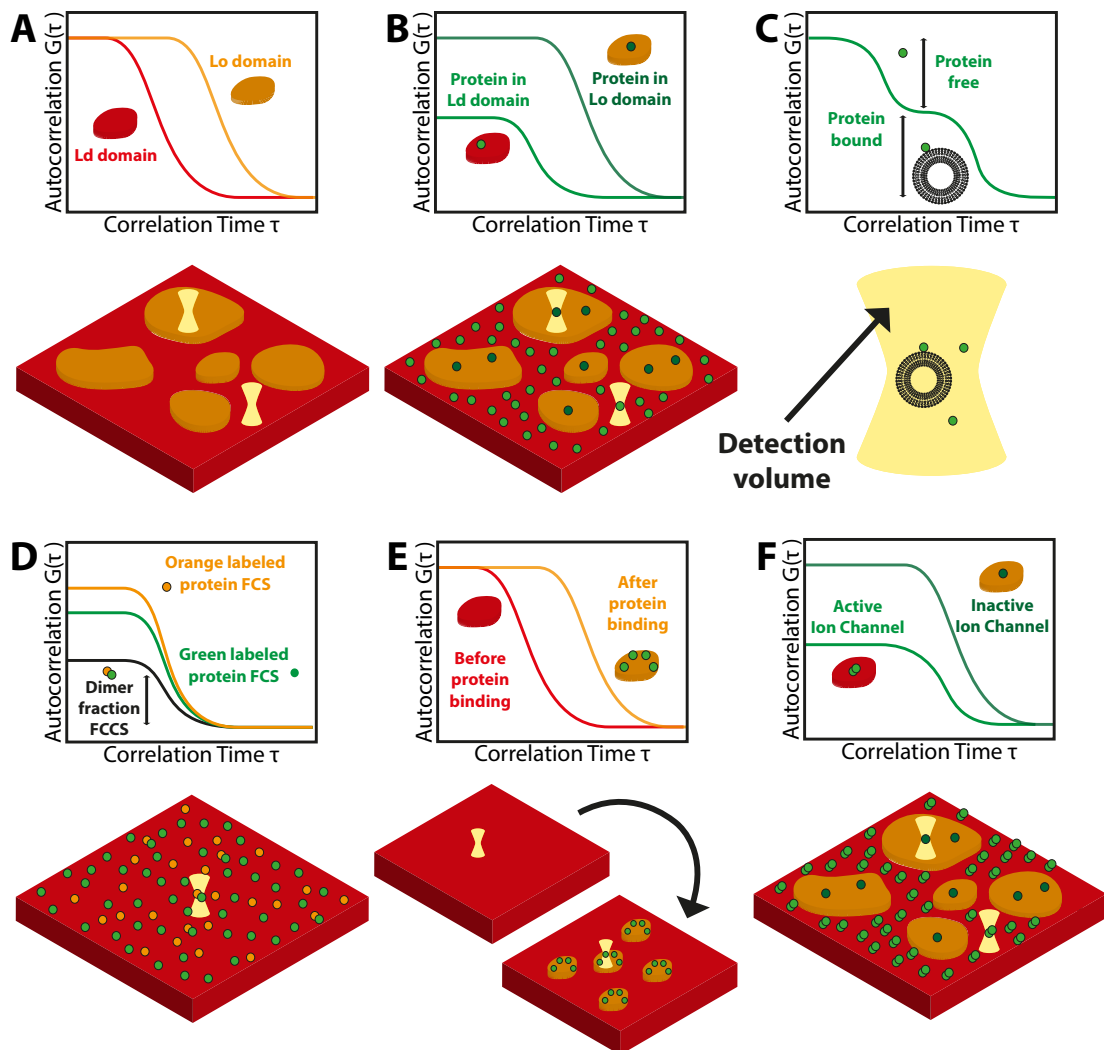


**Figure 1.10** – Characterization of lipid bilayers and lipid-protein interactions with FCS. Standard FCS and its variations have been used to investigate the lateral organization of lipids in a membrane [A], and different aspect of protein-lipid interactions, including: [B] protein partitioning into lipid domains, [C] membrane binding affinity and specificity of peripheral proteins, [D] protein dimerization in membranes, [E] effect of protein binding on membrane structure and dynamics, and [F] effect of lipids on protein structure and function.

**Protein-protein interactions and protein oligomerization in membranes** can be determined performing Fluorescence Cross-Correlation Spectroscopy (FCCS), a FCS variation that allows to quantify protein interactions and their regulation by lipids [79, 80, 81, 82] (Figure 1.10, D).

**Effect of protein binding on membrane structure and dynamics** can be addressed measuring changes in the  $D$  of lipids upon protein binding to the membrane (Figure 1.10, E). These studies demonstrated that proteins can slow down the lateral diffusion of fluorescently labeled lipids not involved in the binding, i.e. inducing or expanding Lo domains [83].

**Effect of lipids on protein structure and function** can be studied combining FCS with other techniques, e.g. electrophysiology, to quantitatively assess the effect of lipid phase separation on ion channel structure and function [84] (Figure 1.11, F).

## 1.5 Experimental approaches to reconstitute unmixing and polarization events in model membranes

In order to reconstitute unmixing and polarization events in a minimal system, we worked with pure lipid systems, whose unmixing is driven by the asymmetric distribution of lipids in the two leaflets, and with a lipid-protein system, whose polarization is instead driven by a reaction-diffusion mechanism (Figure 1.11).

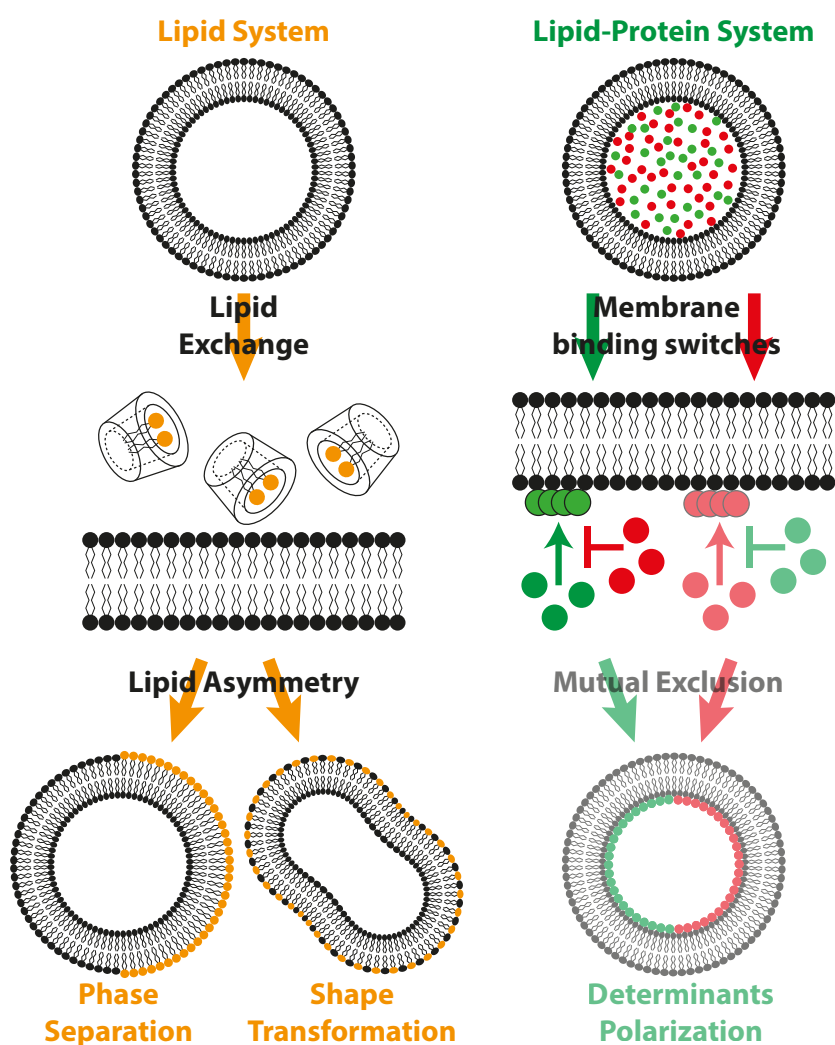


**Figure 1.11** – Experimental approaches to reconstitute unmixing and polarization events in model membranes. In pure lipid systems, lipid unmixing or vesicle shape transformations can be driven by the asymmetric distribution of lipids in the two leaflets. In lipid-protein systems, polarization is driven by a reaction-diffusion mechanism. In particular two determinants can polarize if they reciprocally antagonize their binding to the cortex. The opacified parts of the cartoon were not achieved experimentally.

In the lipid approach, we first reconstitute the transbilayer asymmetry of an eukaryotic plasma membrane producing SLBs and GUVs with lipids asymmetrically distributed among the two leaflets. To do so, we applied a so called cyclodextrin-mediated lipid exchange method [85, 86], which allows to enrich membranes with lipids of choice in a controlled fashion. The enrichment of the membrane with SM and/or Chol triggers the segregation of lipids into two coexisting asymmetric phases both in SLBs and GUVs (Chapter 4 and 6), whereas exchanging different amounts of PhosphatidylGlycerol (PG) with the outer leaflet of the GUV membranes allows us to control vesicle shape (Chapter 5). We then explored how a transmembrane protein, the influenza virus HemAgglutinin (HA), behaves in the presence of asymmetric domains and, more specifically, whether its phase partitioning is affected. Tuning the lipid content of model membranes allowed biologically relevant observations. Small changes in the composition of the inner leaflet (e.g. of the plasma membrane) were found to affect the overall lipid miscibility of the bilayer (Chapter 4), and the HA TransMembrane (TM) domain was found to induce phase separation both in symmetric and asymmetric model membranes (Chapter 6). Similarly, tuning the shape of giant vesicle proved that membrane shape rearrangements, which resemble those taking place in biological systems, are possible in absence of a protein machinery and as a consequence of the lipid redistribution in the membrane (Chapter 5).

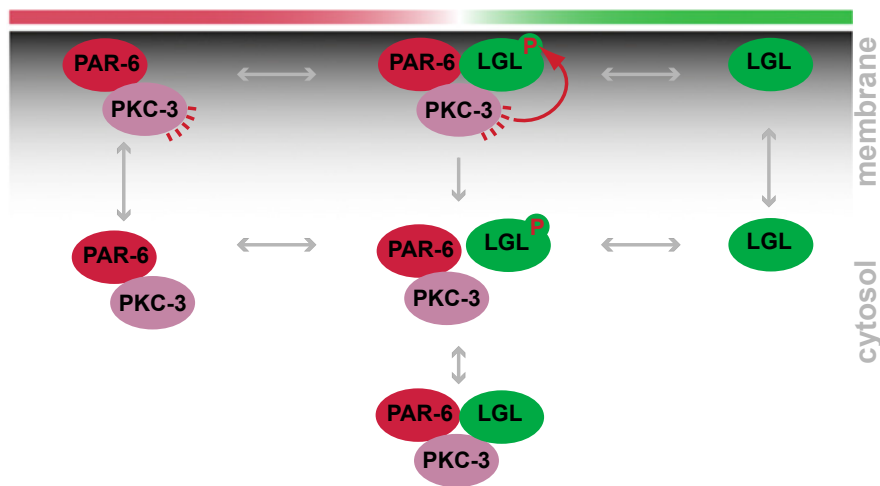


**Figure 1.12** – PAR-6/PKC-3/LGL-1 mutual elimination model. The PAR-6/PKC-3/LGL-1 complex forms at the boundary between the anterior and posterior PAR domains. Here PKC-3 can phosphorylate LGL-1 causing the whole complex to leave the cortex (Adapted from Hoege and colleagues [14]).

In the protein-lipid approach, we aimed to reconstitute a minimal polarization system inspired by the *C. elegans* embryo at one-cell stage. In this system polarity is maintained by the mutual inhibition between aPARs and pPARs, which reciprocally antagonize their binding to the cortex, mutually excluding each other. We focused on LGL-1, which in nematodes acts redundantly with PAR-2 to maintain polarity and can compensate for PAR-2 depletion [14, 15]. Additionally to the several common features shared with PAR-2, LGL-1 offered one interesting advantage, which makes the reconstitution of a minimal polarity system easier: it directly antagonizes the aPARs acting on PAR-6. Based on this, a so-called “mutual elim-

ination model” was proposed (Figure 1.12), in which the PAR-6/PKC-3/LGL-1 complex is formed at the boundary between the anterior and posterior PAR domains. Here PKC-3 can phosphorylate LGL-1 causing the whole complex to leave the cortex [14]. This is the minimal system we intended and partially succeed to reconstitute in GUVs. We first submitted LGL-1 to model membranes, allowing us to identify a very well conserved region of the protein that binds negatively-charged membranes and to determine its lipid binding specificity. Selected LGL-1 mutants were then generated to better understand the electrostatic mechanism involved in the membrane binding. LGL-1 was finally combined together with its antagonist complex to generate a functional LGL/atypical Protein Kinase C (aPKC) membrane binding switch (Chapter 8).

## Part II

# MATERIALS AND METHODS





## Chapter 2

# Materials and sample preparation

## 2.1 Materials

### 2.1.1 Lipids

Cholesterol from ovine wool (Chol), 1,2-DiOleoyl-sn-glycero-3-PhosphoCholine (DOPC), 1-Palmitoyl-2-Oleoyl-sn-glycero-3-PhosphoCholine (POPC), 1,2-Di-(9Z-Octadecenoyl)-sn-glycero-3-Phospho-L-Serine (DOPS), 1-Palmitoyl-2-Oleoyl-sn-glycero-3-Phospho-L-Serine (POPS), 1,2-Dioleoyl-sn-glycero-3-PhosphoAte (DOPA), 1,2-DiOleoyl-sn-glycero-3-Phospho-(1'-rac-Glycerol) (DOPG), L- $\alpha$ -Phosphatidylinositol (Soy) (sPI), Cardiolipin (Heart, Bovine), 1,2-dioleoyl-sn-glycero-3-(phosphoinositol-3-phosphate) (PI(3)P), 1,2-dioleoyl-sn-glycero-3-phospho-(1'-myo-inositol-4'-phosphate) (PI(4)P), 1,2-dioleoyl-sn-glycero-3-phospho-(1'-myo-inositol-5'-phosphate) (PI(5)P), 1,2-dioleoyl-sn-glycero-3-phospho-(1'-myo-inositol-3',4'-bisphosphate) (PI(3,4)P2), 1,2-dioleoyl-sn-glycero-3-phospho-(1'-myo-inositol-3',5'-bisphosphate) (PI(3,5)P2), 1,2-dioleoyl-sn-glycero-3-phospho-(1'-myo-inositol-4',5'-bisphosphate) (PI(4,5)P2), 1,2-dioleoyl-sn-glycero-3-phospho-(1'-myo-inositol-3',4',5'-trisphosphate) (PI(3,4,5)P3), L- $\alpha$ -phosphatidylinositol-4,5-bisphosphate (bPI(4,5)P2), SphingoMyelin from porcine brain extract (bSM) and 1,2-di-(9Z-octadecenoyl)-sn-glycero-3-(N-(5-amino-1-carboxypentyl)iminodiacetic acid)succinyl nickel salt (DGS-NTA(Ni)) were purchased from Avanti Polar Lipids, Inc. (Alabaster, AL). Ganglioside GM1 was purchased from Merck Millipore (Billerica, MA)

### 2.1.2 Protonation of phosphoinositides using acid

All phosphoinositides were protonated to enhance their incorporation into liposomes. The protonation protocol was originally developed by Olga Perisic (MRC Laboratory of Molecular Biology, Cambridge, UK) and used with minor modification. Briefly, lyophilized phosphoinositides were resuspended at 2.5 mM final concentration in subsequent steps with different solvent mixtures: (1) chloroform; (2) 2:1:0.01 (v:v:v) mixture of chloroform, methanol and hydrochloric acid 1N; (3) 3:1 (v:v) mixture of chloroform and methanol; and (4) chloroform. After each step the lipid solution was dried 15 min under N<sub>2</sub>; after step (1) and (2), the solution was additionally dried for 1 h under vacuum. In step (2), the lipid solution was incubated 15 min before drying. The lipid film was finally resuspended in chloroform at 1 mM final concentration and stored at -20°C up to few months.

### 2.1.3 Fluorescent lipids

Atto655 and Atto647N-DOPE were purchased from ATTO-Tec (Siegen, Germany). Atto647N-SM was a gift of Erdinc Sezgin (University of Oxford, UK). 1,2-dioleoyl-sn-glycero-3-phosphoethanolamine-N-(7-nitro-2-1,3-benzoxadiazol-4-yl) (NBD-DOPE) and 1,2-distearoyl-sn-glycero-3-phosphoethanolamine-N-(7-nitro-2-1,3-benzoxadiazol-4-yl) (NBD-DSPE) were purchased from Avanti Polar Lipids. Texas Red<sup>®</sup> 1,2-Dihexadecanoyl-sn-Glycero-3-Phosphoethanolamine (Texas Red DHPE) triethylammonium salt was purchased from Life Technologies Corporation (Carlsbad, CA).

### 2.1.4 Fluorescent dyes

Atto488 NHS-Ester was purchased from ATTO-Tec. Alexa Fluor<sup>®</sup> 488 carboxylic acid, succinimidyl ester (Alexa488), Alexa Fluor<sup>®</sup> 488 hydrazide (Alexa488), Alexa Fluor<sup>®</sup> 647 carboxylic acid, succinimidyl ester (Alexa647) and DiIC<sub>18</sub>(3) (DiI) were purchased from Life Technologies.

### 2.1.5 eGFP-His6 expression and purification

His6 tagged enhanced Green Fluorescent Protein (eGFP-His6) was cloned into the pGEX-6P-1 vector using the restriction enzymes Sall and NotI and expressed in the *E. coli* strain BL21(DE3). The protein was purified using Glutathione Sepharose 4 Fast Flow according to the manufacturer's instructions, followed by direct cleavage of the glutathione S-transferase tag with PreScission Protease on the column.

### 2.1.6 PLAP purification and labeling

Commercially available Alkaline Phosphatase from human PLacenta (PLAP) was further purified and labeled with Alexa647 as previously described [87, 73, 88] with minor modifications. In particular, Triton X-114 was precondensed before usage [89] and Superdex 200 10/300 GL (GE Healthcare, Little Chalfont, United Kingdom) columns were used to both remove the detergent and separate the labeled protein from the free dye. Labeled-PLAP purity and concentration were assessed by SDS-PAGE and absorbance at 280 nm, respectively. The degree of labeling was approximately one dye molecule per PLAP monomer.

### 2.1.7 HA TM peptides synthesis and labeling

HA TM WildType (WT) and GS520AA peptides were a gift of Dr. Jörg Nikolaus (Yale School of Medicine, CT). HA TM peptides contain 28 amino acid residues of the transmembrane segment of the HA (strain Japan/305/57, H2; WT: Rh- $\beta$ A-ILAIYATVAGSLSLAIMMAGISFWMCSN-KKK, Mutant: Rh- $\beta$ A-ILAIYATVAAALSLAIMMAGISFWMCSN-KKK). Both peptides were synthesized using Fmoc-chemistry and 5-(and-6)-carboxyTetraMethylRhodamine (TAMRA), succinimidyl ester at the N-terminus via a  $\beta$ -alanine. Three lysine residues were added at the C-terminal to enhance peptide solubility and membrane insertion [90]. Both peptides were dissolved in 2,2,2-Trifluoroethanol (TFE) at 1 mg/mL and store at -20°C.

### 2.1.8 LGL-1 expression and purification

LGL-1 (469-702) WT was cloned into the pGEX-6P-1 vector in which eGFP-His6 was previously cloned using the restriction enzymes BamHI and NotI. The LGL-1 mutants S661A/S665A/T669A (AAA), S661E/S665E/T669E (EEE) and R658A/K660A/RR671AA (AAAA) were generated with the QuikChange<sup>®</sup> Lightning Site-Directed Mutagenesis Kit (Agilent Technologies, Santa Clara, CA) according to the manufacturer's instructions. All clones were expressed in the *E. coli* strain BL21(DE3). The proteins were purified in presence of 1% Triton X-100 using GSTrap HP columns, followed by direct cleavage of the glutathione S-transferase tag with PreScission Protease on column and a second purification step with a HisTrap HP column according to the manufacturer's instructions. Protein concentrations were determined using the Bicinchoninic Acid (BCA) protein assay. Purified LGL-1 (469-702) was pre-cleared at 120,000 g, 4°C for 30 min in a MLA-130 rotor (Beckman Coulter, Pasadena, CA) and stored at -80°C in presence of 10% glycerol.

### 2.1.9 LGL-1 MTS peptides synthesis and labeling

The LGL-1 Membrane Targeting Sequence (MTS) WT and EEE peptides were synthesized by Stefan Pettera and labeled by Dr. Stephan Uebel (Max Planck Institute of Biochemistry, Martinsried, Germany). The LGL-1 MTS peptide has 26 amino acid residues, which corresponds to the part of the C-terminal LGL-specific domain of the *C. elegans* LGL-1 containing the three phosphorylation sites for PKC-3 (G5EEI1.CAEEL 656-681, acetyl-FQRFKSLKKSLRKTFRRKKKGTETLM-amide). For imaging and FCS experiments the peptides were labeled by coupling Atto488 NHS-Ester at the N-terminus. Both unlabeled and labeled peptides were synthesized using Fmoc-chemistry and purified to > 90% by preparative Reversed-Phase High-Performance Liquid Chromatography (RP-HPLC). Purity and identity of the peptide were checked by analytical RP-HPLC and electrospray mass spectrometry. Both peptides were stored -80°C lyophilized or in water at 1 mg/mL final concentration.

### 2.1.10 Additional materials

$\alpha$ -hemolysin (powder) from *Staphylococcus aureus*, Bovine Serum Albumin (BSA), PLAP, 3-(3-CHolAmidopropyl)dimethylammonio-1-PropaneSulfonate (CHAPS), Ficoll<sup>®</sup> PM 70, (2-HydroxyPropyl)- $\alpha$ -CycloDextrin (HP $\alpha$ CD), Methyl- $\beta$ -CycloDextrin (M $\beta$ CD), mineral oil, 4-nitrophenyl phosphate disodium salt hexahydrate (pNPP), TFE, Triton X-100 and X-114 were purchased from Sigma-Aldrich (St. Louis, MO). The Alexa647 conjugate of Cholera toxin subunit B (CtxB) was purchased from Life Technologies. [ $\gamma$ -32P]ATP was purchased from PerkinElmer (Waltham, MA). Reducing Agent Compatible BCA Protein Assay was purchased by Thermo Fisher Scientific (Waltham, MA). The pGEX-6P-1 vector, Glutathione Sepharose 4 Fast Flow, GSTrap HP 1 mL column, HisTrap HP 1 mL column, PreScission Protease and 100 nm polycarbonate membranes were purchased from GE Healthcare. n-Octyl- $\beta$ -D-Glucopyranoside (OG) was purchased from Glycon Biochemicals GmbH (Luckenwalde, Germany). Active recombinant human PKC- $\zeta$  (PKC- $\zeta$ ) was purchased from Merck Millipore. All solvents were of Uvasol<sup>®</sup> spectroscopic purity grade, other chemicals were of reagent grade.

## 2.2 *In vitro* LGL-1 phosphorylation by human PKC- $\zeta$

*In vitro* phosphorylation was performed similarly as described before [91] with the following modifications. 5.0  $\mu$ M LGL-1 MTS WT and EEE peptides were incubated with 1 nM PKC- $\zeta$  in kinase buffer (20 mM HEPES pH 7.4, 5 mM  $\text{MgCl}_2$ , 1 mM DiThioThreitol (DTT)) containing 60  $\mu$ M cold ATP and 1.315  $\mu$ Ci [ $\gamma$ - $^{32}\text{P}$ ]ATP at Room Temperature (RT). Kinase reactions were carried out by incubating samples on ice (for time 0 samples) or at 30°C and terminated by adding 5X Laemmli loading buffer at different time points (10, 20, 30, 40, and 50 min). Proteins were separated by a handcast 18% Tris-glycine gel, stained with Coomassie, fixed and dried on 1.5 mm filter paper. The dried gels were exposed to radiographic films at RT Over Night (ON) and digitalized with a LAS-3000 (Fujifilm, Tokyo, Japan) exposing them for 1-8 s on a DIA tray. The autoradiographs were analyzed with the gel analysis tool of Fiji (<http://rsb.info.nih.gov/ij/docs/menus/analyze.html#gels>) [92]. LGL-1 MTS WT phosphorylated for 50 min was included in every gel and used as a reference to normalize the amount of phosphorylation.

## 2.3 Model membranes

### 2.3.1 Preparation of SUVs for circular dichroism measurements

DOPC alone or mixed with negatively charged lipids at the desired molar ratio in chloroform was dried 15 min under  $\text{N}_2$  and 1 h under vacuum. The dried lipids were rehydrated in circular dichroism buffer (1 mM  $\text{NaH}_2\text{PO}_4$ , 50 mM NaF, pH 7.4) to a final concentration of 10 mg/mL, vortexed for 5 min and bath sonicated until the solution became clear. SUVs formation was performed at at least 10°C above the highest transition temperature of the lipid used. When the temperature used was higher than RT, the samples were slowly cooled down before further usage. SUVs were used for circular dichroism experiments on the same day they were prepared.

### 2.3.2 Preparation of LUVs

Lipids were mixed in chloroform at the desired molar ratio. After solvent evaporation, the lipid film was rehydrated at 10 mg/mL lipid concentration and resuspended by vortexing. The vesicle suspension was then subjected to eight freeze-thaw cycles and extruded 21 times (Avanti Mini-Extruder, Avanti Polar Lipids) through a polycarbonate membrane.

### LUVs formation for Fluorescence Correlation Spectroscopy measurements

Experiments were carried out in homemade observation chambers obtained by gluing cut PCR tubes on a #1.5 coverslip (Gerhard Menzel GmbH, Thermo Fisher Scientific) with a UV optical adhesive (NOA63, Norland Products Inc., Cranbury, NJ). The wells were passivated with a 2 mg/mL BSA solution for at least 30 min and rinsed with water and working buffer.

For experiments in Chapter 7, DOPC was mixed with 2, 3, 4 or 5 mol% DGS-NTA(Ni) and rehydrated in Phosphate Buffered Saline (PBS) (137 mM NaCl, 2.7 mM KCl, 4.3 mM  $\text{Na}_2\text{HPO}_4$ , 1.4 mM  $\text{KH}_2\text{PO}_4$ , pH 7.4). LUV size and monodispersity were checked via dynamic light scattering (DynaPro NanoStar™, Wyatt Technology Corporation, Santa Barbara, CA) and lipid concentration in LUV preparations was determined by phosphorous assay [93] after extensive dialysis in presence of non-solubilizing concentrations of Triton X-100. The

measured LUV size and lipid concentration were used to calculate the accessible LUV concentration  $[LUV]$  [77] and the number of lipids  $N_{LUV}$  contained in a LUV. LUVs were 10-fold serially diluted in PBS, incubated at the desired final concentrations with 50 nM eGFP-His6 and transferred in the homemade observation chambers.

For experiments in Chapter 8, POPC and POPS were mixed at 4:1 molar ratio and rehydrated in LUVs buffer (100 mM KCl, 10 mM HEPES pH 7.4). Kinase reactions containing 25.60 nM of the labeled LGL-1 MTS peptide were used either in absence (LGL-1 MTS not phosphorylated) or in presence (LGL-1 MTS phosphorylated) of ATP. LUVs were sequentially added to each sample at different final concentrations (0, 1, 10, 100, and 1000  $\mu$ M) and incubated for 5 minutes before measuring.

### LUVs formation for dynamic light scattering and $\zeta$ -potential measurements

DOPC was mixed with DOPS or phosphoinositides at different molar ratios and rehydrated in SLB buffer (10 mM HEPES pH 7.4, 150 mM NaCl) at 1 mg/mL lipid concentration. After extrusion, LUVs were diluted to a final concentration of 100  $\mu$ M, filtered with a 0.45  $\mu$ m mixed cellulose esters filter and aliquoted. Each aliquot was incubated with none or different amounts of the LGL-1 MTS peptide (0, 0.5, 1, 2, 4, 6, and 8  $\mu$ M) for 15 min at RT.

#### 2.3.3 Preparation of GUVs

GUVs were prepared on Platinum (Pt) wires or on Indium Tin Oxide (ITO) coated round coverslips using the electroformation method or using the droplet transfer method.

#### GUVs electroformation on platinum wires

GUVs were prepared in home-made teflon and Pt wires chambers as previously described with minor modifications [94]. Lipid stock solutions were prepared by dissolving lyophilized lipids into chloroform at a final concentration of 1 mg/mL. Lipid stock solutions were either used immediately or stored at -20°C up to few months. When frozen, the lipid stock solutions were allowed to warm to RT before usage. 6  $\mu$ L of the lipid solution were spread uniformly on the Pt wires and dried under vacuum at RT for 1 h to allow complete evaporation of the solvents. Vesicles were formed using the electroformation method [50] with 2 V, 10 Hz for minimum 90 min in a water solution of sucrose matching the osmolarity of the working buffer used for the following experiments. The frequency was then decreased to 2 Hz for ca. 15-30 min, so that the formed GUVs gently detach from the Pt wires. Electroformation was performed at least 10°C above the highest transition temperature of the lipid used. When the temperature used was higher than RT, the samples were slowly cooled down. After electroformation, the GUVs were diluted in working buffer and transferred to an observation chamber (Nunc® Lab-Tek® II chambered coverglass, Thermo Fisher Scientific) previously passivated with a 2 mg/ml BSA solution for at least 30 min and rinsed with water and working buffer.

For experiments in Chapter 7, DOPC were mixed with 2, 3, 4 or 5 mol% DGS-NTA(Ni) and labeled with 0.05 mol% Atto647N-DOPE. 5  $\mu$ L of corresponding 2 mg/mL lipids mixtures were spread and dried onto Pt wires. Experiments were carried out in 120  $\mu$ L MatriCal 384-multiwell plates (Brooks Life Science Systems, Spokane, WA). The wells were passivated with 2 mg/mL BSA for at least 30 min and washed two times with PBS. The obtained GUVs were diluted 1:50 in sucrose solution and then 1:3 in PBS buffer. 20  $\mu$ L of the dilution in PBS were transferred into a well, containing 80  $\mu$ L of PBS buffer.

### GUVs electroformation on ITO-coated round coverslips

GUVs were formed on ITO-coated round coverslips (thickness #1.5, GeSiM, Grosserkmannsdorf, Germany) assembled in a home-built flow chamber [94]. 1.5  $\mu\text{L}$  of the desired lipid mixture at 7.5 mg/mL in chloroform were spread on the ITO glasses at 65°C and allowed to dry. Vesicles were formed using the electroformation method [50] with 1.2 V, 10 Hz for minimum 90 min in a water solution of trehalose or sucrose matching the osmolality of the cyclodextrin-lipid complexes used for the following treatment. If the lipid mixture used contained SM and/or Chol the electroformation was performed at 65°C; in this case the GUVs were slowly cooled down before further usage.

For experiments in Chapter 5, a lipid mixture containing DOPC, SM and Chol at 75, 5 and 20 %mol ratio, respectively, was used. The fluorescent lipid analogue NBD-DOPE was added at a final concentration of 0.5 %mol to the lipid mixture and used to monitor phase separation. This original lipid composition corresponds to the final composition of the inner leaflet of the asymmetric Giant Unilamellar Vesicles (aGUVs).

For experiments in Chapter 5, A lipid mixture containing 100 %mol of DOPC was used. The fluorescent lipid analogue NBD-DOPE was added at a final concentration of 0.5 %mol to the lipid mixture and used to monitor GUVs shape changes. This original lipid composition corresponds to the final composition of the inner leaflet of the aGUVs.

### GUVs formation using the droplet transfer method

GUVs were prepared as previously described [51, 52, 53] with minor modifications. Lipids were first mixed in a glass vial rinsed with acetone and chloroform and dried 15 min under  $\text{N}_2$  and 1 h under vacuum. The lipid film was then dissolved in 5 or 10 mL of mineral oil at a final concentration of 0.5 mg/mL and sonicated in a bath at RT for 20 min (Branson<sup>®</sup> Ultrasonic Cleaners Model 2510, Branson Ultrasonics, Danbury, CT). The oil-lipid mixture was either used immediately or stored at 4°C up to one week. Before each usage, the oil-lipid mixture was allowed to warm to RT and sonicated at RT for 5 min. 500  $\mu\text{L}$  of the outer buffer (20 mM HEPES pH 7.4, 5 mM  $\text{MgCl}_2$ , 100 mM glucose, 1 mM DTT) were placed in a 2 mL tube, overlaid with 500  $\mu\text{L}$  of the oil-lipid mixture, and incubated for at least 2 h at RT to allow a lipid monolayer to assemble at the interface. 15  $\mu\text{L}$  of the internal solution (kinase reactions at 1:5 dilution in internal buffer: 20 mM HEPES pH 7.4, 5 mM  $\text{MgCl}_2$ , 100 mM sucrose, 1 mM DTT, 50 g/L Ficoll 70) were added to 500  $\mu\text{L}$  of the oil-lipid mixture and suspended by gentle pipetting back and forth until a cloudy emulsion was obtained. The whole volume of the emulsion was then slowly poured on top of the oil-lipid mixture, thus resulting in a three-level sample with the outer buffer at the bottom, the oil-lipid mixture in the middle, and the emulsion on top. The tube was then centrifuged in two subsequent steps (10 min at 100 g, 10 min at 350 g) in which emulsion drops of different size passed through the lipid monolayer to form GUVs filled with the internal solution and surrounded by the outer buffer. The outer buffer containing the GUVs was gently collected and transferred to an observation chamber previously passivated with a 2 mg/ml BSA solution for at least 30 min and rinsed with water and outer buffer.

#### 2.3.4 Preparation of SLBs

SLBs were prepared either on freshly cleaved mica or on glass using the VF method [57]. SUVs and SLBs formation was performed at least 10°C above the highest transition temper-

ature of the lipid used. When the temperature used was higher than RT, the samples were slowly cooled down before further usage. SLBs were imaged and Fluorescence Recovery After Photobleaching (FRAP) was recorded to assess the correct formation of the bilayer.

### SLBs formation on freshly cleaved mica

For experiments in Chapter 4, SLBs were prepared on freshly cleaved mica. SUVs were obtained by sonication in an ultrasonic bath. DOPC, SM and NBD-DOPE were mixed in chloroform at different molar ratios; NBD-DOPE concentration was kept at 0.5 %mol for imaging and 0.05 %mol for FCS measurement. After solvent evaporation, the lipid film was rehydrated in SLB buffer at 4 mg/mL lipid concentration and resuspended by vortexing. After sonication, 10  $\mu$ L of the suspension were diluted in SLB buffer to ca. 0.5 mg/mL final lipid concentration and deposited on freshly cleaved mica, glued on a glass coverslip and sealed attaching a plastic cylinder of 7 mm diameter around it. Adding  $\text{CaCl}_2$  to a final concentration of 3 mM induced SUVs fusion and the formation of a lipid bilayer on mica. After 30 min incubation, the sample was vigorously rinsed with SLB buffer to remove any unfused SUVs.

### SLBs formation on glass

For experiments in Chapter 8, SLBs were prepared directly on glass as described for freshly cleaved mica. Pure DOPC or DOPC doped with either 20 %mol DOPS or 7.5 %mol bPI(4,5)P2 were used as lipid mixtures.

## 2.4 Budding of intramembrane domains in GUVs

Budding of intramembrane domains in GUVs was induced as previously described [95] with minor modifications. GUVs were grown from a DOPC:SM:Chol lipid mixture at 36:36:28 %mol ratio in a 12 mM sucrose solution. GM1 and DiI were added to the lipid mixture at a final concentration of 0.1 and 0.5 %mol, respectively, to monitor domain budding. Once cooled down, GUVs were incubated with 10  $\mu$ g/mL CtxB-647 in sucrose for several minutes until the binding to GM1 reached equilibrium. We then incubated the GUVs with 350  $\mu$ L of an ipertonic sucrose solution (26 mM) at RT. After each treatment the sample was delicately washed with 1 mL of a 12 mM sucrose solution.

## 2.5 Protein reconstitution in model membranes

### 2.5.1 PLAP reconstitution in SLBs

PLAP was reconstituted in SLBs either via a direct protein reconstitution method [96] or from proteoliposomes.

In the direct reconstitution method, DOPC SLBs labeled with 0.05 %mol NBD-DOPE formed as described above were incubated with PLAP at 2  $\mu$ g/mL final concentration in presence of 0.22 mM CHAPS for 2 h at RT or overnight at 4°C (Figure 2.1). After PLAP incorporation, SLBs were washed extensively with SLB buffer. No pre-incubation of the membrane with detergent was needed for the incorporation of PLAP into the SLB.

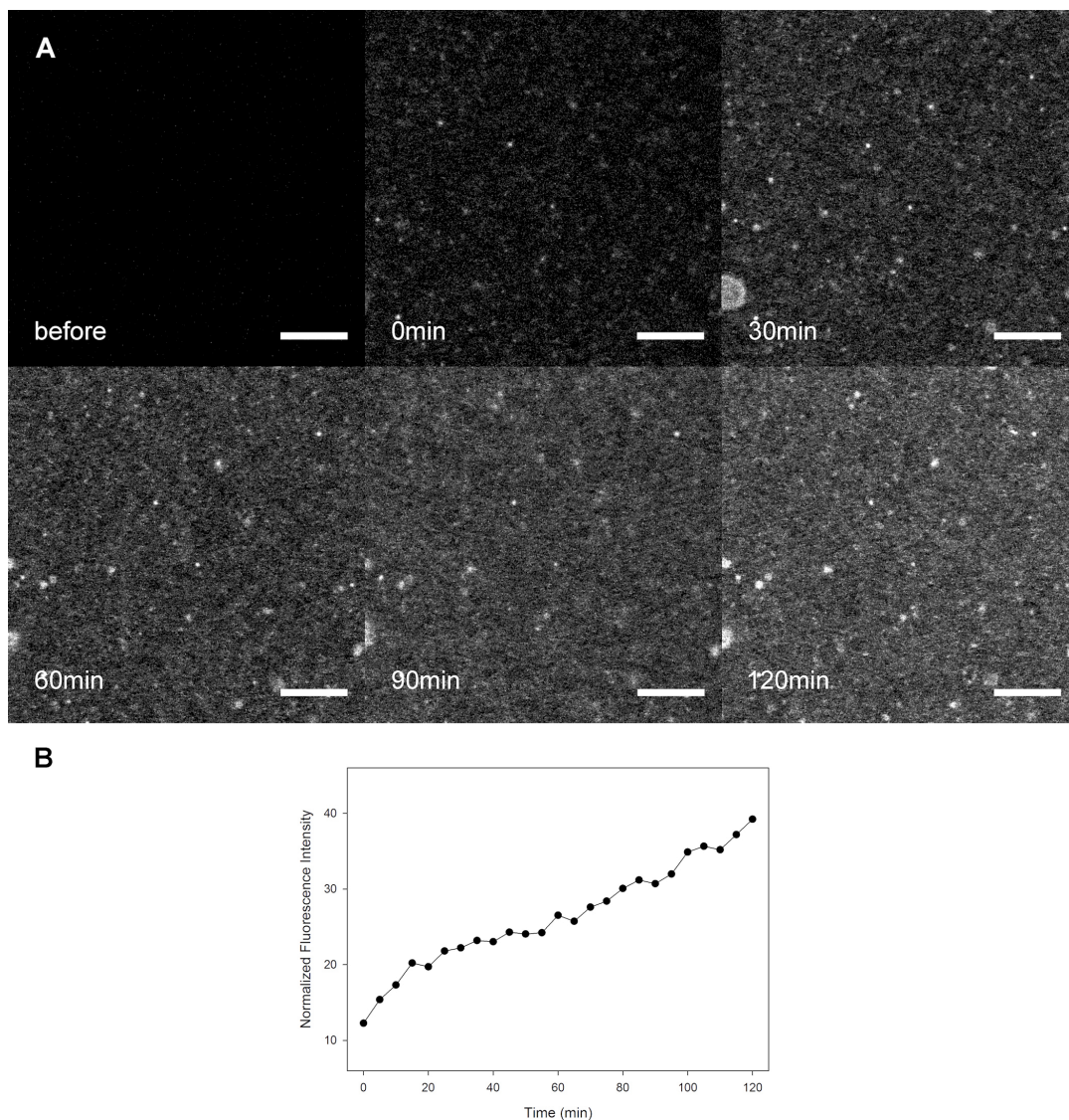


**Figure 2.1** – PLAP reconstitution via direct incorporation. SLBs labeled with 0.05 %mol NBD-DOPE were incubated with Alexa647-PLAP at 2 μg/mL final concentration in presence of 0.22 mM CHAPS for 2 h at RT. [A] Fluorescence confocal images were acquired at the membrane every five min, a selection of these images for a SLB is presented. Scale bars are 10 μm. [B] For each acquired image the mean fluorescence intensity was calculated, normalized to the fluorescence intensity of the NBD-DOPE channel and plotted as a function of time. The intensity of the fluorescently labeled-PLAP increased over time, indicating that the protein is incorporating into the membrane. The incorporation was stopped after 2 h with extensive washing.

In the proteoliposomes method, PLAP was reconstituted into DOPC LUVs as described earlier [88]. PLAP-containing LUVs were incubated 30 min with 0.3 μM NBD-DOPE and used similarly to SUVs to form SLBs as described above. The incorporation and mobility of the reconstituted PLAP in both methods was confirmed by confocal microscopy imaging and FRAP; the activity assessed by pNPP assay in the solution above the SLBs. Briefly, the SLB buffer was changed to glycine buffer (Glycine 0.1 M pH 10.4, 1 mM MgCl<sub>2</sub>, 1 mM ZnCl<sub>2</sub>)



and pNPP at 1 mg/mL final concentration was added. SLBs were then incubated 1 h at RT. The reaction was stopped with 3 N NaOH and the absorbance read at 405 nm.

### 2.5.2 HA TM peptide reconstitution in SLBs

In order to reconstitute the HA TM peptide in supported bilayers, SLBs were prepared in home made chambers as described in 2.3.4. Symmetric SLBs had a lipid composition of DOPC:brain SphingoMyelin (bSM):Chol 2:2:1 (molar ratio). asymmetric Supported Lipid Bilayers (aSLBs) had a lipid composition of DOPC:bSM:Chol 9:1:0 or 7:1:2 before M $\beta$ CD- or HP $\alpha$ CD-mediated lipid exchange, respectively. When the peptide needed to be incorporated directly in the SLB, either 0.1 %mol of the HA TM WT or 0.025 %mol of the GS520AA peptide was mixed with the lipids in TFE before SUVs formation. Alternatively the peptide was incorporated once the SLB was already formed adding 10-25  $\mu$ M peptide to the buffer above the SLB. In this case, non solubilizing amounts of OG (0.5 mM) were eventually added to facilitate the incorporation of the peptide into the bilayer as reported for the direct reconstitution of membrane proteins in SLBs [96].

### 2.5.3 HA TM peptide reconstitution in GUVs

In order to reconstitute the HA TM peptide in giant liposomes, GUVs were prepared as described in 2.3.3. Symmetric GUVs had a lipid composition of DOPC:bSM:Chol 2:2:1, whereas asymmetric GUVs had a lipid composition of DOPC:bSM:Chol 3:3:1, 7:1:4 or 15:1:4 before HP $\alpha$ CD-mediated lipid exchange. 1 %mol of either the HA TM WT or the GS520AA peptide was mixed with the desired lipid mixture as well as 0.5 %mol NBD-DOPE to label the Ld phase of the vesicles. 1.5  $\mu$ L of the lipid-peptide mixture at 7.5 mg/mL in TFE or 100  $\mu$ L at 0.88 mg/mL in TFE were spread on the ITO glasses at 65°C and allowed to dry. Vesicles were formed in a water solution of sucrose matching the osmolarity of the HP $\alpha$ CD-SM complexes used for the following treatment (ca. 100 mOsm/kg). The electroformation was performed at 65°C and the GUVs were slowly cooled down before further usage.

## 2.6 Cyclodextrin-mediated lipid exchange

### 2.6.1 Cyclodextrin-lipid complexes preparation

M $\beta$ CD-SM and M $\beta$ CD-Chol complexes were prepared as described by London and co-workers [86] with minor modifications. For preparing M $\beta$ CD-SM complexes, SM MLVs and M $\beta$ CD were mixed together at 71 and 16 mM final concentration, respectively. The mixture was next incubated with moderate shaking for 2 h at 65°C and centrifuged at 54000 g for 15 min at 4°C. The supernatant contains the M $\beta$ CD-SM complexes and is deprived of any residual MLVs. To prepare M $\beta$ CD-Chol complexes, 80  $\mu$ L of cholesterol 15 mM in isopropanol were slowly added to 2.2 mL of M $\beta$ CD 60 mM in H<sub>2</sub>O pre-heated in a water bath at 80°C. The mixture was then incubated with moderate shaking for 1 h at 60°C and centrifuged at 40000 g for 15 min at 4°C. Incubation and centrifugation temperatures were chosen to optimize the M $\beta$ CD complexes preparation: a high incubation temperature allows the binding reaction to faster reach equilibrium, whereas a low centrifugation temperature enhances the pelleting of any residual SM MLVs. The supernatant was filtered with 0.22  $\mu$ m filters. The osmolarity of both M $\beta$ CD-SM and M $\beta$ CD-Chol complexes was measured (Micro-Sample Osmometer Model

210, Advanced Instruments, Norwood, MA). The nominal M $\beta$ CD concentration was assumed to still be 71 mM and 60 mM in the M $\beta$ CD-SM and M $\beta$ CD-Chol complexes, respectively. This is based on the assumption that no M $\beta$ CD is lost during the incubation with the SM MLVs or cholesterol and in the following centrifugation runs. M $\beta$ CD-SM and M $\beta$ CD-Chol complexes were stored at -20°C until needed or at 4°C and used within few days.

M $\beta$ CD-DOPC, M $\beta$ CD-DOPG and HP $\alpha$ CD-SM were prepared as described for M $\beta$ CD-SM, using DOPC or DOPG instead of SM or HP $\alpha$ CD instead of M $\beta$ CD. To prepare M $\beta$ CD-SM/Atto655-DOPE and HP $\alpha$ CD-SM/Atto655-DOPE complexes, 0.05 %mol Atto655-DOPE was added to SM before forming MLVs. When these cyclodextrin-lipid complexes were prepared, the MLVs-CD mixtures were incubated longer (overnight at 55°C) to reach equilibrium and centrifuged longer and at higher speed (60000 g for 30 min at 4°C) to pellet the residual SM MLVs.

### 2.6.2 Formation of asymmetric SLBs

For experiments in Chapter 4, SLBs were incubated with different concentrations of M $\beta$ CD-SM (5-20 mM) or M $\beta$ CD-Chol (1-10 mM) complexes at RT for 20 and 15 min, respectively. Prolonging the SLB incubation with M $\beta$ CD-SM or M $\beta$ CD-Chol complexes up to 1 h did not influence dramatically the final results.

For experiments in Chapter 6, SLBs were incubated with 12 mM M $\beta$ CD-SM and 5 mM M $\beta$ CD-Chol at RT for 20 and 15 min, respectively. Alternatively, SLBs which already contained cholesterol were treated with 40 mM HP $\alpha$ CD-SM.

After each incubation, samples were delicately washed with SLB buffer. Note that the osmolarity of the CD-SM and M $\beta$ CD-Chol solutions used to treat the bilayers was always matched to the osmolarity of the SLB buffer in which the SLBs were formed.

### 2.6.3 Formation of asymmetric GUVs

aGUVs were prepared as previously described [86] with the following modifications. GUVs were incubated with 350  $\mu$ L of undiluted HP $\alpha$ CD-SM or HP $\alpha$ CD-SM/Atto655-DOPE complexes (nominal concentration of 71 mM) for 30 min at RT. HP $\alpha$ CD does not bind cholesterol and can be used to exchange lipids with a cholesterol-containing bilayer without extracting the cholesterol from the membrane, as recently reported for SUVs [97]. Prolonging the treatment up to 1 h did not dramatically influence the final results. After each treatment the sample was delicately washed with 1 mL trehalose or sucrose isosmotic solution.

### 2.6.4 Cyclodextrin-mediated GUV shape transformation

GUVs were incubated with different concentrations of M $\beta$ CD-DOPG (nominal concentration of 1.42-35.5 mM) up to 1 h at RT. After each treatment the sample was delicately washed with 1 mL trehalose isosmotic solution.

## 2.7 Leaflet specific labeling

### 2.7.1 Leaflet specific labeling in SLBs

In order to probe both leaflets of the same bilayer, each of them was individually labeled with spectrally separated dyes: NBD-DOPE and Atto647N-SM in the lower and upper leaflet,

respectively (Figure 4.1 and 4.12).

NBD-DOPE was directly incorporated in the lipid mixture of SUVs or PLAP-containing LUVs used to produce the SLB. This resulted in the formation of bilayers labeled in both leaflets with NBD-DOPE. The dye in the upper leaflet was then quenched by treatment with sodium dithionite. Quenching of the NBD moiety is a well established strategy to probe asymmetry in vesicles of different sizes [98]. Attempts to treat supported bilayers with sodium dithionite were reported to be not successful [56]. As stated by Crane and colleagues, the exposure of the SLB to high concentrations of sodium dithionite leads to the complete bleaching of the fluorescence in both leaflets of the bilayer, probably due to permeation of the reducing agent through small defects of the membrane. We have systematically tried different conditions and found that when SLBs are exposed to concentrations of dithionite relatively lower in comparison to the concentrations used with vesicles (10-100 ng/mL), the fluorescence of the upper leaflet is preferentially quenched.

To achieve a complete quenching of the NBD-DOPE present in the upper leaflet of the bilayer, each SLB was treated with slightly variable concentrations of sodium dithionite according to the initial amount of NBD-DOPE in the bilayer. In the direct reconstitution method, the SLB was exposed to an amount of detergent that could not solubilize completely the bilayer, but introduced discontinuities in it (data not shown). Those defects in the membrane rendered the SLB even more sensitive to the sodium dithionite treatment. Consequently, the concentration of sodium dithionite had to be decreased in those bilayers to avoid a complete quenching of the NBD-DOPE on both leaflet. To be sure that all the upper NBD was promptly quenched, the total number of NBD-DOPE particles in the laser focus was monitored by point FCS before and after the sodium dithionite treatment and the number of remaining particle after the treatment was kept always inferior to half of the initial NBD-DOPE particle number, assuming the distribution of NBD-DOPE was homogeneous in the two bilayers. In these conditions, we can safely assume that almost the totality of the NBD-DOPE in the upper leaflet (and probably some in the lower leaflet as well) was quenched. Quenching part of the NBD-DOPE particles of the lower leaflet does not negatively influence the FCS measurements.

To label the upper leaflet of the SLB, Atto647N-SM at 5 pg/ $\mu$ L (for FCS measurement) or 250 pg/ $\mu$ L (for imaging) was next added to the buffer above the SLB. The samples were then mixed properly and incubated for 2 min before extensive washing. When a concentration of 5 pg/ $\mu$ L was used, the number of incorporated Atto647N-SM particles was suitable for FCS measurement (1-20 particles in average in the focal volume). When fluorescently labeled PLAP was reconstituted in SLB, no additional probe for the upper leaflet was added.

For experiments in Chapter 6, either NBD-DOPE or NBD-DSPE was used to label the lower leaflet. Labeling of the upper leaflet, on the other hand, was induced by CD-mediated lipid exchange, doping the SM MLV with fluorescently labeled lipids.

### 2.7.2 Leaflet specific labeling in GUVs

GUVs were incubated with 1 mg/mL dithionite in trehalose for 1.5 min. In these conditions, we can safely assume that almost the totality of the NBD-DOPE in the outer leaflet (and probably some in the lower leaflet as well) was quenched. The remaining NBD-DOPE was used as fluorescence probe for the inner leaflet.



# Chapter 3

## Methods

### 3.1 Confocal fluorescence microscopy and correlation spectroscopy

#### 3.1.1 Optical Setup

All measurements were performed on a commercial laser scanning LSM 780 ConfoCor3 system using a water immersion C-Apochromat 40x/1.2 W Corr M27 objective (Carl Zeiss, Jena, Germany). Samples were excited by a 488 nm (green channel, i.e. Alexa488, enhanced Green Fluorescent Protein (eGFP) or Nitro-2-1,3-BenzoxaDiazol-4-yl (NBD)), a 561 nm (orange channel; i.e. DiI, TAMRA or Texas Red DHPE and/or a 633 nm (red channel, i.e. Atto655, Atto647N or Alexa647) lasers. The fluorescence was then collected through appropriate band-pass or long pass filters: green channel, 491-569 nm (imaging in Chapter 7), 493-543 (all measurements in Chapters 5 and 6), 505-575 nm (FCS-GUV measurements in Chapter 7 and all measurements in Chapter 4) or 505-610 nm (FCS-LUV measurements in Chapter 7); orange channel, 569-630 nm (all measurements); and red channel, 638-759 (imaging in Chapter 7) or 655 nm (all other measurements). Pinhole was kept at one airy unit in all measurements, except for FRAP experiments on GUVs. In this case the pinhole was fit to the vesicle size in the Z-plane. A  $\lambda/4$  plate (Melles Griot, Rochester, NY) was implemented into the light pass to generate excitation light with circular polarization and thus to ensure that the laser focus is rotationally symmetric as needed for line-scan FCS [99] as well as to provide an uniform excitation of the GUVs as required for a correct determination of fluorescent intensities [100].

#### 3.1.2 FRAP on GUVs

For FRAP experiments (Chapter 5), GUVs were grown in presence of 0.5  $\mu\text{M}$  Alexa488 and budding was induced via either an hypertonic sucrose solution (control phase separated GUVs) or M $\beta$ CD-DOPG complexes. A square area surrounding one of the two daughter vesicles originated by a budding event was bleached at full power of the laser. The bleaching time was fixed at 50X the acquisition time of the bleached spot. After bleaching, the fluorescence recovery of the square together with the surrounding area were imaged at low laser power with a scan time of 5 s. For each bleaching experiment, three different Region Of Interest (ROI) were selected and measured: (1) the FRAP ROI, corresponding to the bleached daughter vesicle; (2) reference (ref) ROI, corresponding to the unbleached daughter vesicle; and (3) Background (Bkg) ROI, corresponding to an area where no GUVs or vesicles fragments are

present throughout the whole acquisition time (Figure 3.1). To identify a good Bkg ROI all slices of a stack were summed, z-projected and the contrast was strongly enhanced. The ref ROI is used to measure the decay in fluorescence due to acquisition bleaching and/or diffusion of the fluorophore from the unbleached to the bleached vesicle. On the other hand, the Bkg ROI, where there should be no fluorescence, is used to measure the offset intensity. The FRAP ROI average intensity ( $I_{\text{frap}}$ ) was normalized with both a single (Equation 3.1) and double (Equation 3.2) normalization [101]:

$$I_{\text{frap-norm}}(t) = \frac{I_{\text{frap}}(t) - I_{\text{bkg}}(t)}{I_{\text{frap-pre}}} \quad (3.1)$$

$$I_{\text{frap-norm}}(t) = \frac{I_{\text{ref-pre}}}{I_{\text{ref}}(t) - I_{\text{bkg}}(t)} \frac{I_{\text{frap}}(t) - I_{\text{bkg}}(t)}{I_{\text{frap-pre}}} \quad (3.2)$$

where

$$I_{\text{frap-pre}} = \frac{\sum_{t=0}^{t_{\text{bleach}}-1} (I_{\text{frap}}(t) - I_{\text{bkg}}(t))}{f_{\text{prebleach}}} \quad (3.3)$$

$$I_{\text{ref-pre}} = \frac{\sum_{t=0}^{t_{\text{bleach}}-1} (I_{\text{ref}}(t) - I_{\text{bkg}}(t))}{f_{\text{prebleach}}} \quad (3.4)$$

$f_{\text{prebleach}}$  is the number of frames acquired before the bleaching event.

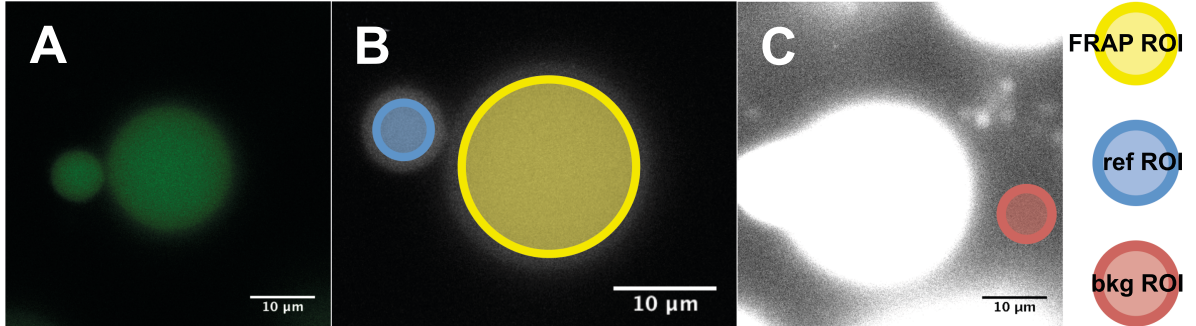


**Figure 3.1** – FRAP ROI. Example of the ROIs used for FRAP analysis: [A] original image; [B] selected FRAP and ref ROIs; [C] Z-project with sum slices of the whole stack and selected Bkg ROIs.

### 3.1.3 Point-FCS on SLBs

For point-FCS measurements on SLBs (Chapter 4), usually 5 to 9 independent SLBs preparations were analyzed. In each preparation, the SLB was typically measured in 6 to 8 randomly chosen membrane spots and for each of them, 10 independent fluorescence intensity time tracks of 10 s were acquired. The FCS correlation curves were calculated using the Zeiss ZEN 2011 Black edition software and fitted using a nonlinear least squares algorithm to a single-component 2D diffusion model. Typical normalized average correlation curves and fitting curves are shown for both upper and lower leaflet probes in a symmetric and aSLB (Figure 3.2). Diffusion times  $\tau_D$  of both probes at each SLB spot were calculated and averaged for all spots in the same preparation. In order to translate  $\tau_D$ s into  $D$ s, the system was calibrated daily using a symmetric DOPC SLB with the same configuration of fluorescent probes as used in the aSLBs. This approach accounts for changes in the confocal volume and allows us to calculate a Relative Diffusion coefficient ( $D^*$ ), i.e. the diffusion coefficient of a probe in an

aSLB relative to the diffusion coefficient of the same probe in a symmetric DOPC SLB.  $D^*$  can be easily calculated from the ratio between the  $\tau_D$  of the probe in the symmetric DOPC SLB used for calibration and the  $\tau_D$  of the probe in the aSLB sample.

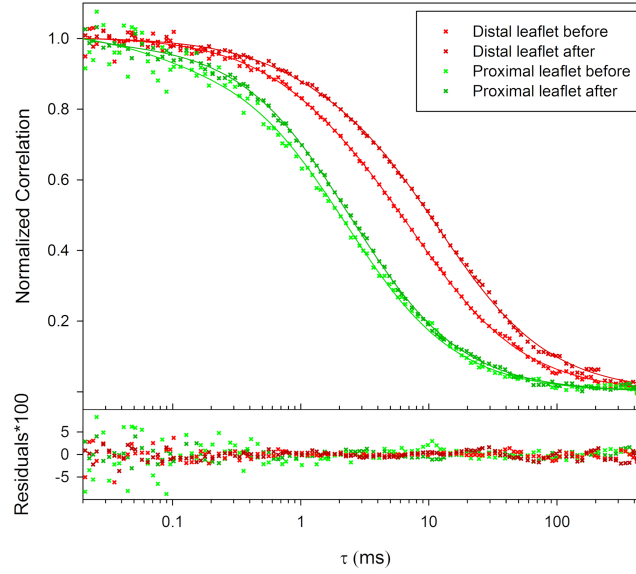


**Figure 3.2** – Point-FCS on lower and upper leaflets. SLBs were labeled with NBD-DOPE and Atto647N-SM in the lower and upper leaflet, respectively and point-FCS was measured before and after M $\beta$ CD-mediated lipid exchange. Typical normalized correlation curves are shown for both lower and upper leaflets. In this example the SLB was treated with 12 mM bSM-M $\beta$ CD complexes. Each curve is the average of 10 correlation curves obtained in a single SLB spot. The solid lines are the best fit of the data to a single-component 2D diffusion model. The lower panel shows the fit residuals.

### 3.1.4 Point-FCS on GUVs and in presence of LUVs

For point-FCS measurements on GUVs and in presence of LUVs (Chapter 7), laser powers were kept very low in order to avoid laser power related problems such as in focus bleaching or saturation [70]. The experiments were carried out at  $26.0 \pm 0.5^\circ\text{C}$ , measured in solution with a digital electrode thermometer Voltcraft K202 (Conrad Electronic, Hirschau, Germany). The setup was calibrated using an aqueous solutions (ca. 50 nM) of freely diffusing Alexa488 ( $D=435 \mu\text{m}^2/\text{s}$   $22.5 \pm 0.5^\circ\text{C}$ [102]) and in case of the GUV assay free Atto655 ( $D=426 \mu\text{m}^2/\text{s}$   $25^\circ\text{C}$ [103]) in a 1:1 ratio. The objective correction collar and the pinhole position were adjusted to maximize the fluorescence intensity. Correction of diffusion coefficients to the measurement temperature [70] and subsequent weighted fit of the auto-correlation curves (Equation 7.7; Alexa488: 3D+T diffusion model, Atto655: 3D diffusion model without triplet correction), allowed us to determine the parameters of the detection volume: the focal radius  $w_0$  (Equation 7.10), the focal volume  $V_{FCS}$  (Equation 7.9) and the focal area  $A_{FCS} = \pi w_0^2$ .

For point-FCS measurements on GUVs, a minimum of eight GUVs per sample were selected and measured at least at five increasing concentrations of eGFP-His6. Before protein addition the background signals in solution and on the membrane were recorded. Images were

taken at approximately their equator using avalanche photodiodes and analyzed by the image analysis method described below. Furthermore, point FCS was performed at the top pole of the GUVs by maximizing the fluorescence intensity and measuring five times 30 s. To get  $N_f$  a measurement of ten times 30 s was conducted in solution. The obtained auto-correlations curves were analyzed using PyCorrFit 0.7.4 [104]. The after pulsing was removed (2  $\mu$ s),  $\tau_T$  fixed to 0.02 ms and  $S$  to the one obtained by the calibration measurement. A non-weighted 3D+T-fit was used to get  $N'_f$ , which was subsequently corrected for the background signal. A weighted fit was used to get  $\tau_D$  of the protein and that average value was used in the following fit of the bound fraction. To obtain  $N'_{2D3D}$ , a non-weighted 2D3D+T-fit (Equation 7.11) was applied and then background corrected. The free and bound protein concentrations were plotted using Origin 9.0.0G (OriginLab Corporation, Northampton, MA) and analyzed by defining a x/y-weighted linear fit in the nonlinear implicit curve fit dialog. From  $\tau_{2D}$  obtained by a weighted 2D3D+T-fit the  $D$  were calculated by rearrangement of Equation 7.10.

For point-FCS measurements in presence of LUVs, each DOPC:DGS-NTA(Ni) molar ratio, at least three independent samples were investigated at eight different LUV concentrations (1 nM - 10 mM). For each LUV concentration, point-FCS was measured four sequential times and for each of them ten independent fluorescence intensity tracks of 10 s each were acquired. The FCS auto-correlation curves were calculated using the Zeiss ZEN 2011 Black edition software and analyzed using PyCorrFit 0.8.1 [104]. The after pulsing was removed (1  $\mu$ s) and  $S$  was fixed to the one obtained by the calibration measurement.  $[P]$  and  $\tau_f$  were measured by point-FCS in absence of LUVs and to calculate the protein concentration in each sample. A non-weighted 3D+T-fit (Equation 7.7) was used to get the number of particles, whereas a weighted fit was used to get the  $\tau_f$ ; the average  $\tau_f$  value was used in the following fits in presence of LUVs. To obtain the total number of particles  $N_{f+m}$  (free + vesicle bound protein) a non-weighted two components 3D+T-fit was applied (Equation 7.23). From  $N_{f+m}$  obtained from the fit, an average normalized  $G(0)$  value was calculated for each LUV concentration of a sample, then plotted against the accessible  $[LUV]$  and fitted to the Equation 7.26 to obtain  $K_d$  using SigmaPlot 12.3 (Systat Software, Inc., San Jose, CA).  $K_{ds}$  were finally converted to  $K_{Ps}$  (Equation 7.27).

### 3.1.5 Line-scan FCS on SLBs and GUVs

Line-scan FCS measurements and analysis (Chapter 6) were performed similarly as previously described [99]. Detectors were set in photon counting mode and the correction collar of the objective was adjusted by maximizing the fluorescence intensity while focusing on the plane of the membrane. Usually 3 to 5 independent SLBs preparations were analyzed. In each preparation, the SLB was typically measured in 4 to 5 randomly chosen membrane spots and for each of them, 10000 line scans of 10.65  $\mu$ m were acquired. The movement of the detection volume was controlled directly with the Zeiss ZEN 2011 Black edition software (Table 3.1), selecting a linear scan path in a SLB image.

On phase-separated SLBs, correlation curves were calculated independently for each lipid phase. The phases could be identified due to the different affinity of the upper and lower fluorescent dyes to the Lo (low affinity, dim) and the Ld phase (high affinity, bright). The line-scans can be visualized as a pseudo-image where the vertical axis is the time. The photon counts per pixel were saved as raw data and analyzed with a self-written MATLAB (MathWorks, Natick, MA) script (Dr. Salvatore Chiantia, Humboldt Universität zu Berlin,



	Parameter	Unit
<b>Line Size</b>	512 x 1	pixel x pixel
<b>Zoom</b>	20	X
<b>Pixel Size</b>	20.80	nm
<b>Speed</b>	13	X
<b>Pixel Dwell Time</b>	0.64	μs
<b>Line Time</b>	0.768	ms
<b>Cycles</b>	10 <sup>4</sup>	X
<b>Scan Time</b>	7.64	s

**Table 3.1** – Line-scan FCS parameters. Optimized parameters for performing line-scan FCS on phase-separated SLBs with a Zeiss LSM 780 system.

Germany). The spatiotemporal correlation curves  $G(\xi, \tau_i)$  were calculated binning the pixels 2x2 and restricting the temporal range to  $\tau_i = \tau_1 - \tau_{30}$  to limit the computation time. When it was necessary to correct for depletion due to photobleaching, a correction scheme which allows to extract correct concentrations from the measurement was applied [99]. The spatiotemporal correlation curves were then fitted using a non-weighted nonlinear least squares fitting algorithm to a single-component 2D flow-diffusion model with a Gaussian detection area:

$$G(\xi, \tau_i) = \frac{1}{C\pi w_0^2} \exp\left(-\frac{\xi^2}{w_0^2 + 4D(\tau_i + \xi/v)}\right) x \left(1 + \frac{4D}{w_0^2} \left(\tau_i + \frac{\xi}{v}\right)\right)^{-1} \quad (3.5)$$

Typical spatiotemporal correlation and fitting curves for  $\tau_i = \tau_1 - \tau_5$  are shown for both upper and lower leaflet probes in aSLBs (Figure 6.2). The focal volume waist ( $w_0$ ) as well as  $D$  and concentrations ( $C$ ) of both probes were obtained directly from the fit to Equation 3.5.

### 3.2 GUV image analysis for determining partitioning coefficients

In order to extract the surface and bulk fluorescence intensities  $I_{2D}$  and  $I_f$  from the confocal GUV images, a semi-automated MATLAB script (Dr. Zdeněk Petrášek, Graz University of Technology, Graz, Austria) was used. For each GUV to analyze, the user enters approximate coordinates of the GUV center and an approximate radius (Figure 3.3). The software then determines the precise GUV center position and approximates the circumference of the GUV cross-section by a smooth closed curve. This allows the extraction of the radial intensity profile of the GUV. From the intensity profile the surface fluorescence intensity  $I_{2D}$  and the solution fluorescence intensity  $I_f$  are determined. Additionally, it is possible to exclude a range of angles (a wedge) from the analysis, which is useful, for example, when two GUVs are in contact. The ring region outside the GUV (an interval of radial distance in the radial intensity profile) from which  $I_{2D}$  is determined is typically constant for all GUVs and need not be adjusted individually. If necessary the background of the GUVs before protein addition was subtracted from mean intensity. Each point was correlated to the corresponding concentration  $[P_{2D}]$  determined by FCS in Origin 9.0.0G and analyzed by a linear fit passing through the origin of the graph. Analogously the averaged mean intensities in solution were related to  $[P_f]$ .

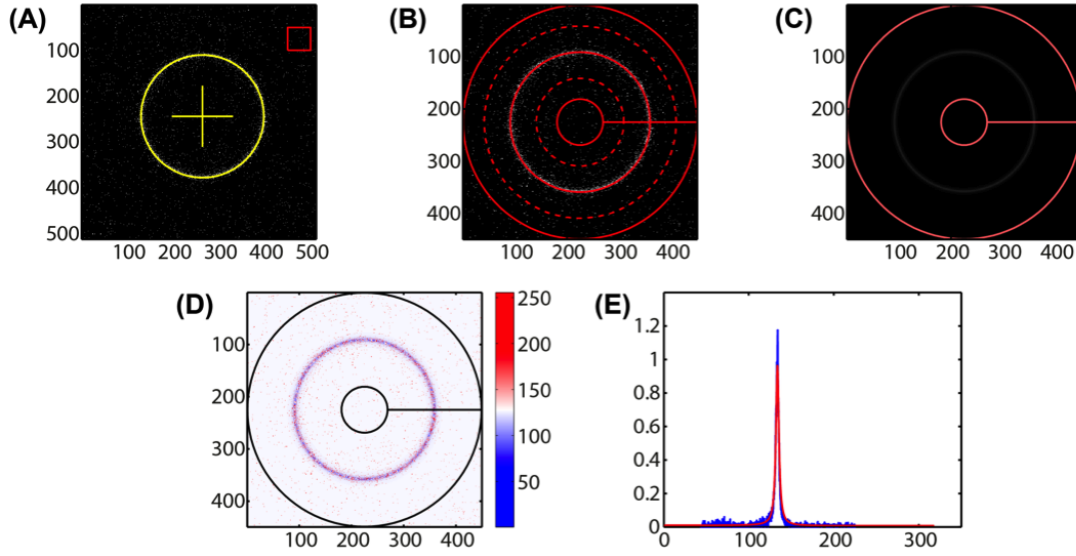


**Figure 3.3** – GUV image analysis. [A] GUV with rescaled intensity and a marked area from which the background intensity is calculated, [B] the ring area between the two dashed lines is used to determine the surface concentration (bound fraction,  $I_2D$ ), the mean intensity inside the GUV is calculated from the innermost ring area, and the intensity outside the GUV from the outermost ring [C] fit of the GUV shape and intensity within the selected area, [D] fit residuals, [E] the experimental (blue) and fitted (red) radial profile of GUV. Image scale: [A]-[D] x- and y-axis in pixel, [E] x-axis in pixel and y-axis in average photons per pixel.

The  $K_P$  of the LGL-1 MTS peptide encapsulated in GUVs was determined similarly as described for solutes incubated outside the GUVs. Briefly, several GUVs for each sample were imaged at the equator, their fluorescence intensities at the GUV membrane and inside the GUV were extracted with the customized MATLAB script and transformed in peptide concentrations at the GUV membrane [ $P_{2D}$ ] and inside the GUV [ $P_f$ ], respectively. In order to perform this conversion, the system was calibrated with different peptide solutions whose concentration were determined by FCS.  $P_{2D}$  and  $P_f$  normalized by the GUV radius  $r_{GUV}$  were plotted against each other and fitted to Equation 8.3 to determine  $K_P$  (Figure 8.14).

### 3.3 Image processing and analysis

Fluorescence confocal images were processed and analyzed with Fiji (<http://fiji.sc/Fiji>). When needed, image contrast was enhanced through normalization.

#### 3.3.1 Measurements in thresholded images

Number and average size of Lo domains (Chapter 4) were measured in locally thresholded images, whereas average fluorescence intensities of the FRAP and ref areas (Chapter 5) were measured using globally thresholded images.

### 3.3.2 Determination of Lo partitioning coefficients in GUVs

The fraction of labeled HA TM peptides partitioning into the Lo phase (Chapter 6) was determined from intensity radial profiles of confocal images using the radial profile angle plug-in (<http://rsbweb.nih.gov/ij/plugins/radial-profile.html>), similarly as described by Sezgin and colleagues [100] for line profiles. The fluorescence intensities of the Lo and Ld phases,  $F_{Lo}$  and  $F_{Ld}$ , were determined from the peaks of the radial profile plots, where the different phases were identified by the Ld phase marker NBD-DOPE (Figure 3.4). The background value obtained from an area outside the vesicles was subtracted from peak values. The Lo partitioning coefficient ( $\%Lo$ ) was calculated as follow:

$$\%Lo = \frac{F_{Lo}}{F_{Lo} + F_{Ld}} \quad (3.6)$$

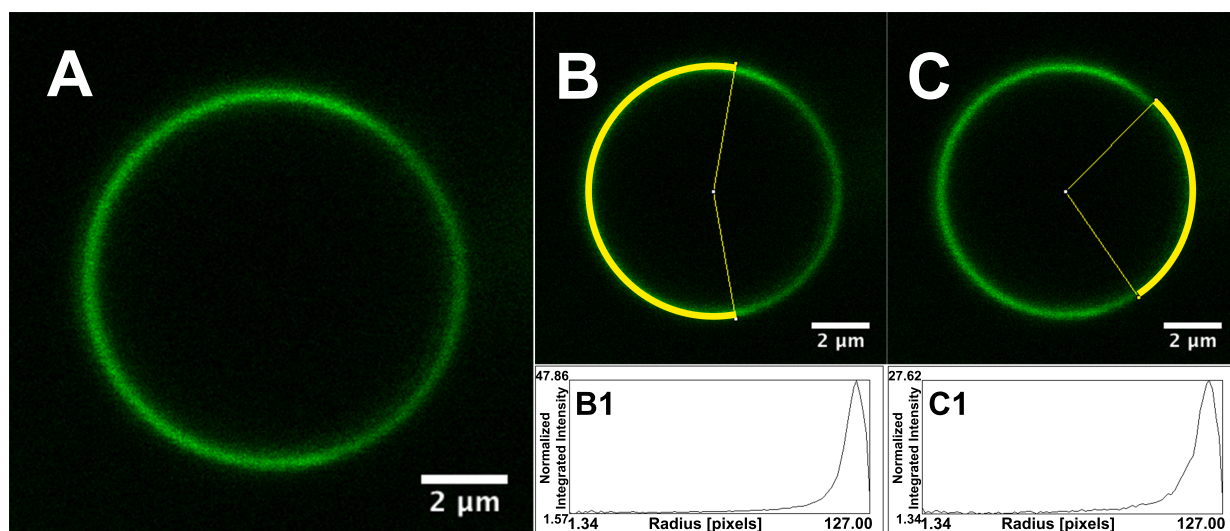


**Figure 3.4** – Determination of Lo partitioning coefficients in GUVs. Example of a phase separated GUVs imaged at its equator and labeled with the Ld phase marker NBD-DOPE. The fluorescence intensities of the Ld [B] and Lo [C] phases,  $F_{Ld}$  and  $F_{Lo}$ , were determined from the peaks of the respective radial profile plots [Ld, B1; Lo, C1].

### 3.3.3 Determination of protein binding to GUVs

The binding of the labeled LGL-1 (469-702) WT and EEE mutant was determined from the picks of the intensity radial profile plots of confocal images taken at GUVs equator using the radial profile angle plug-in (<http://rsbweb.nih.gov/ij/plugins/radial-profile.html>).

### 3.3.4 Determination of protein binding to SLBs

The binding of the labeled LGL-1 (469-702) WT and AAAA mutant was determined from intensity profiles of confocal z-stack images taken parallel at the SLBs plane using the z-project function. LGL-1 fluorescence intensity values were background corrected, averaged and normalized by the value obtained in SLBs containing DOPC only.

### 3.4 Circular dichroism spectroscopy

Far-UV circular dichroism spectra were acquired at 25°C on a Jasco J-715 spectropolarimeter (Jasco, Easton, MD) as previously described [105, 106]. The unlabeled LGL-1 MTS peptide concentration was kept at 50  $\mu$ M and mixed with different amount of SUVs (1:10, 1:50, and 1:100 molar ratio) in circular dichroism buffer. Eight scans were accumulated and background signal (buffer only and lipid only) was subtracted from the spectra. The  $\alpha$ -helix content of the peptide in presence of different lipid mixtures was estimated from the circular dichroism spectra with the CDPro software package (<http://lamar.colostate.edu/~sreeram/CDPro/>) using the CONTIN method and the SMP56 protein set. Circular dichroism spectra of the peptide in absence of lipids in TFE were acquire and used to normalize the  $\alpha$ -helix content of the peptide.

### 3.5 Dynamic light scattering and $\zeta$ -potential

Dinamic Light Scattering (DLS) and  $\zeta$ -potential measurements were performed with a Malvern Zetasizer Nano ZSP system (Malvern, Malvern, UK) as previously described with minor modifications [107]. Ultra-micro UV-transparent spectrophotometry cuvettes (Brand, Essex, CT) and disposable folded capillary cells DTS 1070 (Malvern) were used in DLS and  $\zeta$ -potential measurements, respectively. For DLS experiments 2 scans (13 runs each) were performed at 25°C with an initial equilibration time of 5 min. For  $\zeta$ -potential measurements 15 scans (20-100 runs each) were performed at 25°C with constant voltage of 40 mV and an initial equilibration time of 5 min. After each scan the instrument paused for 90 s and every 5 scans for 5 min. Values of the viscosity and refractive index were set at 0.8882 cP and 1.330, respectively. Experiments were performed in duplicate.

The  $\zeta$ -potential values  $\zeta$  obtained from the instrument software were plotted against the peptide concentration  $[P]$  and fit to Equation 3.7 to obtain the Apparent Binding Constant ( $K_B$ ):

$$\zeta = \frac{\zeta_0 + \zeta_{lim} K_B [P]}{1 + K_B [P]} \quad (3.7)$$

where  $\zeta_0$  is the  $\zeta$ -potential value in absence of peptide and  $\zeta_{lim}$  the  $\zeta$ -potential value at saturating peptide concentration. The fitting was performed using SigmaPlot 12.3.

### 3.6 Statistical analysis

Statistical analysis was performed using SigmaPlot 12.3. When the means of two sets of data were compared (Figure 4.3 B, 4.5, 4.7, 4.9 A, 8.3 B and 8.7 E), a t-test or a paired t-test was used for independent or before-and-after samples, respectively. For both t-tests two-tailed P-values are reported. Comparison of more than two sets of data (Figure 4.3 A, 4.6 and 8.4), were carried out with one-way ANalysis Of VAriance (ANOVA) or one-way repeated measures ANOVA for independent samples or samples measured over time, respectively. To isolate the group or groups that differ from the others, ANOVA was followed up with an all-pairwise multiple comparison procedure (Tukey Test or Holm-Šidák Method). The level of alpha was kept at 0.05 for all statistical analyses.

## Part III

# RESULTS AND DISCUSSION

The experimental work presented in Chapter 4 was designed together with Dr. Salvatore Chiantia (Humboldt Universität zu Berlin, Germany) and Prof. Petra Schwillke (Max Planck Institute of Biochemistry, Martinsried, Germany) .

Size-exclusion chromatography steps of the PLAP purification and labeling were performed by Dr. Sabine Suppman (Biochemistry Core Facility of the Max Planck Institute of Biochemistry, Martinsried, Germany).

## Chapter 4

# Asymmetric supported lipid bilayer formation via methyl- $\beta$ -cyclodextrin mediated lipid exchange

The transversal asymmetry in lipid composition is one of the most challenging features of a biological membrane to reproduce in SLBs. In many eukaryotic cells SM is enriched in the extracellular leaflet of the plasma membrane, whereas phosphatidylethanolamine and negative charged lipids e.g. PS are predominantly located in the cytoplasmic leaflet [3]. To date, the production of aSLB with a specific lipid composition in each leaflet has only been established for the LB/LS deposition and for the hybrid LB/VF method [56, 108]. In few cases, VF has been reported to spontaneously generate asymmetric SLBs depending on lipid mixture, VF conditions and type of support used [109]. For example, electrostatic repulsion/attraction between lipids and support was successfully used to form SLBs containing asymmetrically distributed charged lipids. In particular, PS was preferentially found in the lower leaflet of SLBs on titanium dioxide [110] or in the upper leaflet of SLBs on a silicon block [111]. However, the asymmetry in SLBs produced by VF can be only partially controlled, and a more general approach is still missing.

A M $\beta$ CD-mediated lipid exchange technique was recently devised to prepare SUVs with stable asymmetric lipid compositions [85] and later tailored to produce asymmetric GUVs at high yield [86]. This method is based on the ability of M $\beta$ CD to bind phospholipids [112] and to exchange them with a preformed lipid bilayer. Briefly, in this method a lipid bilayer is exposed to a concentrated solution of M $\beta$ CD loaded with the desired lipid species. Only the accessible leaflet of the bilayer can directly exchange lipids with the M $\beta$ CD complexes, i.e. can be enriched with the lipid previously in complex with the M $\beta$ CD. This confined enrichment generates asymmetry in the lipid composition of the bilayer. The ability of M $\beta$ CD to bind phospholipids or, more generally, lipophilic compounds (e.g. cholesterol) derives from its chemical structure: cyclodextrins are in fact cyclic oligomers of glucose, in which the interior of the circle of glucose units forms a non-polar cavity [113]. The approach of the M $\beta$ CD-mediated lipid exchange method is in principle applicable to every model lipid bilayer, including SLBs.

Individual lipids are not only asymmetrically distributed, but also supposed to be laterally segregated in biological membranes. Lipid lateral organization could be addressed in a variety of membrane model systems using so-called raft-mimicking lipid mixtures. Although their

phase behavior was extensively investigated, the effect of compositional asymmetry on phase separation remains unclear. In a series of seminal articles, Tamm and coworkers [56, 114, 115] investigated the coupling of cholesterol-rich Lo domains in asymmetric bilayers of different lipid composition, and showed for the first time that Lo domains in one leaflet can induce phase separation in an opposing leaflet with lipid compositions that would not spontaneously phase separate. In the cases in which phase separation is not induced, domains are observed in at least one leaflet. At the same time, Collins and Keller [116] showed that a leaflet with a lipid composition that does not phase separate can also suppress domain formation in the leaflet with a lipid composition that would phase-separate in a symmetric bilayer. In these experiments, phase separation was observed either in both leaflets or not at all. The results described in the above-mentioned works were obtained in two quite diverse model membranes (tethered polymer-SLBs and free-standing black lipid membranes). A third independent approach is needed to better understand the observed differences in the two systems. The biological relevance of studying lipid lateral organization in asymmetric membrane systems was recently underlined by the work of Hussain and colleagues; they could demonstrate that bilayer asymmetry influences the sequestering of integrins in raft-mimicking lipid mixtures [117].

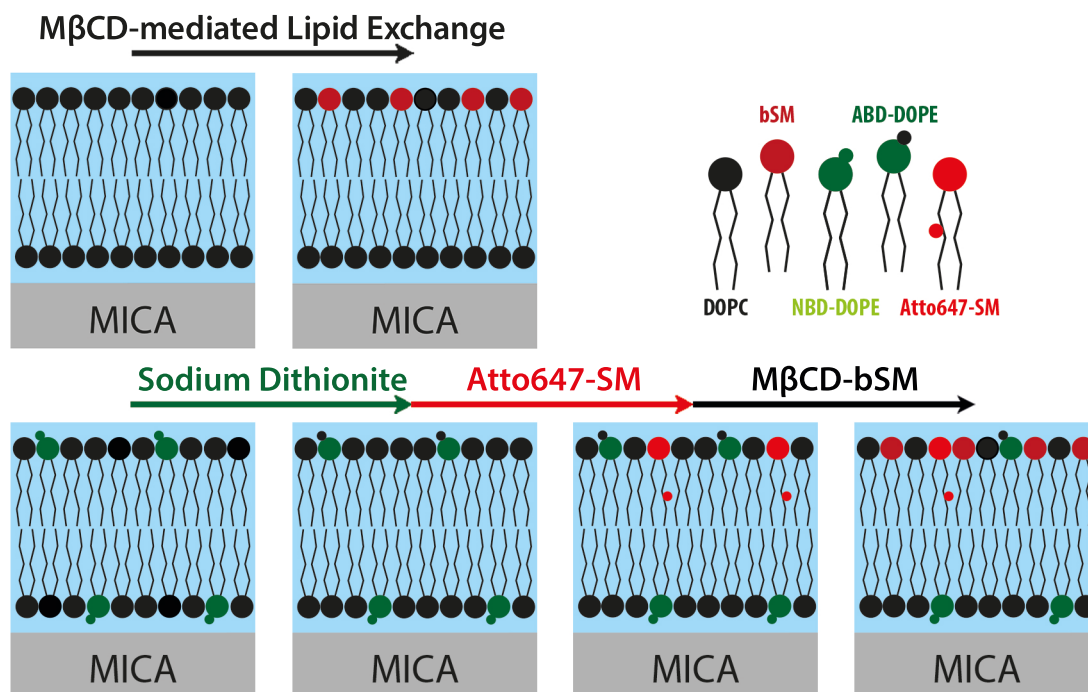


**Figure 4.1** – aSLB leaflet-specific labeling. A schematic diagram of aSLB formation via M $\beta$ CD-mediated lipid exchange and of the leaflet-specific labeling strategy used to quantitatively assess it.

In this chapter we describe how the M $\beta$ CD-mediated lipid exchange method can be applied to SLBs formed by VF to easily produce flat bilayers with asymmetric lipid composition. Specifically we selectively enriched the upper leaflet of a dioleoylphosphatidylcholine SLB



with SM, incubating the bilayer with M $\beta$ CD-SM complexes (Figure 4.1). SM incorporation is known to affect membrane fluidity [86]. Therefore, to assess the asymmetric SM enrichment in the bilayer, we labeled each SLB leaflet with a different fluorescent lipid probe and measured their diffusion by FCS. To selectively label each leaflet, the nitrobenzoxadiazole NBD moiety of the lipids in the upper leaflet was quenched with sodium dithionite and lipids conjugated with a spectrally separated dye were subsequently incorporated in it from the above buffer. Selective labeling of each leaflet allows us to probe both leaflets independently and measure local lipid dynamics. We additionally show that the produced asymmetric SLBs are stable for at least four hours, fully compatible with the most common protein reconstitution methods and suitable for studying phase separation and transbilayer lipid movement of raft-mimicking lipid mixtures.

## **4.1 The upper leaflet of DOPC SLBs can be enriched with SM to form asymmetric bilayers.**

Symmetric DOPC SLBs were prepared on freshly cleaved mica using the VF method [57]. Mica supports typically had an area of 38 mm<sup>2</sup> and were kept hydrated with 200  $\mu$ L of SLB buffer at all times after SLB formation. Assuming the lipid packing constant, the total amount of lipids in SLB samples (ca. 10-10 mol) is two orders of magnitude lower than that typically found in vesicles preparations (e.g. ca. 10-8 mol for GUV samples prepared on ITO glass), for which high concentrations of M $\beta$ CD and SM in solution can be used to produce asymmetric bilayers [85, 86]. High M $\beta$ CD-SM:lipid ratios could lead to extensive extraction and solubilization of lipids from the SLB. To determine whether and at which concentration M $\beta$ CD affects the integrity of the bilayer, several SLBs labeled with 0.05 %mol NBD-DOPE were treated with different concentrations of M $\beta$ CD-SM complexes (Figure 4.2). Treatment of SLBs with high concentrations of M $\beta$ CD-SM (20 mM), comparable to those normally used for the preparation of asymmetric free standing bilayers, results in extensive damage and eventually complete solubilization of the membrane. Time-lapse confocal imaging shows that dark areas form and enlarge in the SLBs. The dark areas are indeed discontinuities of the SLB, as suggested by the absence of NBD-DOPE and confirmed by the addition of a highly hydrophilic fluorescent protein with no membrane affinity (i.e. eGFP) to the buffer above the SLB. The protein colocalizes completely with the dark areas, confirming that in those regions the mica is not covered by a bilayer, but exposed to the buffer (data not shown). In contrast, at lower M $\beta$ CD-SM concentrations (5-16 mM) SLBs showed less or no damage at all, allowing the treatment of SLBs with M $\beta$ CD-SM.

Thus, M $\beta$ CD-SM concentration needs to be low enough to preserve SLBs integrity, but sufficient to enrich the upper leaflet of SLBs with SM. The SM enrichment of a membrane leaflet is generally expected to reduce membrane fluidity, due to the increased lipid order [85, 86]. FCS has been proven to be a very useful tool to characterize the fluidity of lipid bilayers; in particular, the  $D$  of fluorescently labeled lipids measured by FCS have been extensively used to evaluate membrane organization [67]. In case of successful enrichment of a membrane leaflet with SM, the  $D^*$  of a fluorescent probe included therein should decrease. We therefore performed FCS on several DOPC SLBs labeled with Atto647N-SM in the upper leaflet before and after treatment with different M $\beta$ CD-SM concentrations (10-16 mM) to identify the M $\beta$ CD-SM concentration needed to minimize the Atto647N-SM  $D^*$ , i.e. to maximize the SM enrichment (Figure 4.3, A). Atto647N-SM  $D$  differs significantly across the four M $\beta$ CD-

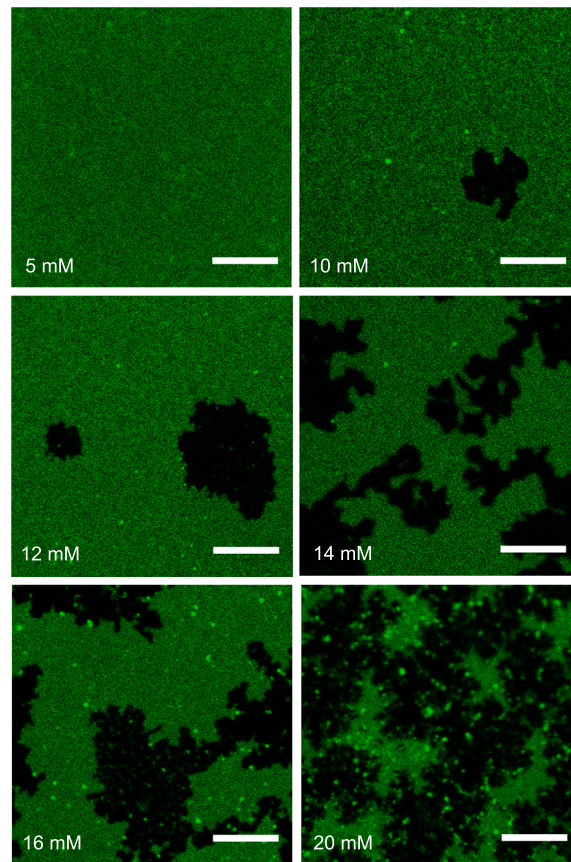


**Figure 4.2** – SLB integrity upon M $\beta$ CD-SM treatment. SLBs labeled with 0.05 %mol NBD-DOPE were treated for 20 min with different concentrations of M $\beta$ CD-SM (5-20 mM). After extensive washing, fluorescence confocal images were acquired. High concentrations of M $\beta$ CD-SM (20 mM) result in a complete destruction of the bilayer. Scale bars are 10 $\mu$ m.

SM concentrations tested (one-way ANOVA,  $F(3, 20)=29.20$ ,  $p<0.001$ ). Tukey post-hoc comparisons confirmed that concentrations equal or above 12 mM minimize the Atto647N-SM  $D$  (12 mM:  $M=66\%$ ,  $SD=1$ ; 14mM:  $M=68\%$ ,  $SD=2$ ; 16mM:  $M=66\%$ ,  $SD=2$ ) and make it significantly lower than that resulting after treatment with 10 mM M $\beta$ CD-SM ( $M=76\%$ ,  $SD=2$ ,  $***p<0.001$ ). Atto647N-SM  $D$  after incubation with 12, 14 and 16 mM M $\beta$ CD-SM are statistically not distinguishable ( $p>0.05$ ). An M $\beta$ CD-SM concentration of 12 mM is sufficient to decrease the  $D^*$  of the upper probe to the lowest value obtained in the M $\beta$ CD-SM concentration range tested, while keeping the damage of the SLBs to a minimum. When a nominal M $\beta$ CD-SM concentration of 12mM is used, the M $\beta$ CD-SM:lipid ratio can be estimated to be approximately 25000:1.

Having optimized the M $\beta$ CD-SM concentration, we then asked whether the enrichment in SM after M $\beta$ CD-SM treatment is confined to the upper leaflet of the SLB, in other words whether an asymmetric SLB is formed. For this purpose, several symmetric DOPC SLBs were labeled with NBD-DOPE and Atto647N-SM in the lower and upper leaflet, respectively. We then measured the mobility of the different probes by point-FCS before and after treatment with 12 mM M $\beta$ CD-SM (Figure 4.3, B). The  $D^*$  of Atto647N-SM decreases to about 67%

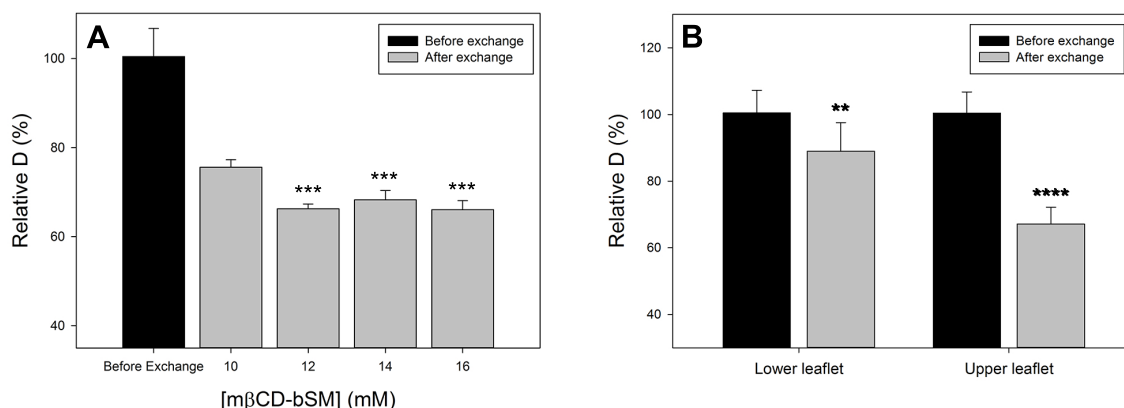


**Figure 4.3** – aSLB formation via M $\beta$ CD-mediated lipid exchange method. [A] Upper leaflet  $D^*$ s are plotted before and after incubation with different concentrations of M $\beta$ CD-SM (10-16 mM). Concentrations equal or above 12 mM minimize the upper leaflet  $D^*$  and make it significantly lower than that resulting after treatment with 10 mM M $\beta$ CD-SM (\*\*\* $p$ <0.001). [B] Lower and upper leaflet  $D^*$ s are plotted before and after incubation with 12 mM M $\beta$ CD-SM. Upper leaflet  $D^*$  significantly decreases to about 67% of the original value (\*\*\*\* $p$ <0.0001), whereas the upper leaflet  $D^*$  exhibits a meaningful but minor reduction of ca. 10% (\*\* $p$ <0.01), suggesting that the incorporation of the SM was mostly limited to the upper leaflet and the formation of asymmetric SLBs was achieved. NBD-DOPE and Atto647N-SM mean relative  $D$  values are plotted with error bars of one standard deviation (A,  $n$ =5; B,  $n$ =9). Reported  $D$  values are relative to those measured in symmetric DOPC SLBs with the same configuration of fluorescent probes.

of the original value ( $M$ =67%,  $SD$ =5; \*\*\*\*Paired  $t$ -test,  $t(8)$ =25.72,  $p$ <0.0001), as expected in case of SM incorporation. From the calibration curve (Figure 4.4), the SM incorporation can be estimated to be 50-70 %mol of the total lipids in the upper leaflet of the membrane. In contrast, the  $D^*$  value of the NBD-DOPE exhibits a very small decrease of ca. 10% ( $M$ =89%,  $SD$ =9; \*\*Paired  $t$ -test,  $t(8)$ =4.94,  $p$ <0.01), probably due to limited interleaflet coupling [118]. The observed decrease in NBD-DOPE diffusion might alternatively be due to the incorporation of small amounts of SM in the lower leaflet during M $\beta$ CD-SM lipid exchange, although this possibility seems less likely (Figure S4 [86]). Altogether, these data suggest that the incorporation of the SM was mostly limited to the upper leaflet and that the formation of an asymmetric bilayer was achieved. Moreover, it is worth noting that the influence of the support on the lower leaflet is not substantially stronger than that exerted on the upper leaflet, as confirmed by unsuccessful attempts to measure differences in the diffusion rate of lipid dyes in each leaflet [60] (Table 6.1). Finally the slower NBD-DOPE dynamics after lipid exchange in the bottom leaflet is not a result of nanoscopic defects introduced in the bilayer through the M $\beta$ CD treatment, as suggested by control experiments in which the SLBs were treated with 12mM M $\beta$ CD-DOPC (Figure 4.5).

## 4.2 Leaflet asymmetry is stable for several hours

Experimentally useful aSLBs need to be stable for a reasonable amount of time required to run the desired experiments. The scrambling of the SLB is supposed to alter the local lipid packing, and consequently, the diffusion coefficient of the lipids in each leaflet. As SM flips

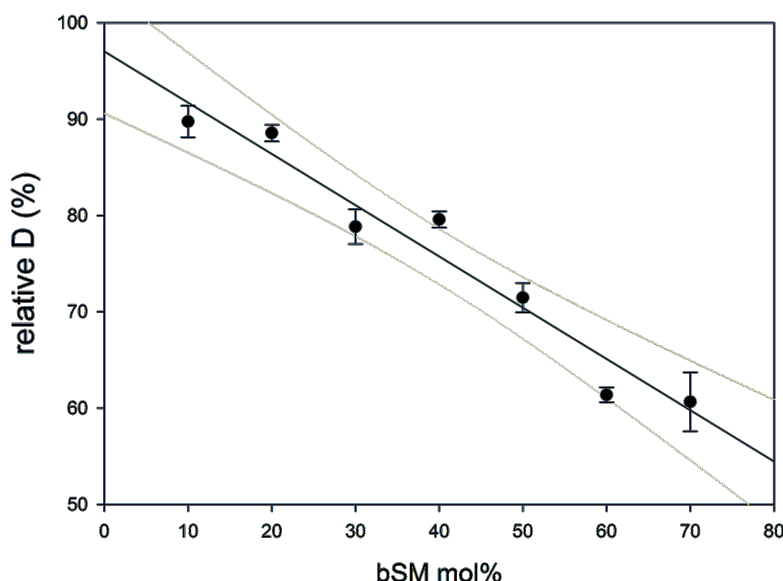


**Figure 4.4** – SLB fluidity in presence of bSM. Symmetric DOPC SLBs containing different amount of bSM were labeled with Atto647N-SM in the upper leaflet and its  $D$  was measured by point-FCS. A relative  $D$  was calculated relatively to symmetric DOPC SLBs without bSM and plotted as a function of the amount of bSM in the bilayer. Each point represents the average of measurements collected from two or more independent SLBs preparations, each of them probed in five to eight randomly chosen spots. Error bars are the corresponding standard deviations. The data points were fit with a linear equation; 95% confidence bands are traced in grey. The obtained curve is used to estimate the amount of bSM incorporated into the upper leaflet of the SLBs after the M $\beta$ CD-mediated lipid exchange, assuming that the behavior of the Atto647N-SM (which is always confined to the upper layer) is similar in both symmetric and asymmetric DOPC SLBs with the same amount of bSM.

from the upper to the lower leaflet during equilibration, the Atto647N-SM  $D^*$  should increase up to the value estimated for symmetric SLB containing 30 %mol SM (ca. 80%, Figure 4.4). Also, the NBD-DOPE  $D^*$  should decrease until the ratio between lower and upper  $D$  is ca. 1 (i.e. fully scrambled lipids and fluorescent lipid probes). To determine how stable aSLBs produced via M $\beta$ CD-mediated lipid exchange are, the  $D^*$  of NBD-DOPE and Atto647N-SM were measured by point-FCS at different times after M $\beta$ CD-SM treatment in randomly chosen positions (Figure 4.6).

The lower/upper  $D^*$  ratio does not decrease significantly until at least 4 hours after the M $\beta$ CD-mediated lipid exchange, suggesting that the asymmetry in the SLB is retained for several hours. However, after one day, the asymmetry seems to be lost. A similar stability in time was reported for asymmetric POPC bilayers prepared by the LB/VF method [56]. Moreover, the time scale of SM flip-flop appears comparable to the previously reported DSPC rates [119, 120]. The major constituent of the used SM is in fact 18:0 SM (Product specification, <http://www.avantilipids.com>), and its flip-flop time scale at RT can be estimated to be of the order of hundreds of minutes. Thus, due to their stability in time, aSLB can be used experimentally as asymmetric membrane models.

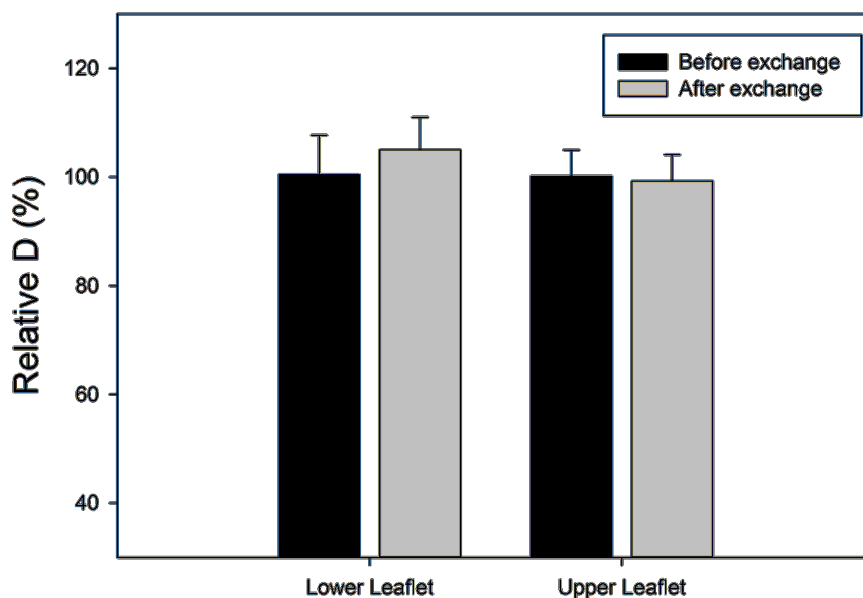


**Figure 4.5** – SLBs treated with M $\beta$ CD-DOPC. SLBs were labeled with NBD-DOPE and Atto647N-SM in the lower and upper leaflet, respectively. NBD-DOPE and Atto647N-SM  $D$  were then measured by point-FCS before and after treatment with 12 mM M $\beta$ CD-DOPC. Both NBD-DOPE and Atto647N-SM  $D$ s do not change significantly (NBD-DOPE:  $M=105\%$ ,  $SD=6$ , Atto647N-SM:  $M=99\%$ ,  $SD=5$ ; Paired t-test,  $p > 0.05$ ), suggesting that the  $D$  decrease observed in bilayers treated with M $\beta$ CD-SM is specifically due to the presence of SM (rather than e.g. bilayer defects introduced by M $\beta$ CD treatment). NBD-DOPE and Atto647N-SM mean relative  $D$  values are plotted with error bars of one standard deviation (NBD-DOPE,  $n=5$ ; Atto647N-SM,  $n=7$ ). Reported  $D$  values are relative to those measured in symmetric DOPC SLBs with the same configuration of fluorescent probes.

### 4.3 The asymmetry in a SLB can also be generated in the presence of a reconstituted membrane protein

To assess whether the M $\beta$ CD-mediated lipid exchange method can be used to produce asymmetric bilayers containing membrane proteins, the PLAP was reconstituted in SLBs, both via direct protein reconstitution [96], and from proteoliposomes [73, 88].

In the direct reconstitution method, a symmetric DOPC SLB was exposed to CHAPS detergent to promote protein incorporation. In the proteoliposomes method, the PLAP-containing SLBs were prepared using the same VF method applied for DOPC SLBs. In both methods, no dye for the upper leaflet was added, since the reconstituted PLAP was previously fluorescently labeled allowing its N-terminal amino group to react with the succinimidyl ester moiety of the Alexa647 dye; thus labeled-PLAP might be used as a probe for the upper leaflet of the SLB. It is worth noting that only in the case of directly reconstituted PLAP, the protein is expected to be confined to the upper leaflet [121]. In contrast, the reconstituted PLAP from proteoliposomes is expected to be present also in the lower leaflet, since the orientation of the protein might be randomized e.g. during proteoliposome fusion and SLB formation. Accordingly, we found that the  $\tau_D$  of the PLAP measured in symmetric SLB is

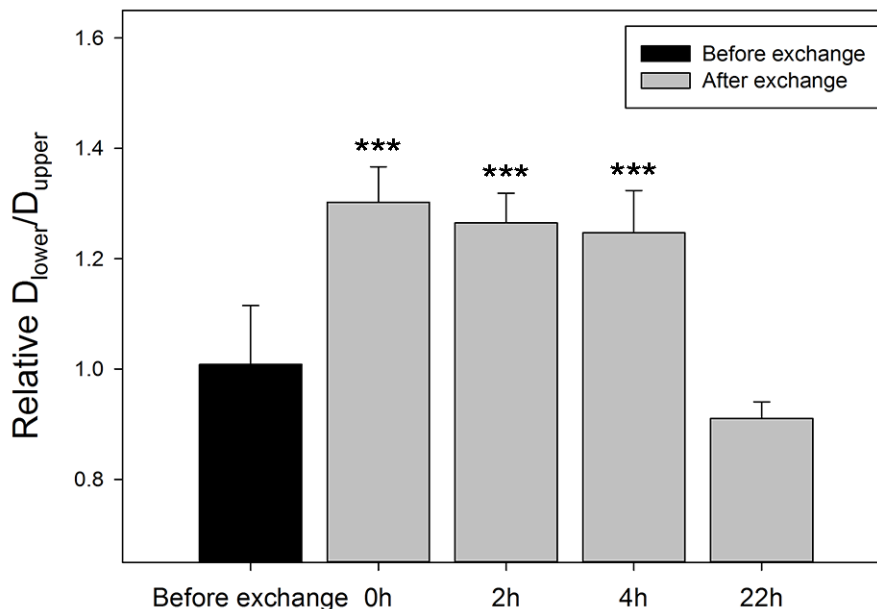


**Figure 4.6** – aSLB stability over time. Lower/upper leaflet  $D^*$  ratios are plotted before and at different times after incubation with 12 mM M $\beta$ CD-SM. Lower/upper  $D^*$  ratio values are expected to be higher than 1 in case of asymmetric enrichment of the SM in the upper leaflet. Lower/upper  $D^*$  ratios differed significantly across the five time points tested (one-way repeated measures ANOVA,  $F(4, 25)=55.65$ ,  $p<0.001$ ). Tukey post-hoc comparisons of the five time points indicate that before ( $M=1.01$ ,  $SD=0.11$ ) and 22 h after treatment ( $M=0.91$ ,  $SD=0.03$ )  $D$  ratios are significantly lower than those at 0, 2 and 4 h after treatment (0h:  $M=1.30$ ,  $SD=0.06$ ,  $***p<0.001$ ; 2h:  $M=1.27$ ,  $SD=0.05$ ,  $***p<0.001$ ; 4h:  $M=1.25$ ,  $SD=0.08$ ,  $***p<0.001$ ). Comparisons between the 0, 2 and 4 h after M $\beta$ CD-SM treatment as well as between before and 22 h after M $\beta$ CD-SM treatment were not statistically significant ( $p>0.05$ ), suggesting that the SLB asymmetry is conserved until at least 4 h after M $\beta$ CD-SM treatment. NBD-DOPE and Atto647N-SM mean  $D^*$  ratios are plotted with error bars of one standard deviation ( $n=6$ ). Reported  $D$  values are relative to those measured in symmetric DOPC SLBs with the same configuration of fluorescent probes.

significantly lower in samples in which the PLAP was directly reconstituted than in those prepared from proteoliposomes (Figure 4.7, A). The lower apparent diffusion rate (i.e. higher  $\tau_D$ ) of proteoliposome-reconstituted proteins in SLB can be explained as a consequence of the interaction between the large ectodomain of the protein in the lower leaflet and the support [63], in contrast to the limited influence of the support on the mobility of lipids in the same leaflet.

The protein-containing SLBs were finally treated with 12 mM M $\beta$ CD-SM to produce asymmetric bilayers. Similarly to protein-free SLBs, the SM enrichment of the upper leaflet results in an increased lipid order, and consequently, a lower lipid mobility that can be probed at the membrane by point-FCS. If SM incorporation is restricted to the upper leaflet of the SLB, only the  $D^*$  of the upper probe will experience a severe decrease. The ratio between the  $D^*$  values of the lower and upper probes will therefore reach values higher than 1. Figure 4.7 B confirms the formation of PLAP-containing aSLBs showing how the lower/upper  $D^*$  ratio increases after M $\beta$ CD-mediated lipid exchange. Interestingly, the  $D^*$  of

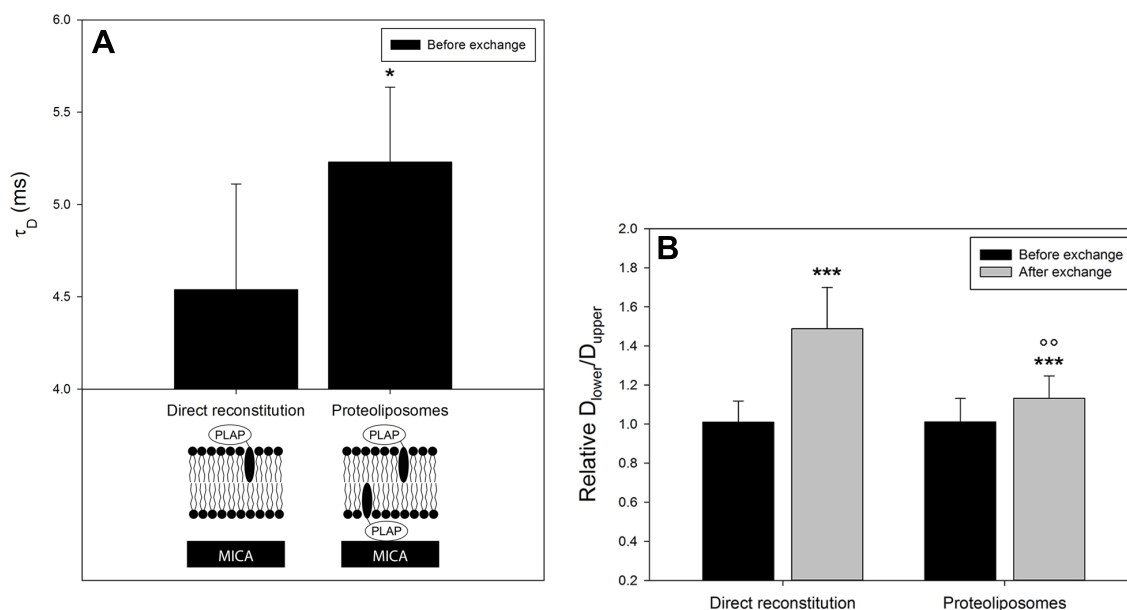


**Figure 4.7** – aSLB formation in the presence of reconstituted PLAP. [A] Labeled-PLAP  $\tau_D$ , and [B] lower/upper leaflet  $D^*$  ratios before and after incubation with 12mM M $\beta$ CD-SM are plotted for both reconstitution methods. The  $\tau_D$  ( $\tau_D = 4.5 \pm 0.6$ ms) of directly reconstituted PLAP is significantly lower (t-test \* $p < 0.05$ ) than the  $\tau_D$  of PLAP prepared from proteoliposomes ( $\tau_D = 5.2 \pm 0.4$ ms,  $D^* = 87 \pm 7\%$  relative to directly reconstituted PLAP). The presence of the PLAP in the lower leaflet and thus its interaction with the mica could explain the lower apparent  $\tau_D$  of the PLAP reconstituted from proteoliposomes. The expected localization of the PLAP in both reconstitution methods tested is depicted underneath the bar plot. Atto647-PLAP mean  $\tau_D$  are plotted with error bars of one standard deviation ( $n=6$ ). Relative lower/upper  $D$  ratio values are expected to be higher than 1 in case of asymmetric enrichment of SM in the upper leaflet. The lower/upper  $D^*$  ratio increases in both reconstitution methods after M $\beta$ CD-mediated lipid exchange (\*\*\*Paired t-test: direct reconstitution,  $t(5)=9.54$ ,  $p < 0.001$ ; proteoliposomes,  $t(5)=8.18$ ,  $p < 0.001$ ) and it is significantly lower in the proteoliposomes samples (t-test:  $t(5)=3.63$ ,  $p < 0.01$ ), most probably due to the fraction of PLAP present in the lower leaflet (i.e. not affected by the lipid exchange). NBD-DOPE and Atto647-PLAP mean  $D^*$  ratios are plotted with error bars of one standard deviation ( $n=6$ ). Reported  $D$  values are relative to those measured in symmetric DOPC SLBs with the same configuration of fluorescent probes.

the reconstituted PLAP decreases in both cases after M $\beta$ CD-mediated lipid exchange (direct reconstitution:  $D^* = 58 \pm 6\%$ ; proteoliposomes:  $D^* = 78 \pm 10\%$ , relative to symmetric SLBs with the same configuration of fluorescent probes). The decrease is lower in the PLAP reconstituted from liposomes, probably as a consequence of the presence of a significant protein fraction in the lower leaflet. The PLAP in the lower leaflet is not affected by SM incorporation and its  $D^*$  should only marginally decrease, similarly to the  $D^*$  of the lower leaflet probe ( $D^* = 86 \pm 7\%$ ). The overall PLAP  $D^*$  (average between upper and lower leaflet) is therefore higher than that measured for the direct reconstitution method, in which the PLAP is confined to the upper leaflet. The  $D^*$  of the lower leaflet probe exhibits a smaller decrease in both cases (direct reconstitution:  $D^* = 87 \pm 16\%$ ; proteoliposomes:  $D^* = 86 \pm 7\%$ ) confirming the asymmetry in the protein-containing SLBs.

Altogether, these results show that the M $\beta$ CD-mediated lipid exchange method is fully



compatible with both the proteoliposomes and the direct reconstitution methods. Used in conjunction with one of the protein reconstitution methods, aSLBs can provide a more physiological protein environment. By making accessible in the same sample the state before and after lipid enrichment (i.e. symmetric and asymmetric state), aSLBs are also a handy tool to study how compositional lipid asymmetry can influence protein structure and function. It is noteworthy that although the proteoliposome reconstitution is the method of choice for many large transmembrane proteins [122], its application in combination with aSLBs has a limited value. The protein is in fact inserted in in both directions and therefore interacts with each leaflet differently.

#### 4.4 SM in the lower leaflet of an aSLB is required for phase separation in both leaflets

aSLBs produced as described before and containing up to 60 %mol SM in the upper leaflet do not show macroscopic liquid/gel coexisting domains, as reported for the corresponding symmetric SLBs [123, 124]. As already proposed for asymmetric GUVs [118], the upper leaflet of aSLBs might either be in a homogeneous liquid phase or contain submicroscopic gel domains. To address the question of whether and how compositional asymmetry affects phase separation, we prepared SLBs and aSLBs with the same overall lipid composition and compared their behavior after addition of cholesterol. In fact, although binary mixtures of lipids were crucial to determine the connection between phase behavior and multiple variables such as lipid composition and temperature, ternary lipid mixtures containing cholesterol show a richer phase behavior and can better model the animal cell plasma membranes [125].

In particular, symmetric DOPC SLBs containing up to 60 %mol of SM and aSLBs containing approximately 60 %mol of SM in the upper leaflet were produced as described before and exposed to 5 mM M $\beta$ CD-Chol complexes. Similarly to M $\beta$ CD-SM complexes, high concentrations of M $\beta$ CD-Chol (10 mM) result in a complete destruction of the bilayer (Figure 4.8, A). A concentration of 5 mM was chosen because it was the lowest concentration at which phase separation could still be induced in symmetric bilayers containing less than 50 %mol SM. When aSLBs were treated with 5 mM M $\beta$ CD-Chol complexes, the incorporation of cholesterol in the lower leaflet could be estimated to be up to 20 %mol of the total lipid content (Figure 4.9). This value correlates well with the observed phase behavior in symmetric and partially asymmetric SLBs, according to a recently improved experimentally-derived phase diagram of the same mixture [123]. Moreover, in absence of opposing evidences, we assume that the cholesterol equilibrates fast and distributes uniformly throughout the leaflets of the aSLB [126].

Only in symmetric SLBs containing more than 30 %mol of SM and in scrambled aSLBs (aSLBs after 22 h incubation time), the incorporation of cholesterol results in the formation of Lo domains registered in both lower and upper leaflets (Figure 4.10, A and C; Figure 4.8, A). Interestingly, in the symmetric SLBs, preexisting gel domains [123] disappeared soon after cholesterol addition and Lo domains appeared both in the same and in new positions (Figure 4.10, A1). Same concentrations of cholesterol-loaded M $\beta$ CD failed to induce phase separation in freshly prepared aSLBs, in which SM is still confined to the upper leaflet (Figure 4.10, B).

The transition from aSLBs to scrambled aSLB and the appearance of phase separation can be followed in time (Figure 4.11, A). Time-lapse fluorescence imaging allows to record the time of appearance of Lo domains in partially scrambled aSLBs. Within a single bilayer, Lo



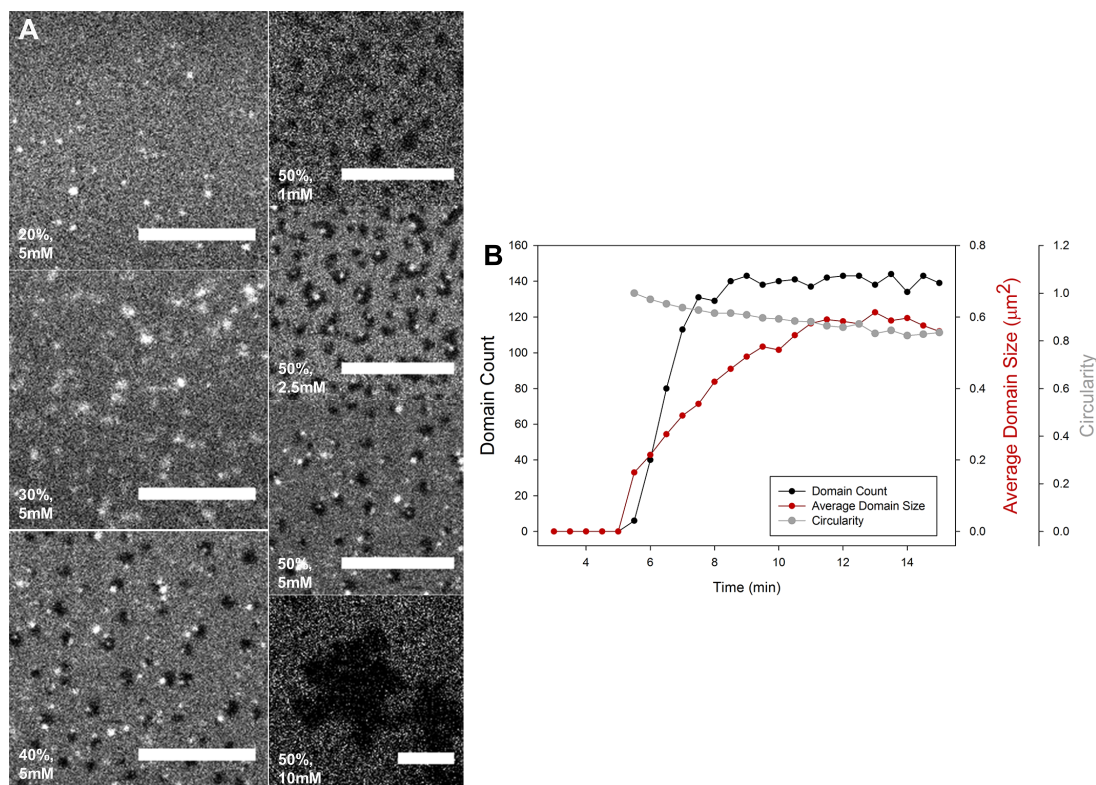


**Figure 4.8** – Phase separation in symmetric SLB after cholesterol addition. SLBs were labeled with 0.5 %mol Atto647N-SM in the upper leaflet and treated for 15 min with 1, 2.5, 5 or 10 mM MβCD-Chol complexes. [A] Confocal fluorescence images of symmetric SLBs containing 20, 30, 40 or 50 %mol bSM were acquired after treatment. Upon cholesterol incorporation, Lo domains formed in both lower and upper leaflets in symmetric bilayer containing 40 and 50 %mol bSM and at all MβCD-Chol concentration tested. High concentrations of MβCD-Chol (10 mM) result in a complete destruction of the bilayer. Scale bars are 10 μm. [B] Domains number, average size and circularity were measured and plotted against time; at 0 min MβCD-Chol was added to the bilayer.

domains appear simultaneously all over the sample, whereas different samples show diverse timing ( $t_{1/2}=372\pm129\text{min}$ ); this is probably due to experimental variation in the SM and cholesterol content of each bilayer. However, once the first domains appear, the time to reach the final number of domains is comparable in all measured samples ( $t_{f-0}=262\pm35\text{min}$ ). Domains keep growing after the final number of domains is reached, suggesting that at this point they are not in equilibrium yet (Figure 4.11, B). As shown before, aSLBs slowly lose their asymmetry through spontaneous flip-flop of lipids causing a gradual and inversely correlated change of the SM amount in each leaflet. Lo domains appearance is most probably due to this SM redistribution across the bilayer and thus to lipid flip-flop in general. The onset of the domain appearance can be then used as an indirect measure of lipid flip-flop rate.

As a consequence of lipid flip-flop in aSLBs, the local concentration of SM in the lower leaflet increases while decreasing in the upper one. This change in transversal lipid composition in turn induces phase separation. In order to understand whether the increase of SM concentration in the lower leaflet (rather than its decrease in the upper leaflet) is determinant in promoting phase separation, we produced aSLBs containing 5-10 %mol SM and ca. 60 %mol SM in the lower and upper leaflet, respectively. To do so, we first formed symmetric

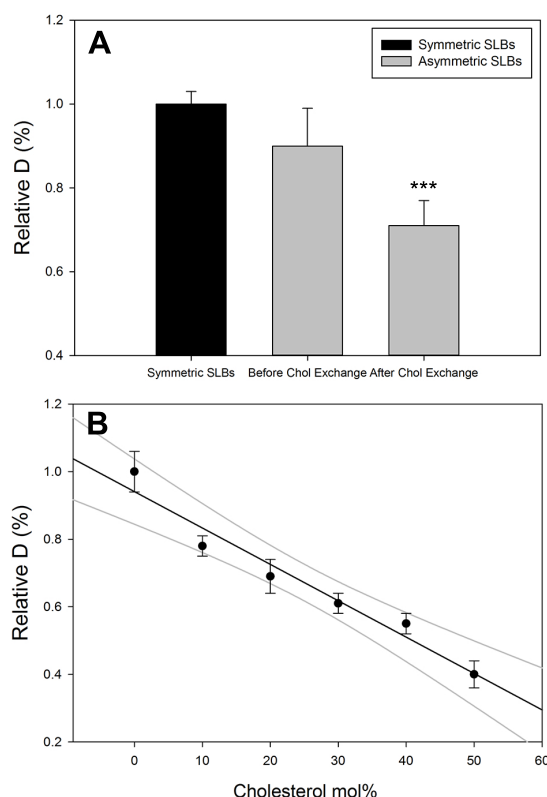


**Figure 4.9** – Cholesterol incorporation in aSLBs. [A] SLBs were labeled with NBD-DOPE in the lower leaflet and its  $D$  was then measured by point-FCS in symmetric SLBs and aSLBs both before and after treatment with 5 mM M $\beta$ CD-Chol. NBD-DOPE  $D$  significantly decreases to about 71% of the original value in symmetric SLBs ( $M=71\%$ ,  $SD=6$ ; \*\*\*Paired t-test,  $t(5)=8.08$ ,  $p<0.001$ ) and to about 80% of the value in aSLBs before M $\beta$ CD-Chol treatment ( $M=80\%$ ,  $SD=2$ ; \*\*\*Paired t-test,  $t(5)=20.46$ ,  $p<0.001$ ). NBD-DOPE mean relative  $D$  are plotted with error bars of one standard deviation ( $n=6$ ). Reported  $D$  values are relative to those measured in symmetric DOPC SLBs with the same configuration of fluorescent probes.[B] Symmetric DOPC SLBs containing different amount of cholesterol were labeled with NBD-DOPE in the lower leaflet and its  $D$  was measured by point-FCS. A relative  $D$  was calculated relatively to symmetric DOPC SLBs without cholesterol and plotted as a function of the amount of cholesterol in the bilayer. Each point represents the average of measurements collected from two independent SLBs preparations, each of them probed in at least three randomly chosen spots. Error bars are the corresponding standard deviations. The data points were fit with a linear equation; 95% confidence bands are traced in grey. The obtained curve is used to estimate the amount of cholesterol incorporated into the lower leaflet of aSLBs after M $\beta$ CD-mediated cholesterol exchange, assuming that the behavior of the NBD-DOPE (which is always confined to the lower layer) is similar in both symmetric and asymmetric DOPC SLBs with the same amount of cholesterol.

DOPC SLBs containing 5-10 %mol SM; this amount of SM is not sufficient to induce phase separation upon cholesterol incorporation (Figure 4.8, A). We then treated the same symmetric SLBs with M $\beta$ CD-SM complexes to obtain a partially aSLB. We assume that these aSLBs have a lipid composition of the upper leaflet similar to those discussed in the previous paragraphs, i.e. ca. 60 %mol SM. Upon cholesterol addition, phase separation could be induced in partially aSLB containing as low as 5 %mol of SM in the lower leaflet. This observation

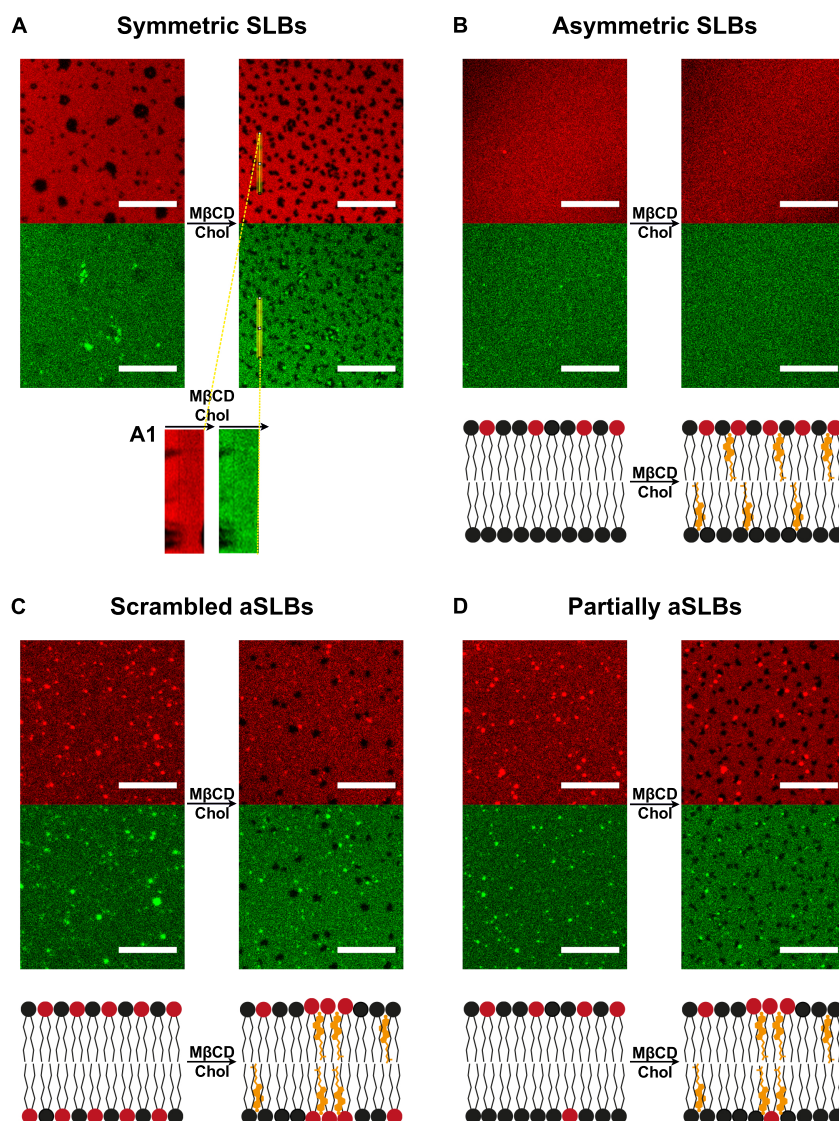


**Figure 4.10** – Phase separation in scrambled, fully and partially asymmetric SLBs after cholesterol addition. Phase separation and coupling in symmetric [A], scrambled [C], and fully [B] or partially [D] asymmetric SLB after cholesterol addition. In symmetric SLBs, scrambled and partially aSLBs Lo domains coupled in both lower and upper leaflets form upon cholesterol incorporation. In fully aSLBs no change in the phase behavior of the bilayer can be observed. [A1] The kymograph shows domain dynamics in symmetric SLBs before and after cholesterol addition at the overlaying line depicted in A. Preexisting gel domains in symmetric SLBs disappeared soon after addition of cholesterol and Lo domains appear both in the same and new positions. Time (30 spf) is along horizontal axis. Scale bars are 10  $\mu$ m.

reinforces the hypothesis that SM is required in the lower leaflet for phase separation in both leaflets (Figure 4.10, D). This is in line with the phase diagram for symmetric bilayers with analogous composition [123]. Depending on the amount of cholesterol, phase separation requires in fact a minimum amount of SM (ca. 10-30 %mol) and persists up to 80-90 %mol SM.

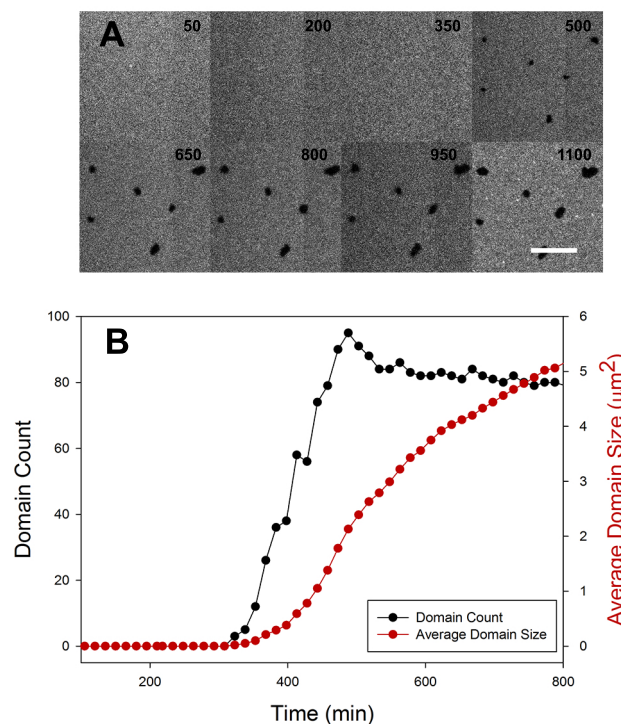


**Figure 4.11** – Phase separation dynamics in aSLBs. [A] Domain appearance in aSLBs treated with 5 mM M $\beta$ CD-Chol. [B] Domains number and average size were measured and plotted against time; at 0 min the aSLB was formed. After the final number of domains is reached, domains grow further, suggesting that at this time point they are not at equilibrium yet.

Furthermore, it is interesting to notice that SM, although more abundant in the extracellular leaflet, is also present in the cytoplasmic leaflet of natural membranes in many cellular types at about 1:10 ratio [127].

The observed differences in terms of phase separation in symmetric or aSLBs provide further experimental evidence that the transversal lipid distribution affect the overall lipid miscibility. In accordance with Collins and Keller [116], the lipid composition of one leaflet strongly influences the phase behavior of the other leaflet, suppressing or priming phase separation; in particular, our results suggest that a minimal amount of SM is required in the nonspontaneously phase separating leaflet for cholesterol to induce phase separation in both leaflets. As also pointed out in the above-mentioned study, the presence of one leaflet with a composition supporting phase separation (in a corresponding symmetric bilayer) is necessary but not sufficient to induce domain formation in the whole bilayer. Of interest, it is well known that lipid mixtures mimicking the outer leaflet of the plasma membrane can give rise to raft-like ordered domains. On the other hand, lipid mixtures corresponding to typical inner leaflet compositions form membranes that are homogeneous [128]. Our results address this incongruence, suggesting that small changes in the composition of the inner leaflet (e.g. even low concentrations of saturated lipids such as SM, not enough to produce phase separation in a corresponding symmetric bilayer) can have a prominent role in the formation of lipid domains spanning the whole bilayers.

Unlike Wan and colleagues [115], we were not able to induce formation of macroscopic Lo domains in a single SM-containing leaflet of an aSLB. This difference can be explained taking into account the individual properties of the two used systems. In the LB/VT approach, domains in the LB leaflet are already present in the original monolayer, which is transferred to a support and stabilized by a tethered polymer cushion. In our system domains form de novo after addition of cholesterol to the bilayer. These systems produce only apparently conflicting results. It might be possible in fact that the LB leaflet resides in a local energy minimum, and the addition of the upper layer might not be enough to perturb its state (i.e. the bilayer system might be kinetically trapped in a nonequilibrium state). The composition of our aSLBs is very similar, although not identical to one of the few compositions tested by Wan and colleagues for which no phase separation could be induced in the upper leaflet (in the presence of domains in the lower leaflet). We therefore speculate that the lipid mixtures that in the LB/VT asymmetric system do not show domain induction from the lower to the upper leaflet are the same that in our system would suppress phase separation in both leaflets. The presence of phase separation in the LB leaflet might be due to the specific leaflet-by-leaflet assembly methodology.

Similar considerations might be extended to the LB/LS system of Garg and colleagues [129], in which both lower and upper leaflets are preformed as monolayers (LB and LS, respectively) with their respectively energetically most favorable phase states and only subsequently assembled on top of each other.

Having observed a different phase behavior in our system, we decided to investigate asymmetric free-standing bilayers with analogous lipid compositions as alternative asymmetric bilayer models (Figure 4.12). Symmetric GUVs labeled with 0.5 %mol of NBD-DOPE and 0.2 %mol of Atto655-DOPE in both leaflets show Lo domains as expected. GUVs originally containing 20 %mol cholesterol and different amounts of SM (0 or 5 %mol) in a DOPC bilayers were labeled with 0.5 %mol NBD-DOPE and Atto655-DOPE in the inner (green channel) and outer (red channel) leaflet, respectively and treated for 30 min with 71 mM HD $\alpha$ CD-SM. Although we did not measure the amount of bSM in the outer leaflet of such GUVs, previous results [97] suggest that the outer leaflet is significantly enriched in SM, compared to the inner leaflet. GUVs originally not containing SM show no changes in the phase behavior of the bilayer upon SM incorporation in the outer leaflet; in those GUVs, Lo domains can be only rarely observed. When SM is present in the original mixture and thus in the inner leaflet, phase separation can readily be induced upon treatment with HD $\alpha$ CD-SM. Similar results were obtained with partially aGUVs containing 10 or 20 %mol SM in the inner leaflet. When observed, Lo domains were always coupled in both inner and outer leaflets. By using aGUVs, we were not only able to completely reproduce the domain registration observed on SLBs, but also to rule out that the domain registration properties observed in our system are influenced by the presence of the support.



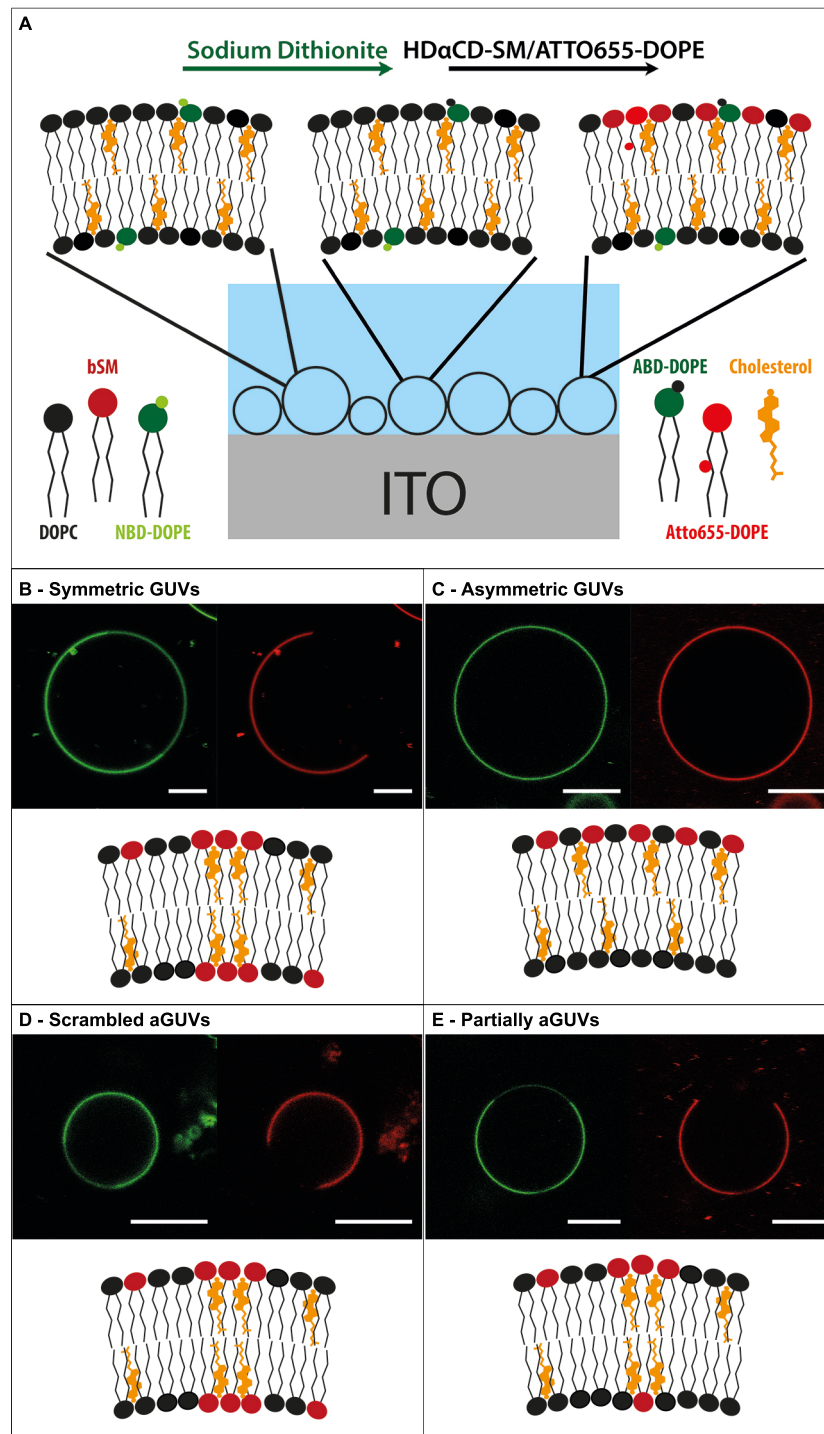


**Figure 4.12** – Phase separation and coupling in symmetric, scrambled, and fully or partially asymmetric GUVs. [A] Schematic diagram of the asymmetric GUVs formation via HD $\alpha$ CD-mediated lipid exchange and of the leaflet-specific labeling. Confocal fluorescence images of [B] symmetric GUVs containing DOPC:bSM:Chol 30:50:20, [C] aGUVs originally containing DOPC:Chol 80:20 soon after HD $\alpha$ CD-SM treatment or [D] after 24 h incubation time (scrambled aGUVs) and [E] aGUVs originally containing DOPC:bSM:Chol 75:5:20 (partially aGUVs). Scale bars are 10  $\mu$ m.



The experimental work presented in Chapter 5 was designed together with Prof. Petra Schwille (Max Planck Institute of Biochemistry, Martinsried, Germany).



## Chapter 5

# Shape transformations of asymmetric giant unilamellar vesicles

Although GUVs have been successfully used to reconstitute single- [130, 131, 132] or multi-proteins systems [72, 133, 134, 135], their size and shape are still difficult to control [136]. Alternative approaches to confine the protein and/or lipid machinery in compartments with a defined size and shape were recently developed. Micro-fabricated square chambers with the approximate dimensions of an eukaryotic cell (10-15  $\mu\text{m}$  wide; 2.6  $\mu\text{m}$  deep,) were successfully used to reconstitute the interaction between dynein and dynamic microtubule ends and to reliably center microtubule asters [137]. Similarly Min protein oscillations could be generated in rodlike compartments resembling *E. coli* shapes and covered with SLBs [138]. Although these 2D in vitro systems have been proven to be a valuable tool in selected bottom-up approaches, the influence of the support on protein behavior remains a major obstacle for the functional reconstitution of several minimal systems. For example when the co-reconstitution of FtsZ with the MinCDE system, already achieved on SLBs [139], was attempted in the above-mentioned rodlike compartments, FtsZ filaments bundles could be spatially positioned, but failed to compact in a Z-ring like structure (Katja Zieske and Dr. Ariadna Martos, Max Planck Institute of Biochemistry, Martinsried, Germany, personal communication). This behavior is most probably due to the hindrance exerted by the support to freely protein diffusion at the membrane [63]. Thus, free-standing membranes with shapes more similar to the biological counterpart than nearly spherical ones would be desirable.

Besides nearly spherical shapes, GUVs exhibit many different shapes that are reminiscent of cell morphologies, such as, e.g., stomatocytes or a necklace of small vesicles [140, 141]. The great variety of non-spherical shapes of vesicles is determined by bending elasticity as introduced independently in three seminal papers (Canham 1970, Helfrich 1973, Evans 1974). Vesicles will acquire the shape at which their curvature energy subject to the appropriate constraints is minimal [142]. These shapes can be transformed into one another by mechanical stress, by changing the pH, the osmotic conditions, the composition of the lipid, or the temperature [140, 141]. Additionally, shape changes can occur through local or global modifications of the relative area of the two bilayer leaflets, for example due to asymmetric lipid transbilayer diffusion [143]. This behavior was observed by Farge and Devaux [141], which induced shape changes of GUVs manipulating the fraction of phospholipids in each monolayer.

In particular, they changed the distribution of egg PG through the bilayer by means of a pH gradient and added or removed LysoPhosphatidylCholine (L-PC) from the outer monolayer. Similarly Khalifat and colleagues showed that local acidification of PG-containing vesicles promotes inward tubulations [143].

GUVs exhibiting phase coexistence of Lo and Ld phases were also predicted to undergo different shapes transformation which resemble biological membranes processes (i.e. budding) and depend on the elasticity and boundary properties of the coexisting domains [144, 145]. Using high-resolution fluorescence imaging and two dyes which preferentially label the Lo or Ld phase, Baumgart and colleagues [146] showed for the first time experimentally that domain composition and local membrane curvature are indeed directly correlated. In particular they observed circular, stripe and ring domains in GUVs formed from a ternary mixture of the lipids sphingomyelin, phosphatidylcholine and cholesterol. These domains show long-range ordering in the form of locally parallel stripes and hexagonal arrays of circular domains as well as curvature-dependent sorting. Later the role of several sterols other than cholesterol was investigated in GUVs by Bacia and colleagues [95]. The authors showed that the structure of sterols used for the preparation of GUVs determines whether a positive or negative curvature of the sterol-dependent phase is formed. In both cases vesicle were produced in low osmolarity sucrose solutions (100 and 12 mM, respectively). If the same experiments are reproduced in presence of salt or at higher osmolarity (300 mM sucrose) closer to the physiological value the domains do not bulge out (Diego Ramirez and Dr. Henri Franquelim, Max Planck Institute of Biochemistry, Martinsried, Germany, personal communication). Indeed both sugars and salts are known to influence the bending rigidity of membranes [147]. When GUVs are exposed to mono- and oligosaccharide solutions with concentration up to around 300 mM a strong decrease in the bending rigidity of membranes was observed [148]. The reduction of the bending rigidity could be explained by the thinning of the membrane which was reported to take place in the used concentration range [149]. On the other hand, the effect of salts on the bending rigidity of membranes is not fully understood and a unified vision is still missing [147]. that is, it is not clear whether upon adsorption salts decrease [150], increase [151] or not change [152] the bending rigidity of the membrane. Independently from the underlying mechanism, the absence of bulging in presence of salts and high concentrations of sugars makes these phase separated GUVs not suitable for protein studies which require the usage of physiological buffers for the reconstituted proteins to correctly function.

In this chapter we described how transbilayer lipid asymmetry can induce changes in the shape of giant liposomes. We first show that asymmetric intramembrane domains can bulge out in conditions in which symmetric domains do not, such as at high osmolarity or in absence of any Lo specific dyes. We then report four different GUV transformations that can be induced by enriching the outer leaflet of the vesicles with PG: (1) prolate ellipsoid to spherical vesicle, (2) discocyte to stomatocyte, (3) vesicle budding, and (4) vesicle endocytosis. We finally developed a FRAP assay to determine whether the two daughter vesicles originated by a budding event are still connected or if they are completely separated.

## 5.1 Bulging of intramembrane asymmetric domains in GUVs

In chapter 4 we showed that asymmetric domains can be formed in DOPC GUVs originally containing 20 %mol cholesterol and at least 5 %mol bSM if the outer leaflet of the GUVs was enriched in bSM via cyclodextrin-mediated lipid exchange [86]. For this purpose HP $\alpha$ CD

needed to be used. Having a smaller ring size than M $\beta$ CD (Figure 5.1, A-B), HP $\alpha$ CD shows no or little affinity for cholesterol, whereas it is still able to mediate phospholipid exchange [97]. These features are extremely advantageous in our experimental setup, allowing the exchange of DOPC for bSM without extracting cholesterol from the membrane. Thus, we are able to move from a single fluid phase to a coexistence of fluid ordered and disordered phases, keeping the temperature (25°C) and the cholesterol molar ratio fixed (Figure 5.1, C).

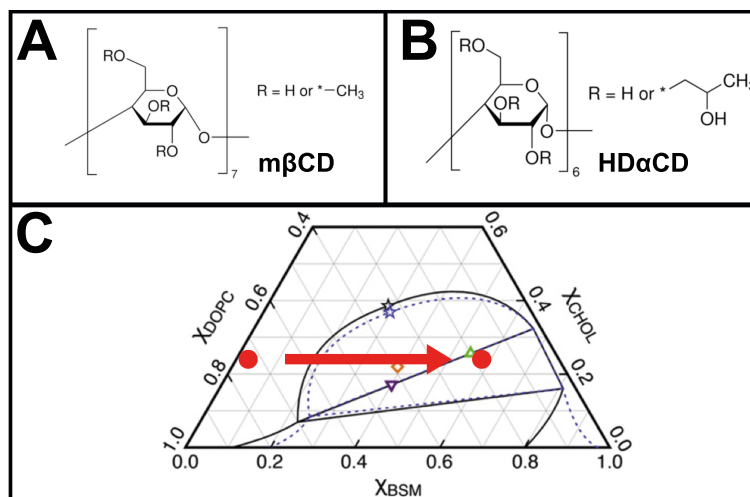


**Figure 5.1** – HP $\alpha$ CD-mediated asymmetric domain induction in GUVs. [A-B] chemical structures of M $\beta$ CD and HP $\alpha$ CD, respectively. Both adapted from <http://www.sigmaaldrich.com/>. [C] Phase diagrams for bSM/DOPC/Chol at 15°C (solid) and 25°C (dotted) adapted from Petruzielo and colleagues [123]. Red dots and arrow visualize the position of the external leaflet of the GUVs in the phase diagram before and after HP $\alpha$ CD-bSM mediated lipid exchange.

The asymmetric Lo domains bulged out in a fraction of the asymmetric GUVs exhibiting coexistence of Lo and Ld phases. Importantly the bulging out of Lo domains was only observed in samples containing 5 %mol bSM in the inner leaflet, but not in samples containing 10 or 20 %mol bSM, and it was lost together with the leaflet asymmetry after 24 h incubation. Additionally, the bulging out of the Lo domain was rarely observed in GUVs containing a single Lo domain, whereas it was common in GUVs containing multiple Lo domains. In particular two different geometries were observed: GUVs with several Lo domains regularly arranged throughout the vesicle surface (Figure 5.2, A) and GUVs with two or three Lo domains irregularly arranged throughout the vesicle surface (Figure 5.2, B-C). In both cases Lo domains in a GUVs can be of similar or various size. The curvature of each Lo domain can be estimated by measuring its Radius of curvature ( $R$ ) that is the radius of the circular arc which best approximates the Lo domain curve.  $R$  is defined as the inverse of the curvature. In the former geometry Lo/GUV  $R$  is significantly higher than in the latter one ( $0.61 \pm 0.19$  vs  $0.41 \pm 0.06$ ;  $p < 0.001$ ). One possible explanation for this difference is the way GUVs adhere to the support; lower  $R$ s were measured in GUVs whose adhesion area included the edges of Lo domains. The direct contact between surface and Lo domains could stabilize the bulging out of the domain.

Similar geometries were already described for symmetric GUVs exhibiting coexistence of Lo and Ld phases [146]. However several observations suggest that the bulging in our system is directly related to the asymmetric nature of the domains rather than exclusively due to

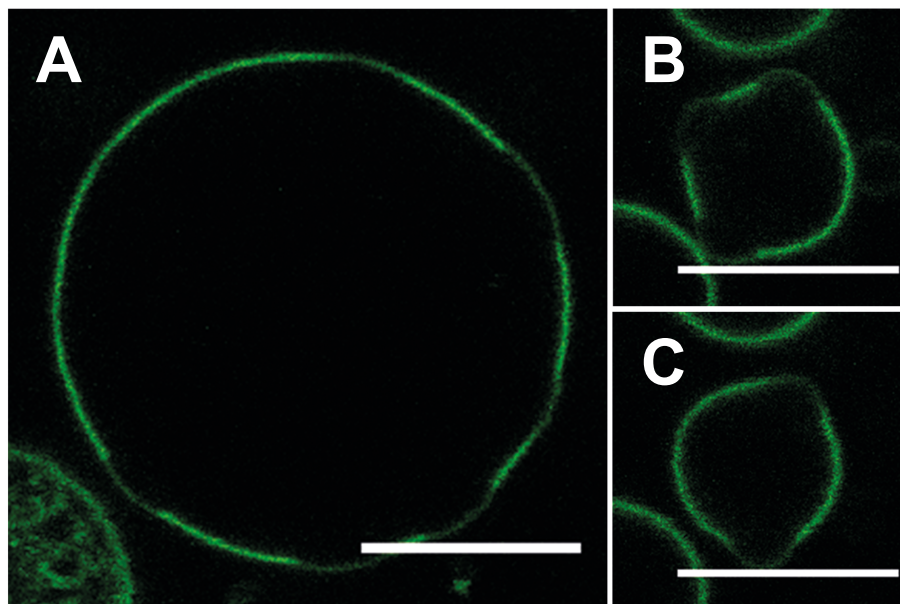


**Figure 5.2** – Bulging of intramembrane asymmetric Lo domains in GUVs. GUVs were labeled with NBD-DOPE in the inner leaflet and fluorescence confocal images were taken after HP $\alpha$ CD-mediated lipid exchange. Scale bars are 10  $\mu$ m.

the presence of intramembrane domains. First of all bulging out is absent in symmetric, scrambled (after 24h incubation time) or poorly asymmetric GUVs (containing 10 or 20%mol bSM in the inner leaflet). Secondly bulging out takes place in conditions in which it is usually not observed in symmetric GUVs such as high osmolarity, absence of cholera toxin, other Lo specific dyes or a hyperosmotic external buffer.

## 5.2 Shape transformations in GUVs asymmetrically enriched with PG

To further investigate the role of transbilayer lipid asymmetry on membrane shape, we selectively enrich the outer leaflet of GUVs with PG, which is known to effect vesicle shape when asymmetrically distributed across the membrane leaflets [141, 143]. In particular DOPC GUVs were incubated with different amount of M $\beta$ CD-DOPG complexes and time-lapse images were acquired every 30 s up to 1 h in several areas of the sample chamber. When a high concentration of M $\beta$ CD-DOPG complexes was used (nominal concentration of 35.5 mM) the most common shape change observed was the transformation from a prolate ellipsoid to a spherical vesicle (Figure 5.3). Sometimes the transformation reversed back to the original shape. It should be note that most GUVs did not survive when treated with high concentrations of M $\beta$ CD-DOPG.

When the concentration of the M $\beta$ CD-DOPG complexes was lowered to 7.1 mM, further shape changes could be observed. In particular discocytes transform into stomatocytes (Figure 5.4). The invagination can eventually form an inside budded vesicle. Moreover spherical vesicles undergo vesicle budding after transforming into a pear-like (Figure 5.5) vesicles. At this concentration, most GUVs survived the treatment with M $\beta$ CD-DOPG.

When an even lower concentration of M $\beta$ CD-DOPG complexes was used (nominal con-



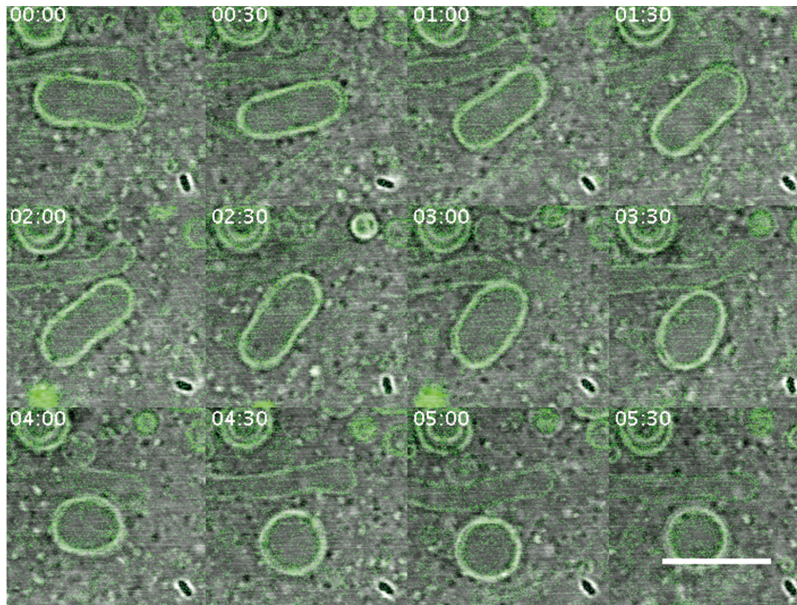


**Figure 5.3** – GUV transformation: prolate ellipsoid to spherical vesicle. GUVs were labeled with NBD-DOPE and time lapse confocal fluorescence images were taken while treating with high concentrations of M $\beta$ CD. The scale bar is 10  $\mu$ m and time labels are in m:s from the observation start.

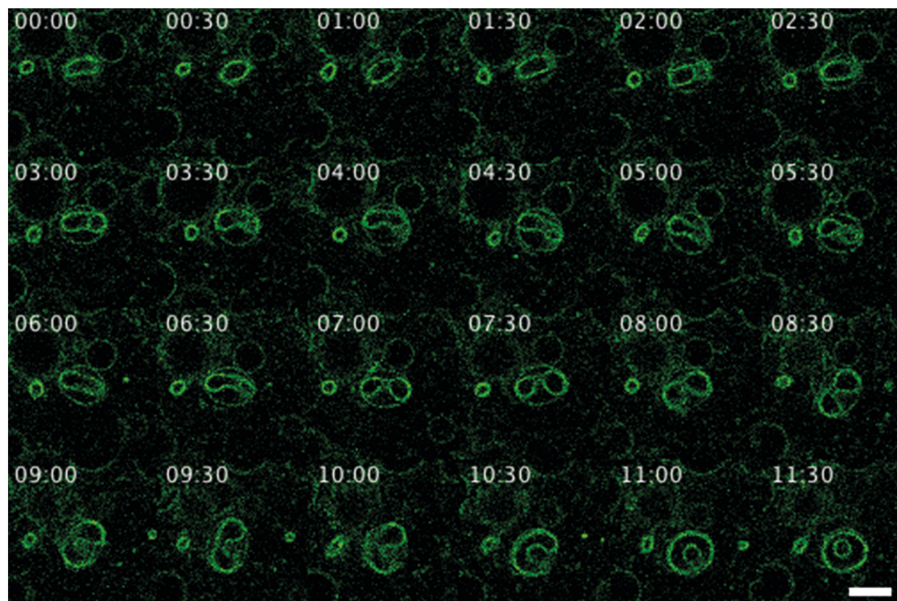


**Figure 5.4** – GUV transformation: discocyte to stomatocyte. GUVs were labeled with NBD-DOPE and time lapse confocal fluorescence images were taken while treating with intermediate concentrations of M $\beta$ CD. The scale bar is 10  $\mu$ m and time labels are in m:s from the observation start.

centration 1.42 mM) invagination and endocytosis of long tubular structure is commonly taking place. First, spherical vesicles protrude in a pear-like shape, then membrane tubules invaginate from the protrusion tip. The tubules are finally released inside the vesicle while the vesicle itself becomes spherical again. Very few GUVs were lost when treated with this

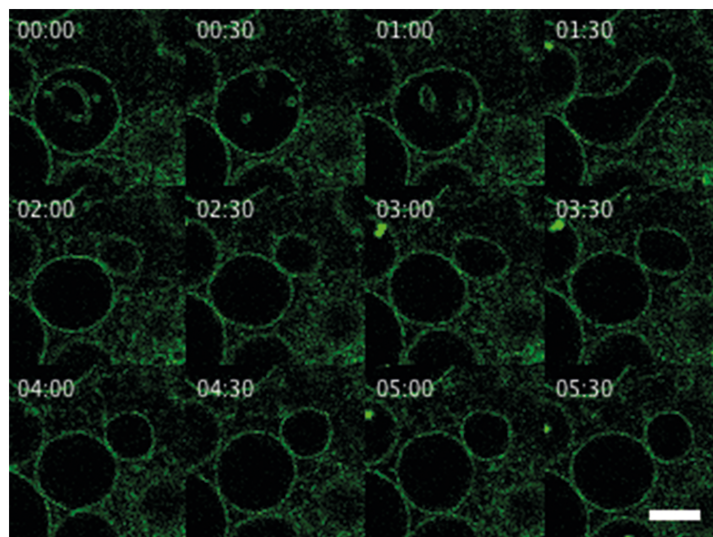


**Figure 5.5** – GUV transformation: vesicle budding. GUVs were labeled with NBD-DOPE and time lapse confocal fluorescence images were taken while treating with intermediate concentrations of M $\beta$ CD. The scale bar is 10  $\mu$ m and time labels are in m:s from the observation start.

low concentration of M $\beta$ CD-DOPG.

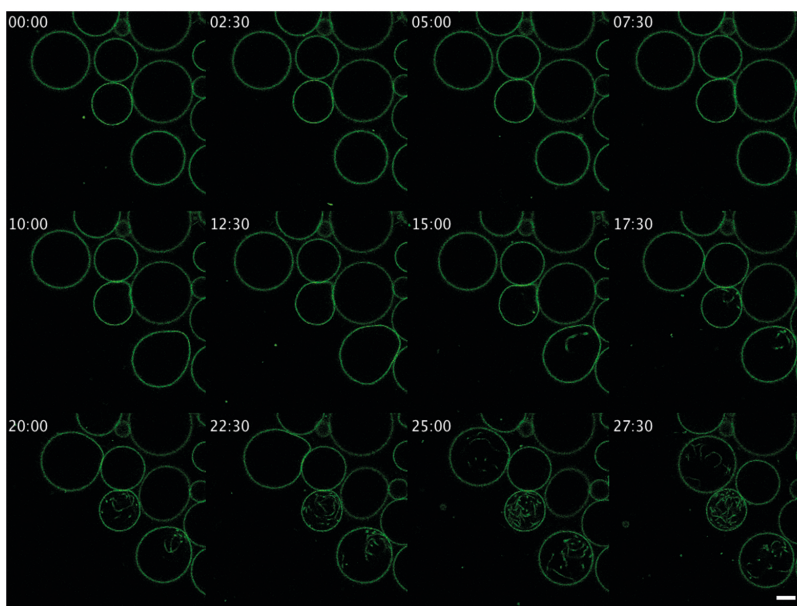


**Figure 5.6** – GUV transformation: endocytosis. GUVs were labeled with NBD-DOPE and time lapse confocal fluorescence images were taken while treating with low concentrations of M $\beta$ CD. The scale bar is 10  $\mu$ m and time labels are in m:s from the observation start.

The fact that so different GUV transformations can take place upon treatment with M $\beta$ CD-DOPG is probably due to a specific combination of lipid extraction and exchange exerted on the GUV membrane by different amount of M $\beta$ CD. As shown for SLBs (Figure 4.2), the effect of M $\beta$ CD on membranes changes dramatically according to its concentration. At high concentration M $\beta$ CD can extensively extract lipids from the bilayer whereas at low

concentrations lipid extraction is not detectable any more and lipid exchange takes place. In a narrow range of intermediate concentrations lipid exchange is maximized while lipid extraction is still present. We assume that similar processes are taking place when GUVs are exposed to different amounts of M $\beta$ CD-DOPG, namely predominantly lipid extraction at high concentrations, predominantly lipid exchange at low concentrations and both lipid extraction and exchange at intermediate concentrations. The described transformations were already experimentally observed, for example in DMPC vesicles upon temperature changes [153]. When the temperature is increased the membrane expands more than the enclosed volume, thus varying the excess area  $A_e$ , that is the difference between the actual area and that which would be required to form a sphere of the same volume. In our system we can change the  $A_e$  keeping the temperature fix, but depleting, exchanging or enriching the lipids in the outer leaflet of the vesicle membrane. The transformation from a spherical vesicle to a prolate ellipsoid requires an increased  $A_e$  while its transition back a reduction. This transition was in fact observed at high concentrations of M $\beta$ CD-DOPG when the lipid extraction is predominant. Both the transition from discocyte to stomatocyte with formation of an inside budded vesicle and from prolate ellipsoid to pear-like vesicle with formation of an outside budded vesicle requires a higher increase in  $A_e$ . This is achieved at intermediate concentrations of M $\beta$ CD-DOPG, when the lipid exchange is maximized. Finally the inward budding of protruded and tethered vesicles was reported at very low  $A_e$ , which could be the case of GUVs treated with very low concentrations of M $\beta$ CD-DOPG.

### 5.3 FRAP assay for vesicle fission

Among the observed transformations, vesicle budding attracted our attention because it resembles the corresponding biological processes of cell division and exocytosis. It is particularly interesting to verify whether a vesicle can divide in two daughter cells in absence of intramembrane domains [154] and/or without the help of membrane shaping peptides or proteins [155], but only because of the transbilayer lipid asymmetry. Therefore we developed a FRAP assay to determine whether the two daughter vesicles are still connected via a neck or if they are completely distinct. When two adjacent vesicles are imaged at their equators it is not possible to distinguish if they are completely separated from each other or not, unless the neck is big enough, that is, bigger than the resolution limit of the optical setup used (Figure 5.7).

The idea underlying the FRAP assay is described in Figure 5.8. Briefly only one of the two daughter vesicles is bleached and the fluorescence intensity is monitored in both vesicles. If the two vesicles are separated no change in the average intensity will be detected; on the other hand if the two vesicles are still connected, the intensity of the bleached vesicle will eventually recover while the fluorescence intensity of the unbleached vesicle will decrease. In order to perform this assay, the original GUVs need to be filled with a fluorescence probe.

To validate the method, we used a well known artificial budding system [95]. In this system, domain budding can be induced in GUVs made of a canonical raft lipid mixture in a low osmotic medium by increasing the osmolarity of the external buffer (Figure 5.9, B). Both Ld and Lo domains can be specifically labeled (Figure 5.9, A). Most of the known lipid dyes and fluorescently labelled lipids partition preferentially into the Ld phase, allowing to select within a large spectrum of dyes. To label the Lo phases on the other hand only few strategies are available [156]: fluorescent polycyclic aromatic hydrocarbons with a flat ring system i.e. perylene, [146] or fluorescently labeled Cholera Toxins bound to GM1 [64]. In the



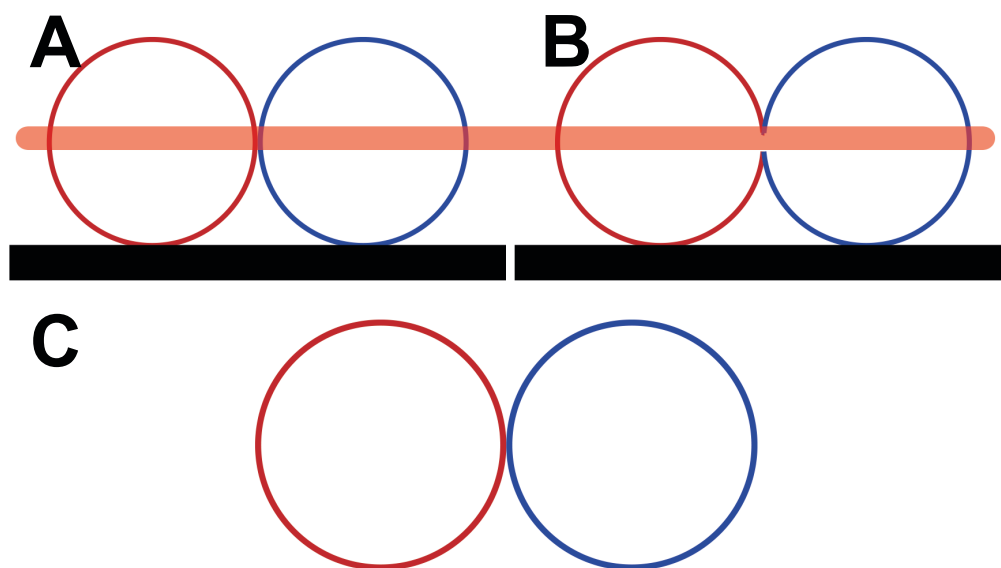


**Figure 5.7** – Imaging of adjacent GUVs. Schematic representation of two adjacent GUVs: fully separated [A] and connected by a neck smaller than resolution limit of the optical setup used [B]. If imaged at their equator both GUVs pairs appears as two touching circles. [C]

latter strategy GM1, which partitions preferentially into the Lo phase, must be previously incorporated in the GUV lipid mixture at low molar ratio to avoid changes in the lipid spatial distribution.

Phase-separated GUVs filled with AlexaFluor 488 were subjected to hyperosmotic shock and underwent budding. For each GUV pair analyzed, only one of the two daughter vesicles was bleached; the average fluorescence intensity inside the bleached GUV was then monitored for several minutes, single (Bkg) or double (Bkg/ref) normalized and plotted against time. We first select GUV pairs for which it was obvious to determine whether or not the vesicle fission took place. In GUV pairs still connected by an optical resolvable neck (Figure 5.10, A; image), the diffusion of the dye between the two vesicles is fast and the mixing is complete within the bleaching time. This results in an apparent simultaneous bleaching of both daughter vesicles as shown by the double corrected curve (Figure 5.10, A; graph). Even if there is a net loss of fluorescence intensity, both bleached and unbleached vesicles experience the same degree of fluorescence loss. In GUV pairs clearly separated from each other (Figure 5.10, B; image), no recovery of fluorescence signal is detected within the bleached vesicle. If very little acquisition bleaching is present, the two single and double normalized curves lay on top of each other (Figure 5.10, B; graph). Among the measured vesicles, we could identify GUV pairs which were only apparently separated (Figure 5.10, C; image) or connected (Figure 5.10, D; image). In the first case, the small size of the neck slows the diffusion of the dye between the two vesicles which does not reach equilibrium within the bleaching time. This allows us to record the fluorescence recovery inside the bleached vesicle (Figure 5.10, C; graph). In the second case both normalized curves will show no recovery of fluorescence signal (Figure 5.10, D; graph) as expected for vesicles after fission.



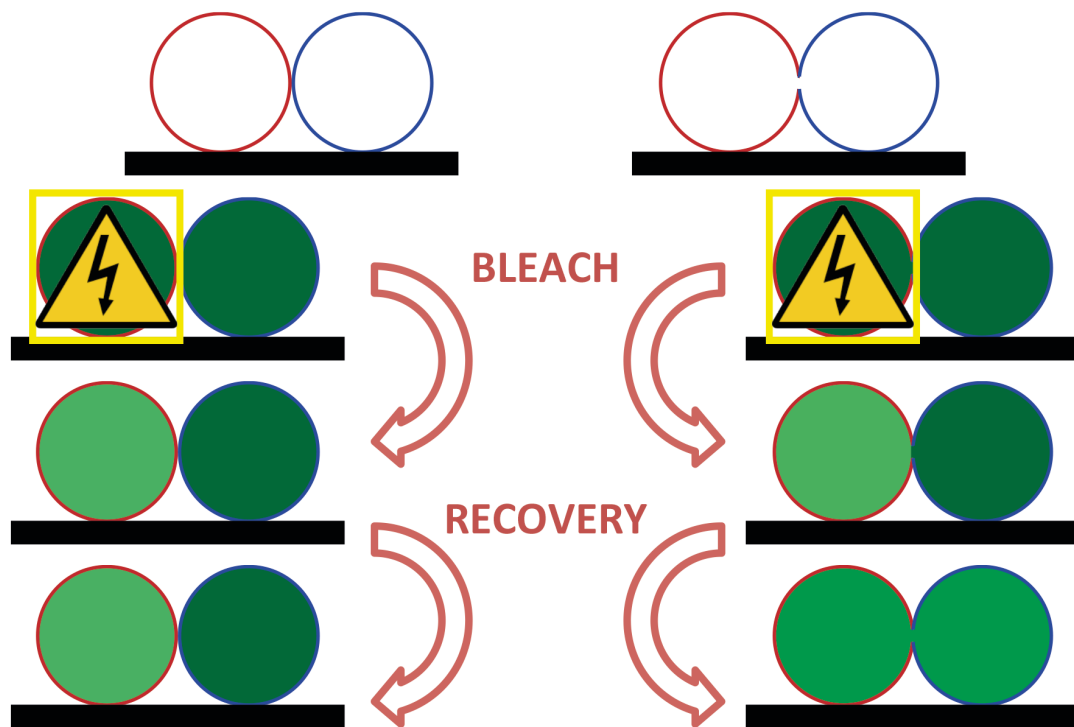


**Figure 5.8** – FRAP assay for vesicle fission. Schematic representation of the FRAP assay developed to distinguish complete budding events.

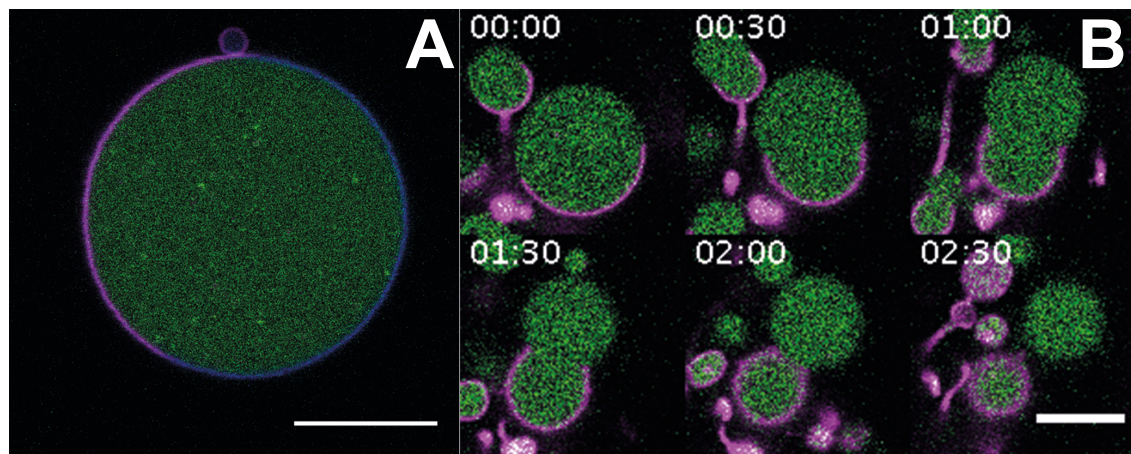


**Figure 5.9** – Budding of intramembrane domains after hyperosmotic shock. [A] GUV filled with AlexaFluor 488 (green) exhibiting coexistence of Lo and Ld phases labeled with DiI (magenta) and CtxB-647 (blue) bound to GM1, respectively. [A] GUV undergoing budding after hyperosmotic shock. Only the Ld phase is labeled. Scale bars are 10  $\mu\text{m}$  and time labels are in m:s from the observation start.

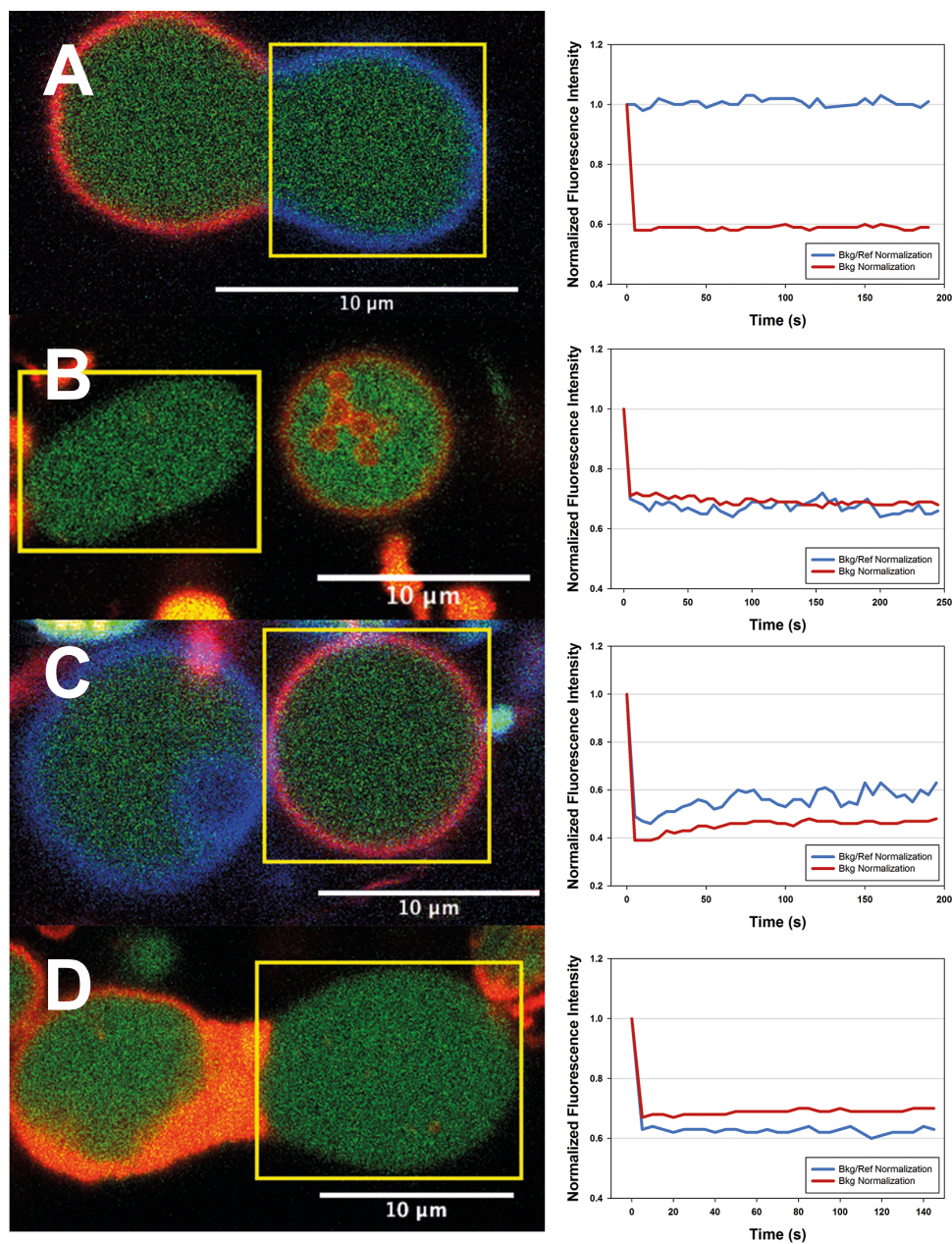


**Figure 5.10** – FRAP measurements of budded intramembrane domains after hyperosmotic shock. [A-D] Phase-separated GUVs filled with AlexaFluor 488 (green) underwent budding after hyperosmotic shock. One of the two daughter vesicles was bleached (yellow square) and the average fluorescence intensity was monitored for several minutes, normalized for either only Bkg or Bkg/ref and plotted next to the corresponding vesicle pair. Lo and Ld phases were originally labeled with DiI (red/magenta) and eventually with CtxB-647 (blue) bound to GM1, respectively.



The experimental work presented in Chapter 6 was designed together with Dr. Salvatore Chiantia (Humboldt Universität zu Berlin, Germany).

## Chapter 6

# Lateral organization of the influenza virus hemagglutinin transmembrane helix into asymmetric model membranes

Influenza virus HA is one of two types of glycoproteins embedded in the viral lipid envelope. Although the name originates from its ability to agglutinate erythrocytes *in vitro* [157], HA pathological functions are not related to agglutination. HA is instead responsible for the recognition of the host cells, binding to terminal sialic acids of glycoproteins and glycolipids of the host cell membranes, as well as for the fusion of the viral envelope with the host cell lysosomal membranes [158]. The structure of HA in the pre-fusion state was solved in 1981 [159]. HA is a homotrimeric integral membrane protein; each monomer is synthesized as precursors that is proteolytically cleaved in the Golgi into two disulfide-linked subunits, HA1 and HA2. The HA2 subunit consists of a helical chain anchored in the membrane by a TM helix.

HA has been found to be enriched in Detergent Resistant Membrane (DRM) fractions [160]. Scheiffele and colleagues could demonstrate that the raft association is indeed an intrinsic property of the TM domain of the protein. Mutant HA molecules with foreign TM domains lose their ability to associate with lipid raft. The same effect is exerted by selected mutations of the HA TM domain, i.e. the GS520AA mutation, showing that hydrophobic residues in contact with the exoplasmic leaflet of the membrane play a role in the protein partitioning behavior. This is supported by the observation that the influenza virus envelope is enriched in raft lipids [161] and by *in vivo* Förster Resonance Energy Transfer (FRET) studies [162, 163]. Interestingly the HA TM domain is able to form heat-resistant oligomers composed of two to five subunits in SDS micelles [164] and stable dimers when expressed in cells [162]. However when the reconstitution of the HA full length protein or of its TM domain was attempted both in GUVs and Giant Plasma Membrane Vesicles (GPMVs), they did not partition into Lo domains [131].

Possible explanations for the different partitioning behavior of the HA in cell and model membranes are: the reduced lipid packing of Lo domains in cell membranes and the absence of cytoskeletal components or transbilayer asymmetry in model membranes. Combining confocal spectroscopy XY-scan and photon-counting histogram analyses, Hussain and colleagues

could recently demonstrate that bilayer asymmetry influences integrins partitioning in raft-mimicking lipid mixtures [117]. In particular they showed that integrins which partition into the Ld domains of symmetric bilayers, sequester preferentially to the Lo phase in the asymmetric counterparts. Similarly DRM partitioning and FRET studies showed that the induction of transbilayer asymmetry leads to a preferential partitioning of the nicotinic acetylcholine receptor in Lo domains [165]. Therefore, we hypothesized that the lack of asymmetry in the used model membranes could also be the reason why HA partitions into Ld domains rather than into Lo domains.

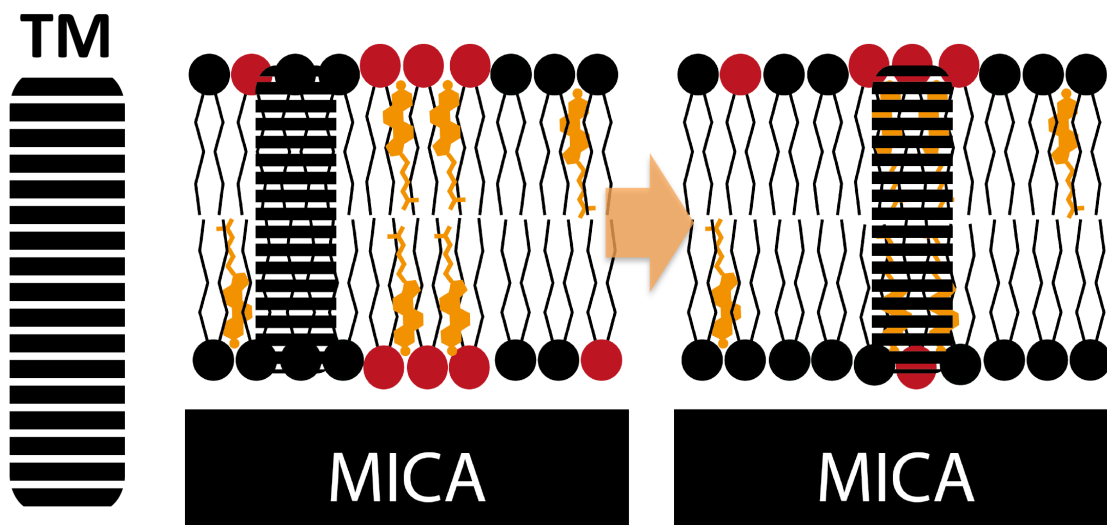


**Figure 6.1** – Partitioning of the HA TM peptide in SLBs containing symmetric and asymmetric domains. Schematic diagram of the working hypothesis: the HA TM peptide partitions differently in symmetric and asymmetric SLBs, that is into Ld and Lo domains, respectively.

In this chapter we investigate the role of lipid bilayer asymmetry in the partitioning behavior of HA in model membranes (Figure 6.1). A peptide corresponding to the HA TM domain and its GS520AA mutant were reconstituted in asymmetric phase-separated SLBs and in GUVs. In both model systems, the asymmetry was induced via cyclodextrin-mediated lipid exchange whereas the %Lo was measured following two different approaches: line-scan FCS for SLBs and confocal microscopy for GUVs. Line-scan FCS was successfully used to accurately measure diffusion coefficients and concentrations in model membranes [99]. It offers interesting advantages to conventional point-FCS: it is a calibration-free technique and thus it is insensitive to optical artifacts, saturation, or incorrect positioning of the laser focus, it is virtually unaffected by photobleaching, and, most importantly for us, it allows to simultaneously probe adjacent domains, thus to drastically reduce measuring time. Line-scan FCS can be performed also on the top pole of GUVs; however the probability that a Ld and a Lo domain are simultaneously at the top pole of a GUV and stay there for the time required for the measurement is extremely low. For this reason, we opted for a more conventional approach to determine the %Lo in GUVs, that is measuring the fluorescence intensities of the Ld and Lo phases in confocal images taken at the GUV equatorial plane [100]. Our data clearly show that the HA TM peptide partitioning in both SLBs and GUVs asymmetric model systems do not change significantly in comparison to the respective symmetric systems, ruling out the hypothesis that transbilayer asymmetry plays a major role in the HA raft association.

## 6.1 Line-scan FCS can probe lipid dynamics independently in each SLB leaflet

Line-scan FCS using a commercial CLSM was used to accurately measure diffusion and Lo partition coefficients of fluorescent lipids in phase-separated SLBs of commonly used raft-mimicking mixtures [99]. Similarly we aimed to use line-scan FCS to quantify the %Lo of the HA TM peptide in SLBs containing symmetric and asymmetric domains. For this purpose we collect line scans with a Zeiss LSM 780 system and analyzed them with a self-written MATLAB script (Dr. Salvatore Chiantia, Figure 6.2).

In order to optimize the scanning parameters (Table 3.1), we first characterized the lipid dynamics of both Lo and Ld domains in SLBs with an asymmetric lipid composition (original SLB composition: DOPC:bSM:Chol 7:1:2). To induce asymmetry and domain formation the bilayer was treated with 40 mM HD $\alpha$ CD-SM, as previously shown for SUVs. We probed each leaflet independently applying the leaflet-specific labeling described in Chapter 4; Atto655-DOPE was used instead of Atto647N-SM as a fluorescent lipid for the upper layer. The diffusion coefficients obtained by line-scan FCS for both Ld and Lo domains as well as the %Los (Figure 6.2, Table 6.1) are in line with previously published values for symmetric SLBs [99]. In contrast to our results, previous measurements performed in asymmetric systems failed to detect differences in lipid packing between Lo and Ld phases [117, 114]. On the other hand, Ld and Lo diffusion coefficients do not differ dramatically between the two leaflets, suggesting that there are no substantial differences in the lipid packing of each phase across the bilayer.

	$D_{Ld}$ [ $\mu\text{m}^2/\text{s}$ ]	$D_{Lo}$ [ $\mu\text{m}^2/\text{s}$ ]	%Lo
<b>Upper Leaflet</b>	$3.06 \pm 0.49$	$0.25 \pm 0.12$	0.01
<b>Lower Leaflet</b>	$3.42 \pm 0.37$	$0.46 \pm 0.26$	0.28

**Table 6.1** – Diffusion and Lo partitioning coefficients of fluorescent lipids in each leaflet of asymmetric SLBs.  $D$  and %Lo of Atto655-DOPE (upper leaflet dye) and NBD-DOPE (lower leaflet dye) in asymmetric SLBs (mean  $\pm$  standard deviation).

## 6.2 Partitioning of influenza HA into symmetric and asymmetric domains in SLBs

To quantify the %Lo of the HA TM peptides in symmetric and asymmetric SLBs, the peptides were either mixed with the phospholipids to form SUVs or incorporated into the bilayer after the SLB was already formed, adding the peptide in the solution above the bilayer with or without the help of non solubilizing concentrations of OG. In the latter case, the domain formation was induced either before or after the peptide was incorporated. To induce domain formation the bilayer was treated as described in Chapter 4 with 12 mM M $\beta$ CD-SM and subsequently with 5 mM M $\beta$ CD-Chol. Alternatively SLBs which already contained cholesterol were directly treated with HD $\alpha$ CD-SM.

Regardless the chosen reconstitution methods and the asymmetry/domain formation strategy used, the %Los of both WT and GS520AA mutant peptides did not change significantly in comparison to their symmetric counterpart. Results averaged from all symmetric and asymmetric samples are summarized in Table 6.2.



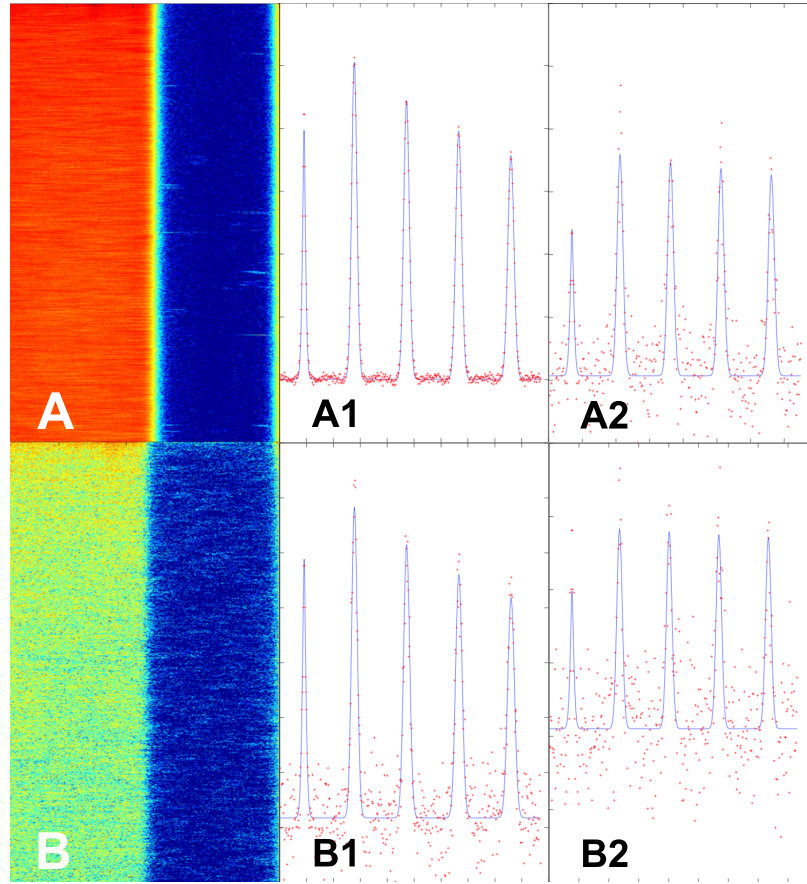


**Figure 6.2** – Line-scan FCS on SLBs containing asymmetric domains. Line scans of the upper [A] and lower leaflet [B] can be arranged in a pseudo-image where the vertical axis is the time. The line-scan was performed through an Ld (bright left region) and Lo phase (dim right region). Typical spatiotemporal correlation curves of the upper [Ld A1, Lo A2] and lower leaflet [Ld, B1; Lo, B2] for  $\tau_1 = \tau_1 - \tau_5$  with best fit to Equation 3.5.

HA TM	WT	GS520AA
<b>Symmetric SLBs</b>	$0.04 \pm 0.003$	$0.01 \pm 0.004$
<b>Asymmetric SLBs</b>	$0.03 \pm 0.018$	$0.01 \pm 0.008$

**Table 6.2** – Lo partitioning coefficients of HA TM peptides in symmetric and asymmetric SLBs. %Los of the HA TM WT and GS520AA mutant peptides in symmetric and asymmetric SLBs (mean  $\pm$  standard deviation).

Independently whether it was incorporated before or after SLB formation, the peptide had a patchy appearance (Figure 6.3, A) and its diffusion coefficient ( $D_{Ld}$  WT  $0.22 \pm 0.18 \mu\text{m}^2/\text{s}$ ) was lower than expected for a single TM helix especially in a Ld phase [166]. In line with the observations of Hussain and colleagues [117], but still surprisingly the diffusion coefficients of the HA TM peptide in asymmetric Ld and Lo domains do not show any statistically significant difference ( $D_{Lo}$  WT  $0.11 \pm 0.02 \mu\text{m}^2/\text{s}$ ; Mann-Whitney Rank Sum Test,  $t(4)=18$ ,  $p=1$ ). This behavior could be explained with the formation of peptide clusters whose diffusion is not majorly affected by the surrounding phase state of the membrane. To rule out an hypothetical influence of the support on the peptide clustering and thus on the partitioning behavior of the



HA TM [63], we run specular experiments in the GUV free-standing membrane model, where the HA peptide can be homogeneously incorporated [131] (Figure 6.3, B) and its diffusion coefficient is in the expected range ( $D_{Ld}$  WT  $3.43 \pm 0.50 \mu\text{m}^2/\text{s}$ ).

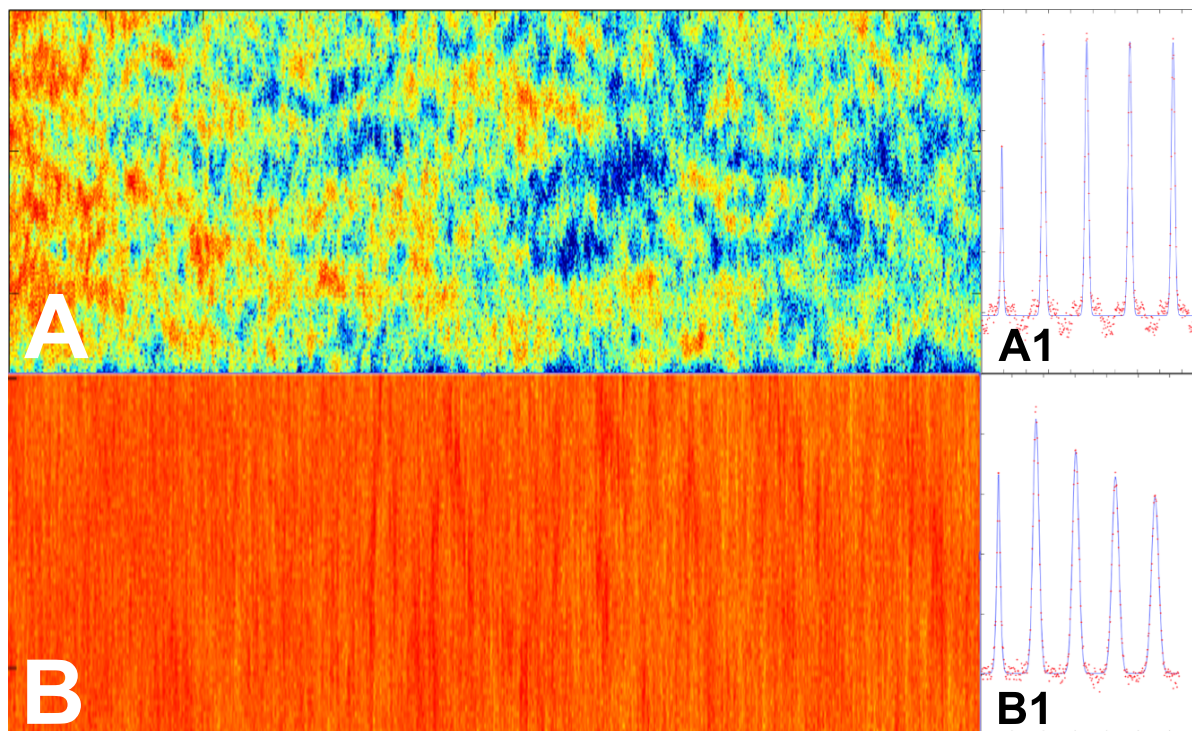


**Figure 6.3** – Line-scan FCS on SLBs and GUVs containing the HA WT peptide. Line scans of a typical SLB [A] and GUV [B] containing the HA WT peptide arranged in a pseudo-image where the horizontal axis is the time. The line-scans were performed through a SLB Ld domain and on top of a GUV in Ld phase, respectively. Typical spatiotemporal correlation curves of the SLB [A1] and the GUV [B1] for  $\tau_i = \tau_1 - \tau_5$  with best fit to Equation 3.5.

## 6.3 Partitioning of influenza HA into symmetric and asymmetric domains in GUVs

### 6.3.1 Both WT and GS520AA mutant HA TM peptides partition into the Ld domains of symmetric GUVs

To compare differences between the partitioning of the HA TM peptide into symmetric and asymmetric domains of GUVs, we first controlled the behavior of both WT and GS520AA peptides in symmetric vesicles. To do so, we reproduced a set of experiments previously published [131]. Similarly to Nikolaus and colleagues, we directly incorporated the labeled peptides in the lipid mixture together with a fluorescently labeled lipid (NBD-DOPE) which is known to partition in the Ld phase [156] and confirmed that both peptides has a strong preference (%*Lo* WT  $0.20 \pm 0.06$ ; GS520AA  $0.11 \pm 0.02$ ) for the Ld phase as shown by the fluorescence overlap with the Ld dye NBD-DOPE (Figure 6.4).

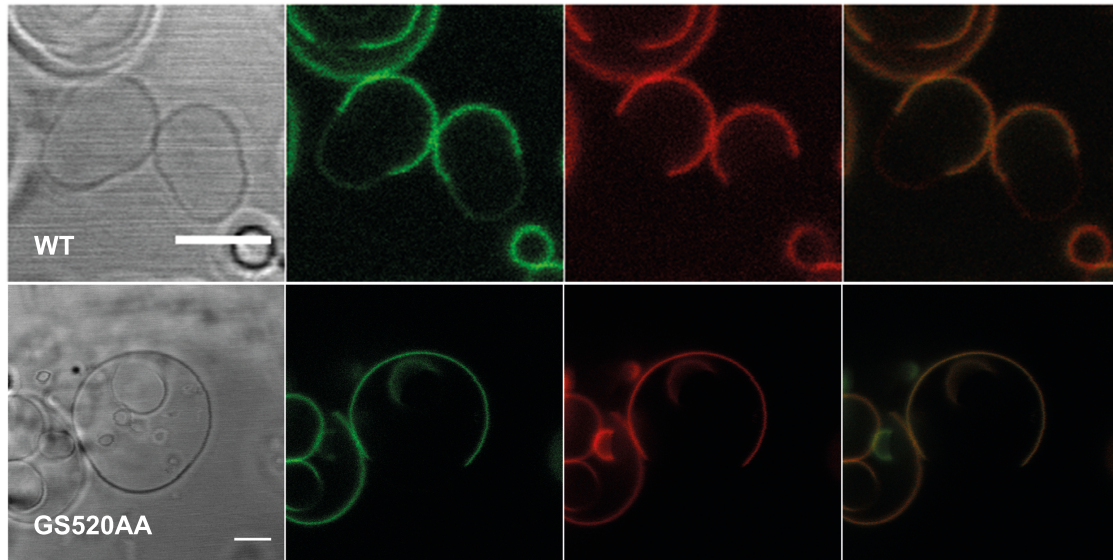


**Figure 6.4** – Partitioning of the HA TM WT and GS520AA peptides into the symmetric domains of GUVs. GUVs with a lipid composition of DOPC:bSM:Chol (2:2:1, molar ratio) containing 0.5 %mol NBD-DOPE as Ld label and 1 %mol of either the WT or the GS520AA peptide were formed and imaged. Both peptides has a strong preference for the Ld phase. Scale bars are 5  $\mu$ m.

### 6.3.2 Both WT and GS520AA mutant HA TM peptides partition into the Ld domains of asymmetric GUVs

To study the partitioning behavior of the HA TM peptides in asymmetric GUVs, we prepared vesicles with different DOPC:bSM:Chol lipid ratios (3:3:1, 7:1:4 and 15:1:4) and treated them with HD $\alpha$ CD-SM to enrich the bSM content of the outer leaflet, similarly as described in Chapter 4 and 5. These GUVs had the same total amount of cholesterol and presumably the same outer leaflet composition, but differ in the amount of bSM of the internal leaflet (20, 10, 5 and 0 %mol). Independently of the composition of the internal leaflet, both WT and GS520AA peptides partition preferentially into the Ld domains as shown by the fluorescence overlap with the Ld dye NBD-DOPE (Figure 6.5). The %*Los* of the HA TM WT and GS520AA peptides do not significantly differ between symmetric and asymmetric GUVs with different original DOPC:bSM:Chol lipid ratios (Table 6.3).

DOPC:bSM:Chol	Symmetric	Asymmetric		
	2:2:1	3:3:1	7:1:4	15:1:4
WT	0.20 $\pm$ 0.06	0.16 $\pm$ 0.14	0.05 $\pm$ 0.03	NA
GS520AA	0.11 $\pm$ 0.02	0.09 $\pm$ 0.04	0.11 $\pm$ 0.04	0.13 $\pm$ 0.03

**Table 6.3** – Comparison of *Lo* partitioning coefficients. %*Los* of the HA TM WT and GS520AA peptides in symmetric and asymmetric GUVs with different original DOPC:bSM:Chol lipid ratios (mean  $\pm$  standard deviation).

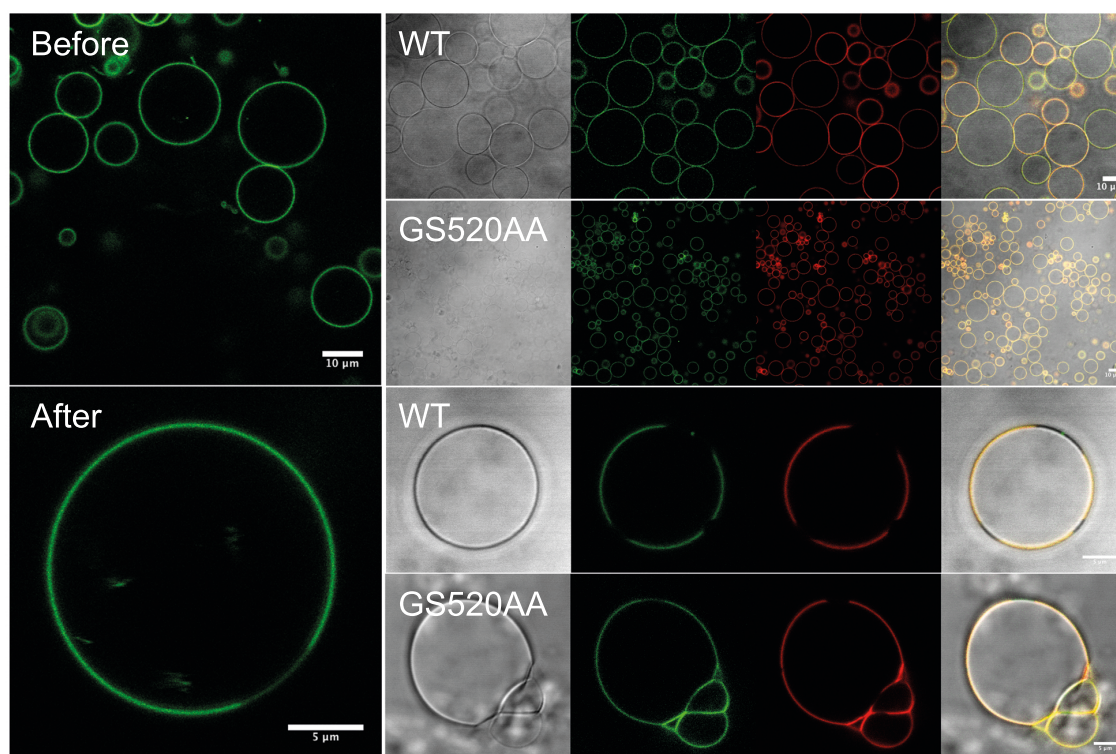


**Figure 6.5** – Partitioning of the HA TM WT and GS520AA peptides into the asymmetric domains of GUVs. GUVs with a lipid composition of DOPC:bSM:Chol (7:1:2, molar ratio) containing 0.5 %mol NBD-DOPE as Ld label and none (Before and After bigger images) or 1 %mol of either the WT or the GS520AA peptide were formed, treated with HD $\alpha$ CD-SM and imaged.

### 6.3.3 The WT HA TM peptide induce phase separation in symmetric and asymmetric GUVs

Although significant differences in the partitioning behavior of the HA TM peptides could not be detected, an unexpected observation was made during the same set of experiments. The HA TM WT peptide was able to induce phase separation in symmetric GUVs, which contain 20 %mol of both bSM and cholesterol (Figure 6.6) as well as in asymmetric GUVs, which do not contain bSM in the internal leaflet (Figure 6.7). Both GUV mixtures do not show phase separation in absence of HA TM WT peptide nor in presence of the HA TM GS520AA peptide.

## 6.4 Discussion

Lo domains have been extensively employed as model system for lipid rafts in cells and have provided many clues about their possible nature [167]. However cell membranes are more complex than model membranes [168]. Not only the higher lipid diversity, but also the presence of high amount of proteins (up to 60% dry mass [169]) in biological membranes makes model membranes not always an ideal experimental tool. The importance of a crowded protein environment in biological membranes was recently pointed out by Parton and colleagues [170]. Using Coarse-Grained Molecular Dynamics (CG MD) simulations, they investigated the



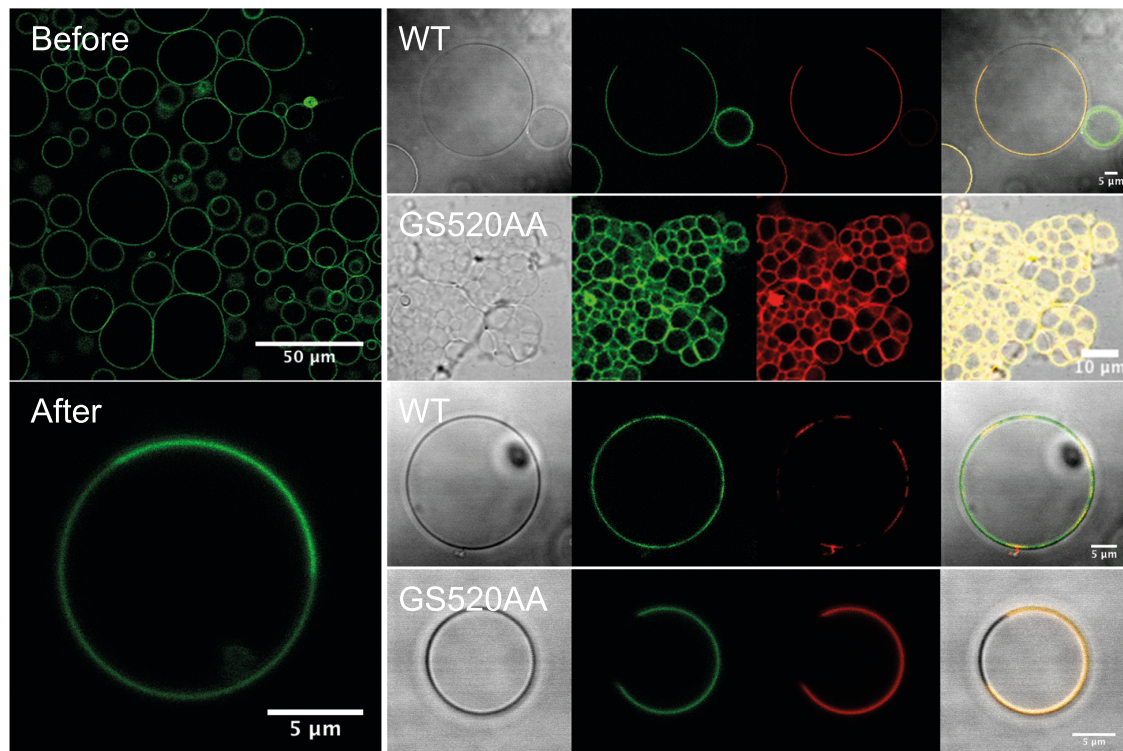


**Figure 6.6** – The WT HA TM peptide induces phase separation in symmetric GUVs. GUVs with a lipid composition of DOPC:bSM:Chol (3:3:1, molar ratio) containing 0.5 %mol NBD-DOPE as Ld label and none (Before and After bigger images) or 1 %mol of either the WT or the GS520AA peptide were formed, treated with HD $\alpha$ CD-SM and imaged. Only in presence of the HA TM WT peptide, GUVs showed phase separation even before lipid exchange.

interactions between HA and raft lipids in phase separated membranes and could show that raft lipids are enriched within dynamic nanoclusters of HA proteins when the HA is included at a high concentration, comparable to that of a typical cell membrane or of an influenza virus [170]. This suggests that a high local concentration of HA may trigger its association to rafts. Unfortunately, it is not possible to incorporate such amounts of protein/peptide into model membranes, yet; thus this hypothesis is not easy to prove experimentally.

More generally, TM helices are expected to poorly partition into Lo domains irrespective of the hydrophobic mismatch and amino acid sequence, and thus TM proteins to locate in Ld rather than in Lo domains [171, 172, 173]. Although detergent insolubility studies have proven that some TM proteins exhibit a tendency to locate in rafts, the same TM proteins have shown low affinity for Lo domains in model membranes. This is the case of the HA. Additional factors that could explain this affinity difference include: TM helix oligomerization, inclusion of the TM proteins in Ld puddles embedded within larger Lo domains and, covalent attachment of palmitoyl fatty acyl groups to TM proteins [168]. Dimerization, for example, has being proven to be responsible for the raft partitioning of the urokinase plasminogen activator receptor both in cells and model membranes [174], whereas multimerizable HIV Gag derivative failed to bind Lo phases in model membranes [175]. Palmitoylation together with other saturated lipid modifications is considered to be important for protein association with membrane rafts [176]; in the case of the HA, the non-palmitoylated full protein and

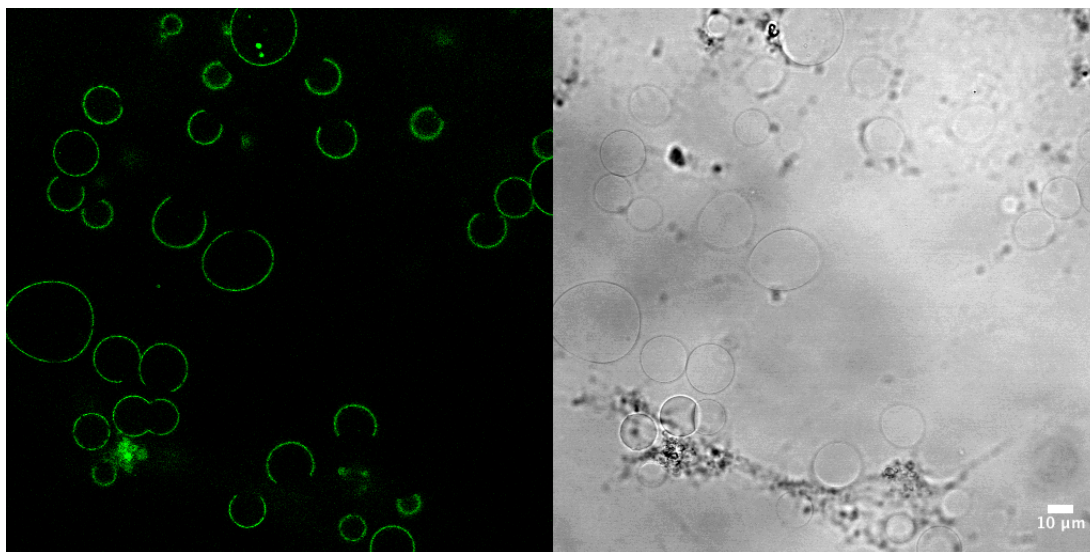


**Figure 6.7** – The WT HA TM peptide induces phase separation in asymmetric GUVs. GUVs with a lipid composition of DOPC:bSM:Chol (4:0:1, molar ratio) containing 0.5%mol NBD-DOPE as Ld label and 1%mol of the WT HA TM peptide were formed, treated with HD $\alpha$ CD-SM and imaged. Only in presence of the WT peptide, GUVs showed phase separation after lipid exchange.

TM peptide show a lower affinities for rafts, both in DRM partitioning and FRET studies [162, 163], but at the same time palmitoylation is not sufficient to rescue the DRM partitioning of HA mutated in the TM domain [160].

The observation that the HA TM WT helix can induce domain formation both in symmetric and asymmetric GUVs was unexpected. Similar observations are rare, but present and discussed in the literature. Two major mechanisms have been hypothesized to explain this behavior. On one hand, proteins could influence domain formation because of their strong affinity for Lo domains which increases the mutual insolubility of high T<sub>m</sub> and low T<sub>m</sub> lipids [168]. Cholera toxin represents the best example of this mechanism. It has been shown to induce phase separation in model membrane vesicles whose lipid composition would be either in a homogeneous Ld or Lo phase in absence of the protein [177]. Moreover, the HA TM peptide and several fusion peptides, including the wt20 fusion peptide from the the influenza HA, are known to increase membrane-ordering upon binding [164, 178]. On the other hand, proteins could influence domain formation because they strongly associate with lipids that form Ld domains and thus act as nucleators. This mechanism is easier to imagine for TM helices. [168] Using CG MD, Domański and colleagues showed that TM helices which preferentially bind to one lipid component can amplify non-ideal lipid mixing and bring the system closer to a miscibility critical point, thus inducing domain formation [179]. In all simulations TM helices partitioned into the Ld phase. Additionally cytochrome c, which preferentially adsorbs onto Lo domains, was shown to induce micron-sized domains and to expand the region of coexistence of Lo and Ld phases [180].

The theory and experimental work presented in Chapter 7 was designed together with Dr. Franziska Thomas (FT, Max Planck Institute of Biochemistry, Martinsried, Germany), Dr. Zdeněk Petrášek (Graz University of Technology, Graz, Austria), Dr. Fabian Heinemann (Roche Diagnostics, GmbH, Penzberg, Germany) and Prof. Petra Schwille (Max Planck Institute of Biochemistry, Martinsried, Germany).

Measurements and data analysis presented in Figures 7.3-7.6 and Table 7.1 (GUV-FCS and GUV-imaging) - 7.2 were performed by FT.

## Chapter 7

# Quantification of protein partitioning into giant unilamellar vesicles by fluorescence correlation spectroscopy and confocal imaging

Peripheral membrane proteins are involved in various key cellular processes, e.g. signaling and cell division [181, 182]. They can interact with lipid membranes in different ways, for example by lipid modifications or through membrane targeting domains. Besides a direct interaction with a specific lipid molecule, the membrane binding site of a protein can selectively interact with several outer head groups and/or with the internal hydrocarbon backbone of a lipid area [183, 184, 185]. The quantification of membrane affinity of peripheral proteins is challenging but crucial, in order to elucidate the role of lipid composition and the properties of anchoring segments on binding specificity. The  $K_P$  is an important parameter that describes the affinity of a molecular species for lipid bilayers independently from the underlying binding mechanism. For  $K_P$  determination in model membrane systems, several methods are known, e.g. equilibrium dialysis, centrifugation or calorimetry. Besides specific advantages, all of them have particular experimental drawbacks, such as changes in lipid and/or protein concentration during the measurement and low sensitivity. These methods and their drawbacks were discussed in detail in several review articles [186, 187, 188, 189].

Besides the above-mentioned established approaches, few additional microscopy based methods have been proposed to determine the affinity of diverse molecular species for lipid membranes. A quantitative FRAP approach was applied in live cells to obtain the association and dissociation rate constants  $k_{on}$  and  $k_{off}$  of intracellular binding-reaction diffusion processes [190]. Total Internal Reflection Fluorescence (TIRF) imaging was used to determine the membrane-binding equilibrium constants of a peptide binding to supported lipid bilayers [191]. Finally, confocal imaging of single liposomes was employed to investigate curvature sensing motifs [192]. However, none of these assay-specific microscopy based methods is generally applicable to determine  $K_{PS}$ .

FCS, on the other hand, has been used to determine the  $K_P$  of fluorescently labeled peptides to LUVs [74]. In this approach the vesicle-bound and free peptide fractions can be distinguished by their different correlation times. Although this method offers appealing advantages (e.g. measurement time, extended accessible concentration range) and could be

successfully applied [181, 78, 182, 76, 75], numerous potential pitfalls in the data analysis were reported [183, 193, 184, 194, 185, 195]. In particular, the determination of the  $K_P$  can be negatively affected by multiple peptides binding to a single vesicle, light scattering and not point-like diffusing particles. In addition, protein aggregation at high vesicle concentrations, as well as variations in protein concentration throughout the measurements are experimental challenges which may sometimes preclude the use of this approach. A generalized method that still profits from the advantages of using FCS to study membrane dynamics [186, 71, 187, 67, 188, 68, 189], e.g. sensitivity, and at the same time overcomes the above-mentioned drawbacks is desirable.

In this chapter we describe a new and robust assay in which GUVs are employed. This well-established model membrane system possesses the advantage to be free standing, and thus, protein-lipid interactions are not affected by any support. GUVs have a diameter of 1-100  $\mu\text{m}$ , which easily allows imaging by confocal fluorescence microscopy and permits the simultaneous measurement of both free and bound protein fractions. Also, protein binding to GUVs is hardly affected by curvature, being the GUV membrane virtually flat on the nanoscale. Furthermore, GUVs can in principle be produced with any biologically relevant lipid composition and by various methods [190, 49].

In our assay, the concentrations of both free and GUV-bound protein are determined at increasing protein concentrations via FCS or confocal fluorescence microscopy. Both approaches provide the advantages to account for potential loss of protein during the measurement (e.g. by protein interaction with the surface of the measurement chamber) as well as for changes in the lipid concentration (e.g. by GUV bursting), and to be sensitive down to nanomolar range. In addition, the partitioning coefficient can be directly calculated from the measured concentrations, bypassing the problems reported for the data analysis of LUVs assay. For the validation of the method, we chose the well-characterized system of HexaHistidine (His6) binding to Nickel Nickel (Ni) chelated with NitriloTriacetic Acid (NTA) [191, 196, 197]. We used eGFP with a C-terminal His6-Tag (eGFP-His6) as membrane associating protein and GUVs containing 2-5 mol% NTA(Ni) functionalized lipid as membrane model (Figure 7.1). Finally, to prove the accuracy of our results, we performed the LUV assay [74], whose data analysis was improved to take into account multiple binding of peptides to a single vesicle.

## 7.1 Theory

As illustrated in Figure 7.2 A, molecules with high membrane affinity partition proportionally more into the bilayer than molecules with low membrane affinity. The affinity of molecular species for membrane surfaces is described by the relation between the concentration  $[P_f]$  ( $\text{mol}/\text{m}^3$ ) of the unbound species freely diffusing in solution, and the concentration  $[P_m]$  ( $\text{mol}/\text{m}^3$ ) of the membrane associated fraction. If the total accessible lipid concentration  $[L]$  ( $\text{mol}/\text{m}^3$ ) is sufficiently large  $[L] \gg [P_m]$ , so that no saturation of the binding sites under the used experimental condition takes place, and given that the volume of the sample chamber  $V$  and  $[L]$  of the system are kept constant, the relation between the two concentrations is linear:

$$[P_m] = \alpha[P_f] \quad (7.1)$$

The proportionality constant  $\alpha$  is dimensionless and depends on the amount of surface (expressed, for example, by the lipid concentration) and on the characteristics of the interaction between the molecule and the surface.  $K_P$  can be derived from  $[P_m]$  and  $[P_f]$  as follows:



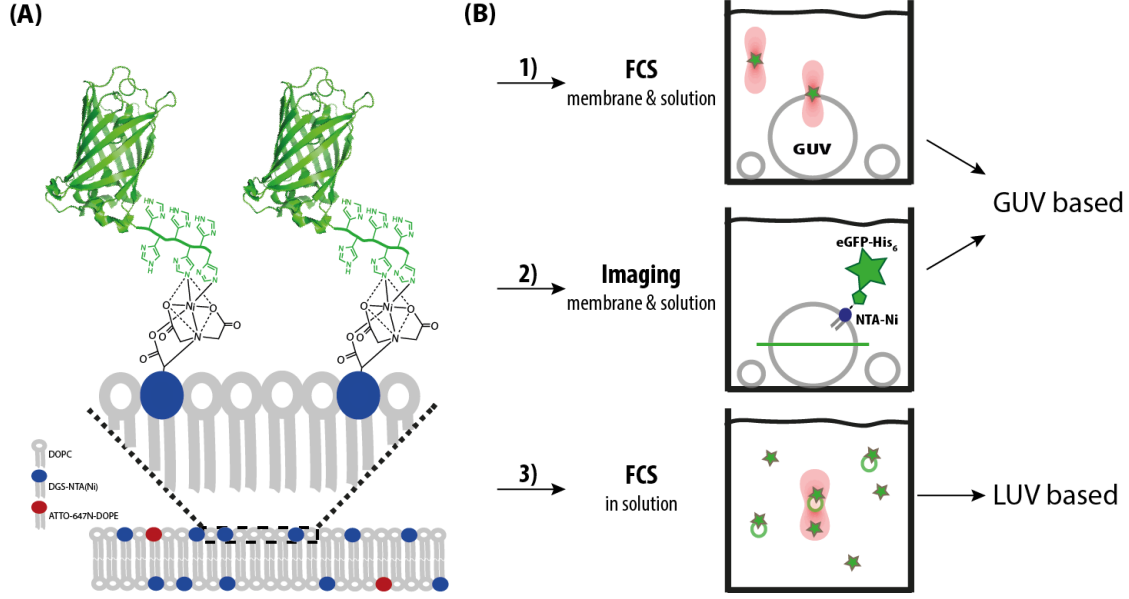


**Figure 7.1** – GUV- and LUV-based methods to measure protein-lipid affinity. Schematic representation of [A] a lipid bilayer containing DGS-NTA(Ni) lipids and their coordination by two adjacent histidine residues of a His-tagged eGFP, and [B] the three applied methods to determine the  $K_P$  of this interaction.

$$[K_P] = \frac{[P_m]/[L]}{[P_f]/[W]} \quad (7.2)$$

according to the equilibrium of chemical potentials. A detailed derivation as well as a discussion of the required assumptions can be found in White and colleagues [192, 186]. The water concentration  $[W]$  is constant with  $[W] = W = 55.5M$ .  $[L]$  is also constant in a given sample and can be expressed by:

$$[L] = \frac{A}{A_L N_A V} \quad (7.3)$$

In Equation 7.3,  $A$  is the total accessible lipid area,  $A_L$  the area per lipid, and  $N_A$  the Avogadro's constant. The advantage of Equation 7.2 is that it does not make any assumptions about the binding stoichiometry. Nevertheless, if the stoichiometry is known and appropriate to describe the protein-lipid binding, an alternative approach not depending on the area per lipid can be formulated using the Dissociation constant ( $K_d$ ). In equilibrium, an identical number of molecules  $P$  will dissociate from and associate to the lipid phase  $L$  per area and time  $P + nL \rightarrow nPL$ . For 1:1 binding stoichiometry  $n = 1$ ,  $K_d$  is defined as:

$$K_d = \frac{[P_f][L_f]}{[PL]} \quad (7.4)$$

where  $[PL] = [P_m]$  and  $[L_f] = [L] - [L_m]$  with  $[L] \gg [L_m]$ . Thus,

$$K_d = \frac{[P_f][L]}{[P_m]} = \frac{k_{off}}{k_{on}} \quad (7.5)$$

Comparing Equation 7.5 with Equation 7.2 leads to the following conversion:

$$\frac{K_P}{W} = \frac{1}{K_d} \quad (7.6)$$

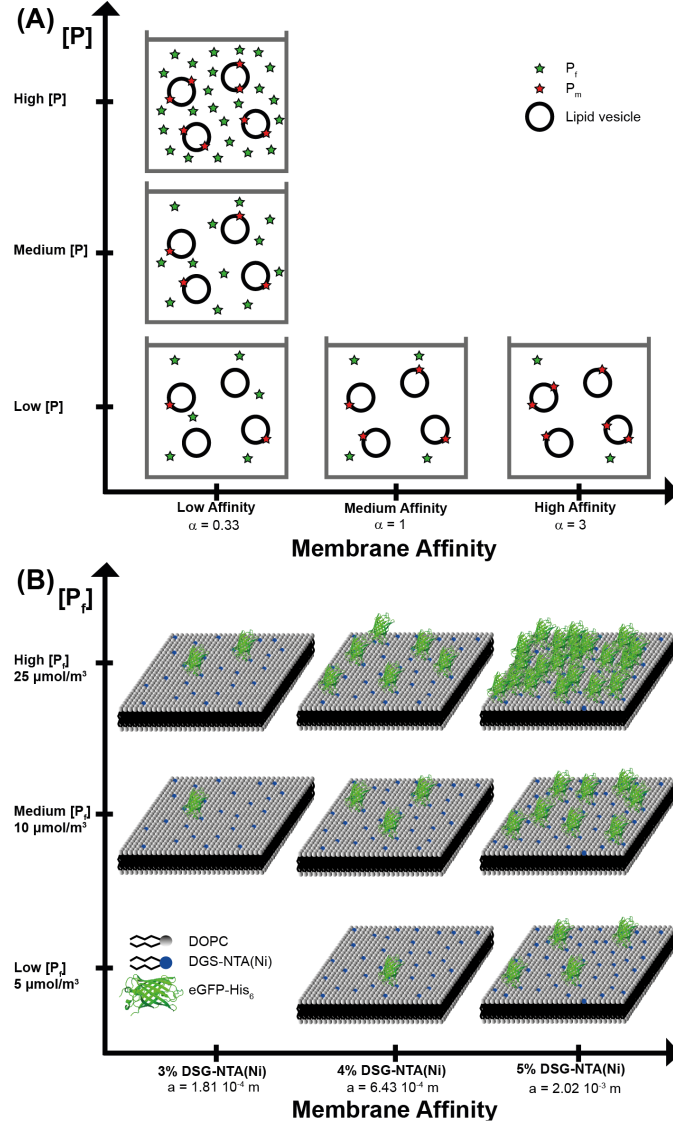


**Figure 7.2** – Membrane volume and surface concentrations of proteins with different membrane affinities. Schematic representation of how molecules equilibrate between the liquid phase and the lipid vesicles according to their membrane affinity. [A] At fixed volume and lipid surface, the ratio  $\alpha$  (dimensionless, Equation 7.1) between membrane associated and freely diffusing molecules is constant independently from the concentration of molecules. [B] Schematic representation of how the number of molecules per lipid surface varies according to their membrane affinity  $K_P$  and to the concentration of free molecules in solution. The slope  $a$  (unit of length (m), Equation 7.17) is constant for a lipid system and depends on both the partitioning coefficient  $K_P$  and the lipid surface concentration  $[L_{2D}]$ . In this example, the number of eGFP-His<sub>6</sub> molecules associated to a lipid patch of 30x30 lipids (10.8 nm<sup>2</sup>) were calculated with Equation 7.18 for membranes with different amount of DGS-NTA(Ni).  $K_P$ s values measured by FCS in GUVs (Table 7.1) and  $A_L$  calculated as described in Section 7.2 were used.  $[P_f]$  concentrations were chosen in the range of the GUV assay.

### 7.1.1 Measurement of $K_P$ by fluorescence correlation spectroscopy in GUVs

A convenient way to determine the concentrations in question is to conduct FCS.  $[P_f]$  can be quantified performing FCS on free molecules in solution. In particular, the number of free

particles  $N'_f$  in the FCS observation volume can be obtained from the fit of the fluorescence auto-correlation curves with the suitable FCS model function for 3D diffusion:

$$G(\tau) = \frac{1}{N'_f(1+\frac{\tau}{\tau_D})(1+\frac{\tau}{S^2\tau_D})^{1/2}}(1 + \frac{\tau}{1-T}\exp(-\frac{\tau}{\tau_T})) \quad (7.7)$$

Here, the variable  $\tau$  is the correlation time,  $\tau_D$  the diffusion time,  $\tau_T$  the triplet lifetime, and  $T$  the fraction of molecules in the triplet state. Especially at low protein concentrations, and therefore at low fluorescence intensities, the fluorescence background will affect the particle number  $N'_f$  obtained from the fit. Thus  $N'_f$  should be background corrected [198] to get  $N_f$ .  $[P_f]$  can be calculated from  $N_f$  as follows:

$$[P_f] = \frac{N_f}{V_{FCS}N_A} \quad (7.8)$$

The focal volume  $V_{FCS}$  can be determined by:

$$V_{FCS} = \pi^{3/2}Sw_0^3 \quad (7.9)$$

where the values for the structural parameter  $S$  and the focal waist  $w_0$  were obtained from a calibration measurement using a dye with known diffusion coefficient  $D$ :

$$w_0 = \sqrt{4D\tau_D} \quad (7.10)$$

$[P_m]$  can be obtained by measuring FCS on the membrane of the GUVs. Conveniently, in our assay it is sufficient to measure the surface concentration  $[P_{2D}]$  (mol/m<sup>2</sup>) on the top pole of the GUVs[70] instead of determining  $[P_m]$ . In particular, the number of GUV-bound particles  $N_{2D}$  in the FCS observation area  $A_{FCS} = \pi w_0^2$  can be obtained from the fit of the fluorescence auto-correlation curves with a combined FCS model function for 2D-3D diffusion. Both freely diffusing and membrane bound molecules are, in fact, present in the detection volume:

$$G(\tau) = \frac{1}{N'_{2D3D}}((1-F)\frac{1}{(1+\frac{\tau}{\tau_2D})} + F(\frac{1}{(1+\frac{\tau}{\tau_3D})(1+\frac{\tau}{S^2\tau_3D})^{1/2}}))(1 + \frac{\tau}{1-T}\exp(-\frac{\tau}{\tau_T})) \quad (7.11)$$

The diffusion time in solution  $\tau_{3D}$  should be fixed to the value obtained using the free molecular species. From the fit, the fraction  $F$  of free protein in solution and the total particle number  $N'_{2D3D}$  in the focal volume will be obtained. After correcting  $N'_{2D3D}$  for the background,  $N_{2D}$  and  $[P_{2D}]$  can be calculated:

$$N_{2D} = (1-F)N'_{2D3D} \quad (7.12)$$

$$[P_{2D}] = \frac{N_{2D}}{A_{FCS}N_A} \quad (7.13)$$

$[P_{2D}]$  can be converted to  $[P_m]$  by multiplying it with the total accessible lipid area  $A$ :

$$[P_m] = [P_{2D}]\frac{A}{V} \quad (7.14)$$

A rearrangement of Equation 7.2 yields in analogy to Equation 7.1:

$$[P_m] = \frac{K_P[L]}{W}[P_f] \quad (7.15)$$

Combining Equation 7.15 with Equations 7.3 and 7.14 gives the following main equation (A and V cancel out):

$$[P_{2D}] = \frac{K_P}{A_L N_A W} [P_f] \quad (7.16)$$

Thus, measuring a set of  $[P_{2D}]$ ,  $[P_f]$  pairs for several concentrations of the binding species lead to a linear behavior with slope:

$$a = \frac{K_P}{A_L N_A W} \quad (7.17)$$

When the  $A_L$  for the used lipid mixture is known,  $K_P$  can be obtained from  $a$ , which is not dimensionless (unit of length (m)) but is analog to  $\alpha$ . Moreover,  $\frac{1}{A_L N_A}$  is the lipid surface concentration  $[L_{2D}]$  (mol/m<sup>2</sup>), which is constant for a given lipid mixture. Therefore by knowing  $K_P$  and  $[P_f]$  of the system, one can always calculate the number of molecules per lipid surface, which depends on the combined constant  $c = \frac{[L_{2D}]}{W}$  (Figure 7.2, B):

$$[P_{2D}] = c K_P [P_f] \quad (7.18)$$

Similarly  $K_d$  can be calculated combining Equations 7.6 and 7.17:

$$K_D = \frac{1}{a A_L N_A} \quad (7.19)$$

### 7.1.2 Measurement of $K_P$ by fluorescence confocal imaging in GUVs

Alternatively, both  $[P_f]$  and  $[P_{2D}]$  can be determined imaging GUVs at their equator. A similar approach was reported for analysis of living cells [199]. When a GUV is imaged at its equatorial plane the fluorescence intensity of its surface  $I_{2D}$  is proportional to the concentration of the membrane bound molecules  $[P_{2D}]$ , whereas the fluorescence intensity  $I_f$  of the surrounding solution is proportional to the concentration of the free molecules  $[P_f]$ :

$$[P_{2D}] = b_{2D} I_{2D} \quad (7.20)$$

$$[P_f] = b_f I_f \quad (7.21)$$

The two proportionality constants  $b_{2D}$  and  $b_f$  can be determined by calibration with FCS. The semi-automated software described in Chapter 3 has been used to extract the intensity values  $I_{2D}$  and  $I_f$  from confocal images of GUVs.

### 7.1.3 Measurement of $K_P$ by fluorescence correlation spectroscopy in LUVs

When LUVs are mixed with lipid binding protein an equilibrium between free and LUV-bound protein is established. This equilibrium can be described by  $K_d$  using Equation 7.5, where  $[L]$  is total LUV concentration  $[LUV] = \frac{[L]}{N_{LUV}}$ ,  $N_{LUV}$  the number of lipids contained in a LUV,  $[P_m] = m[LUV]$  and  $m$  the mean number of protein bound to one LUV. Thus:

$$K_D = \frac{[P_f]}{m} \quad (7.22)$$

If LUVs are much larger than the protein, FCS can be used to determine the free  $F$  and bound fractions  $1-F$  of protein on basis of their different diffusion times. The autocorrelation function, consisting of two diffusion components, can be expressed as:

$$G(\tau) = \frac{1}{N} \left( \frac{F}{(1+\frac{\tau}{\tau_f})(1+\frac{\tau}{S^2\tau_f})^{1/2}} + \frac{1-F}{(1+\frac{\tau}{\tau_m})(1+\frac{\tau}{S^2\tau_m})^{1/2}} \right) \left( 1 + \frac{\tau}{1-T} \exp(-\frac{\tau}{\tau_T}) \right) \quad (7.23)$$

where  $N$  is the total number of protein and the diffusion time of the molecules bound to LUVs  $\tau_m$  is much larger than the diffusion time of the free molecules  $\tau_f$ :  $\tau_m > \tau_f$ . The free and LUV-bound fractions can be written as the autocorrelation amplitudes  $g_{f0} = \frac{F}{N}$  and  $g_{m0} = \frac{1-F}{N}$ , respectively.

Assuming that the number of the protein bound to one LUV is Poisson-distributed with the mean value  $m$ , the two autocorrelation amplitudes are related to the total LUV  $[LUV]$  and protein concentrations  $[P] = [P_f] + m[LUV]$  in the following way:

$$g_{f0} = \frac{1}{[P]V} \frac{1}{1+\frac{[P]}{K_d}} \quad (7.24)$$

$$g_{m0} = \frac{1}{[P]V} \frac{1}{K_d+[LUV]} \left( 1 + \frac{[P]}{K_d+[LUV]} \right) \quad (7.25)$$

It is useful to consider the autocorrelation amplitude  $G'(0)$  normalized by its value in the absence of LUV ( $[LUV] = 0$ ),  $\frac{1}{[P]V}$ :

$$G'_0 = [P]V(g_{f0} + g_{m0}) = 1 + \frac{[P][LUV]}{(K_d+[LUV])^2} \quad (7.26)$$

By varying (increasing) the LUV concentration while keeping  $[P]$  constant and measuring  $G'(0)$ ,  $K_d$  can be found by fitting  $G'(0)$  to Equation 7.26.  $[P]$  can be determined by FCS before the addition of LUV. Knowing  $N_{LUV}$ ,  $K_d$ s can be converted to  $K_P$ s using Equation 7.5:

$$K_P = \frac{WN_{LUV}}{[K_d]} \quad (7.27)$$

## 7.2 GUV-FCS assay

For the calculation of the partitioning coefficient  $K_P$ , it is essential to precisely determine the amount of both freely diffusing and DGS-NTA(Ni)-coordinated eGFP-His6. In order to quantify both concentrations, we conducted point-FCS in solution and on the top pole of several GUVs per probe.

Before measurement of each sample, the system was carefully calibrated with Alexa488 to calculate the focal waist  $w_0$ ,  $V_{FCS}$  and  $A_{FCS}$ . The later two need to be determined precisely, since an error of their values propagates in the calculation of all protein concentrations. The average values obtained of all measurements are  $w_0 = 218.0 \pm 6.0$  nm (mean $\pm$ s.e.m,  $n = 19$ ),  $V_{FCS} = 3.98 \pm 0.36 \cdot 10^{-19}$  m<sup>3</sup> (mean $\pm$ s.e.m,  $n = 19$ ) and  $A_{FCS} = 1.49 \pm 0.08 \cdot 10^{-13}$  m<sup>2</sup> (mean $\pm$ s.e.m,  $n = 19$ ). As an additional control, the red channel was calibrated as well using Atto655, which has a focal waist  $w_0 = 246.2 \pm 4.6$  nm (mean $\pm$ s.e.m,  $n = 19$ ) due to greater diffraction.

Thereafter, an overall image of the well in which the experiment was carried out was taken by a tile scan. Sequentially, more GFP-His6 was added into the chamber and incubated until

equilibrium was reached. For each protein concentration, the auto-correlation functions of both the free and bound protein signal were recorded. The system was very stable over time and therefore for each of the increasing amounts of protein exactly the same GUVs could be surveyed. Additionally the Atto647N-DOPE signal was taken simultaneously as control. In case the fluorescence time traces showed a strange behavior, the curves of both channels were rejected. At higher concentrations of DGS-NTA(Ni), the laser power of the 488 laser line needed to be reduced to avoid detector saturation, which does not significantly affect the concentration measurement by FCS, but has to be considered for the image analysis by using an appropriate calibration curve.

The successive auto-correlation curves taken in solution were fitted using a 3D function in PyCorrFit [104] and Equation 7.8 was used to calculate  $[P_f]$ . The average diffusion time of eGFP-His6 in solution is  $\tau_D = 1.23 \pm 0.02 \cdot 10^{-4}$  s (mean  $\pm$  combined s.e.m.,  $n = 890$ ), from which the average diffusion coefficient can be calculated. The obtained value of  $D = 103 \pm 6 \mu\text{m}^2/\text{s}$  (mean  $\pm$  combined s.e.m.;  $26.0 \pm 0.5^\circ\text{C}$ ) is in agreement with previous measurement [102]. Analogously, the corresponding auto-correlation functions taken on membrane were fitted using 2D3D fit function to get the average number of particles, which was used to calculate the bound protein concentration  $[P_{2D}]$  according to Equations 7.12 and 7.13.

In Figure 7.3 a typical graph of a measurement is shown with the obtained  $[P_f]$  and  $[P_{2D}]$  plotted against each other. The relatively high error bars for  $[P_{2D}]$  are possibly a result of uneven distribution of the DGS-NTA(Ni) among the GUVs in the sample [200]. As assumed in the theory, the linear relation between  $[P_f]$  and  $[P_{2D}]$  confirm that no saturation of the binding sites takes place.

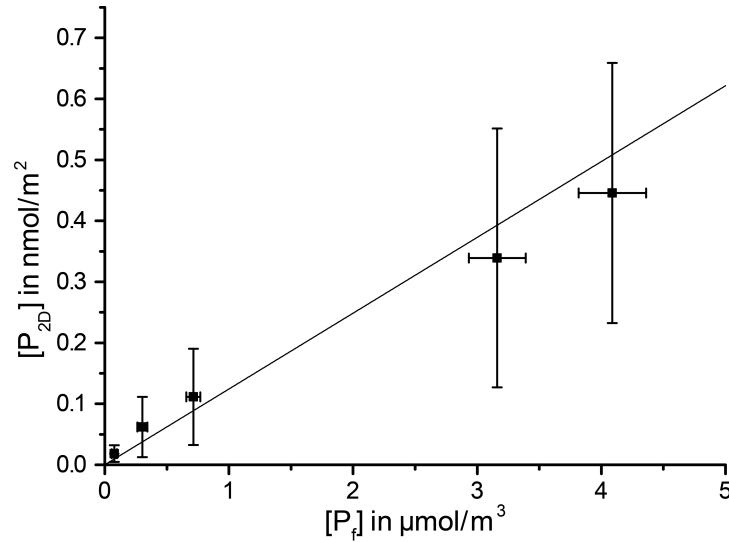


**Figure 7.3** – Protein concentrations determined by GUV-FCS assay.  $[P_{2D}]$  plotted vs.  $[P_f]$  for an individual sample of 2% DGS-NTA(Ni). Error bars represent the standard deviation. The ratio of  $[P_{2D}]/[P_f]$  stays constant with increasing protein concentrations. No saturation occurs.

To calculate the partitioning coefficient  $K_P$  for a particular percentage of DGS-NTA(Ni), the slope  $a$  and  $A_L$  for the given system are required. For our calculations, we used  $72.4 \text{ \AA}^2$  for DOPC [201] and for DGS-NTA(Ni) an  $A_L$  of  $60.0 \text{ \AA}^2$  [202]. We estimated  $A_L$  by linear interpolation of the two values, yielding  $72.2 \text{ \AA}^2$ ,  $72.0 \text{ \AA}^2$ ,  $71.9 \text{ \AA}^2$  and  $71.8 \text{ \AA}^2$  for the molar ratios 2%, 3%, 4% and 5% of DGS-NTA(Ni) in the lipid mixture with DOPC.

Fitting all data points of at least three independent measurements results in a slope  $a$  for the percentage of DGS-NTA(Ni), out of which the  $K_P$  was calculated using Equation 7.17. In Table 7.1 and Figure 7.4, A the results of our investigations are summarized.

DGS-NTA(Ni)	$A_L$	$K_P$ GUV-FCS	$K_P$ GUV-imaging	$K_P$ LUV-FCS*
2%	$72.2\text{\AA}^2$	$2.54 \pm 0.27 \cdot 10^6$	$2.79 \pm 0.10 \cdot 10^6$	$1.33 \pm 0.23 \cdot 10^6$
3%	$72.0\text{\AA}^2$	$4.34 \pm 0.88 \cdot 10^6$	$4.56 \pm 0.34 \cdot 10^6$	$1.74 \pm 0.10 \cdot 10^6$
4%	$71.9\text{\AA}^2$	$1.54 \pm 0.11 \cdot 10^7$	$1.35 \pm 0.05 \cdot 10^7$	$1.90 \pm 0.18 \cdot 10^6$
5%	$71.8\text{\AA}^2$	$4.82 \pm 1.13 \cdot 10^7$	$3.55 \pm 0.14 \cdot 10^7$	$2.21 \pm 0.22 \cdot 10^6$

**Table 7.1** – Comparison of  $K_P$ s. Calculated partitioning coefficients by fitting all data points for increasing amounts of DGS-NTA(Ni) via the GUV and LUV methods (mean $\pm$ combined s.e.m.).

\*Differences at higher DGS-NTA(Ni) molar fraction (3-5 mol%) between GUV and LUV assays are most likely due to the increased LUVs aggregation at high DGS-NTA(Ni) molar fraction.

Identical values are gained by averaging the individual measurements and using a combined standard deviation, small variations are due to differences in sample size.

Assuming that the binding stoichiometry of eGFP-His6 coordinated to DGS-NTA(Ni) is 1:1 [203, 196], we could easily calculate the dissociation constant  $K_d$  for our system from the partitioning coefficient  $K_P$  (Equation 7.6) or directly from the slope  $a$  (Equation 7.19).

In Table 7.2 and Figure 7.4 B the values of the dissociation constant  $K_d$  are given for different contents of DGS-NTA(Ni). They correspond to the upper range of values reported in the literature, which vary from 10 nM to 10  $\mu$ M [204, 203, 205]. The  $K_d$  of the NTA(Ni)-His6 system depends in fact primarily on the NTA-backbone itself as well as on the attachment side of the His-tag. Our results clearly show that eGFP-His6 binds stronger to the membrane of the GUVs with increasing amounts of DGS-NTA(Ni) in the lipid mixtures.

DGS-NTA(Ni)	$K_d$ in M
2%	$2.18 \pm 0.23 \cdot 10^{-5}$
3%	$1.28 \pm 0.26 \cdot 10^{-5}$
4%	$3.60 \pm 0.27 \cdot 10^{-6}$
3%	$1.15 \pm 0.27 \cdot 10^{-6}$

**Table 7.2** –  $K_d$  determined by GUV-FCS assay. Calculated dissociation constants by fitting all data points for increasing amounts of DGS-NTA(Ni) via the GUV method (mean $\pm$ combined s.e.m.).

Additionally, we determined the average diffusion constants of eGFP-His6 attached to DGS-NTA(Ni) in the lipid bilayer and of Atto647N-DOPE as a control (Figure 7.5). A statistical analysis indicated a significance of deviation for the average diffusion constant of eGFP-His6 in presence of different DGS-NTA(Ni) concentrations (one-way ANOVA,  $F(3, 78) = 19.48$ ,  $p < 0.001$ ). With increasing amount of DGS-NTA(Ni), the eGFP-His6 average diffusion constant decreases from  $D = 4.36 \pm 1.12 \text{ }\mu\text{m}^2/\text{s}$  (mean $\pm$ combined s.e.m.,  $n = 548$ ) to  $D = 1.90 \pm 1.01 \text{ }\mu\text{m}^2/\text{s}$  (mean $\pm$ combined s.e.m.,  $n = 593$ ). In contrast, the average diffusion constant of Atto647N-DOPE was  $D = 9.81 \pm 0.70 \text{ }\mu\text{m}^2/\text{s}$  (mean $\pm$ combined s.e.m.,  $n = 3123$ ) and did not show any statistical significant difference (one-way ANOVA,  $F(3, 86) = 3.24$ ,  $p = 0.026$ ). The reduction of the eGFP-His6/DGS-NTA(Ni)  $D$  with increasing amounts of DGS-NTA(Ni) might be explained by a higher surface crowding of the bulky eGFP-His6 compared to the smaller labeled lipid probe Atto647N-DOPE [196].

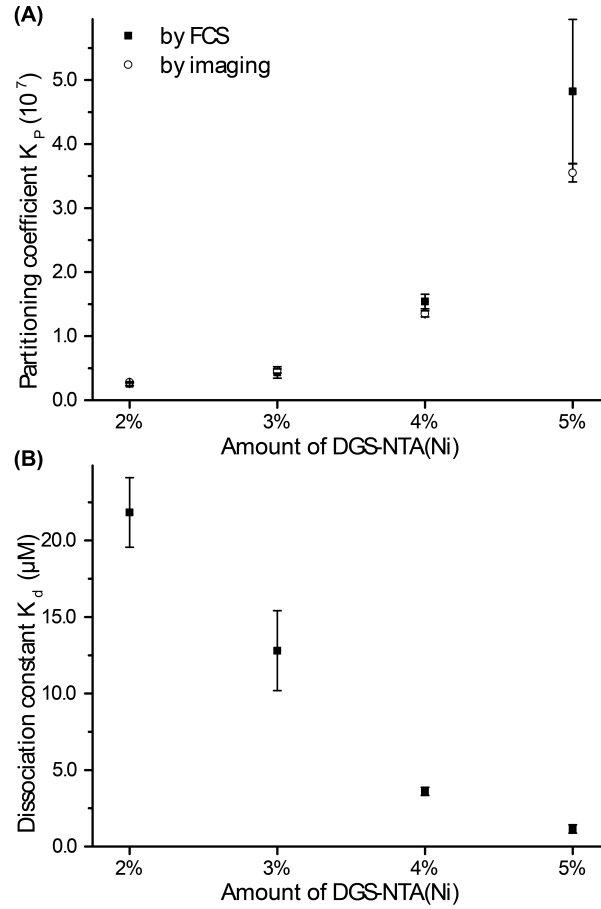


**Figure 7.4** –  $K_P$  and  $K_d$  determined by GUV assay. Graphic presentation of [A] partitioning coefficients  $K_P$ s obtained by fitting of all data points from FCS analysis (filled squares) and image analysis (circles) for a certain concentration of DGS-NTA(Ni); [B] dissociation constant  $K_d$  obtained by FCS analysis. Error bars represent the combined standard error of mean.  $K_P$  shows a stronger-than-linear behavior. Results of LUV-FCS are excluded, since they are presumably distorted by LUV aggregation (See Section 7.4).

### 7.3 GUV-imaging assay

Besides measuring FCS on the top pole of the GUVs as described in the previous paragraph, we additionally imaged the equator of the same GUVs. In Figure 3.3 A-E, the typical output of the analysis of a GUV image is shown. It is necessary to correlate only once the mean intensity obtained by image analysis to the concentration determined by another method, in our case FCS.

In Figure 7.6 example plots of all pairs of data points for 2% DGS-NTA(Ni) for  $[P_{2D}]$  and  $[P_f]$  and their corresponding mean intensities  $I_{2D}$  and  $I_f$  are shown. The slope  $b$  obtained by a linear fit does not depend on the amount of DGS-NTA(Ni), neither for the free nor for the bound eGFP-His6. Hence, the combined mean slope  $b_{2D}$  and the mean intensity of the membrane bound eGFP-His6 for a particular laser power can be used to calculate the concentration of membrane bound protein  $[P_{2D}]$ . Similarly,  $[P_f]$  can be determined using  $b_f$  and the mean intensity of the free eGFP-His6.  $K_P$ s were calculated as described for the GUV-FCS assay. The results (Table 7.1) are equivalent to those obtained with the GUV-FCS



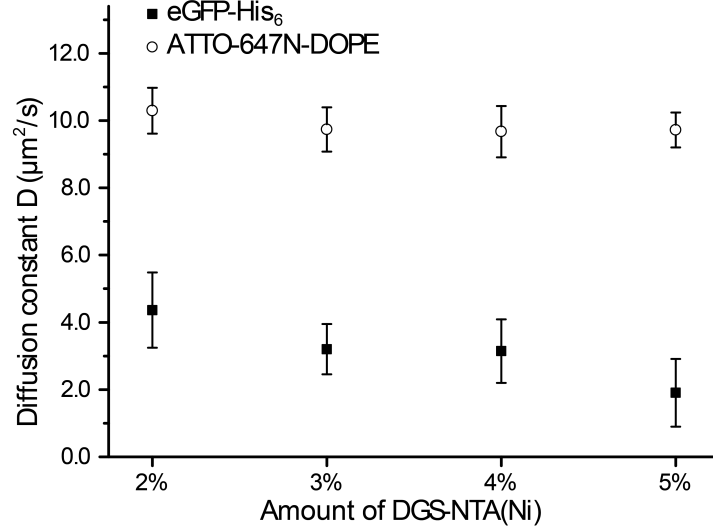


**Figure 7.5** – Diffusion coefficients determined by GUV-FCS assay.  $D_{ss}$  of the His-tagged eGFP coordinated to NTA(Ni) (filled squares) and of the fluorescently-labeled lipid Atto647N-DOPE (circles) plotted vs increasing amounts of DGS-NTA(Ni). Error bars represent the combined standard error of mean. The Atto647N-DOPE  $D$  shows no significant differences, whereas eGFP-His6  $D$  decreases with increasing amounts of DGS-NTA(Ni).

approach.

## 7.4 LUV-FCS assay

To validate our assay, we measured the affinity of eGFP-His6 for DGS-NTA(Ni)-containing vesicles with an alternative LUV-based FCS assay [74]. Here, the calculation of  $K_P$  relies on the precise measurement of the total amount  $N_{f+m}$  of eGFP-His6 particles in solution; eGFP-His6 particles can be both freely diffusing or coordinated to the DGS-NTA(Ni) embedded in the vesicles. In order to quantify the total amount of eGFP-His6 particles, we performed one-color point-FCS in solution at different time points per probe.

Before measuring each sample, the system was calibrated using Alexa488 as described for the GUV-FCS assay. The average values obtained for all measurements are  $w_0 = 205.7 \pm 1.6$  nm (mean  $\pm$  s.e.m,  $n = 15$ ) and  $V_{FCS} = 2.98 \pm 0.10 \cdot 10^{-19}$  m<sup>3</sup> (mean  $\pm$  s.e.m,  $n = 15$ ).

In contrast to the GUV-FCS assay, the amount of eGFP-His6 was kept constant and equilibrated with different LUV concentrations. In particular, eGFP-His6 was gently mixed with the vesicles and subsequently transferred to the observation chamber to assure that the protein would be evenly distributed all over the chamber and the binding equilibrium would be reached faster. Moreover, to minimize changes in the total volume of the sample, each LUV concentration was sequentially probed in a separate chamber; FCS measurements were performed always at the same distance from the bottom of the chamber to avoid any surface related dependencies [206, 207]. In these conditions background correction was not necessary, since the eGFP signal is stable and significantly higher than the background level.

The auto-correlation functions of eGFP-His6 in solution were recorded in the absence of LUVs and fitted using a 3D+T function to obtain  $[P]$  and the average diffusion time  $\tau_f = 0.96 \pm 0.05 \cdot 10^{-4}$  s ( $D = 110 \pm 7$  μm<sup>2</sup>/s; mean  $\pm$  combined s.e.m.; 26.0  $\pm$  0.5°C), respectively.

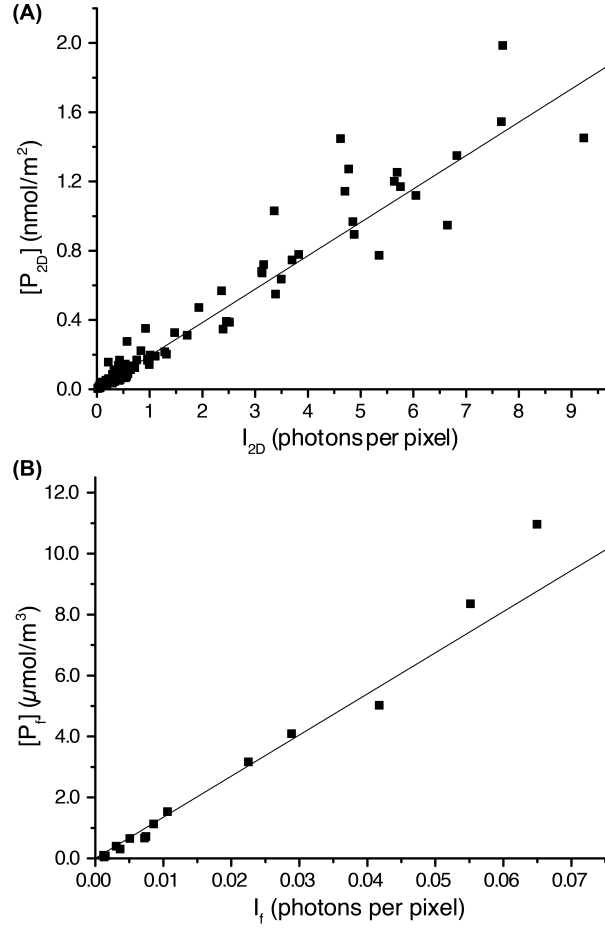


**Figure 7.6** – Calibration curve for GUV-image analysis. Mean intensities obtained by image analysis plotted against concentrations determined by FCS [A] on the membrane and [B] in solution for all 2% DGS-NTA(Ni) samples. Both curves show a linear behavior and the slopes  $b_{2D}$  and  $b_f$  are used to calculate the protein concentrations directly from the mean intensities.

The auto-correlation functions of eGFP-His6 in presence of increasing amounts of LUVs were fitted with a two component 3D+T function, keeping  $\tau_f$  constant, to get the total number of eGFP-His6 particles  $N_{f+m}$ . As expected, the eGFP-His6 diffusion time increases upon binding to LUVs (Figure 7.7, A), as far as the vesicles are significantly larger than the protein. At the same time,  $N_{f+m}$  decreases, meaning that more than a single eGFP-His6 molecule bind each LUV. At higher LUVs concentration  $N_{f+m}$  starts increasing again to reach the original value of freely diffusing eGFP-His6, suggesting that upon further addition of LUVs the eGFP-His6 molecules redistribute so that the probability of more than one eGFP-His6 binding to one LUV is negligible (Figure 7.7, B).

From the total number of eGFP-His6 particles values measured in at least three independent samples (e.g. Figure 7.7, B), a  $G(0)$  was calculated for each LUV concentration and normalized to the  $G(0)$  in absence of LUVs. The data points were then fitted with Equation 7.26 to obtain  $K_d$  for a particular percentage of DGS-NTA(Ni) in the lipid mixture. The protein and accessible lipid concentration values used for the fit were determined experimentally. The total protein concentrations were calculated from the number of eGFP-His6

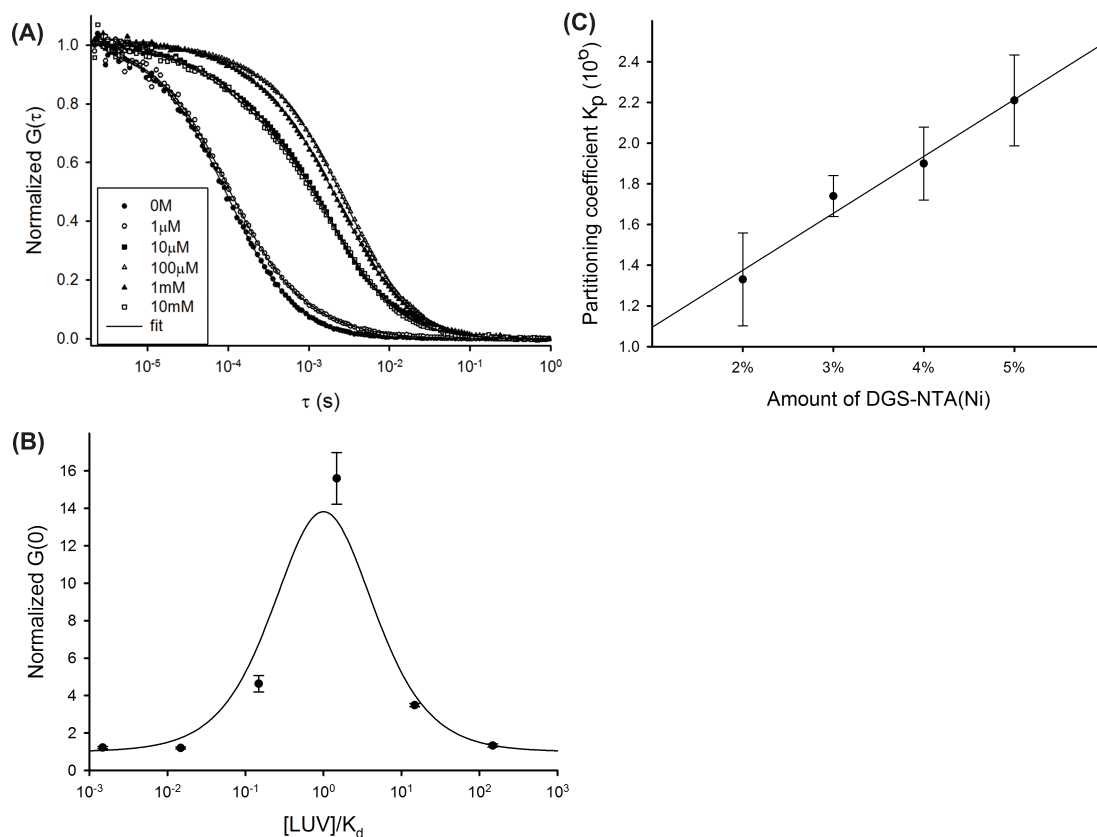


**Figure 7.7** – LUV-FCS assay. [A] Auto-correlation curves obtained in solution for eGFP-His6 in absence (0 M) and presence of increasing amounts of LUVs (1  $\mu$ M, 10  $\mu$ M, 100  $\mu$ M, 1 mM, and 10 mM). Solid lines are the best fit of the data to a single (0 M) or two-components (all other curves) 3D diffusion model. [B] Normalized  $G(0)$  data points for a single 2% DGS-NTA(Ni) sample are plotted against the ratio  $[LUV]/K_d$ . The solid line is the best fit of the data to Equation 7.26. [C] Graphic presentation of partitioning coefficients  $K_P$ s calculated from  $K_d$  (Equation 7.27) by a combined fit of all data points for each DGS-NTA(Ni) concentration.

particles measured by FCS in absence of LUVs, whereas the accessible lipid concentrations were obtained measuring both the total lipid concentrations and vesicle sizes (see Chapter 2 for details). The dissociation constant  $K_d$  values were finally transformed into  $K_P$  values for comparison applying Equation 7.27 (Figure 7.7, C).

## 7.5 Comparison of methods

In both GUV based approaches, GFP-His6 shows a strong affinity for the membrane, which derives from the nature of the His-tag NTA(Ni) chelation, which is not purely electrostatic, but involves the formation of a more stable coordination bond. GFP-His6 affinity for the membrane clearly increases with higher contents of Nickel-lipid in the bilayer in a stronger-than-linear fashion. B. Ernst and colleagues analyzed the binding/dissociation of different oligo-His-tags to NTA(Ni) [196] and showed that for high surface densities of NTA(Ni) a rebinding effect plays an important role. Under these conditions eGFP-His6 might interact

with several DGS-NTA(Ni) [208, 209]. Hence, for higher DGS-NTA(Ni) contents, the equilibrium is strongly shifted to the bound fraction, resulting in stronger-than-linear increase of  $K_P$ . The LUVs assay failed to capture this trend.

The results obtained for GUVs and LUVs containing equal amounts of DGS-NTA(Ni) are shown in Table 7.1. At low DGS-NTA(Ni) molar fraction (2 mol%), the  $K_P$ s measured with both GUV- and LUV-methods differ by a factor of two (GUV-method:  $2.51 \pm 0.19 \cdot 10^6$ ; LUV-method:  $1.33 \pm 0.23 \cdot 10^6$ ), whereas at higher DGS-NTA(Ni) molar fraction (3-5 mol%) they differ up to one order of magnitude. We assume that the observed differences are an artifact of the LUV-FCS method, due to LUV aggregation, which increases with DGS-NTA(Ni) molar fraction. It was shown that vesicles containing DGS-NTA(Ni) can aggregate after addition of synthetic peptides with poly-histidine residues and that the aggregation is dependent on the DGS-NTA(Ni) amount present in the vesicles [210]. Vesicle aggregation causes partial loss of the vesicles available for the eGFP-His6 to bind, thus apparently reducing its affinity. On the other hand, in both GUVs based approaches, the protein and accessible lipid concentrations need to be carefully chosen in order to measure precisely in solution and at the membrane. For high binding affinities, the concentration at the membrane could be already high while there are no detectable amounts of proteins in solution. Interestingly the GUV-FCS approach appears to be less precise than the GUV-imaging one, as shown by the relatively high error bars for  $[P_{2D}]$ . This can be explained taking into account how the free protein concentration is measured in the FCS and imaging approaches, only once for the whole chamber and close by each GUV, respectively. Technically it should be enough to measure the free protein concentration once, but more precise values can be determined with the GUV-imaging approach. The precision of the GUV-FCS assay could be improved measuring FCS in solution next to each GUV, but this would almost double the measuring time.

	GUV-FCS	GUV-imaging	LUV- FCS
Measurement time per sample	5 h	2 h	2h
Accuracy/Precision	High/Low*	High/High	Low**/High
Accessible lipid concentration	$10^{-9}$ - $10^{-6}$ M	$10^{-9}$ - $10^{-6}$ M	$10^{-6}$ - $10^{-3}$ M [74]
Protein concentration	$10^{-9}$ - $10^{-6}$ M	$10^{-8}$ - $10^{-4}$ M	$10^{-9}$ - $10^{-6}$ M [74]

**Table 7.3** – Comparison of methods.\*if the free protein concentration is calculated only once; \*\*for protein exhibiting rebinding effect.

Importantly, both GUV based approaches possess the advantage over the LUV method of directly visualizing the binding event and thus of being able to correct anomalies in the sample. Having an overview of the whole chamber, it is possible to select and continuously measure the same GUVs after repeated protein additions as well as to discard samples with unevenly distributed eGFP-His6 within the chamber or samples in which the lipid concentration varies over the measuring time (i.e. due to GUVs burst). Moreover, the lipid dynamics of each GUV can be probed simultaneously, thus adding a further control point.

Finally, one should consider the actual measurement time of each of these assays. In order to be able to precisely measure the average number of particles as well as the diffusion time in the GUV-FCS approach, it is necessary to collect data over a time period of several minutes. Thus, the time for an experiment easily sums up when averaging several GUVs per protein concentration. On the other hand, in both GUV-imaging and LUV-FCS assays the actual measurement time reduces to less than two hours, while having approximately the same work

load for calibration and data treatment.

The experimental work presented in Chapter 8 was inspired by the collaboration with the research group of Prof. Tony Hyman, in particular with Dr. Carsten Hoege (Max Planck Institute of Molecular Cell Biology and Genetics, Dresden, Germany); and designed together with Prof. Petra Schulle (Max Planck Institute of Biochemistry, Martinsried, Germany).

Part of the measurements presented in Table 8.1 and Figure 8.4 were performed by Lisa Tübel during her traineeship and submitted as a project report to the Berufskolleg für Biotechnologie (Staatsschule für gartenbau und landwirtschaft, Landwirtschaftliche Schule Hohenheim, Stuttgart, Germany).

Measurements and data analysis presented in Figure 8.5 and 8.6 were performed under the guidance of Elisabeth Weyher-Stingl (Biochemistry Core Facility of the Max Planck Institute of Biochemistry, Martinsried, Germany).

## Chapter 8

# Reconstitution of a functional LGL/aPKC membrane binding switch

In the PAR polarization process two subsequent steps can be distinguished: a symmetry breaking or establishment phase and a maintenance phase [211]. aPARs are originally distributed throughout the cortex whereas pPARs are predominantly in the cytoplasm. The symmetry breaking is initiated by an asymmetric contraction of the actomyosin cortex which generates a cortical flow that carries the aPARs toward the anterior pole of the cell. The displacement of aPARs by cortical flows allows pPARs to load on the posterior cortex. pPARs can also access the posterior cortex in absence of cortical flows via a mechanism that involves a temporary interaction between the microtubules nucleated by the paternal centrosome and PAR-2 [91]. The maintenance phase is instead governed by a complex set of interactions among the PAR proteins: aPARs and pPARs reciprocally antagonize their binding to the cortex, mutually excluding each other, as well as promote their own binding to the cortex and activation, generating positive feedback loops. The details of these interactions are described in several recent reviews, which summarized the experimental and modeling work of the last three decades [11, 212, 213].

Several mathematical models have been developed to help describing the emergence of polarity in the *C. elegans* embryos [214, 215, 216, 217]. Besides individual differences, all models are based on a reaction-diffusion system with bistable kinetics [28], in which the anterior and posterior PARs, taken as two single entities, shuffle between an active slow diffusing membrane-bound and an inactive fast diffusing cytosolic form. Tostevin and Howard assumed both mutual exclusion and cooperative binding of both aPARs and pPARs in their model, and introduced a contracting actomyosin cortex on top of it. aPARs are assumed to have higher affinity for the cortex and at the same time promote its contraction [214]. Goehring and colleagues [216] combined mutual exclusion with cytoplasmic depletion of the unbound PARs and, similarly to Tolstevin and Howard, introduced a cortical flow to account for the symmetry breaking. In this model, the aPARs do not exhibit an higher affinity for the contracting cortex, but are advectively transported by the flowing cortex. Even if both models are based on experimental evidences and measurements, they do not account for the observation that actomyosin asymmetry is not essential for symmetry breaking [91]. The model of Dawes and Munro on the other hand generates stable PAR domains without an

actomyosin, allowing aPARs to dimerize and thus introducing nonlinearity in the mutual exclusion mechanism [215]. In agreement with this model, PAR-3 has an oligomerization domain that is important for the localization and activity of the aPARs complex [218].

Taken together, experimental and modeling findings suggest that the PAR system does not rely only on the mutual exclusion of the aPARs and pPARs to robustly polarize the *C. elegans* embryos; redundancy of the symmetry breaking inputs and positive feedback loops are required to make the system more robust [5] and to buffer the network from imprecisions in the aPARs/pPARs balance [11]. The tumor-suppressor protein LGL is the main player of one of these redundant circuits [26].

In *C. elegans* embryos LGL-1 acts redundantly with PAR-2 to maintain polarity and can compensate for PAR-2 depletion [14, 15]. In contrast to PAR-2, which is only found in the genus *Caenorhabditis* [219], LGL is highly conserved in eukaryotes [26] where it takes over the role of PAR-2 in counteracting the action of the aPARs. The domain structure of LGL proteins is also well conserved; the N-terminal part of the protein contains multiple WD40 domains which fold into  $\beta$ -propeller structures providing a docking platform for interaction with multiple proteins [26]. In *Drosophila* for example the N-terminal WD40 domain-containing part of LGL was predicted to fold into two  $\beta$ -propeller structures [220], and has been shown to interact with both the C-terminus of LGL itself as well with PAR-6 [221, 222]. The C-terminal part of LGL consists of an LGL-specific domain which contains several conserved sites for serine and/or threonine phosphorylation by aPKC [26]. It was proposed that the not phosphorylated LGL is the active form of the protein and it assumes an open conformation, whereas the phosphorylated LGL is inactive because its C-terminus interacts intramolecularly with the N-terminus closing the protein in an auto-inhibitory state [220].

Interestingly LGL-1 and PAR-2 share several common features in the *C. elegans* early embryos: they both localize to the posterior cortex, their activity is regulated by PKC-3 phosphorylation, and they can displace anterior aPARs from the posterior cortex [11]. PAR-2 acts indirectly, recruiting PAR-1 to the membrane [13, 91], which phosphorylates PAR-3 on a conserved site in the C-terminal domain [223]; whereas LGL-1 is thought to act directly on PAR-6. LGL-1 in fact has been shown to bind PKC-3 and PAR-6 in immunoprecipitation assay [14] and to lower both cortical and cytoplasmatic PAR-6 levels [224]. Based on these data two non exclusive models emerged. On one hand, Hoege and colleagues proposed the so called “mutual elimination model”, in which the PAR-6/PKC-3/LGL-1 complex is formed at the boundary between the aPARs and pPARs domains, where PKC-3 can phosphorylate LGL-1 causing the whole complex to leave the cortex [14]. On the other hand LGL-1 could act as a buffer against the expansion of the aPARs domain [224], similarly to the mechanism described for the peripheral nervous system of *Drosophila* [225]. Even if evidences supporting or contradicting one or the other model are accumulating, the molecular mechanism of LGL remains elusive.

In this chapter we focus on the cortex localization of LGL-1. We identified a region of the protein that can directly bind negatively charged membranes. The binding specificity depends on a stretch of positively charged amino acids surrounding the PKC-3 phosphorylation sites. Differently from what described for the Myristoylated Alanine-Rich C Kinase Substrate (MARCKS) effector domain peptide, which is unstructured and elongated both in solution and when bound to membranes [226, 128], the LGL-1 MTS folds in an helical conformation upon membrane binding. In the membrane bound helix, three regions can be identified: a positive charged area responsible for the lipid specificity, a switch area containing the three PKC-3 phosphorylation sites and a hydrophobic area which is probably buried in



the membrane. Phosphorylation reduces dramatically the binding affinity of the LGL-1 MTS to negatively charged model membranes inducing its detachment. We were able to directly visualize the phosphorylation-induced detachment of the LGL-1 MTS in GUVs as well as to determine its partitioning coefficient  $K_P$  with two independent approaches.

## 8.1 LGL-1 directly binds membranes containing negatively charged lipids via a stretch of basic amino acids

It was recently shown that PAR-2 can interact with phospholipids and in particular with phosphoinositides [91]. *In vivo* localization of PAR-2 to the posterior cortex depends on a central domain rich in basic amino acids, suggesting that PAR-2 uses electrostatic interactions to interact with phospholipids at the plasma membrane [227, 11].

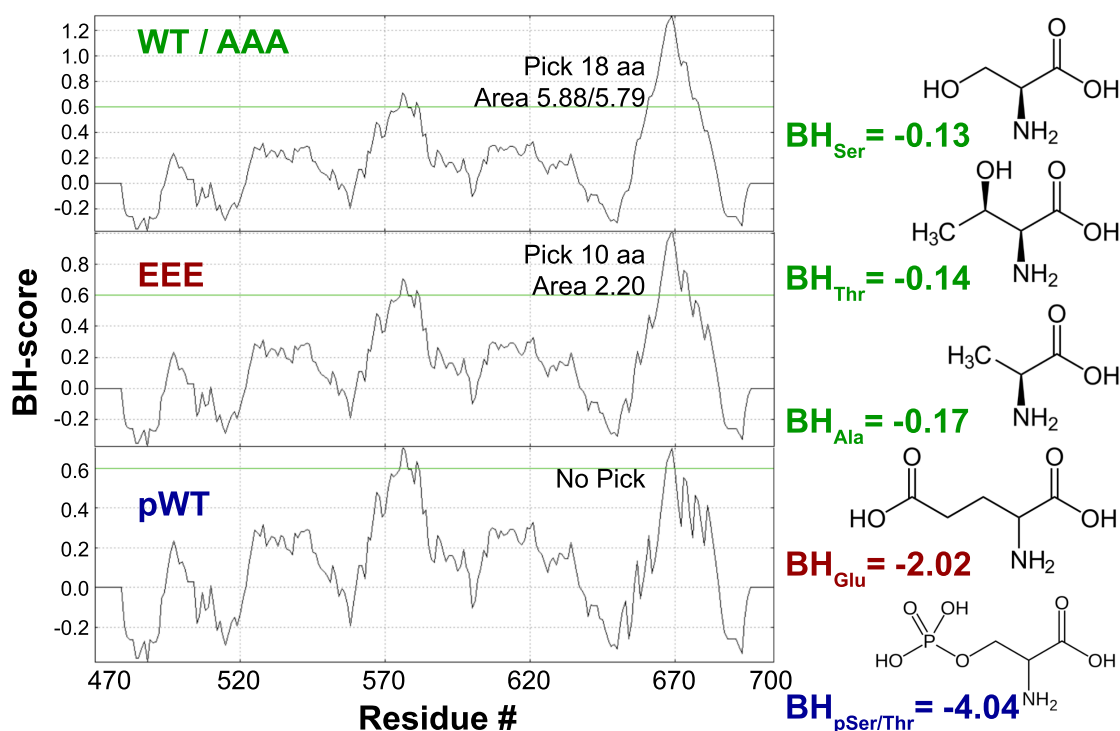


**Figure 8.1** – BH-search identified a putative membrane binding region in LGL-1. BH-search score plots for LGL-1 WT, nonphosphorylatable AAA mutant, phosphomimetic EEE mutant and fully phosphorylated LGL-1 are reported. Pick length in number of amino acid (aa) and area are given next to the identified region. The BH parameters used for selected amino acids are shown next to the corresponding chemical structures.

We hypothesized that LGL-1 uses a similar mechanism to localize to the cell cortex. To identify putative membrane binding regions in LGL-1, we analyzed its sequence with an experimentally-based search program (BH-search) which is able to identify unstructured membrane-binding sites [228]. LGL-1 in fact possesses neither hydrophobic membrane-penetrating segments nor lipid-binding domains with highly defined tertiary structures. BH-search identified a single region in the LGL-1 protein which can putatively bind membranes

(Figure 8.1; WT, Peak 1: 659-FKSLKKSLRKTFRKKKG-676 (18 aa), area 5.88). Interestingly, this region contains the three phosphorylation sites for PKC-3 (S661/S665/T669) and, similarly to PAR-2, is rich in positively charged amino acids (7K, 3R).

In order to experimentally confirm that this region is able to directly bind phospholipids, a fragment of LGL-1 corresponding to the part of the C-terminal LGL-specific domain which contains the PKC-3 phosphorylation sites (469-702) was expressed in *E. coli* as a fusion protein with eGFP-His6. The endings of the fragment were chosen based on a previous solubilization screening (Dr. Carsten Hoege, personal communication). The purified LGL-1(469-702):eGFP-His6 fragment was incubated with GUVs containing different lipid mixtures and imaged with a CLSM. LGL-1(469-702) did not bind to GUVs containing pure DOPC (Figure 8.2, A), but it bound to GUVs doped with different negatively charged phospholipids (Figure 8.2, C-F). The relative amount of each negatively charged lipid was chosen in order to maximize the overall GUV charge and to keep it constant [229]. As a positive control we used GUVs doped with DGS-NTA(Ni) (Figure 8.2, B), which is able to bind His6 tagged proteins [230]. Among several acidic phospholipids screened, LGL-1(469-702) was found to bind to GUVs containing phosphatidylserine or PIP2, the most abundant phospholipid and phosphoinositide of the cytosolic side of the cell membrane, as well as phosphatidylglycerol or cardiolipin, which do not normally belong to the plasma membranes. These findings support the hypothesis that LGL-1, analogously to PAR-2, localizes to the membrane interacting electrostatically with negatively charged phospholipids through a MTS containing a stretch of positively charged amino acids.

### 8.1.1 The position of the basic amino acids modulate LGL-1 membrane binding specificity

We further investigate the role of the positively charged amino acids of the LGL-1 MTS observing the effect of selected mutations on membrane binding. In a membrane yeast two-hybrid screening [231] the positive charged amino acids of the LGL-1 MTS were systematically mutated and only two mutations R658A/K660A and RR671AA were found to compromise the yeast growth at a higher temperature (Dr. Carsten Hoege, personal communication). LGL-1(469-702):eGFP-His6 carrying a combined quadruple mutation R658A/K660A/RR671AA (LGL-1-AAAA) was incubated with SLBs containing pure DOPC or DOPC doped with either DOPS or bPI(4,5)P2. Upon binding, the fluorescence signal at the level of the SLB membrane is maximized while the fluorescence signal in the buffer above the membrane decreases (Figure 8.3, A). Z-scans of several region of each SLB were acquired with CLSM and fluorescence intensity values at the membrane were extracted from the picks in the z-stack intensity profiles. Interestingly the LGL-1-AAAA mutant maintains the ability to bind DOPS-containing membranes, whereas its binding to bPI(4,5)P2-containing membranes decreases (Figure 8.3, B: WT =  $5.83 \pm 0.81$ , AAAA =  $3.00 \pm 0.98$ ). These data suggest that the positively charged amino acids in the LGL-1 MTS are not only contributing to the membrane binding with their charges, but also with their individual positions, which may enable the binding to specific phospholipids, i.e. phosphoinositides.

### 8.1.2 LGL-1 binds preferentially PIP2-containing membranes

Besides numerous well characterized globular domains which bind, more or less specifically, acidic phospholipids at the membrane surface [232], short basic amino acids sequences are also

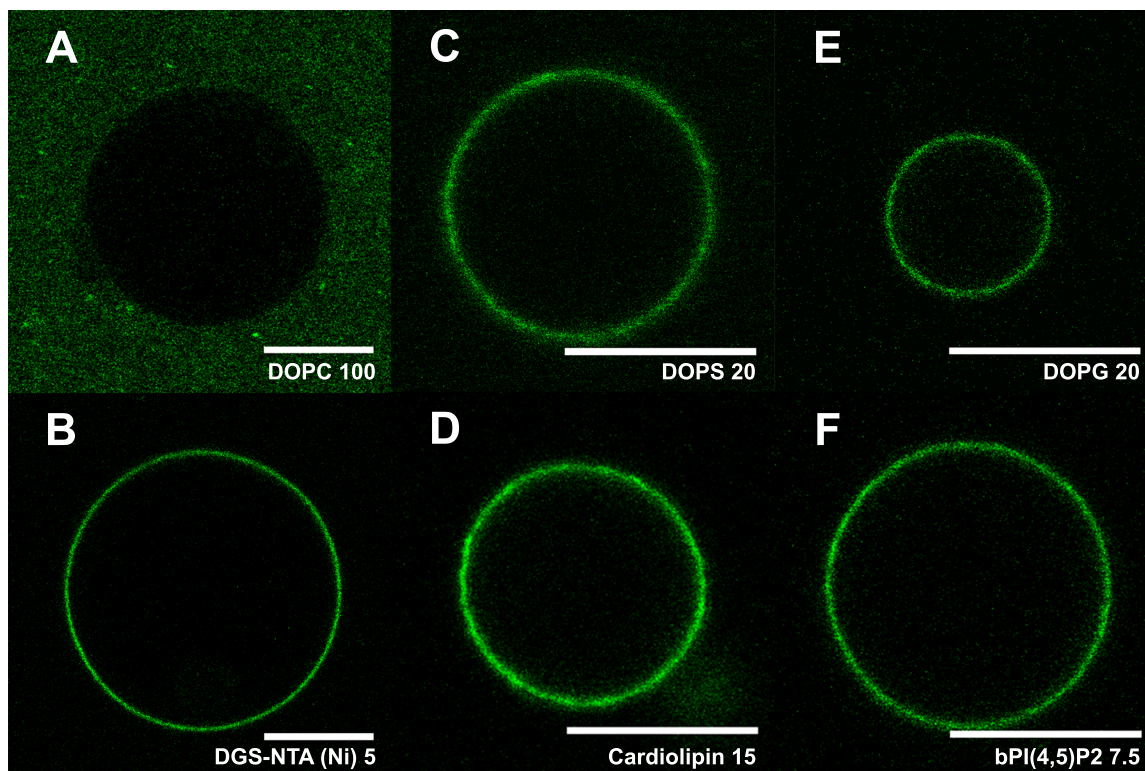


**Figure 8.2** – LGL-1 binds GUVs containing negative-charged lipids. LGL-1(469-702):eGFP-His6 was expressed in *E. coli*, purified and incubated with GUVs containing different lipid mixtures: [A] DOPC 100; [B] DOPC:DGS-NTA(Ni) 95:5; [C] DOPC:DOPS 80:20; [D] DOPC:Cardiolipin 85:15; [E] DOPC:DOPG 80:20; [F] DOPC:bPI(4,5)P2 92.5:7.5. GUVs were imaged at the equator with a confocal laser scanning microscope. Scale bars are 10  $\mu\text{m}$ .

known to interact electrostatically with phosphoinositides. As an example, the unstructured basic effector domain of MARCKS binds with high affinity but little headgroup specificity PI(4,5)P2 to form an electroneutral complex [233, 234]. In order to determine if the LGL-1 MTS binds phosphoinositides and in particular PI(4,5)P2 with higher affinity than other acidic phospholipids we incubate a peptide corresponding to the LGL-1 MTS with DOPC LUVs containing DOPS or phosphoinositides and measured their electrokinetic potential ( $\zeta$ ) at different peptide concentrations.  $\zeta$ -potential is not a direct measure of a particle charge, but it is used to quantify its magnitude [235]. The  $\zeta$ -potential is defined as the electric potential that exists at the slipping plane, that is, the boundary within the diffuse liquid layer surrounding a particle, beyond which the movements of the particle and its counterions are decoupled [236]. It was recently demonstrated that  $\zeta$ -potential can be used to determine binding affinities of positively charged peptides to negatively charged liposomes [107]. The rationale behind this approach is simple: the more peptide binds to the vesicles, the higher the  $\zeta$ -potential of the vesicle-peptide complex becomes until it eventually reaches zero or positive values. Care was taken to ensure that no vesicle aggregation took place in the peptide concentration range used and during the measurements. For this reason, the particle size was checked with DLS before and after addition of the peptide (Figure 8.4, A) as well as at the end of the measurement runs. The particle size and Polydispersity Index (PdI) increase with higher LGL-1 MTS concentrations (Table 8.1), due to the increasing amount of peptide

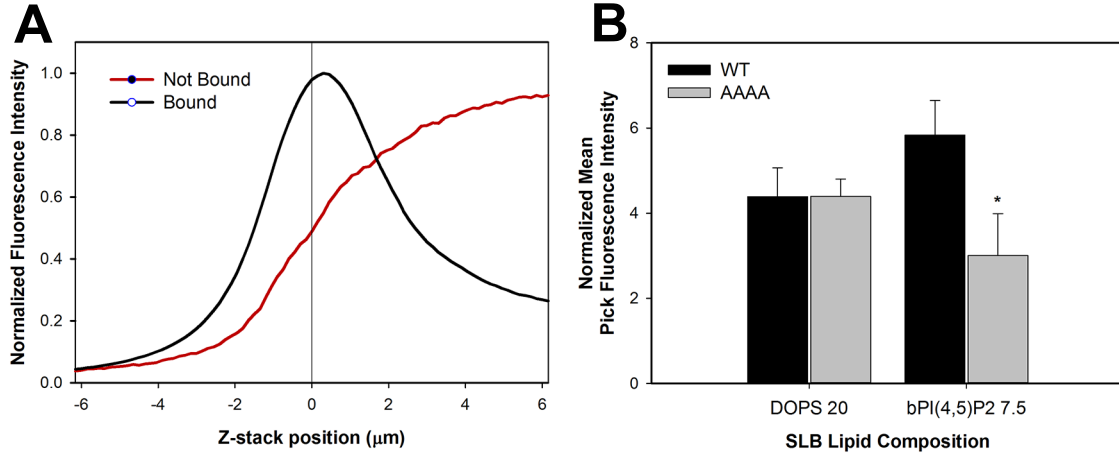


**Figure 8.3** – LGL-1-AAAA binds bPI(4,5)P2-containing membranes less than LGL-1-WT. LGL-1(469-702):eGFP-His6 R658A/K660A/RR671AA (LGL-1-AAAA) was incubated with SLBs containing different lipid mixtures: DOPC 100, DOPC:DOPS 80:20, and DOPC:bPI(4,5)P2 92.5:7.5. [A] Typical z-scans intensity profiles acquired with CLSM for LGL-1 bound (black) or not bound (red) to the SLB. [B] LGL-1 fluorescence intensity values at the membrane were extracted from the picks in z-stack intensity profiles, background corrected, averaged and normalized by the value obtained in SLBs containing DOPC only. \*t-test,  $t(4)=3.84$ ,  $p=0.02$

bound to the vesicles and due to the presence of vesicles with different amounts of peptide bound, respectively.

LGL-1 MTS Concentration [ $\mu\text{M}$ ]	Particle Size [nm]	PdI
0.00	120.33 $\pm$ 6.72	0.09 $\pm$ 0.04
0.50	132.19 $\pm$ 4.17	0.11 $\pm$ 0.02
1.00	137.97 $\pm$ 8.19	0.13 $\pm$ 0.04
2.00	159.67 $\pm$ 23.61	0.15 $\pm$ 0.03
4.00	175.61 $\pm$ 29.50	0.13 $\pm$ 0.03
8.00	162.04 $\pm$ 32.15	0.16 $\pm$ 0.05

**Table 8.1** – Particle Size and polydispersity index values. Particle Size and PdI for LUVs in absence and presence increasing concentration of LGL-1 MTS.

For the LGL-1 MTS peptide the  $\zeta$ -potential does not increase linearly with increasing peptide concentrations (Fig. 1.4, B), thus the mathematical model proposed by Freire and colleagues [107] could not be used to fit our data and obtain a partition coefficient. An alternative mathematical model was used to fit the  $\zeta$ -potential curves and an apparent binding constant  $K_B$  was obtained [237] (Figure 8.4, B). The peptide shows the highest  $K_B$ s for PI(3,4)P2 and PI(4,5)P2 containing LUVs, followed by PI(3,5)P2, the three monophosphoinositides, PI(3,4,5)P3 and DOPS (Figure 8.4, C). Interestingly, in both PI(3,4)P2 and PI(4,5)P2 the phosphate groups seats in two adjacent positions of the inositol ring. The ionization behavior of the phosphoinositides is known to be linked to the specific position of the phosphate groups and most importantly to the ability of a protein to target a specific membrane environment [238]. Similarly to the basic effector domain of MARCKS, LGL-1 MTS  $K_B$ s for PIP2 are in the  $\mu\text{M}$  range [74], however the  $K_B$  for DOPS is higher, resulting in an even less pronounced headgroup specificity; the affinity for PI(3,4)P2 and PI(4,5)P2 is

in fact approximately one order of magnitude higher than for DOPS. Nevertheless PI(4,5)P2 is most probably the *in vivo* partner of LGL-1: the PI(4,5)P2 generating enzyme PPK-1 is in fact posteriorly enriched in the *C. elegans* embryos, suggesting that PI(4,5)P2 localized synthesis contributes to the polarized distribution of LGL-1 [239]. More generally PI(4,5)P2 is the most abundant phosphoinositide of the inner leaflet of the plasma membrane and is normally targeted by phosphoinositide recognition domains with low headgroup specificity [232].

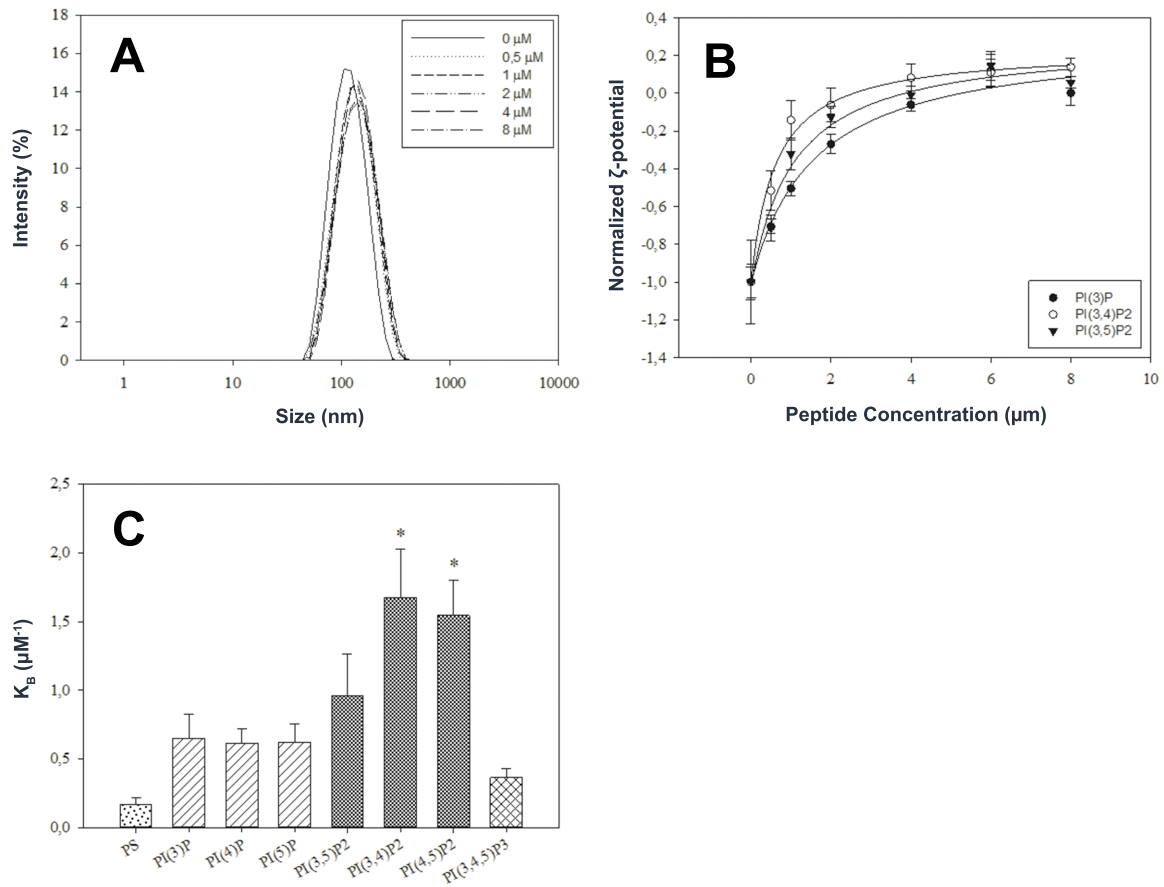


**Figure 8.4** – LGL-1 MTS binds preferentially PIP2-containing membranes. LGL-1 MTS was incubated with DOPC LUVs containing different acidic lipids: DOPS 5%, PI(3)P, PI(4)P or PI(5)P 2.5%, PI(3,4)P2, PI(3,5)P2 or PI(4,5)P2 1.67%, and PI(3,4,5)P3 1.25%. The relative amount of each negatively charged lipid was chosen in order to keep the over all LUVs charge constant at 5%. [A] Typical Intensity Particle Size Distribution (PSD) plot acquired for vesicles in absence (continuous line) or presence (dashed lines) of increasing concentration of LGL-1 MTS. [B] ζ-potential mean values obtained for PI(3)P, PI(3,4)P2 and PI(3,5)P2 at increasing LGL-1 MTS concentration; the values were normalized by the value obtained in absence of peptide and fit to Equation 3.7 to get the apparent binding constant  $K_B$ . [C] Mean  $K_B$ s values obtained for each lipid mixture (one-way ANOVA,  $F(7, 359)=6.62$ ,  $p<0.001$ ). Holm-Šídák post-hoc comparisons confirmed that the presence of either PI(3,4)P2 and PI(4,5)P2 in the LUVs maximize LGL-1 MTS  $K_B$  (\* $p<0.05$  for all comparisons except with PI(3,5)P2).

### 8.1.3 LGL-1 MTS fold into an $\alpha$ -helix upon binding to negatively charged membranes

We next investigate the conformation of the LGL-1 MTS at the membrane. To do so we measured the circular dichroism of the corresponding peptide in absence and present of SUVs containing different acidic lipids. Although it was reported that accurate circular dichroism spectra can be collected in the presence of LUVs [240], in our hands the light scattering was too high to allow reliable measurements. In circular dichroism buffer or in presence of pure DOPC vesicles, to which the peptide does not bind, LGL-1 MTS shows a clear random coil circular dichroism spectra with a residual  $\alpha$ -helicity of about 7% (Figure 8.5, A; red line). In order to check if the peptide has a propensity to fold into an  $\alpha$ -helix, we acquired the circular dichroism spectra of the peptide in TFE, which is known to stabilize secondary structure strengthening the peptide H-bonds [241]. In TFE, LGL-1 MTS shows a clear  $\alpha$ -helix circular dichroism spectrum with the two characteristic minima at 208 and 220 nm (Figure 8.5, A; blue line). The  $\alpha$ -helix content was estimated to be ca. 66%. Similar circular dichroism spectra were obtained when the LGL-1 MTS peptide was mixed with SUVs containing acidic lipids (Figure 8.5, A; green/gray/yellow lines). The estimated  $\alpha$ -helix content increases with increasing vesicle:protein ratios (Figure 8.5, B), strongly suggesting that the peptide fold into an  $\alpha$ -helix upon binding to negatively charged vesicles. The isodichroic point in this type of circular dichroism spectra indicates that there are only two peptide populations: disordered in solution and largely helical at the membrane [186].

This behavior was previously described, among others, for melittin [186]. On the other side, LGL-1 MTS conformation is different from what described for the basic effector domain of MARCKS, which binds the membrane in an extended conformation with the five Phe residues penetrating to the level of the acyl side chains [74].

## 8.2 Phosphorylation by aPKC abolishes the binding of LGL-1 to negatively charged membranes

LGL-1 activity in *C. elegans* is regulated by PKC-3 phosphorylation. More specifically, the nonphosphorylatable LGL-1 mutant in which the three PKC-3 sites were mutated to alanines (AAA) is not restricted to the posterior pole anymore, but localizes uniformly to the whole cortex; whereas the phosphomimetic LGL-1 mutant, in which the three PKC-3 sites were mutated to glutamates (EEE), is unable to associate with the cortex, even in the absence of a functional PAR complex [14]. Having demonstrated that LGL-1 can directly bind lipid membranes, we hypothesized that the phosphorylation by PKC-3 interferes with its membrane binding ability. This hypothesis was initially supported by the results obtained with the BH-search program. When the sequences of the AAA and EEE mutants are fed into the search program, two different outcomes are generated. The AAA mutant score does not substantially differ from the LGL-1 WT (Figure 8.1, AAA, : 659-FKSLKKSLRKTFRRKKKG-676 (18 aa), area 5.79), whereas the EEE mutant shows a shorter sequence and a lower pick area (Figure 8.1, EEE, : 663-KKSLRKTFRR-672 (10 aa), area 2.20). BH parameters are not available for phosphoserine and phosphothreonine, but are expected to be similar to the glutamate value if not more negative, that is, unfavorable for membrane localization. We therefore introduced a customized parameter for phosphoserine and phosphothreonine. A value of -4.04 was enough to completely loose the potential membrane binding site (Figure 8.1, pWT). These data

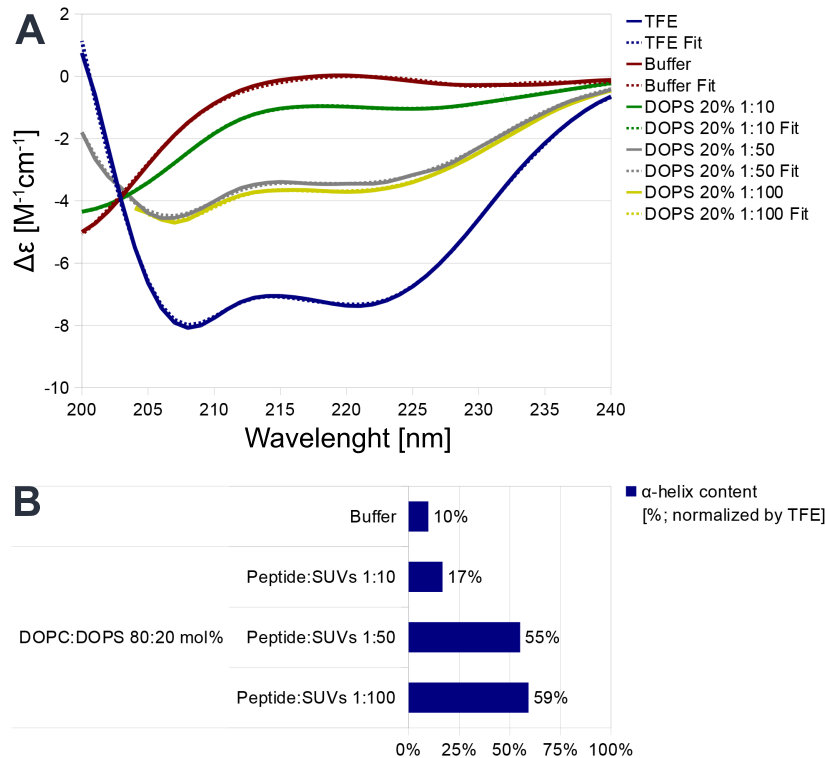


**Figure 8.5** – LGL-1 MTS fold into an  $\alpha$ -helix upon binding to negatively charged membranes. [A] Circular dichroism spectra (data, continuous lines; fits, dashed lines) of LGL-1 MTS in circular dichroism buffer, TFE and in presence of different protein:lipid ratios of DOPC:DOPS 80:20 SUVs; [B]  $\alpha$ -helix content estimated with the CONTIN method was normalized by the value obtained in TFE and plotted for each spectrum in A.

suggest that phosphorylation should change the membrane affinity of LGL-1 substantially.

### 8.2.1 Phosphomimetic LGL-1 does not bind SUVs containing negatively charged lipids

To prove this point we performed parallel experiments in different membrane model systems. We first repeated the SUV binding assay with purified LGL-1 proteins which carried either the AAA or the EEE mutation. Similarly to what described for the LGL-1 WT, we incubated the LGL-1 mutants with SUVs containing DOPC:bPI(4,5)P2 92.5:7.5 and imaged them with CLSM. As expected LGL-1 AAA retains its ability to bind SUVs containing PI(4,5)P2, whereas EEE does not. (Figure 8.7).

### 8.2.2 LGL-1 can be phosphorylated *in vitro* by the human PKC- $\zeta$

We next worked with *in vitro* phosphorylated LGL-1. In order to confirm that LGL-1 can be phosphorylated *in vitro* by PKC- $\zeta$  [221] and to optimize the phosphorylation conditions, we visualized the incorporation of radiolabeled phosphate groups in the LGL-1 MTS peptide via autoradiography (Figure 8.8). When the Protein Kinase C (PKC) phosphorylation serines/threonines were mutated, the radiolabeled phosphates groups could



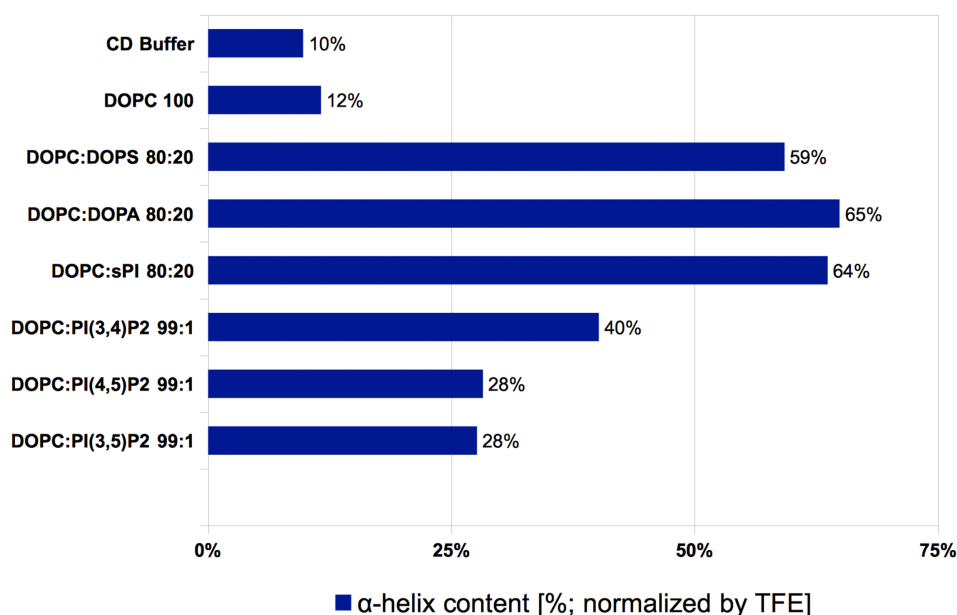


**Figure 8.6** – LGL-1 MTS  $\alpha$ -helix content. The  $\alpha$ -helix content was estimated with the CONTIN method for each lipid mixtures at 1:100 protein:lipid ratio, normalized by the value obtained in TFE and plotted.

not be incorporated, thus the phosphorylation did not take place. The corresponding LGL peptide in *D. Melanogaster* covering the amino acid positions 651 to 676 (651-LSRRKSFKKSLRESFRKLRKGRSTRT-676) was reported to inhibit the kinase activity of the associated aPKC enzyme [242]. Our data clearly show that the LGL peptide is not an inhibitor of aPKC, but a substrate. The LGL peptide in the experiments of Kalmes and colleagues acted most probably antagonistically to the full length protein, being a more accessible phosphorylation target for the aPKC.

### 8.2.3 Phosphorylation of LGL-1 inside GUVs induce its detachment from the vesicle membrane

Both phosphorylated and not phosphorylated LGL-1 MTS peptides were encapsulated in GUVs using the droplet transfer method originally described by Pautot and colleagues [51]. For these experiments we used DOPS instead of PI(4,5)P2 because the amount of lipids required is too high to keep the price per experiment at a reasonable level. Although the affinity of the LGL-1 MTS peptide for DOPS is one order of magnitude lower than for PI(4,5)P2 (Figure 8.4), we do not expect a different behavior upon phosphorylation. The same kinase reaction used to phosphorylate LGL-1 MTS in the radioassay was encapsulated in DOPS-containing GUVs either in presence or in absence of ATP. As expected, the peptide binds the membrane in the mixture without ATP, that is in the mixture where no phosphorylation can take place (Figure 8.9, A). On the other hand, LGL-1 MTS appears homogeneously distributed inside the GUV and does not bind the inner membrane when ATP was present in the kinase mixture, that is when human PKC- $\zeta$  could phosphorylate the LGL-1 MTS peptide



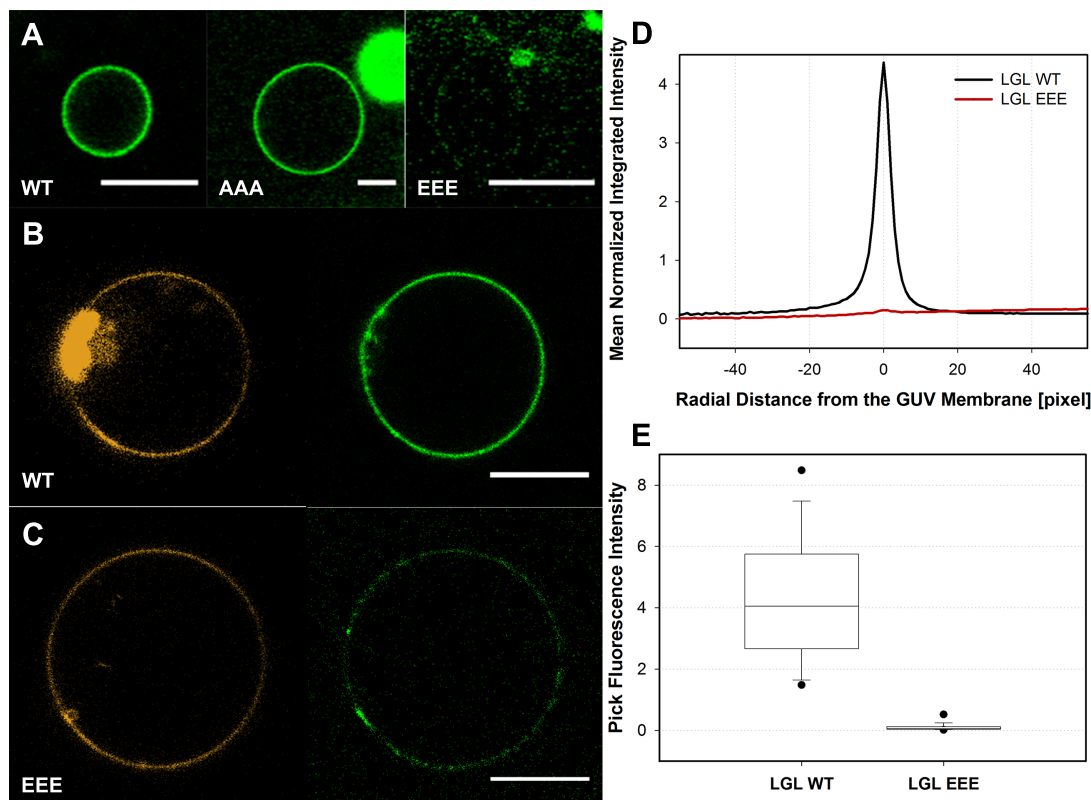


**Figure 8.7** – The phosphomimetic LGL-1 EEE mutant does not bind GUVs containing negative-charged lipids. Purified LGL-1 WT, AAA and EEE were incubated with GUVs containing DOPC:bPI(4,5)P2 92.5:7.5 and Texas Red DHPE as lipid dye [B-C]. GUVs were imaged at the equator with CLSM. Intensity radial profile plots were determined for each GUV [D] and pick values were plotted [E]. \*t-test,  $t(121)=14.549$ ,  $p=2.405 \cdot 10^{-28}$ . Scale bars are 10  $\mu\text{m}$ .

(Figure 8.9, B).

We finally wanted to trigger the phosphorylation *in situ* inside the GUVs and thus visualize the detachment of the LGL-1 MTS peptide from the membrane. In order to perform this experiment, we used a strategy developed by Pontani and colleagues to induce actin polymerization at the inner membrane of giant liposomes [53]. The GUVs are permeabilized by adding  $\alpha$ -hemolysin in the buffer outside the vesicles.  $\alpha$ -hemolysin is a toxin secreted by *Staphylococcus aureus*; it is monomeric in solution, but it can bind lipid membrane where it assembles in a hexameric ring structure and forms a transmembrane pore, which is permeable to ions and small solutes [243, 244]. Once the pore are formed, ATP and  $\text{MgCl}_2$ , both required for the human PKC- $\zeta$  to work, are sequentially added to the external solution, enter the vesicles where they eventually trigger the phosphorylation of the LGL-1 MTS peptide. LGL-1 originally localizes at the membrane where it remains after the addition of both  $\alpha$ -hemolysin and ATP (Figure 8.10, A-C); however it detaches after  $\text{MgCl}_2$  is added (Figure 8.10, D).

Several but not all GUVs in each sample show unbinding of the LGL-1 peptide; moreover the unbinding takes place at different times after the addition of  $\text{MgCl}_2$ . This asynchronous behavior is most probably due to diffusion of the single added components. In order to minimize the movement of the GUVs which were tracked over the all process, each component was added in few  $\mu\text{l}$  without pipetting and even if the chamber was allowed to equilibrate after

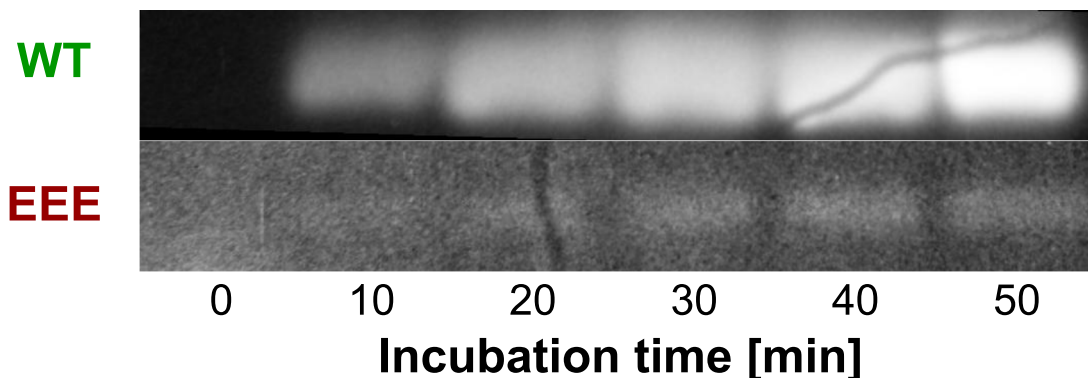


**Figure 8.8** – LGL-1 can be phosphorylated *in vitro* by the human PKC- $\zeta$ . LGL-1 MTS WT and EEE peptides were incubated with recombinant human PKC- $\zeta$  in presence of  $[\gamma\text{-}^{32}\text{P}]\text{ATP}$ . Kinase reactions were terminated at different time points, separated electrophoretically, and visualized with autoradiography.

each addition, solutes might be still inhomogeneous distributed in the chamber. Interestingly when the same experiment is attempt with GUVs containing 20 %mol DOPS the unbinding of LGL-1 does not take place, suggesting that when the peptide is completely bound to the membrane, is not accessible for the human PKC- $\zeta$  and thus it cannot be phosphorylated. A similar observation was made for PAR-2, whose binding to microtubules is sufficient to protect it from the action of aPKC [91]. This mechanism of protection could also explain why in some GUVs LGL-1 MTS only partially stays at the membrane forming a domain which shrinks with time until it eventually disappears (Figure 8.11).

Taken together these findings support the hypothesis that phosphorylation by aPKC, or phosphomimetic mutations of the PKC-3 sites, interferes with the binding of LGL-1 to negatively charged lipids, as similarly described for Par-2 [91].

### 8.3 Determination of the LGL-1 partitioning coefficient to negatively charged membranes

#### 8.3.1 $K_P$ can be determined from images of GUVs encapsulating LGL-1

We showed that the LGL-1 MTS peptide can be encapsulated in GUVs. The fraction of the peptide bound to the inner leaflet of the vesicles can be modulated varying the DOPS molar ratio in the lipid mixture (Figure 8.12).

Additionally, the amount of peptide encapsulated within a GUV is variable, meaning that the vesicles in one preparation are filled with different amounts of peptide, which can be up to one hundred times more concentrated than in the original internal solution (Figure 8.13). A similar observation was previously made for the spontaneous formation of liposomes in aqueous phase [245, 246] and recently theoretically investigated [247, 248].

Both abilities to modulate the peptide bound fraction, and to encapsulate the peptide at different concentrations proved to be extremely convenient for measuring the peptide membrane partitioning coefficient  $K_P$  directly from GUVs confocal images. In particular, the DOPS molar ratio can be set at 5 %mol, a value for which the peptide is easily detectable both in solution and at the membrane and the inherent encapsulation variability of the peptide provides a wide range of peptide concentrations in a single experiment. Similarly to

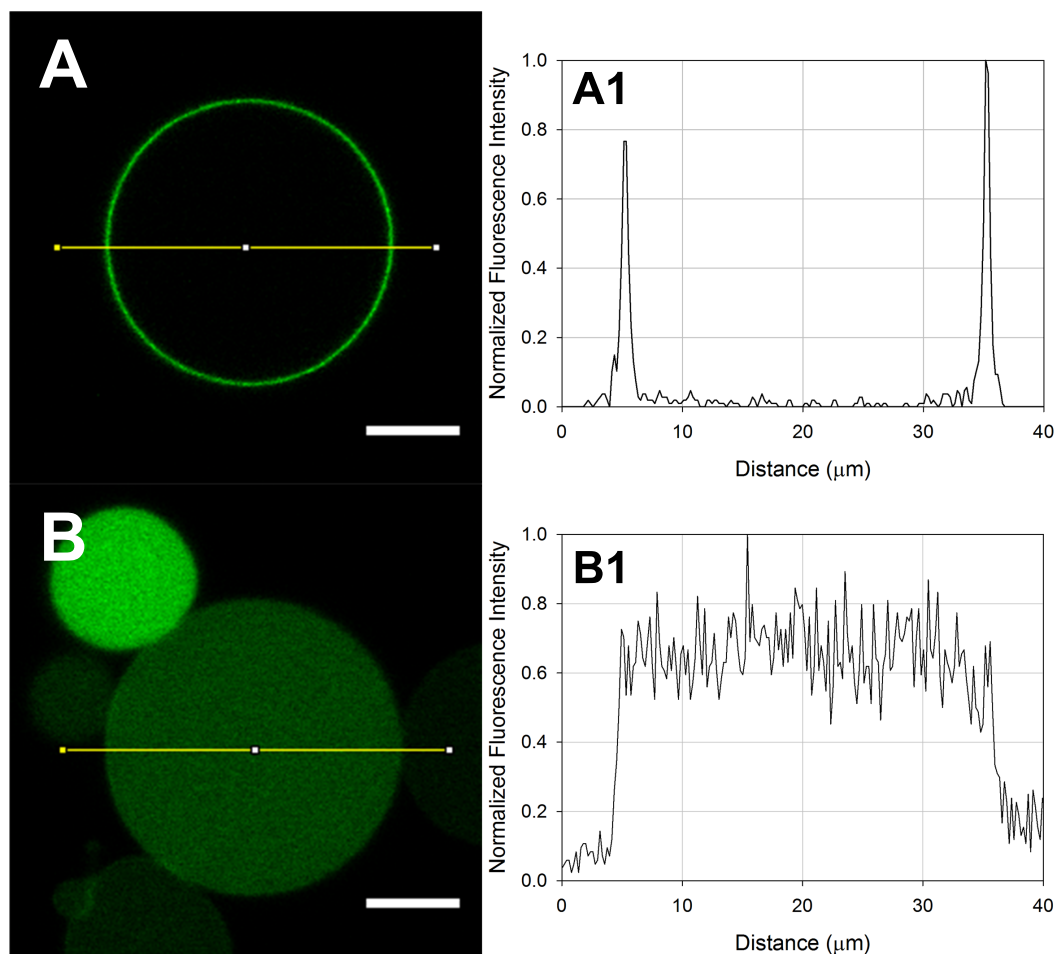


**Figure 8.9** – Phosphorylated LGL-1 MTS does not bind GUVs containing negative-charged lipids. The same kinase reaction used to phosphorylate LGL-1 MTS in the radioassay was encapsulated in GUVs containing 20 %mol DOPS either in absence [A] or in presence of ATP [B]. Images of representative GUVs are reported with their corresponding normalized intensity profiles [A1-B1]. Scale bars are 10  $\mu\text{m}$ .

the image approached described in details in Chapter 7, the fluorescence intensities at the membrane and inside the GUVs can be extracted with a customized MATLAB script and converted into concentrations ( $[P_{2D}]$ , bound;  $[P_f]$ , free), provided that a calibration curve was previously acquired using an independent measuring method (i.e. FCS). The membrane binding molecules are in this case encapsulated in a close environment, whose internal area serves as an interacting surface. Here not only the water concentration  $W$  ( $5.53 \times 10^{-14} \text{ mol}/\mu\text{m}^3$ ), but also the lipid surface concentration  $[L_{2D}]$  ( $2.30 \times 10^{-18} \text{ mol}/\mu\text{m}^2$  for DOPC:DOPS 95:5 [249]) is constant.

The binding of a peptide to a lipid membrane was described by White and colleagues as a partitioning between two immiscible fluid phases (water and lipid membrane) [186]:

$$K_P = \frac{[P_m]/[L]}{[P_f]/W} \quad (8.1)$$

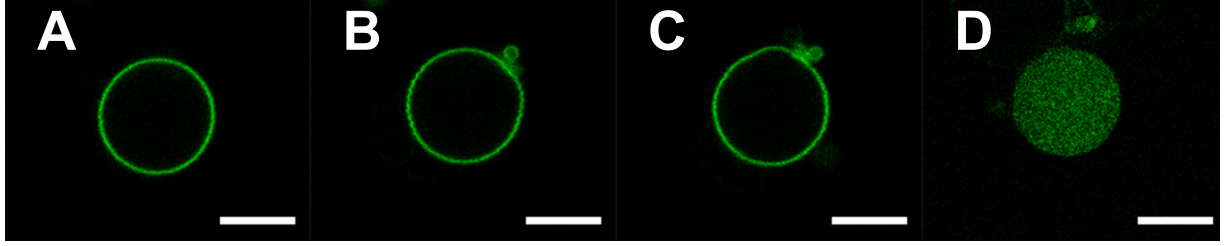


**Figure 8.10** – *In situ* LGL-1 phosphorylation inside a GUV. LGL-1 MTS was encapsulated in GUVs containing 5 %mol DOPS.  $\alpha$ -hemolysin [B], ATP [C], and  $\text{MgCl}_2$  [D] were sequentially added to the external solution. Images of a representative GUV are reported before [A] and after each addition [B-D]. Scale bars are 10  $\mu\text{m}$ .

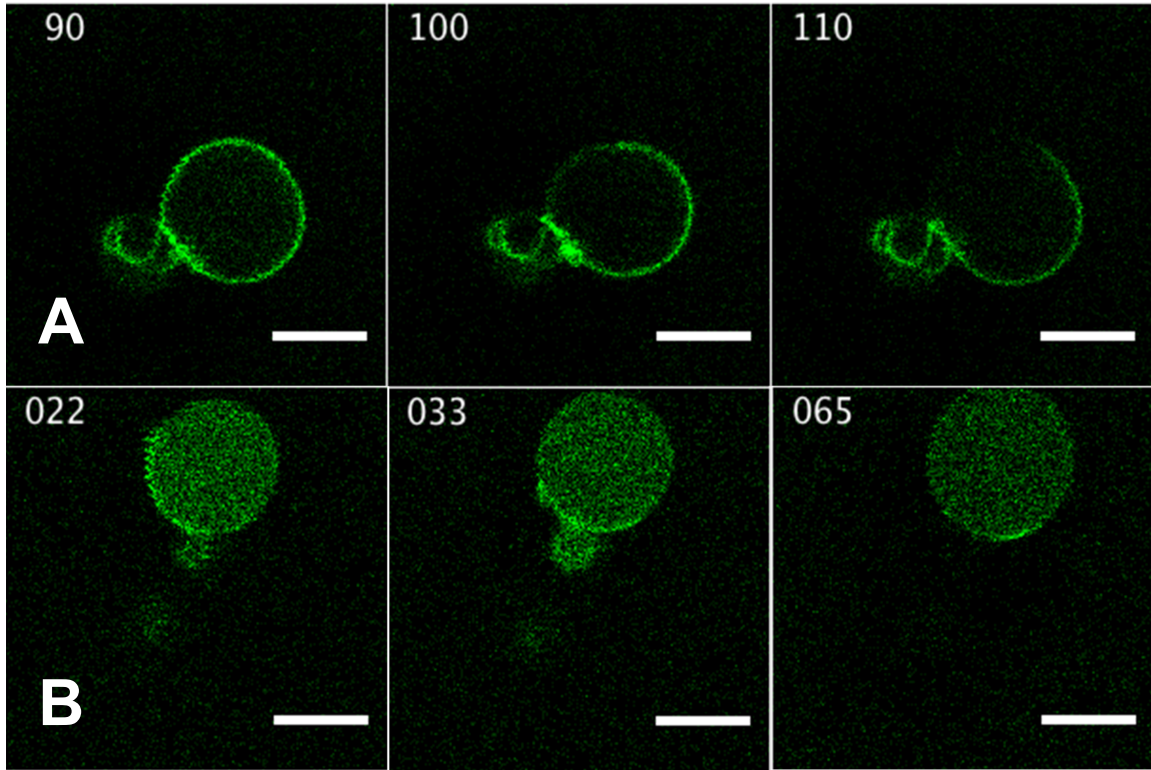


**Figure 8.11** – LGL-1 bound to the membrane is protected from the action of PKC- $\zeta$ . LGL-1 MTS was encapsulated in GUVs containing 5 %mol DOPS and  $\alpha$ -hemolysin, ATP, and  $\text{MgCl}_2$  were sequentially added to the external solution. Images taken at different time points after the addition of  $\text{MgCl}_2$  are reported for two representative GUVs. Scale bars are 10  $\mu\text{m}$  and labels in minutes.

Here  $[L]$  is the lipid volume concentration, whereas  $[P_m]$  and  $[P_f]$  are the peptide concentrations at the GUV membrane and inside the GUV, respectively. In Chapter 7, we show that the lipid  $[L_{2D}]$  and peptide  $[P_{2D}]$  surface concentrations can be used instead of the respective volume concentrations and that both  $[P_{2D}]$  and  $[P_f]$  can be extracted directly from confocal images:

$$K_P = \frac{[P_{2D}]/[L_{2D}]}{[P_f]/W} \quad (8.2)$$

The ratio between surface  $A_{GUV}$  and volume  $V_{GUV}$  of a vesicle is not constant, but it

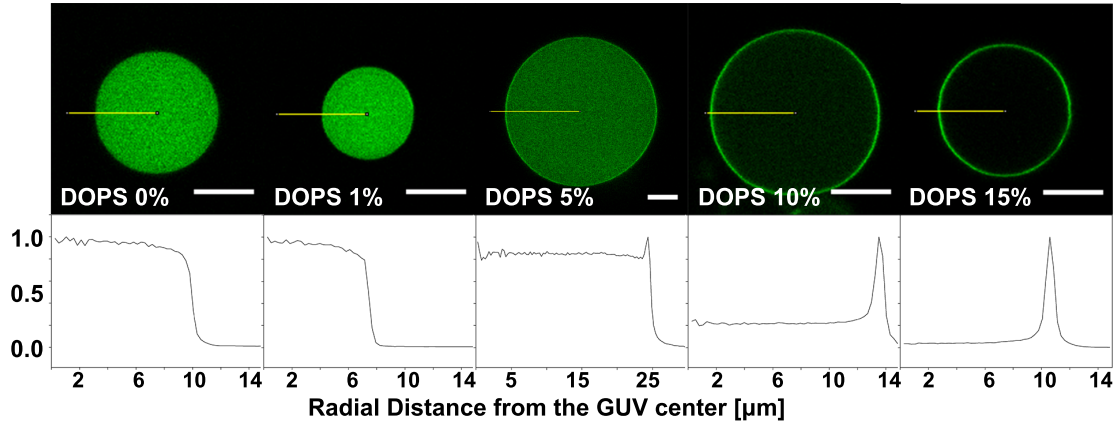


**Figure 8.12** – LGL-1 MTS encapsulated in GUVs via droplet transfer method. LGL-1 MTS was encapsulated in GUVs containing different molar ratios of DOPS. Images of representative GUVs are reported with their corresponding normalized intensity radial profiles. Scale bars are 10  $\mu\text{m}$ .

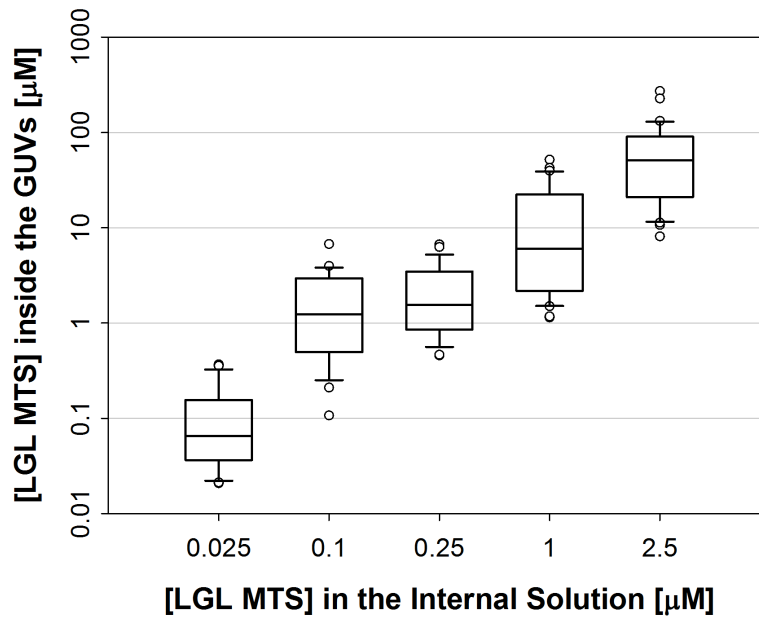


**Figure 8.13** – LGL-1 MTS encapsulation variability. Internal solutions with different LGL-1 MTS concentrations were used to generate GUVs containing 5 %mol DOPS. The actual peptide concentrations in the GUVs are plotted against the corresponding peptide concentrations in the original internal solutions.

scales with the radius  $A_{GUV}/V_{GUV} = 3/r_{GUV}$ . The total number of particles attached to the internal surface of a GUV  $P_{2D} = [P_{2D}]A_{GUV}$  and free inside the GUV  $P_f = [P_f]V_{GUV}$  can be calculated knowing  $r_{GUV}$ . When several  $P_{2D}$ ,  $P_f/r_{GUV}$  pairs are plotted against each other,  $K_P$  can be determined fitting the data points to equation:

$$P_{2D} = \frac{3K_P[L_{2D}]}{[W]} \frac{P_f}{r_{GUV}} \quad (8.3)$$

The partitioning coefficient of the LGL-1 MTS peptide to GUVs containing 5 %mol DOPS can be therefore estimated to be  $9.05 \pm 0.2 \times 10^4$  (Figure 8.14).

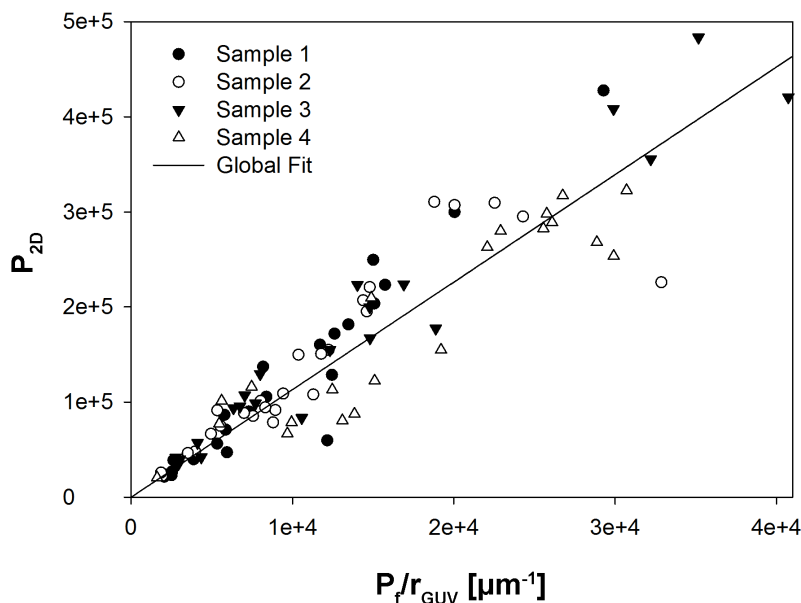


**Figure 8.14** – Determination of the LGL-1 MTS partitioning coefficient in GUVs. LGL-1 MTS at 25 nM initial concentration was encapsulated in GUVs containing 5 %mol DOPS. Fluorescence intensities at the membrane and inside the GUV were extracted from 117 GUVs belonging to four independent samples, converted into number of molecules and plotted against each other. A global linear fitting to Equation 8.3 was applied in order to determine the LGL-1 MTS partitioning coefficient  $K_P$ .

Model Membrane	Membrane Composition	Method	LGL-1 MTS $K_P$
GUVs	PS 5 %mol	Imaging	$9.05 \pm 0.2 \times 10^4$
LUVs	PS 20 %mol	FCS	$6.48 \pm 0.5 \times 10^5$
Model Membrane	Membrane Composition	Method	LGL-1 MTS $K_B$ [ $M^{-1}$ ]
LUVs	PS 5 %mol	ζ-potential	$0.17 \pm 0.05 \times 10^{-6}$
LUVs	PI(3)P 2.5 %mol	ζ-potential	$0.65 \pm 0.17 \times 10^{-6}$
LUVs	PI(4)P 2.5 %mol	ζ-potential	$0.61 \pm 0.11 \times 10^{-6}$
LUVs	PI(5)P 2.5 %mol	ζ-potential	$0.62 \pm 0.14 \times 10^{-6}$
LUVs	PI(3,5)P2 1.67 %mol	ζ-potential	$0.96 \pm 0.30 \times 10^{-6}$
LUVs	PI(3,4)P2 1.67 %mol	ζ-potential	$1.67 \pm 0.35 \times 10^{-6}$
LUVs	PI(4,5)P2 1.67 %mol	ζ-potential	$1.55 \pm 0.26 \times 10^{-6}$
LUVs	PI(3,4,5)P3 1.25 %mol	ζ-potential	$0.36 \pm 0.07 \times 10^{-6}$

**Table 8.2** – LGL-1 MTS  $K_P$  and  $K_B$  values. LGL-1 MTS  $K_P$ s and  $K_B$ s values to vesicles containing different acidic lipids measured by a FCS, imaging or ζ-potential approach.

### 8.3.2 LGL-1 $K_P$ determined with a LUV-FCS based method

The partitioning coefficient  $K_P$  of the LGL-1 MTS peptide to negatively charged membranes was alternatively measured with the LUV-FCS method [74] described in details in Chapter 7. The kinase reaction mix described above for the *in vitro* phosphorylation of the LGL-1 MTS peptide was used and the LUV-FCS binding assay was performed either in presence or absence of ATP, that it with phosphorylated and not phosphorylated peptides. When LUVs were increasingly added to the chamber containing the not phosphorylated peptide, fluorescent spikes appeared (Figure 8.15, A; LGL-1 MTS). These spikes originate from vesicles, to which the fluorescent peptide is bound, passing through the focal volume. The different heights of the spikes suggest that more than one single peptide molecule can bind each vesicle. The phosphorylated peptide cannot bind the vesicles, thus no fluorescence spikes could be detected in its presence (Figure 8.15, A; LGL-1 MTS P). FCS of both phosphorylated and not phosphorylated peptides was measured in solution before and after each vesicle addition. The autocorrelation curves of the not phosphorylated peptide move left with increasing LUVs concentrations (Figure 8.15, B; LGL-1 MTS), meaning that the diffusion of the peptide decreases with increasing LUVs concentrations. This is due to the fact that more and more peptide binds the vesicles and consequently diffuses slower than in the unbound state. Conversely the autocorrelation curves of the phosphorylated peptide do not change (Figure 8.15, B; LGL-1 MTS P), as well as the peptide diffusion. LGL-1 MTS P in fact does not bind the vesicle and thus its diffusion do not decrease with increasing LUVs concentrations. The autocorrelation functions were fitted to a two components 3D+T diffusion model (Equation 7.23), an averaged normalized  $G(0)$  value for each LUVs concentration was then calculated and plotted against the vesicle concentration itself (Figure 8.15, C). All data points were finally fitted to Equation 7.26 and converted with Equation 7.27. The partitioning coefficient of the LGL-1 MTS peptide to LUVs containing 20 %mol POPS could be therefore estimated to be  $6.48 \pm 0.5 \times 10^5$ . This value is in line with those obtained for other conditional peripheral proteins [250] and higher than the one measured with the imaging approach in GUVs (Table 8.2). The amount of acidic lipids in the LUVs was in fact four times higher than in the GUVs.



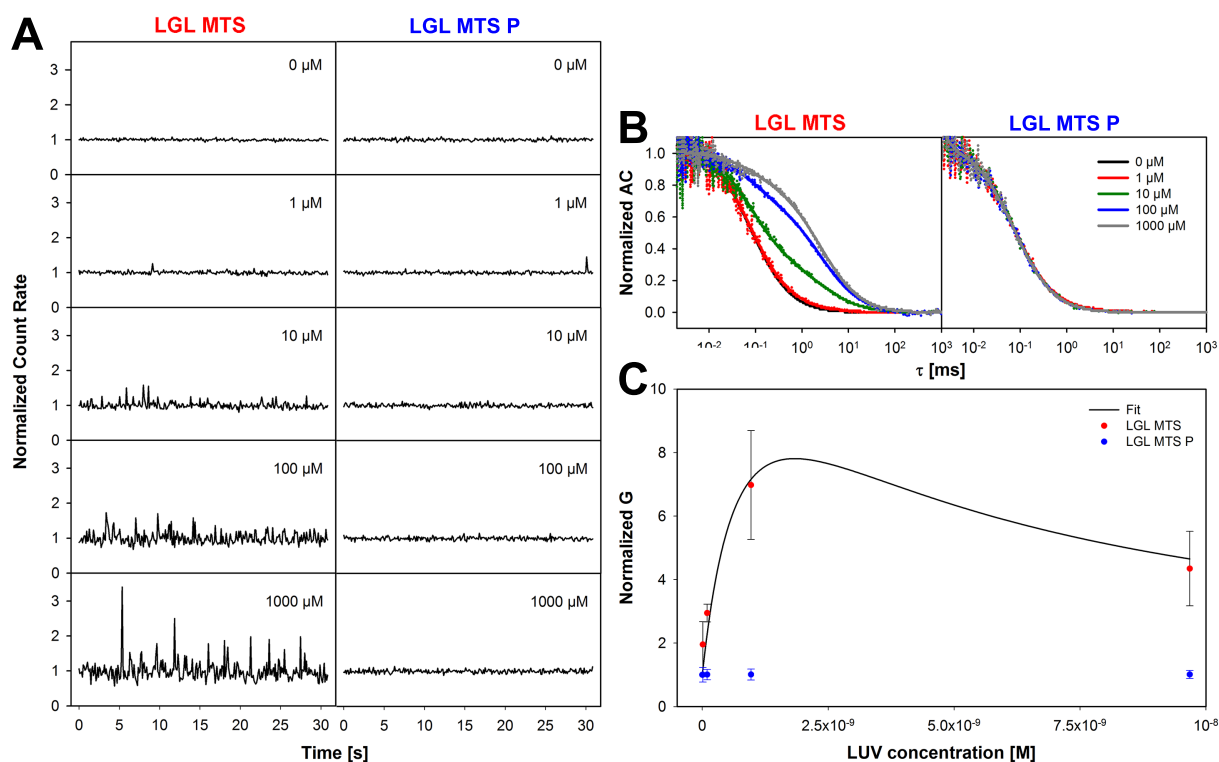


**Figure 8.15** – Determination of the LGL-1 MTS partitioning coefficient with the LUV-FCS method. Not phosphorylated and phosphorylated (P) LGL-1 MTS peptides at 50 nM initial concentration were incubated with increasing concentrations of LUVs containing 20 %mol POPS. FCS was measured in solution in absence and after each vesicle addition [A]. The autocorrelation functions were fitted to a two components 3D+T diffusion model (Equation 7.23) [B], then G values for each LUVs concentration were calculated and the data points were fitted to Equation 7.26 and converted with Equation 7.27 to determine the LGL-1 MTS partitioning coefficient  $K_P$  [C].



## Part IV

# CONCLUSION AND OUTLOOK



## Chapter 9

# Conclusion and Outlook

In this thesis, we explored different “bottom-up” approaches to reconstitute membrane un-mixing and cell polarization events in model membranes. On one hand, we worked with pure lipid systems, in which we exchanged selected lipids to generate lipid transbilayer asymmetry, induce lipid lateral segregation, and trigger vesicle shape transformations. On the other hand, we reconstituted a functional LGL/aPKC membrane binding switch in GUVs as a first module of a minimal polarization system inspired by the *C. elegans* embryo at one-cell stage. In both cases, we collected observations that helped us understanding the biological inspiring processes. Moreover, because of their reduced complexity, the reconstituted systems could be readily characterized by biophysical methods. In particular, we made use of both fluorescent imaging and correlation spectroscopy to quantify lipid dynamics and phase behavior as well as protein-lipid interactions in the very same system used to reconstitute the desired membrane proteins. The ability to retrieve quantitative information is, in fact, a generally desirable and increasingly required feature of any minimal synthetic system.

### 9.1 Pure lipid systems

#### 9.1.1 Reconstitution of lipid transbilayer asymmetry in model membranes

In Chapter 4, we described how the cyclodextrin-mediated lipid exchange method can be extended to SLBs formed by VF to produce temporarily stable asymmetric SLBs. This approach is quick and easy to implement, does not require organic solvents, nor specialized equipment or skills, and can be used with a variety of different lipids to produce bilayers with the desired composition in each leaflet, as already showed for LUVs and GUVs [85, 86, 251, 97]. It also provides a more naturally generated asymmetric system in the way that specific lipids are incorporated when the bilayer already exists. The local lipid composition of biological membranes is, in fact, known to change continuously because of membrane recycling and enzymatic activity [125]. This is the case, for example, of SM, being synthesized at the endoplasmic reticulum and Golgi apparatus and eventually transported to the plasma membrane, or directly at the outer leaflet of the plasma membrane by the SphingoMyelin Synthase 2 (SMS2). Our approach has additionally the potential to be combined with other conventional SLB preparation techniques to fine-tune the lipid composition of the bilayer, as suggested by the successful vesicle-mediated phospholipids exchange recently reported for tethered bilayers [252].

### 9.1.2 Reconstitution of lipid lateral segregation in model membranes

In Chapters 4, we also showed that aSLBs generated via cyclodextrin-mediated lipid exchange are a suitable membrane model system to study phase separation of raft-mimicking lipid mixtures. Using such a system, we showed how small changes in the composition of the inner leaflet (e.g. of the plasma membrane), although not sufficient to support phase separation in a corresponding symmetric bilayer, affect the overall lipid miscibility of the whole bilayer. Our system provides an alternative strategy to follow domain dynamics without heating/cooling the sample above/below its phase transition temperature. In fact, de novo formation of Lo domains is induced through cholesterol incorporation in the bilayer rather than by temperature control. Moreover, in contrast to what was described for other aSLB systems [129], the support does not exert any negative influence on domain registration in our system; when domains can be formed, they are always in registration. If the total cholesterol amount of a single bilayer could be precisely measured, for example, with mass spectrometry, our system could be also used to investigate how cholesterol distributes between the lower and upper leaflet of SM-containing aSLBs. In fact, even if cholesterol is expected to preferentially interact with SM, experiments performed in various cells types revealed that cholesterol is enriched in the cytosolic leaflet of biological membranes [253]. For example recent quantitative quenching analysis in CHO cells indicated that 60-70% of the plasma membrane sterols resides in the cytoplasmic leaflet [254].

### 9.1.3 Using lipid transbilayer asymmetry to induce shape transformations of GUVs

In Chapter 5, we showed that cyclodextrin-mediated lipid exchange can be used to induce changes in the shape of GUVs. Varying the amount of cyclodextrin results in different vesicle transformations: prolate ellipsoid to spherical vesicle transformations are observed at high cyclodextrin concentrations, discocyte to stomatocyte transformations and vesicle budding at intermediate cyclodextrin concentrations, whereas vesicle endocytosis is common at low cyclodextrin concentrations. Additionally it would be beneficial to stop the vesicles from further changing once they reach the desired shape. Although we did not try it yet, we are confident that removing the cyclodextrin-lipid complexes in excess by extensive wash would be enough to freeze the vesicle shape.

Besides PG, we expect that other lipids could be employed to induce shape transformation in giant liposomes. Those lipids should be cone- (i.e. phosphatidylethanolamine) or inverted cone-shaped (i.e. lysolipids) [255] to significantly modify the area of the outer leaflets relative to the inner one. L-PC, for example, is known to induce vesicle fission in GUVs, but only if GUVs are in Lo phase [256, 257]. We therefore plan to use the described FRAP assay to determine whether or not cyclodextrin mediated lipid exchange is able to induce vesicle fission in absence of intramembrane domains [154], phase transition [258] or protein machineries [155] and as a consequence of the transbilayer lipid asymmetry only.

## 9.2 Lipid-protein systems

### 9.2.1 Lipid transbilayer asymmetry is not sufficient to restore the correct lateral organization of the influenza virus HA TM helix in model membranes

In Chapter 4, we also demonstrated that the cyclodextrin-mediated lipid exchange can produce asymmetric bilayers in the presence of reconstituted proteins. Interestingly, this method offers the advantage of providing in the same sample the state before and after the establishment of the asymmetry or of the shape transformation, thus opening the possibility of directly probing the effect of leaflet-specific lipid composition and system geometry on protein structure and function.

In Chapter 6, we hypothesized that the lack of asymmetry of the Lo domains in model membranes could be the reason why raft-associating proteins, such as the influenza HA, partition into Ld domains, rather than into Lo domains. Unexpectedly, our results do not support this hypothesis. In both SLBs and GUVs asymmetric model system, we could not observe any significant difference in the partitioning behavior of the HA TM peptide. There must be additional features of the lipid rafts in cells that model membranes still fail to mimic. Further development of model membranes, beyond their asymmetry, are therefore needed to truly mimic the partitioning behavior of raft-associated proteins and TM helices. In particular, protein crowding should be implemented. GPMVs are often presented as a better alternative to GUVs as far as they resemble the lipid and protein diversity of native biological membranes closer than any other model membrane [259]. However, at least in the case of the influenza HA, they did not help to correctly reproduce the raft-partitioning observed in cell membranes [131].

### 9.2.2 Direct quantification of protein-lipid interactions in GUVs

In Chapter 7, we provided a new and versatile method to determine  $K_{PS}$ , which overcomes several disadvantages of established assays. Moreover, we showed how to understand the relation between  $K_P$  and the number of molecules per lipid surface (Equation 7.18), which can always be determined for a protein-lipid system, whose soluble protein and lipid surface concentrations are known. To our knowledge, this is the first assay based on GUVs, which combines confocal imaging with FCS to precisely determine protein concentrations at equilibrium. Small amounts of sample are needed, since the measurement can be conducted in low volume chambers and FCS as well as photon-counting imaging are known to be sensitive down to the nanomolar range. In addition, our assay accounts for loss of protein due, for example, to unspecific interactions with the chamber or pipetting errors, since free and membrane associated protein are always directly determined. The use of free standing membranes excludes any effects of the support on protein-lipid interaction. Apart from studying the interaction of peripheral proteins with lipid membranes, any fluorescent species, e.g. labeled peptides or small molecules, could be investigated with this assay.

The comparison of our results with a FCS-based LUV assay revealed that the latter method is not accurate for the NTA(Ni)-His6 system, even when the multiple binding of peptides to a single vesicle is taken into account. Due to vesicle aggregation, no significant increase of the partitioning coefficient was detected (one-way ANOVA,  $F(3, 14) = 3.3$ ,  $p = 0.061$ ) even in presence of 2.5 times the amount of binding sites in the membrane. The  $K_{PS}$

obtained with our dual approach correspond to the upper range of the values reported in the literature and clearly show a dependence on the content of NTA(Ni) lipids in the membrane.

Our imaging-based GUV assay could be readily combined with an automated GUVs analysis software [260] or performed in a microarray setup [261] to directly extract the mean intensities of several GUVs in one image or simultaneously probe different lipid-binding proteins in a single experiment, while significantly reducing both measuring and analysis time.

### 9.2.3 Reconstitution of a functional LGL/aPKC membrane binding switch

In Chapter 8, we were able to reconstitute a functional LGL/aPKC membrane binding switch in GUVs. In this system a PKC- $\zeta$  co-encapsulated with the LGL-1 MTS peptide can be activated, thus it phosphorylates LGL-1 MTS inducing the detachment of the peptide from the vesicle inner membrane. This direct visualization of the phosphorylation-dependent LGL-1 MTS detachment, together with complementing experiments, indicates that phosphorylation by PKC-3 regulates LGL-1 cortex localization lowering dramatically its affinity for negatively-charged membranes.

In order to reconstitute LGL-1 in model membranes, we had to clarify the mechanism of the LGL-1 localization at the cortex. We identified a region (659-676) in the C-terminal LGL-specific domain, which is rich in positively charged amino acids and can directly bind negatively charged membranes. Although the membrane binding takes place independently of what type of acidic lipid is used, LGL-1 shows the highest affinity for the diphosphoinositides PI(3,4)P2 and PI(4,5)P2, whose phosphate groups seat in two adjacent positions of the inositol ring. This finding has a biological relevance: the PI(4,5)P2 generating enzyme PPK-1 of *C. elegans* is, in fact, enriched in the posterior domain, where LGL-1 localizes [239]. Upon membrane binding, LGL-1 MTS folds into an  $\alpha$ -helix, which forms three regions with distinct properties: (1) all basic amino acids align and form a positive charged patch; (2) the three amino acids that serve as phosphorylation sites for PKC-3 are located close to each other, creating a “switch” area; and (3) all remaining hydrophobic adjacent residues are probably buried in the membrane (Figure 9.1, A).

Interestingly, only mutations of specific basic amino acids of the positive patch interfere with the cortical localization of LGL-1 in yeast. A combined quadruple mutation of those residues lowers the affinity of LGL-1 MTS for PI(4,5)P2-containing membranes in our *in vitro* GUV binding assay, suggesting that the position of the single basic amino acids in the LGL-1 MTS is important for its membrane binding specificity (Figure 9.1, B).

The observation that LGL-1 binds the membrane through the same region that controls its cortex/membrane localization is consistent with the intramolecular auto-inhibition model proposed by Betschinger and colleagues [220] and complements it, although they assumed that the membrane association takes place through the N-terminal  $\beta$ -propeller domains. When LGL does not bind the membrane, its MTS has a random coil conformation and acts as a flexible hinge, allowing the N- and C- termini of the protein to come together. This condition can be triggered or stabilized by PKC-dependent phosphorylation, having the phosphorylated LGL low membrane affinity. On the other hand, when LGL binds the membrane, the MTS folds into an  $\alpha$ -helix structure with reduced flexibility [262], eventually preventing the intramolecular association of the N- and C- termini of the protein. In this condition LGL is protected from the PKC-3 action [91], signaling that an additional player must be involved in the LGL activation/deactivation cycle. PAR-6 for example through its direct association with LGL [222] could enable PKC-3 to phosphorylate LGL even in its membrane-bound state.

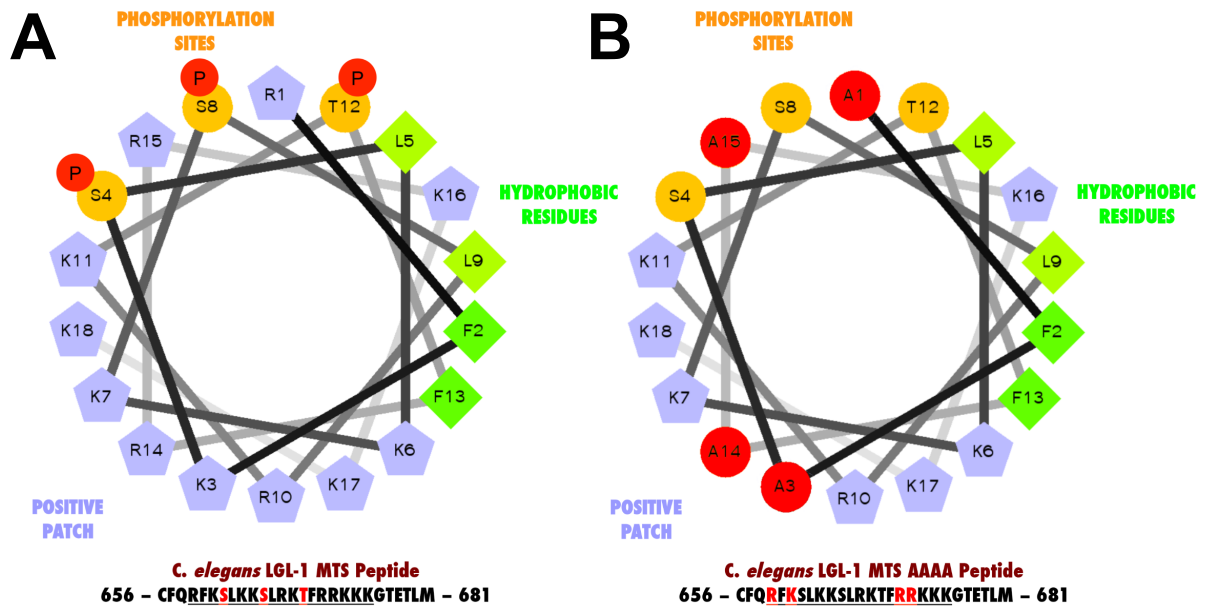


**Figure 9.1** – Secondary structure of the LGL-1 MTS WT and AAAA peptide at the membrane. Upon membrane binding, LGL-1 MTS folds into an  $\alpha$ -helix structure with three distinct regions: a positive charged area responsible for the lipid specificity, a switch area containing the three PKC-3 phosphorylation sites and a hydrophobic area which is probably buried in the membrane [A]. Mutation of four basic residues R658A/K660A/RR671AA changes the affinity of LGL-1 MTS for PI(4,5)P<sub>2</sub>-containing membranes.

PAR-6 is, in fact, known to activate aPKC, given that its CRIB/PDZ domain, the same involved in the binding with LGL, is engaged in a binding with Cdc42 [263]. Nevertheless, additional experimental work is needed to prove the truth of this model.

We finally adapted the GUV-imaging method described in Chapter 7 to directly measure the partitioning coefficient of the LGL-1 MTS encapsulated in GUVs. Besides the  $K_P$  value obtained, which is in line with the values of other conditional peripheral proteins [250], this modified version of the GUV-imaging method provides an experimental advantage. It can be used even with peptides/proteins that strongly adhere to glass surfaces and plastic tubing, like LGL-1, without compromising its accuracy.





# Acronyms

*D* Diffusion coefficient. 13–15, 33–36, 44–50, 53, 73, 85, 89, 91

*D\** Relative Diffusion coefficient. 33, 34, 44–47, 49, 50

*K<sub>B</sub>* Apparent Binding Constant. 39, 102, 103, 112

*K<sub>P</sub>* Partitioning Coefficient. 14, 37, 81–84, 86–91, 93, 94, 99, 108, 111–114, 119, 121

*K<sub>d</sub>* Dissociation constant. 83, 86, 87, 89, 90, 92, 93

%*Lo* Lo partitioning coefficient. 38, 72–74, 76

$\tau_D$  Diffusion time. 13, 14, 33, 35, 48–50

**aa** amino acid. 99, 100, 104

**ActA** Actin assembly-inducing protein. 8, 9

**ADF** Actin Depolymerizing Factor. 8

**aGUV** asymmetric Giant Unilamellar Vesicle. 26, 30, 56, 57

**AJ** Adherens Junction. 3

**ANOVA** ANalysis Of VAriance. 39, 45, 49, 89, 103, 119

**aPAR** anterior PAR. 4, 17, 97, 98

**APD** Avalanche PhotoDiode. 13

**aPKC** atypical Protein Kinase C. 18, 98, 106, 108, 117, 120, 121

**Arp2/3** Actin-Related-Protein 2 and 3 complex. 8

**aSLB** asymmetric Supported Lipid Bilayer. 29, 33, 34, 36, 42, 43, 46, 47, 49, 51–56, 118

**BCA** Bicinchoninic Acid. 23

**Bkg** Background. 32, 33, 66, 68

**bPI(4,5)P2** L- $\alpha$ -phosphatidylinositol-4,5-bisphosphate. 21, 100–102, 105, 107

**BSA** Bovine Serum Albumin. 23–26

- bSM** brain SphingoMyelin. 29, 34, 47, 52, 56, 57, 60–62, 73, 76–79
- CHAPS** 3-(3-CHolAmidopropyl)dimethylammonio-1-PropaneSulfonate. 23, 27, 28, 48
- Chol** Cholesterol. 12, 17, 26, 27, 29, 30, 51–53, 55, 57, 61, 73, 76–79
- CLSM** Confocal Laser Scanning Microscope. 13, 73, 100, 102, 105, 107
- CtxB** Cholera toxin subunit B. 23
- DGS-NTA(Ni)** 1,2-di-(9Z-octadecenoyl)-sn-glycero-3-(N-(5-amino-1-carboxypentyl)iminodiacetic acid)succinyl nickel salt. 21, 24, 25, 83, 84, 87–94, 100, 101
- DiI** DiIC<sub>18</sub>(3). 22, 27, 32, 67, 68
- DLS** Dinamic Light Scattering. 39, 101
- DOPA** 1,2-DioleOyl-sn-glycero-3-PhosphAte. 21
- DOPC** 1,2-DiOleoyl-sn-glycero-3-PhosphoCholine. 21, 24–30, 33–35, 38, 44–51, 53, 56, 57, 60–62, 73, 76–79, 88, 100–105, 107, 109
- DOPG** 1,2-DiOleoyl-sn-glycero-3-Phospho-(1'-rac-Glycerol). 21, 30, 32, 62–65, 101
- DOPS** 1,2-Di-(9Z-Octadecenoyl)-sn-glycero-3-Phospho-L-Serine. 21, 25, 27, 100–103, 105, 106, 108–112
- DRM** Detergent Resistant Membrane. 71, 72
- DTT** DiThioThreitol. 24, 26
- eGFP** enhanced Green Fluorescent Protein. 32, 44, 82
- eGFP-His6** His6 tagged enhanced Green Fluorescent Protein. 22, 23, 25, 34, 82, 84, 87–94, 100–102
- FCCS** Fluorescence Cross-Correlation Spectroscopy. 15
- FCS** Fluorescence Correlation Spectroscopy. 12–16, 23, 27, 31–37, 44, 45, 47–49, 53, 72, 73, 81, 82, 84–94, 109, 112–114, 119
- FRAP** Fluorescence Recovery After Photobleaching. 27, 28, 32, 33, 37, 60, 65, 67, 81, 118
- FRET** Förster Resonance Energy Transfer. 71, 72
- GPMV** Giant Plasma Membrane Vesicle. 71, 119
- GUV** Giant Unilamellar Vesicle. x, 10, 12, 14, 17, 18, 25–27, 29–32, 34–38, 42, 44, 51, 56, 57, 59–68, 71–79, 82, 84–91, 93, 94, 99–101, 105–113, 117–121
- HA** HemAgglutinin. x, 17, 22, 29, 38, 71–79, 119
- His6** HexaHistidine. 82, 100, 119

**HP $\alpha$ CD** (2-HydroxyPropyl)- $\alpha$ -CycloDextrin. 23, 29, 30, 60–62

**ITO** Indium Tin Oxide. 25, 26, 29, 44

**L-PC** LysoPhospatidylCholine. 59, 118

**LB** Langmuir-Blodgett. 10, 11, 42, 47, 56

**Ld** Liquid disordered. 12, 14, 29, 35, 38, 60, 61, 65, 67, 68, 72–79, 119

**LGL** Lethal (2) Giant Larvae. 6, 18, 23, 98, 100, 106, 117, 120, 121

**Lo** Liquid Ordered. 12, 14, 15, 35, 37, 38, 43, 51, 52, 54, 56, 60–62, 65, 67, 68, 71–74, 118, 119

**LS** Langmuir-Schaeffer. 10, 11, 42, 56

**LUV** Large Unilamellar Vesicle. 10, 14, 24, 25, 28, 31, 32, 34, 35, 81, 82, 86, 87, 89–94, 101–104, 112–114, 117, 119

**M $\beta$ CD** Methyl- $\beta$ -CycloDextrin. 23, 29, 30, 32, 34, 42–53, 55, 60–65, 73

**MARCKS** Myristoylated Alanine-Rich C Kinase Substrate. 98, 101, 102, 104

**MLV** MultiLamellar Vesicles. 9, 10, 29–31

**MTS** Membrane Targeting Sequence. 23–25, 37, 39, 98–114, 120, 121

**NBD** Nitro-2-1,3-BenzoxaDiazol-4-yl. 32

**NBD-DOPE** 1,2-dioleoyl-sn-glycero-3-phosphoethanolamine-N-(7-nitro-2-1,3-benzoxadiazol-4-yl). 22, 26–31, 34, 38, 44–50, 53, 56, 62–64, 73, 75–79

**NBD-DSPE** 1,2-distearoyl-sn-glycero-3-phosphoethanolamine-N-(7-nitro-2-1,3-benzoxadiazol-4-yl). 22, 31

**Ni** Nickel. 82, 119, 120

**NPF** Nucleation Promoting Factor. 8, 9

**NTA** NitriloTriacetic Acid. 82, 119, 120

**OG** n-Octyl- $\beta$ -D-Glucopyranoside. 23, 29, 73

**ON** Over Night. 24

**PAR** PARtitioning defective. 4, 17, 18, 97, 98, 104

**PBS** Phosphate Buffered Saline. 24

**PdI** Polydispersity Index. 101, 102

**PE** PhosphatidylEthanolamine. 3, 4

- PG** PhosphatidylGlycerol. 17, 59, 60, 62, 118
- PI(3)P** 1,2-dioleoyl-sn-glycero-3-(phosphoinositol-3-phosphate). 21, 103, 112
- PI(3,4)P2** 1,2-dioleoyl-sn-glycero-3-phospho-(1'-myo-inositol-3',4'-bisphosphate). 21, 102, 103, 112, 120
- PI(3,4,5)P3** 1,2-dioleoyl-sn-glycero-3-phospho-(1'-myo-inositol-3',4',5'-trisphosphate). 21, 102, 103, 112
- PI(3,5)P2** 1,2-dioleoyl-sn-glycero-3-phospho-(1'-myo-inositol-3',5'-bisphosphate). 21, 102, 103, 112
- PI(4)P** 1,2-dioleoyl-sn-glycero-3-phospho-(1'-myo-inositol-4'-phosphate). 21, 103, 112
- PI(4,5)P2** 1,2-dioleoyl-sn-glycero-3-phospho-(1'-myo-inositol-4',5'-bisphosphate). 21, 101–103, 105, 106, 112, 120, 121
- PI(5)P** 1,2-dioleoyl-sn-glycero-3-phospho-(1'-myo-inositol-5'-phosphate). 21, 103, 112
- PKC** Protein Kinase C. 105, 120
- PKC- $\zeta$**  active recombinant human PKC- $\zeta$ . 23, 24, 105–108, 120
- PLAP** Alkaline Phosphatase from human PLacenta. 22, 23, 27, 28, 31, 48–50
- pNPP** 4-nitrophenyl phosphate disodium salt hexahydrate. 23, 28, 29
- POPC** 1-Palmitoyl-2-Oleoyl-sn-glycero-3-PhosphoCholine. 21, 25
- POPS** 1-Palmitoyl-2-Oleoyl-sn-glycero-3-Phospho-L-Serine. 21, 25, 113, 114
- pPAR** posterior PAR. 4, 97, 98
- PS** PhosphatidylSerine. 3, 4, 42, 112
- PSD** Particle Size Distribution. 103
- Pt** PlaTinum. 25
- R** Radius of curvature. 61
- ref** reference. 32, 37, 68
- ROI** Region Of Interest. 32, 33
- RP-HPLC** Reversed-Phase High-Performance Liquid Chromatography. 23
- RT** Room Temperature. 24–30, 47
- SLB** Supported Lipid Bilayer. 10–12, 14, 17, 25–31, 33–36, 38, 42–54, 56, 59, 64, 72–75, 100, 102, 117, 119
- SM** SphingoMyelin. 3, 4, 17, 22, 26, 27, 29–31, 34, 42, 44–57, 73, 76–79, 117, 118

**SMS2** SphingoMyelin Synthase 2. 117

**sPI** L- $\alpha$ -Phosphatidylinositol (Soy). 21

**SUV** Small Unilamellar Vesicles. 10, 11, 24, 26–31, 39, 42, 73, 104, 105

**TAMRA** 5-(and-6)-carboxyTetrAMethylRhodAmine. 22, 32

**Texas Red DHPE** Texas Red<sup>®</sup> 1,2-Dihexadecanoyl-sn-Glycero-3-Phosphoethanolamine. 22, 32, 107

**TFE** 2,2,2-Trifluoroethanol. 22, 23, 29, 39, 104–106

**TIRF** Total Internal Reflection Fluorescence. 81

**TJ** Tight Junction. 3

**TM** TransMembrane. x, 17, 22, 29, 38, 71–79, 119

**VF** Vesicle Fusion. 11, 26, 42–44, 47, 48, 117

**WASp** Wiskott-Aldrich Syndrome protein. 8

**WT** WildType. 22–24, 29, 38, 73–79, 99, 100, 104, 105, 107, 108



# References

- [1] Thompson, B. J. *Development* **2013**, *140*, 13–21.
- [2] Nature Publishing Group; *Cell polarity*; 2015; [Online; accessed 20-January-2015]. <http://www.nature.com/subjects/cell-polarity>.
- [3] Raggars, R. J.; Pomorski, T.; Holthuis, J. C.; Kälin, N.; van Meer, G. *Traffic (Copenhagen, Denmark)* **2000**, *1*, 226–234.
- [4] Simons, K.; Sampaio, J. L. *Cold Spring Harbor Perspectives in Biology* **2011**, *3*, a004697.
- [5] Chau, A. H.; Walter, J. M.; Gerardin, J.; Tang, C.; Lim, W. A. *Cell* **2012**, *151*, 320–332.
- [6] St Johnston, D.; Ahringer, J. *Cell* **2010**, *141*, 757–774.
- [7] Swaney, K. F.; Huang, C.-H.; Devreotes, P. N. *Annual review of biophysics* **2010**, *39*, 265–289.
- [8] Inagaki, N.; Toriyama, M.; Sakumura, Y. *Developmental neurobiology* **2011**, *71*, 584–593.
- [9] Horton, A. C.; Ehlers, M. D. *Neuron* **2003**, *40*, 277–295.
- [10] Slaughter, B. D.; Smith, S. E.; Li, R. *Cold Spring Harbor Perspectives in Biology* **2009**, *1*, a003384.
- [11] Motegi, F.; Seydoux, G. *Philosophical transactions of the Royal Society of London. Series B, Biological sciences* **2013**, *368*, 20130010.
- [12] Guo, S.; Kemphues, K. J. *Cell* **1995**, *81*, 611–620.
- [13] Boyd, L.; Guo, S.; Levitan, D.; Stinchcomb, D. T.; Kemphues, K. J. *Development* **1996**, *122*, 3075–3084.
- [14] Hoege, C.; Constantinescu, A.-T.; Schwager, A.; Goehring, N. W.; Kumar, P.; Hyman, A. A. *Current Biology* **2010**, *20*, 1296–1303.
- [15] Beatty, A.; Morton, D. G.; Kemphues, K. *Development* **2010**, *137*, 3995–4004.
- [16] Etemad-Moghadam, B.; Guo, S.; Kemphues, K. J. *Cell* **1995**, *83*, 743–752.
- [17] Watts, J. L.; Etemad-Moghadam, B.; Guo, S.; Boyd, L.; Draper, B. W.; Mello, C. C.; Priess, J. R.; Kemphues, K. J. *Development* **1996**, *122*, 3133–3140.

- [18] Tabuse, Y.; Izumi, Y.; Piano, F.; Kempfues, K. J.; Miwa, J.; Ohno, S. *Development* **1998**, *125*, 3607–3614.
- [19] Coradini, D.; Casarsa, C.; Oriana, S. *Acta pharmacologica Sinica* **2011**, *32*, 552–564.
- [20] Cramer, L. P. *Frontiers in bioscience: a journal and virtual library* **1997**, *2*, d260–70.
- [21] Mogilner, A.; Allard, J.; Wollman, R. *Science* **2012**, *336*, 175–179.
- [22] Seydoux, G. *Nature Cell Biology* **2013**, *15*, 9–10.
- [23] Wodarz, A.; Näthke, I. *Nature Cell Biology* **2007**, *9*, 1016–1024.
- [24] Etienne-Manneville, S. *Oncogene* **2008**, *27*, 6970–6980.
- [25] Macara, I. G.; McCaffrey, L. *Philosophical transactions of the Royal Society of London. Series B, Biological sciences* **2013**, *368*, 20130012.
- [26] Vasioukhin, V. *Developmental Neuroscience* **2006**, *28*, 13–24.
- [27] Goldstein, B.; Macara, I. G. *Developmental Cell* **2007**, *13*, 609–622.
- [28] Turing, A. M. *Philosophical Transactions of the Royal Society of London. Series B, Biological Sciences* **1952**, *237*, 37–72.
- [29] Gierer, A.; Meinhard, H. *Kybernetik* **1972**, *12*, 30–39.
- [30] Meinhardt, H. *Current Opinion in Genetics & Development* **2007**, *17*, 272–280.
- [31] Deplazes, A. *EMBO reports* **2009**, *10*, 428–432.
- [32] Diez, M. S.; Lam, C. M. C.; Leprince, A.; dos Santos, V. A. P. M. *Biotechnology journal* **2009**, *4*, 1382–1391.
- [33] Nandagopal, N.; Elowitz, M. B. *Science* **2011**, *333*, 1244–1248.
- [34] Gibson, D. G.; et al. *Science* **2008**, *319*, 1215–1220.
- [35] Benner, S. A.; Hutter, D.; Sismour, A. M. *Nucleic acids research. Supplement No. 3* **2003**, 125–126.
- [36] Luisi, P. L. *The Anatomical record* **2002**, *268*, 208–214.
- [37] Schwille, P.; Diez, S. *Critical Reviews in Biochemistry and Molecular Biology* **2009**, *44*, 223–242.
- [38] Schwille, P. *Science* **2011**, *333*, 1252–1254.
- [39] Loisel, T. P.; Boujemaa, R.; Pantaloni, D.; Carlier, M. F. *Nature* **1999**, *401*, 613–616.
- [40] Bernheim-Groswasser, A.; Wiesner, S.; Golsteyn, R. M.; Carlier, M.-F.; Sykes, C. *Nature* **2002**, *417*, 308–311.
- [41] Upadhyaya, A.; Chabot, J. R.; Andreeva, A.; Samadani, A.; van Oudenaarden, A. *Proceedings of the National Academy of Sciences of the United States of America* **2003**, *100*, 4521–4526.



- [42] Loose, M.; Schwille, P. *Journal of structural biology* **2009**, *168*, 143–151.
- [43] Cameron, L. A.; Footer, M. J.; van Oudenaarden, A.; Theriot, J. A. *Proceedings of the National Academy of Sciences of the United States of America* **1999**, *96*, 4908–4913.
- [44] Pantaloni, D.; Le Clainche, C.; Carlier, M. F. *Science* **2001**, *292*, 2012–2012.
- [45] Giardini, P. A.; Fletcher, D. A.; Theriot, J. A. *Proceedings of the National Academy of Sciences of the United States of America* **2003**, *100*, 6493–6498.
- [46] Yarar, D.; To, W.; Abo, A.; Welch, M. D. *Current Biology* **1999**, *9*, 555–558.
- [47] Lacayo, C. I.; Soneral, P. A. G.; Zhu, J.; Tsuchida, M. A.; Footer, M. J.; Soo, F. S.; Lu, Y.; Xia, Y.; Mogilner, A.; Theriot, J. A. *Molecular Biology of the Cell* **2012**, *23*, 614–629.
- [48] Avanti Polar Lipids, I.; *What is an SUV and LUV and how do they differ?*; 2015; [Online; accessed 09-February-2015]. [https://www.avantilipids.com/index.php?view=items&cid=5&id=14&option=com\\_quickfaq&Itemid=385](https://www.avantilipids.com/index.php?view=items&cid=5&id=14&option=com_quickfaq&Itemid=385).
- [49] Walde, P.; Cosentino, K.; Engel, H.; Stano, P. *ChemBioChem* **2010**, *11*, 848–865.
- [50] Angelova, M. I.; Dimitrov, D. S. *Faraday Discussions* **1986**, *81*, 303–311.
- [51] Pautot, S.; Frisken, B. J.; Weitz, D. A. *Langmuir* **2003**, *19*, 2870–2879.
- [52] Pautot, S.; Frisken, B. J.; Weitz, D. A. *Proceedings of the National Academy of Sciences of the United States of America* **2003**, *100*, 10718–10721.
- [53] Pontani, L.-L.; van der Gucht, J.; Salbreux, G.; Heuvingh, J.; Joanny, J.-F.; Sykes, C. *Biophysical Journal* **2009**, *96*, 192–198.
- [54] Sanderson, J. M. *Molecular Membrane Biology* **2012**, *29*, 118–143.
- [55] Tamm, L. K.; McConnell, H. M. *Biophysical Journal* **1985**, *47*, 105–113.
- [56] Crane, J. M.; Kiessling, V.; Tamm, L. K. *Langmuir* **2005**, *21*, 1377–1388.
- [57] Brian, A. A.; McConnell, H. M. *Proceedings of the National Academy of Sciences of the United States of America* **1984**, *81*, 6159–6163.
- [58] Visco, I.; Chiantia, S.; Schwille, P. *Langmuir* **2014**, *30*, 7475–7484.
- [59] Johnson, S. J.; Bayerl, T. M.; McDermott, D. C.; Adam, G. W.; Rennie, A. R.; Thomas, R. K.; Sackmann, E. *Biophysical Journal* **1991**, *59*, 289–294.
- [60] Zhang, L.; Granick, S. *The Journal of chemical physics* **2005**, *123*, 211104.
- [61] Przybylo, M.; Sýkora, J.; Humpolíckova, J.; Benda, A.; Zan, A.; Hof, M. *Langmuir* **2006**, *22*, 9096–9099.
- [62] Schmitt, J.; Danner, B.; Bayerl, T. M. *Langmuir* **2001**, *17*, 244–246.
- [63] Wagner, M. L.; Tamm, L. K. *Biophysical Journal* **2000**, *79*, 1400–1414.

- [64] Kahya, N.; Scherfeld, D.; Bacia, K.; Poolman, B.; Schwille, P. *Journal of Biological Chemistry* **2003**, *278*, 28109–28115.
- [65] Chiantia, S.; Ries, J.; Kahya, N.; Schwille, P. *Chemphyschem : a European journal of chemical physics and physical chemistry* **2006**, *7*, 2409–2418.
- [66] MAGDE, D.; Webb, W. W.; ELSON, E. *Physical Review Letters* **1972**, *29*, 705–708.
- [67] García-Sáez, A. J.; Schwille, P. *Methods* **2008**, *46*, 116–122.
- [68] Chiantia, S.; Ries, J.; Schwille, P. *Biochimica et Biophysica Acta* **2009**, *1788*, 225–233.
- [69] Ries, J.; Schwille, P. *Physical Chemistry Chemical Physics* **2008**, *10*, 3487–3497.
- [70] Heinemann, F.; Betaneli, V.; Thomas, F. A.; Schwille, P. *Langmuir* **2012**, *28*, 13395–13404.
- [71] Betaneli, V.; Schwille, P. *Methods in Molecular Biology (Clifton, N.J.)* **2013**, *974*, 253–278.
- [72] Bacia, K. *Journal of Biological Chemistry* **2004**, *279*, 37951–37955.
- [73] Kahya, N.; Brown, D. A.; Schwille, P. *Biochemistry* **2005**, *44*, 7479–7489.
- [74] Rusu, L.; Gambhir, A.; McLaughlin, S.; Rädler, J. *Biophysical Journal* **2004**, *87*, 1044–1053.
- [75] Rhoades, E.; Ramlall, T. F.; Webb, W. W.; Eliezer, D. *Biophysical Journal* **2006**, *90*, 4692–4700.
- [76] Blin, G.; Margeat, E.; Carvalho, K.; Royer, C. A.; Roy, C.; Picart, C. *Biophysical Journal* **2008**, *94*, 1021–1033.
- [77] Middleton, E. R.; Rhoades, E. *Biophysical Journal* **2010**, *99*, 2279–2288.
- [78] Horner, A.; Goetz, F.; Tampé, R.; Klussmann, E.; Pohl, P. *Journal of Biological Chemistry* **2012**, *287*, 42495–42501.
- [79] Kahya, N.; Wiersma, D. A.; Poolman, B.; Hoekstra, D. *The Journal of biological chemistry* **2002**, *277*, 39304–39311.
- [80] Liu, P.; Sudhakaran, T.; Koh, R. M. L.; Hwang, L. C.; Ahmed, S.; Maruyama, I. N.; Wohland, T. *Biophysical Journal* **2007**, *93*, 684–698.
- [81] García-Sáez, A. J.; Ries, J.; Orzáez, M.; Pérez-Payà, E.; Schwille, P. *Nature Structural & Molecular Biology* **2009**, *16*, 1178–1185.
- [82] Worch, R.; Bokel, C.; Hofinger, S.; Schwille, P.; Weidemann, T. *Proteomics* **2010**, *10*, 4196–4208.
- [83] Forstner, M. B.; Yee, C. K.; Parikh, A. N.; Groves, J. T. *Journal of the American Chemical Society* **2006**, *128*, 15221–15227.

- [84] Honigsmann, A.; Walter, C.; Erdmann, F.; Eggeling, C.; Wagner, R. *Biophysical Journal* **2010**, *98*, 2886–2894.
- [85] Cheng, H.-T.; Megha; London, E. *The Journal of Biological Chemistry* **2009**, *284*, 6079–6092.
- [86] Chiantia, S.; Schwille, P.; Klymchenko, A. S.; London, E. *Biophysical Journal* **2011**, *100*, LO1–LO3.
- [87] Schroeder, R.; London, E.; Brown, D. *Proceedings of the National Academy of Sciences of the United States of America* **1994**, *91*, 12130–12134.
- [88] Chiantia, S.; Ries, J.; Chwastek, G.; Carrer, D.; Li, Z.; Bittman, R.; Schwille, P. *Biochimica et Biophysica Acta (BBA) - Biomembranes* **2008**, *1778*, 1356–1364.
- [89] Doering, T. L.; Englund, P. T.; Hart, G. W. *Current Protocols in Protein Science / editorial board, John E. Coligan ... [et al.]* **2001**, Chapter 12, Unit 12.5.
- [90] Nikolaus, J.; Stoeckl, M.; Langosch, D.; Volkmer, R.; Herrmann, A. *Biophysical Journal* **2010**, *98*, 1192–1199.
- [91] Motegi, F.; Zonies, S.; Hao, Y.; Cuenca, A. A.; Griffin, E.; Seydoux, G. *Nature Cell Biology* **2011**, *13*, 1361–1367.
- [92] Miller, L. P.; *Analyzing gels and western blots with ImageJ*; 2010; [Online; accessed 13-January-2015]. <http://lukemiller.org/index.php/2010/11/analyzing-gels-and-western-blots-with-image-j/>.
- [93] Rouser, G.; Fkeischer, S.; Yamamoto, A. *Lipids* **1970**, *5*, 494–496.
- [94] García-Sáez, A. J.; Carrer, D. C.; Schwille, P. *Methods in Molecular Biology (Clifton, N.J.)* **2010**, *606*, 493–508.
- [95] Bacia, K.; Schwille, P.; Kurzchalia, T. *Proceedings of the National Academy of Sciences of the United States of America* **2005**, *102*, 3272–3277.
- [96] Milhiet, P.-E.; Gubellini, F.; Berquand, A.; Dosset, P.; Rigaud, J.-L.; Le Grimmellec, C.; Lévy, D. *Biophysical Journal* **2006**, *91*, 3268–3275.
- [97] Lin, Q.; London, E. *PLoS One* **2014**, *9*, e87903.
- [98] McIntyre, J. C.; Sleight, R. G. *Biochemistry* **1991**, *30*, 11819–11827.
- [99] Ries, J.; Chiantia, S.; Schwille, P. *Biophysical Journal* **2009**, *96*, 1999–2008.
- [100] Sezgin, E.; Levental, I.; Grzybek, M.; Schwarzmann, G.; Mueller, V.; Honigsmann, A.; Belov, V. N.; Eggeling, C.; Coskun, U.; Simons, K.; Schwille, P. *Biochimica et Biophysica Acta (BBA) - Biomembranes* **2012**, *1818*, 1777–1784.
- [101] Miura, K.; *Analysis of FRAP Curves*; European Molecular Biology Laboratory, Heidelberg, Germany; 2012.
- [102] Petrášek, Z.; Schwille, P. *Biophysical Journal* **2008**, *94*, 1437–1448.

- [103] Dertinger, T.; Pacheco, V.; von der Hocht, I.; Hartmann, R.; Gregor, I.; Enderlein, J. *Chemphyschem : a European journal of chemical physics and physical chemistry* **2007**, *8*, 433–443.
- [104] Müller, P.; Schwille, P.; Weidemann, T. *Bioinformatics (Oxford, England)* **2014**, *30*, 2532–2533.
- [105] Szeto, T. H.; Rowland, S. L.; Rothfield, L. I.; King, G. F. *Proceedings of the National Academy of Sciences of the United States of America* **2002**, *99*, 15693–15698.
- [106] Szeto, T. H.; Rowland, S. L.; Habrukowich, C. L.; King, G. F. *Journal of Biological Chemistry* **2003**, *278*, 40050–40056.
- [107] Freire, J. M.; Domingues, M. M.; Matos, J.; Melo, M. N.; Veiga, A. S.; Santos, N. C.; Castanho, M. A. R. B. *European Biophysics Journal* **2011**, *40*, 481–487.
- [108] Fabre, R. M.; Talham, D. R. *Langmuir* **2009**, *25*, 12644–12652.
- [109] Wacklin, H. P. *Langmuir* **2011**, *27*, 7698–7707.
- [110] Rossetti, F. F.; Textor, M.; Reviakine, I. *Langmuir* **2006**, *22*, 3467–3473.
- [111] Stanglmaier, S.; Hertrich, S.; Fritz, K.; Moulin, J. F.; Haese-Seiller, M.; Rädler, J. O.; Nickel, B. *Langmuir* **2012**, *28*, 10818–10821.
- [112] Anderson, T. G.; Tan, A. M.; Ganz, P.; Seelig, J. *Biophysical Journal* **2004**, *86*, 174A–174A.
- [113] Pitha, J.; Irie, T.; Sklar, P. B.; Nye, J. S. *Life Sciences* **1988**, *43*, 493–502.
- [114] Kiessling, V.; Crane, J. M.; Tamm, L. K. *Biophysical Journal* **2006**, *91*, 3313–3326.
- [115] Wan, C.; Kiessling, V.; Tamm, L. K. *Biochemistry* **2008**, *47*, 2190–2198.
- [116] Collins, M. D.; Keller, S. L. *Proceedings of the National Academy of Sciences of the United States of America* **2008**, *105*, 124–128.
- [117] Hussain, N. F.; Siegel, A. P.; Ge, Y.; Jordan, R.; Naumann, C. A. *Biophysical Journal* **2013**, *104*, 2212–2221.
- [118] Chiantia, S.; London, E. *Biophysical Journal* **2012**, *103*, 2311–2319.
- [119] Liu, J.; Conboy, J. C. *Biophysical Journal* **2005**, *89*, 2522–2532.
- [120] Anglin, T. C.; Cooper, M. P.; Li, H.; Chandler, K.; Conboy, J. C. *The Journal of Physical Chemistry. B.* **2010**, *114*, 1903–1914.
- [121] Dezi, M.; Di Cicco, A.; Bassereau, P.; Lévy, D. *Proceedings of the National Academy of Sciences of the United States of America* **2013**, *110*, 7276–7281.
- [122] Salafsky, J.; Groves, J. T.; Boxer, S. G. *Biochemistry* **1996**, *35*, 14773–14781.
- [123] Petruzielo, R. S.; Heberle, F. A.; Drazba, P.; Katsaras, J.; Feigenson, G. W. *Biochimica et Biophysica Acta (BBA) - Biomembranes* **2013**, *1828*, 1302–1313.

- [124] Feigenson, G. W. *Annual Review of Biophysics and Biomolecular Structure* **2007**, *36*, 63–77.
- [125] Feigenson, G. W. *Biochimica et Biophysica Acta* **2009**, *1788*, 47–52.
- [126] Choubey, A.; Kalia, R. K.; Malmstadt, N.; Nakano, A.; Vashishta, P. *Biophysical Journal* **2013**, *104*, 2429–2436.
- [127] Kiessling, V.; Wan, C.; Tamm, L. K. *Biochimica et Biophysica Acta* **2009**, *1788*, 64–71.
- [128] Wang, T. Y.; Silviu, J. R. *Biophysical Journal* **2001**, *81*, 2762–2773.
- [129] Garg, S.; R  he, J.; L  dtke, K.; Jordan, R.; Naumann, C. A. *Biophysical Journal* **2007**, *92*, 1263–1270.
- [130] Kahya, N.; P  cheur, E.-I.; de Boeij, W. P.; Wiersma, D. A.; Hoekstra, D. *Biophysical Journal* **2001**, *81*, 1464–1474.
- [131] Nikolaus, J.; Scolari, S.; Bayraktarov, E.; Jungnick, N.; Engel, S.; Plazzo, A. P.; St  ckl, M.; Volkmer, R.; Veit, M.; Herrmann, A. *Biophysical Journal* **2010**, *99*, 489–498.
- [132] Betaneli, V.; Petrov, E. P.; Schwille, P. *Biophysical Journal* **2012**, *102*, 523–531.
- [133] Liu, A. P.; Fletcher, D. A. *Biophysical Journal* **2006**, *91*, 4064–4070.
- [134] Merkle, D.; Kahya, N.; Schwille, P. *ChemBioChem* **2008**, *9*, 2673–2681.
- [135] Kaufmann, A.; Beier, V.; Franquelim, H. G.; Wollert, T. *Cell* **2014**, *156*, 469–481.
- [136] Martos, A.; Jim  nez, M.; Rivas, G.; Schwille, P. *Trends in Cell Biology* **2012**, *22*, 634–643.
- [137] Laan, L.; Pavin, N.; Husson, J.; Romet-Lemonne, G.; van Duijn, M.; L  pez, M. P.; Vale, R. D.; J  licher, F.; Reck-Peterson, S. L.; Dogterom, M. *Cell* **2012**, *148*, 502–514.
- [138] Zieske, K.; Schwille, P. *Angewandte Chemie-International Edition* **2013**, *52*, 459–462.
- [139] Arumugam, S.; Petr   ek, Z.; Schwille, P. *Proceedings of the National Academy of Sciences of the United States of America* **2014**, *111*, E1192–200.
- [140] Berndl, K.; K  s, J.; Lipowsky, R.; Sackmann, E.; Seifert, U. *Europhysics Letters* **1990**, *13*, 659–664.
- [141] Farge, E.; Devaux, P. F. *Biophysical Journal* **1992**, *61*, 347–357.
- [142] Seifert, U. *Advances in Physics* **1997**, *46*, 13–137.
- [143] Khalifat, N.; Rahimi, M.; Bitbol, A.-F.; Seigneuret, M.; Fournier, J.-B.; Puff, N.; Arroyo, M.; Angelova, M. I. *Biophysical Journal* **2014**, *107*, 879–890.
- [144] J  licher, F.; LIPOWSKY, R. *Physical Review E* **1996**, *53*, 2670–2683.
- [145] Jiang, Y.; Lookman, T.; Saxena, A. *Physical Review E* **2000**, *61*, R57–R60.
- [146] Baumgart, T.; Hess, S. T.; Webb, W. W. *Nature* **2003**, *425*, 821–824.

- [147] Dimova, R. *Advances in Colloid and Interface Science* **2014**, *208*, 225–234.
- [148] Vitkova, V.; Genova, J.; Mitov, M. D.; Bivas, I. *Molecular Crystals and Liquid Crystals* **2006**, *449*, 95–106.
- [149] Andersen, H. D.; Wang, C.; Arleth, L.; Peters, G. H.; Westh, P. *Proceedings of the National Academy of Sciences of the United States of America* **2011**, *108*, 1874–1878.
- [150] Bouvrais, H.; Duelund, L.; Ipsen, J. H. *Langmuir* **2014**, *30*, 13–16.
- [151] Pabst, G.; Hodzic, A.; Strancar, J.; Danner, S.; Rappolt, M.; Laggner, P. *Biophysical Journal* **2007**, *93*, 2688–2696.
- [152] Petrache, H. I.; Zemb, T.; Belloni, L.; Parsegian, V. A. *Proceedings of the National Academy of Sciences of the United States of America* **2006**, *103*, 7982–7987.
- [153] Käs, J.; Sackmann, E. *Biophysical Journal* **1991**, *60*, 825–844.
- [154] Lipowsky, R. *Journal De Physique II* **1992**, *2*, 1825–1840.
- [155] Bacia, K.; Futai, E.; Prinz, S.; Meister, A.; Daum, S.; Glatte, D.; Briggs, J. A. G.; Schekman, R. *Scientific Reports* **2011**, *1*.
- [156] Baumgart, T.; Hunt, G.; Farkas, E. R.; Webb, W. W.; Feigenson, G. W. *Biochimica et Biophysica Acta (BBA) - Biomembranes* **2007**, *1768*, 2182–2194.
- [157] Hirst, G. K. *Science* **1941**, *94*, 22–23.
- [158] Skehel, J. J.; Wiley, D. C. *Annual Review of Biochemistry* **2000**, *69*, 531–569.
- [159] Wilson, I. A.; Skehel, J. J.; Wiley, D. C. *Nature* **1981**, *289*, 366–373.
- [160] Scheiffele, P.; Roth, M. G.; Simons, K. *The EMBO Journal* **1997**, *16*, 5501–5508.
- [161] Scheiffele, P.; Rietveld, A.; Wilk, T.; Simons, K. *The Journal of Biological Chemistry* **1999**, *274*, 2038–2044.
- [162] Scolari, S.; Engel, S.; Krebs, N.; Plazzo, A. P.; De Almeida, R. F.; Prieto, M.; Veit, M.; Herrmann, A. *The Journal of Biological Chemistry* **2009**, *284*, 15708–15716.
- [163] Engel, S.; Scolari, S.; Thaa, B.; Krebs, N.; Korte, T.; Herrmann, A.; Veit, M. *Biochemical Journal* **2010**, *425*, 567–573.
- [164] Tatulian, S. A.; Tamm, L. K. *Biochemistry* **2000**, *39*, 496–507.
- [165] Perillo, V. L.; Peñalva, D. A.; Avelaño, M. I.; Barrantes, F. J.; Antollini, S. S. *Biophysical Journal* **2014**, *106*, 711a.
- [166] Ramadurai, S.; Holt, A.; Schäfer, L. V.; Krasnikov, V. V.; Rijkers, D. T. S.; Marrink, S. J.; Killian, J. A.; Poolman, B. *Biophysical Journal* **2010**, *99*, 1447–1454.
- [167] Lingwood, D.; Simons, K. *Science* **2009**, *327*, 46–50.
- [168] London, E. *Biochimica et Biophysica Acta (BBA) - Molecular Cell Research* **2005**, *1746*, 203–220.

- [169] Guidotti, G. *Annual Review of Biochemistry* **1972**, *41*, 731–752.
- [170] Parton, D. L.; Tek, A.; Baaden, M.; Sansom, M. S. *PLoS Computational Biology* **2013**, *9*, e1003034.
- [171] van Duyl, B. Y.; Rijkers, D. T.; de Kruijff, B.; Killian, J. A. *FEBS Letters* **2002**, *523*, 79–84.
- [172] Fastenberg, M. E.; Shogomori, H.; Xu, X.; Brown, D. A.; London, E. *Biochemistry* **2003**, *42*, 12376–12390.
- [173] Schaefer, L. V.; de Jong, D. H.; Holt, A.; Rzepiela, A. J.; de Vries, A. H.; Poolman, B.; Killian, J. A.; Marrink, S. J. *Proceedings of the National Academy of Sciences of the United States of America* **2011**, *108*, 1343–1348.
- [174] Ge, Y.; Siegel, A. P.; Jordan, R.; Naumann, C. A. *Biophysical Journal* **2014**, *107*, 2101–2111.
- [175] Keller, H.; Kräusslich, H.-G.; Schwille, P. *Cellular Microbiology* **2013**, *15*, 237–247.
- [176] Levental, I.; Grzybek, M.; Simons, K. *Biochemistry* **2010**, *49*, 6305–6316.
- [177] Goins, B.; Freier, E. *Biochemistry* **1985**, *24*, 1791–1797.
- [178] Ge, M.; Freed, J. H. *Biophysical Journal* **2009**, *96*, 4925–4934.
- [179] Domański, J.; Marrink, S. J.; Schäfer, L. V. *Biochimica et Biophysica Acta (BBA) - Biomembranes* **2012**, *1818*, 984–994.
- [180] Patarraia, S.; Liu, Y.; Lipowsky, R.; Dimova, R. *Biochimica et Biophysica Acta* **2014**, *1838*, 2036–2045.
- [181] Cho, W.; Stahelin, R. V. *Annual Review of Biophysics and Biomolecular Structure* **2005**, *34*, 119–151.
- [182] Munro, S. *Current Opinion in Cell Biology* **2002**, *14*, 506–514.
- [183] Murphy, J.; Knutson, K.; Hinderliter, A. *Methods in Enzymology* **2009**, *466*, 431–453.
- [184] Lomize, A. L.; Pogozheva, I. D.; Lomize, M. A.; Mosberg, H. I. *BMC Structural Biology* **2007**, *7*, 44.
- [185] Mulgrew-Nesbitt, A.; Diraviyam, K.; Wang, J.; Singh, S.; Murray, P.; Li, Z.; Rogers, L.; Mirkovic, N.; Murray, D. *Biochimica et Biophysica Acta* **2006**, *1761*, 812–826.
- [186] White, S. H.; Wimley, W. C.; Ladokhin, A. S.; Hristova, K. *Methods in Enzymology* **1998**, *295*, 62–87.
- [187] Cho, W.; Bittova, L.; Stahelin, R. V. *Analytical Biochemistry* **2001**, *296*, 153–161.
- [188] Zhao, H.; Lappalainen, P. *Molecular Biology of the Cell* **2012**, *23*, 2823–2830.
- [189] Scott, J. L.; Musselman, C. A.; Adu-Gyamfi, E.; Kutateladze, T. G.; Stahelin, R. V. *Integrative Biology : quantitative biosciences from nano to macro* **2012**, *4*, 247–258.

- [190] Kang, M.; Day, C. A.; DiBenedetto, E.; Kenworthy, A. K. *Biophysical Journal* **2010**, *99*, 2737–2747.
- [191] Fox, C. B.; Wayment, J. R.; Myers, G. A.; Endicott, S. K.; Harris, J. M. *Analytical Chemistry* **2009**, *81*, 5130–5138.
- [192] Hatzakis, N. S.; Bhatia, V. K.; Larsen, J.; Madsen, K. L.; Bolinger, P.-Y.; Kunding, A. H.; Castillo, J.; Gether, U.; Hedegård, P.; Stamou, D. *Nature chemical biology* **2009**, *5*, 835–841.
- [193] Wu, B.; Chen, Y.; Mueller, J. D. *Biophysical Journal* **2008**, *94*, 2800–2808.
- [194] Engelke, H.; Dorn, I.; Raedler, J. O. *Soft Matter* **2009**, *5*, 4283–4289.
- [195] Melo, A. M.; Prieto, M.; Coutinho, A. *Biochimica et Biophysica Acta (BBA) - Biomembranes* **2011**, 1–10.
- [196] Knecht, S.; Ricklin, D.; Eberle, A. N.; Ernst, B. *Journal of Molecular Recognition* **2009**, *22*, 270–279.
- [197] Khan, F.; He, M.; Taussig, M. J. *Analytical Chemistry* **2006**, *78*, 3072–3079.
- [198] Rüttinger, S.; Buschmann, V.; Krämer, B.; Erdmann, R.; Macdonald, R.; Koberling, F. *Journal of Microscopy* **2008**, *232*, 343–352.
- [199] Weidemann, T.; Wachsmuth, M.; Knoch, T. A.; Muller, G.; Waldeck, W.; Langowski, J. *Journal of Molecular Biology* **2003**, *334*, 229–240.
- [200] Larsen, J.; Hatzakis, N. S.; Stamou, D. *Journal of the American Chemical Society* **2011**, *133*, 10685–10687.
- [201] Pan, J.; Tristram-Nagle, S.; Kučerka, N.; Nagle, J. F. *Biophysical Journal* **2008**, *94*, 117–124.
- [202] Oh, K. J.; Barbuto, S.; Pitter, K.; Morash, J.; Walensky, L. D.; Korsmeyer, S. J. *The Journal of Biological Chemistry* **2006**, *281*, 36999–37008.
- [203] Guignet, E. G.; Hovius, R.; Vogel, H. *Nature Biotechnology* **2004**, *22*, 440–444.
- [204] Hintersteiner, M.; Weidemann, T.; Kimmerlin, T.; Filiz, N.; Buehler, C.; Auer, M. *ChemBioChem* **2008**, *9*, 1391–1395.
- [205] Lauer, S. A.; Nolan, J. P. *Cytometry* **2002**, *48*, 136–145.
- [206] Enderlein, J.; Ruckstuhl, T.; Seeger, S. *Applied Optics* **1999**, *38*, 724–732.
- [207] Ries, J.; Petrov, E. P.; Schwille, P. *Biophysical Journal* **2008**, *95*, 390–399.
- [208] Patel, J. D.; O’Carra, R.; Jones, J.; Woodward, J. G.; Mumper, R. J. *Pharmaceutical Research* **2007**, *24*, 343–352.
- [209] Kapanidis, A. N.; Ebright, Y. W.; Ebright, R. H. *Journal of the American Chemical Society* **2001**, *123*, 12123–12125.



- [210] Chikh, G. G.; Li, W. M.; Schutze-Redelmeier, M.-P.; Meunier, J.-C.; Bally, M. B. *Biochimica et Biophysica Acta* **2002**, *1567*, 204–212.
- [211] Cuenca, A. A.; Schetter, A.; Aceto, D.; Kemphues, K.; Seydoux, G. *Development* **2003**, *130*, 1255–1265.
- [212] Hoegge, C.; Hyman, A. A. *Nature Reviews Molecular Cell Biology* **2013**, *14*, 315–322.
- [213] Goehring, N. W. *Experimental cell research* **2014**, *328*, 258–266.
- [214] Tostevin, F.; Howard, M. *Biophysical Journal* **2008**, *95*, 4512–4522.
- [215] Dawes, A. T.; Munro, E. M. *Biophysical Journal* **2011**, *101*, 1412–1422.
- [216] Goehring, N. W.; Trong, P. K.; Bois, J. S.; Chowdhury, D.; Nicola, E. M.; Hyman, A. A.; Grill, S. W. *Science* **2011**, *334*, 1137–1141.
- [217] Kravtsova, N.; Dawes, A. T. *Bulletin of mathematical biology* **2014**, *76*, 2426–2448.
- [218] Benton, R.; St Johnston, D. *Current Biology* **2003**, *13*, 1330–1334.
- [219] Ndifon, A. N.; Ph.D. thesis; Mathematisch-Naturwissenschaftlichen Fakultät der Universität zu Köln; 2013.
- [220] Betschinger, J.; Eisenhaber, F.; Knoblich, J. A. *Current Biology* **2005**, *15*, 276–282.
- [221] Betschinger, J.; Mechtler, K.; Knoblich, J. A. *Nature* **2003**, *422*, 326–330.
- [222] Plant, P. J.; Fawcett, J. P.; Lin, D.; Holdorf, A. D.; Binns, K.; Kulkarni, S.; Pawson, T. *Nature Cell Biology* **2003**, *5*, 301–308.
- [223] Benton, R.; St Johnston, D. *Cell* **2003**, *115*, 691–704.
- [224] Beatty, A.; Morton, D. G.; Kemphues, K. *Development* **2013**, *140*, 2005–2014.
- [225] Wirtz-Peitz, F.; Nishimura, T.; Knoblich, J. A. *Cell* **2008**, *135*, 161–173.
- [226] Qin, Z. H.; Cafiso, D. S. *Biochemistry* **1996**, *35*, 2917–2925.
- [227] Hao, Y.; Boyd, L.; Seydoux, G. *Developmental Cell* **2006**, *10*, 199–208.
- [228] Brzeska, H.; Guag, J.; Remmert, K.; Chacko, S.; Korn, E. D. *Journal of Biological Chemistry* **2010**, *285*, 5738–5747.
- [229] Carvalho, K.; Ramos, L.; Roy, C.; Picart, C. *Biophysical Journal* **2008**, *95*, 4348–4360.
- [230] Schmitt, L.; Dietrich, C.; Tampe, R. *Journal of the American Chemical Society* **1994**, *116*, 8485–8491.
- [231] Brückner, A.; Polge, C.; Lentze, N.; Auerbach, D.; Schlattner, U. *International Journal of Molecular Sciences* **2009**, *10*, 2763–2788.
- [232] Lemmon, M. A. *Nature Reviews Molecular Cell Biology* **2008**, *9*, 99–111.
- [233] Lemmon, M. A. *Traffic (Copenhagen, Denmark)* **2003**, *4*, 201–213.

- [234] McLaughlin, S.; Wang, J.; Gambhir, A.; Murray, D. *Annual Review of Biophysics and Biomolecular Structure* **2002**, *31*, 151–175.
- [235] Wikipedia; *Zeta potential* — *Wikipedia, The Free Encyclopedia*; 2014; [Online; accessed 13-January-2015]. [http://en.wikipedia.org/w/index.php?title=Zeta\\_potential&oldid=634117055](http://en.wikipedia.org/w/index.php?title=Zeta_potential&oldid=634117055).
- [236] Malvern Instruments Ltd.; Enigma Business Park, Grovewood Road, Malvern, Worcestershire WR14 1XZ, United Kingdom; *Zetasizer Nano User Manual MANO485*; 1st ed.; April 2013.
- [237] Franquelim, H. G.; Veiga, A. S.; Weissmüller, G.; Santos, N. C.; Castanho, M. A. R. B. *Biochimica et Biophysica Acta (BBA) - Biomembranes* **2010**, *1798*, 1234–1243.
- [238] Kooijman, E. E.; King, K. E.; Gangoda, M.; Gericke, A. *Biochemistry* **2009**, *48*, 9360–9371.
- [239] Panbianco, C.; Weinkove, D.; Zanin, E.; Jones, D.; Divecha, N.; Gotta, M.; Ahringer, J. *Developmental Cell* **2008**, *15*, 198–208.
- [240] Ladokhin, A. S.; Fernández-Vidal, M.; White, S. H. *Journal of Membrane Biology* **2010**, *236*, 247–253.
- [241] Luo, P.; Baldwin, R. L. *Biochemistry* **1997**, *36*, 8413–8421.
- [242] Kalmes, A.; Merdes, G.; Neumann, B.; Strand, D.; Mechler, B. M. *Journal of Cell Science* **1996**, *109* ( Pt 6), 1359–1368.
- [243] Bhakdi, S.; Tranumjensen, J. *Microbiological Reviews* **1991**, *55*, 733–751.
- [244] Song, L. Z.; Hobaugh, M. R.; Shustak, C.; Cheley, S.; Bayley, H.; Gouaux, J. E. *Science* **1996**, *274*, 1859–1866.
- [245] Luisi, P. L.; Allegretti, M.; Pereira de Souza, T.; Steiniger, F.; Fahr, A.; Stano, P. *ChemBioChem* **2010**, *11*, 1989–1992.
- [246] Pereira de Souza, T.; Steiniger, F.; Stano, P.; Fahr, A.; Luisi, P. L. *ChemBioChem* **2011**, *12*, 2325–2330.
- [247] van Hoof, B.; Markvoort, A. J.; van Santen, R. A.; Hilbers, P. A. J. *The Journal of Physical Chemistry B* **2012**, *116*, 12677–12683.
- [248] van Hoof, B.; Markvoort, A. J.; van Santen, R. A.; Hilbers, P. A. J. *The Journal of Physical Chemistry B* **2014**, *118*, 3346–3354.
- [249] Murugova, T. N.; Balgavý, P. *Physical Chemistry Chemical Physics* **2014**, *16*, 18211–18216.
- [250] Arbuzova, A.; Wang, L.; Wang, J.; Hangyás-Mihályné, G.; Murray, D.; Honig, B.; McLaughlin, S. *Biochemistry* **2000**, *39*, 10330–10339.
- [251] Son, M.; London, E. *The Journal of Lipid Research* **2013**, *54*, 3385–3393.

- 
- [252] Budvytyte, R.; Mickevicius, M.; Vanderah, D. J.; Heinrich, F.; Valincius, G. *Langmuir* **2013**, *29*, 4320–4327.
- [253] Gibson Wood, W.; Igbavboa, U.; Müller, W. E.; Eckert, G. P. *Journal of Neurochemistry* **2011**, *116*, 684–689.
- [254] Mondal, M.; Mesmin, B.; Mukherjee, S.; Maxfield, F. R. *Molecular Biology of the Cell* **2008**, *20*, 581–588.
- [255] Sprong, H.; van der Sluijs, P.; van Meer, G. *Nature reviews. Molecular cell biology* **2001**, *2*, 504–513.
- [256] Tanaka, T.; Sano, R.; Yamashita, Y.; Yamazaki, M. *Langmuir* **2004**, *20*, 9526–9534.
- [257] Inaoka, Y.; Yamazaki, M. *Langmuir* **2007**, *23*, 720–728.
- [258] Leirer, C.; Wunderlich, B.; Myles, V. M.; Schneider, M. F. *Biophysical Chemistry* **2009**, *143*, 106–109.
- [259] Sezgin, E.; Kaiser, H.-J.; Baumgart, T.; Schwille, P.; Simons, K.; Levental, I. *Nature Protocols* **2012**, *7*, 1042–1051.
- [260] Hermann, E.; Bleicken, S.; Subburaj, Y.; García-Sáez, A. J. *Bioinformatics (Oxford, England)* **2014**, *30*, 1747–1754.
- [261] Saliba, A.-E.; Vonkova, I.; Ceschia, S.; Findlay, G. M.; Maeda, K.; Tischler, C.; Deghou, S.; van Noort, V.; Bork, P.; Pawson, T.; Ellenberg, J.; Gavin, A.-C. *Nature Methods* **2014**, *11*, 47–50.
- [262] Emberly, E. G.; Mukhopadhyay, R.; Wingreen, N. S.; Tang, C. *Journal of Molecular Biology* **2003**, *327*, 229–237.
- [263] Yamanaka, T.; Horikoshi, Y.; Suzuki, A.; Sugiyama, Y.; Kitamura, K.; Maniwa, R.; Nagai, Y.; Yamashita, A.; Hirose, T.; Ishikawa, H.; Ohno, S. *Genes to Cells* **2001**, *6*, 721–731.



# Acknowledgement

My PhD studies were for me an unexpectedly perilous but at the same time extremely enlightening journey, during which I grew scientifically and personally. This growth was possible only through a fruitful interaction with my colleagues and collaborators and with the constant support of my friends and family members. In particular I would like to thank:

Prof. Petra Schuille for giving me the possibility of join her research group but mostly for her advices and for the extraordinary scientific independence I could experience.

Dr. Salvatore Chiantia for his precious mentoring, for having given me new perspectives when I needed and for having taught me to be a scientist.

Prof. Kirsten Jung for agreeing in representing my PhD thesis and for all her valuable advices.

Dr. Carsten Hoege and Prof. Tony Hyman for their essential inputs in the LGL/aPKC reconstitution project.

My former colleagues Dr. Franziska Thomas, Dr. Fabian Heinemann and Dr. Zdeněk Petrášek for the great teamwork in establishing new methods to measure partitioning coefficients in GUVs.

Dr. Jörg Nikolaus for sharing the HA TM peptides as well as his knowledge about HA reconstitution in model membranes.

Dr. David Drechsel and Dr. Barbara Borgonovo of the Protein Expression and Purification and Chromatography Facilities of the Max Planck Institute of Molecular Cell Biology and Genetics in Dresden for helping me in solving protein purification issues.

Elisabeth Weyher-Stingl, Dr. Sabine Suppmann, Stefan Pettera and Dr. Stephan Uebel of the Biochemistry Core Facility of the Max Planck Institute of Biochemistry in Martinsried for helping me with circular dichroism and mass spectrometry measurements, with the PLAP purification and with the synthesis and labeling of the LGL MTS peptides, respectively.

Former and present members of the lab, Alena Khmelinskaia, Dr. Aleksander Czogalla, Alex Mestiashvili, Andrea Tassinari, Carina Ehrig, Caterina Macrini, Christoph Faigle, Dr. Christoph Herold, Daniela Garcia, Diego Ramirez, Dr. Erdinc Sezgin, Dr. Eugene Petrov, Dr. Frank Siedler, Dr. Grzegorz Chwastek, Dr. Harekrushna Sahoo, Dr. Heiko Keller, Dr. Hetvi Gandhi, Dr. Jakob Schweizer, Dr. Janine Tittel, Dr. Jens Ehrig, Jonas Mücksch, Katja Zieske, Dr. Leon Harrington, Dr. Markus Burkhardt, Dr. Martin Loose, Philipp Blumhardt, Philipp Glock, Dr. Remigiusz Worch, Dr. Senthil Arumugam, Simon Kretschmer, Sonal, Dr. Sven Vogel, Dr. Thomas Weidemann, Dr. Tobias Härtel and Dr. Viktoria Betaneli for having shared your knowledge, critics and comments with me, for the intensive time spent together, for being a colorful acquired family. Special thanks to Dr. Henri Franquelim and Dr. Ariadna Martos Sanchez for the unique mixture of scientific and personal aspects that binds us, Gosia Poczopko and Anna Kaufmann for your stimulating friendship and Dr. Matias Hernandez for having taught me to dance salsa.

Lisa Tübel, a very talented student, who performed part of the  $\zeta$ -potential measurements.

Former and present technicians of the lab, Anke Borrmann, Beatrix Scheffer, Brigitte Hartl, Helge Vogl, Kerstin Andersson, Michaela Schaper, Sabine Knappe and Sarah Herrmann for their ready helpfulness. Special thanks to Karin Crell and Sigrid Bauer for their daily support in Dresden and Martinsried, respectively.

Former and present secretaries of the lab, Claudia Schwäger and Silke Leuze-Bütün for having made my move to Dresden and Martinsried easy and for their everyday help with paper work.

BiPS people and in particular Dr. Kristina Kurgonaitė for the constructive and unforgettable time in Dresden.

My family and all friends coming from my pre-PhD life for being a solid backbone during this challenging time.

And finally Konrad, for having been the perfect partner in my life, without his comfort and encouragement I would have never made it till here.

# Curriculum Vitae

**Ilaria Visco**

**Date and Place of Birth** 3rd of October 1984 in Latina (Italy)

**Nationality** Italian

## Further Education

<b>Sept 2012 — Present</b> Institute  Supervisor	<b>PhD student in Biophysics</b> Max Planck Institute of Biochemistry, Martinsried, Germany Prof. Dr. Petra Schwille
<b>May 2009 — Aug 2012</b> Institute  Supervisor	<b>PhD student in Biophysics</b> Biotechnology Center of the Dresden University of Technology, Dresden, Germany Prof. Dr. Petra Schwille
<b>Sep 2006 — Oct 2008</b> Rank University Supervisor Project	<b>Master of Science in Medical Biotechnology</b> 110/110 cum laude Catholic University of the Sacred Heart, Rome, Italy Prof. Dr. Enzo Ricci Identification of novel modulatory strategies to induce the IBM mesoangioblasts skeletal muscle differentiation
<b>Sep 2003 — Oct 2006</b> Rank University Supervisor Project	<b>Bachelor of Science in Sanitary Biotechnology</b> 110/110 cum laude Catholic University of the Sacred Heart, Rome, Italy Prof. Dr. Massimo Castagnola Identification of cornifin beta isoforms in pre-term newborns' saliva via an HPLC/MS and MALDI/TOF combined approach

## Additonal International Research Experiences

<b>May 2007 — Aug 2007</b>	<b>Summer student of The SickKids Summer Research Program</b>
Institute	The Hospital for Sick Children, Toronto, Canada
Supervisor	Prof. Dr. Charles M. Deber
Project	The calnexin transmembrane segment as a sensor for protein misfolding/assembling in bilayers

## Work related Activities and Responsibilities

	<b>Student Mentoring</b>
<b>2010-2014</b>	Project supervisor for bachelor, master and technical students
<b>Sep 2009 - Aug 2012</b>	Supervisor for lab practicals in biophysical methods
<b>Jun 2009 - Oct 2009</b>	BIOTEC team supervisor iGEM09
	<b>Student Representation</b>
<b>Dec 2014 - Present</b>	Open Access Ambassador, Max Planck Institute of Biochemistry, Martinsried, Germany
<b>Jan 2014 - Present</b>	Department Student Representative, Max Planck Institute of Biochemistry, Martinsried, Germany
<b>Sep 2010 - Sep 2011</b>	Co-founders and Student Representative of the PhD Student Association BiPS, Dresden, Germany
	<b>Outreach Activities</b>
<b>Nov 2014</b>	Open day at the MPI, Max Planck Institute of Biochemistry, Martinsried, Germany
<b>Winter Semester 2011</b>	School Project - Science Goes To School, Dresden, Germany
<b>Jul 2010 - Jul 2012</b>	The Long Night of Sciences, Dresden, Germany

## Academic Achievements

### Publications

**Visco, I.**; Chiantia, S.; Schwille, P. Asymmetric Supported Lipid Bilayer Formation via Methyl-B-Cyclodextrin Mediated Lipid Exchange: Influence of Asymmetry on Lipid Dynamics and Phase Behavior. *Langmuir* 2014, 30, 7475-7484.

Thomas, F.; **Visco, I.**; Petrasek Z.; Heinemann, F.; Schwille, P. Introducing a Fluorescence-based Standard to Quantify Protein Partitioning into Membranes. *Biochim. Biophys. Acta, Biomembr.* submitted.

### Awards

<b>Dec 2010</b>	<b>Registration Award</b> awarded by the 3rd European Workshop on Advanced Fluorescence Imaging and Dynamics
-----------------	--



---

<b>Oct 2008</b>	<b>Special Mention Award</b> in recognition of the academic results awarded by the Catholic University of the Sacred Heart
	<b>Conferences</b>
<b>Feb 2014</b>	<b>Poster</b> Annual Meeting of the Biophysical Society, San Francisco, USA
<b>Dec 2010</b>	<b>Talk</b> European Workshop on Advanced Fluorescence Imaging and Dynamics, Munich, Germany
<b>Aug-Sep 2010</b>	<b>Poster</b> WE Heraeus Seminar: Selforganization in Cell Assemblies and Tissues, Bad Honnef, Germany
<b>Jun 2010</b>	<b>Talk</b> Cell Model Systems Summer School, Rome, Italy